DEVELOPMENTS IN NUCLEAR MICROPROBE ANALYSIS

THE MEASUREMENT OF THE SPATIAL DISTRIBUTION OF STABLE ISOTOPE TRACERS

BY

P. M. POLLARD

A DOCTORAL THESIS

SUBMITTED IN PARTIAL FULFILMENT OF THE REQUIREMENTS
FOR THE AWARD OF

DOCTOR OF PHILOSOPHY OF THE LOUGHBOROUGH UNIVERSITY OF TECHNOLOGY

SEPTEMBER 1981

M A R I T O E T F A M I L I A E P R O
O P E A U X I L I O Q U E P E R P E T U O

ACKNOWLEDGMENTS

It is with great pleasure that I wish to thank Mr. J. W. McMillan of A.E.R.E. Harwell for helpful advice, interest and stimulating enthusiasm throughout this investigation, which has been greatly appreciated. I also wish to thank Dr. D. J. Malcolme-Lawes of Loughborough University for his supervision and continued interest and advice.

I also wish to express my gratitude to:

Mr. F.C.W. Pummery, Dr. M. J. Bennett and Mr. M. R. Houlton of A.E.R.E. Harwell for their collaboration in the carburization experiments with PE16.

Dr. D. Clarkson and Mr. J. Sanderson of A.R.C. Letcombe Laboratory for their collaboration in the labelling of Barley roots with ^{15}N.

Mr. R.A.P. Wiltshire of A.E.R.E. Harwell for the loan of high quality α-sources and advice on α-spectrometry.

Dr. J. M. Adams, Dr. J. A. Cookson, Dr. N.E.B. Cowern, Dr. G. Dearnaley, Mr. F. D. Pilling and Dr. C. J. Sofield all of A.E.R.E. Harwell for very useful discussions on various aspects of the work.

The operating staff of the Harwell I.B.I.S. accelerator for their willing assistance and co-operation, in particular providing good microbeams of very low intensity.

The operating staff of the Harwell 6 MeV Van de Graaf and Tandem Van de Graaf accelerators.

The skill of the staff of B.220 (A.E.R.E. Harwell) Engineering workshops in manufacturing accelerator chamber equipment was invaluable and greatly appreciated.

I also wish to acknowledge the Science Research Council for my research grant and A.E.R.E. Harwell of the U.K.A.E.A. for allowing the use of their many experimental facilities and financial support through the granting of an Extramural Research Contract.

ABSTRACT

The potential of the nuclear microprobe for the determination of spatial distributions of stable isotope tracers has been examined.

In a preliminary study the sensitivity of the isotope selective modes of operation of the microprobe (backscattering and nuclear reaction analysis) for the measurement of stable isotopes was examined using Mg, Si, Ni and Co as examples. The use of backscattering analysis coupled with high resolution detectors and heavy ion beams was assessed using Mg, Si, Ni and Ag as examples and found to be of limited application for stable isotope tracer studies. Nuclear reaction methods were considered to be most suitable for the measurement of low atomic number elements, and tracer studies involving ^{7}Li, ^{13}C and ^{15}N were carried out to demonstrate the application of the method.

^{7}Li is effectively a stable isotope tracer produced in B_4C assemblies within fast reactors. It can be used as an indicator for the boron burn-up, and to this end ^{7}Li profiles were determined for some sample assemblies using the $^{7}Li(p,\alpha)\alpha$ reaction.

A comprehensive study of ^{1}H, ^{2}H, ^{3}He and ^{4}He induced reactions with ^{12}C and ^{13}C and of the value of these reactions for the measurement of ^{13}C and $^{13}C/^{12}C$ ratios was carried out. Samples of the alloy PE16 which had been exposed to ^{13}C labelled CO_2 were examined using the $^{13}C(d,p)^{14}C$ and $^{12}C(d,p)^{13}C$ reactions to determine the $^{13}C/^{12}C$ and ^{13}C profiles. The $^{16}O(d,p)^{17}O$ reaction was used for the simultaneous measurement of oxygen profiles, thus allowing correlations between oxidation and carburization to be made.

Nitrogen uptake profiles were measured across barley roots which had received various treatments in ^{15}N labelled NH_4NO_3, using the $^{14}N(d,p)^{15}N$ and $^{15}N(p,\alpha\gamma)^{12}C$ reactions. This investigation involved the development of handling and measurement techniques for studying extremely beam-damage-sensitive organic materials with focussed ion microbeams.

LIST OF CONTENTS

LIST OF FIGURES

FIGURE 8.7 γ spectrum of natural urea using 1.9 MeV deuteron beam. (GeLi Detector).

FIGURE 8.8 Photographs of 100 μm barley root sections mounted on nickel blocks with a 2 μm carbon flash.
(i) Before and
(ii) After bombardment using microbeams.

FIGURE 8.9 3 of the 16 spectra of a 2d γ spectrum of an enriched urea standard (44.5 wt. % ^{15}N) obtained using a $^{15}N(p\alpha\gamma)^{12}C$ reaction and a NaI(Tl) detector.

FIGURE 8.10 3 of the 16 spectra of a 2d proton spectrum of a natural urea standard obtained using the $^{14}N(d,p)^{15}N$ reaction and a $150mm^2$ annular surface barrier detector.

FIGURE 8.11 Schematic diagram showing the mounting of barley root sections ready for microbeam analysis.

FIGURE 8.12 Dual parameter gamma spectrum of a barley root labelled for 48 hours in the ^{15}N labelling culture B (given in Table 8.4) obtained using the $^{15}N(p,\alpha\gamma)^{12}C$ reaction and a GeLi detector.

FIGURE 8.13 Dual parameter proton spectrum of a 100 μm thick barley root section treated for 24 hours in the ^{15}N labelling culture B (Table 8.4). Beam scanned across the section's central xylen vessel.

FIGURE 8.14 Profile of the average ratio wt. % ^{15}N : wt. % ^{14}N across barley root sections labelled for 2 hours in ^{15}N culture B.

FIGURE 8.15 Profile of the average ratio of wt. % ^{15}N : wt. % ^{14}N across barley root sections labelled for 24 hours in ^{15}N culture B.

FIGURE 8.16 Profile of the average ratio of wt. % ^{15}N : wt. % ^{14}N across barley root sections treated initially for 24 hours in ^{15}N culture B and subsequently in ^{14}N culture A for a further 24 hours.

CHAPTER 1

INTRODUCTION

Over recent years there has been an increasing demand for stable isotope tracers, particularly for the study of physicochemical and biochemical processes [1, 2]. This upsurge in their use can be attributed to increased availability, the introduction of better methods of analysis and the non-existence or unsuitability of radioactive tracers for some elements for example for oxygen and nitrogen. In some cases the introduction of a radioactive tracer might be barred or the radioactivity of the tracer may be overwhelmed by the inherent radioactivity of the sample. Thus the use of a stable isotope tracer can be an attractive alternative especially since in the investigation of many processes isotope ratio values, rather than tracer concentrations alone, are far more informative. In addition to measuring stable isotopes used as tracers in mechanistic studies one may also wish to examine the isotopic composition of some elements which have been disturbed by nuclear transmutations, for example the stable isotope ratios of elements in meteorites [3].

1.1 AVAILABLE TECHNIQUES FOR THE DETERMINATION OF STABLE ISOTOPE TRACERS

There are several techniques which have been used for the determination of stable isotopes, namely mass spectrometry, emission spectrometry, infrared spectrometry, nuclear magnetic resonance and nuclear methods of analysis. These techniques are discussed in succession below.

1.1.a Mass Spectrometry

Mass Spectrometry [4, 5] is probably the most frequently applied technique. Part of the sample under interrogation is converted into positive or negative ions, often these ions are then accelerated and then analysed by their behaviour on transmission through electrostatic or magnetic fields. Qualitative information is obtained from the ion trajectory which is used to identify the mass charge ratios of the ions and hence parent atoms or molecules and quantitative data can be obtained by relating the ion intensity to the concentration. The detailed behaviour of and and the equations governing, the ion trajectories under the influence of a magnetic field are given in Section 2.3 and under the influence of an electrostatic field in Section 3.1.a. Mass spectrometry has an

excellent sensitivity and is capable of measuring small changes in isotopic abundance. Isotope dilution mass-spectrometry can be used to monitor small changes in isotopic abundance and is often used where the significant impurity elements have already been identified and analysis of just one or two specific elements is required. For this type of analysis a known amount of isotopically enriched tracer of the required element is added to a known amount of that element, isotopic exchange ensues before separation and purification of the required element ready for mass-spectrometry. Sensitivities [6] as low as 10^{-11} to 10^{-15}g have been reported.

There are many different ways of producing the ions ready for mass spectrometry including d.c. arc methods, thermal ionisation, electron impact and inductively coupled plasmas. An important method is that used in a probe modification of mass spectrometry, secondary ion mass spectrometry (S.I.M.S.). The sample is sputtered by ion bombardment as shown in Figure 1.1. The bombarding ion beam will either loose all of its energy within the sample in a collision cascade process or it can eject a sample particle as an ion or neutral. In a typical analysis system the sputtered ion beam then passes through an extractor lens, thence through a double focussing (mass and energy) analyser to an ion detection system. Secondary ion mass-spectrometry [8] in its probe modification has a good spatial resolution, < 10μm, which is comparable to that of the nuclear microprobe described in Chapter 2, however it is more typically run with a resolution of 70μm with an absolute sensitivity of $<10^{-8}$g [4]. It is acceptable for the measurement of mass ratio values but suffers from notorious difficulties in measuring absolute concentrations. These difficulties primarily arise because the yield of secondary ions varies dramatically with the chemical state. A familiar disadvantage is that the sampling technique is destructive as discussed above.

A new technique related to S.I.M.S., laser probe mass spectrometry [9] has been developed and appears to have a similar capability for the spatial determination of stable isotopes in both thick and thin targets. A spatial resolution as high as ≃1μm can be attained and typically the absolute sensitivity range is about 10^{-18} to 10^{-20}g [9]. A laser probe mass spectrometer which is particularly interesting is that detailed by Hillenkamp [10] which is particularly suited to the analysis

of biological samples, a sample type discussed in detail in Chapter 8. The samples must be thin (0.1 to 2 μm) enough to be perforated by the laser shot. Thin sections of organic materials, metal foils, coatings of evaporated materials, dust particles and various biological specimens (teeth, hair, smears of cells, wood) can be investigated. Hillenkamp used a frequency doubled ruby laser. The laser shot is focused on to the specimen by an incident light microscope to a spot nominally 0.5 μm. The microplasma generated from each irradiated volume is analysed in a time-of-flight mass spectrometer, providing the capability of multielement analysis. Since chemical separation cannot be used prior to the spatial investigations of the samples using either of these two mass spectrometry probe techniques the problem of overlap of identical mass/charge ratios will tend to occur more frequently than in conventional bulk analysis using mass spectrometry.

1.1.b Emission Spectrometry

Emission Spectrometry [11] while having good sensitivity is much less popular. Although for arc emission spectroscopy absolute sensitivities in the range 4×10^{-9}g to 1×10^{-5}g [12] and for copper and graphite spark spectroscopy 2×10^{-10}g to 2×10^{-6}g have been obtained it is extremely difficult to resolve isotopes and depending on the isotopes involved, isotopic sensitivites will be considerably poorer. Many variations of emission spectroscopy techniques exist, being based on the phenomena of light emission after excitation of valence electrons and at wavelengths characteristic of the isotopes present. The differences in wavelengths of photons emitted from different isotopes are very small, demanding the use of a very high resolution wavelength dispersive system. (The isotopic shifts are greater for light elements than for heavier elements because of their larger relative differences in isotope mass. The greater the effective difference between masses the more influence is exerted on charge distribution of electrons in the nucleus and the greater the effect on the emission lines). Using high resolution systems isotopes of the elements of up to uranium have been detected. Generally only bulk information can be obtained although spatial resolutions of 10-50 μm have been reported [11] using a Laser Spark Microprobe, but in non-isotopic applications.

1.1.c Infrared Spectrometry

Infrared Spectrometry [13] gives information about molecular structure by virtue of the changes in molecular rotational and vibrational energy that occur under certain conditions by the interaction of infrared radiation with samples. It has primarily been used with gases and with liquids and solids which are transparent to most of the wavelengths of interest. Unfortunately metals are inherently opaque to infrared radiation because the free electrons which give metallic characteristics follow the applied oscillating electric field and do not allow the field to penetrate the metal to any significant extent. A technique, "infrared reflection-absorption spectroscopy" [4], has been developed to try to observe metal samples, however it is a difficult technique in practise and the absorption bands obtained are very weak.

The presence of different isotopes can greatly alter the appearance of an I.R. spectrum due to changes in the spacings of vibrational and rotational levels as the same force constant acts upon an increased nuclear mass. Changes in the relative intensities and frequencies of vibrational transitions are observed. For instance the effect on measured bondstretch frequencies of the ^{1}H and ^{2}H isotopes of hydrogen in ethene are given below in Table 1.1.

TABLE 1.1: VARIATION OF BONDSTRETCH FREQUENCIES IN ETHENE WITH ISOTOPIC SUBSTITUTION

Molecule	Wavenumber for the double bond (cm^{-1})	Wavenumbers for the four single bonds (cm^{-1})
$H_2C = CH_2$	1623	2990, 3010, 3106, 3108.
$D_2C = CD_2$	1515	2200, 2251, 2304, 2345.

As a surface analysis technique infrared spectroscopy has the advantage of barely disturbing the sample surface, although the technique is limited in sample application and is better suited to bulk rather than spatial analysis.

1.1.d Nuclear Magnetic Resonance

Nuclear Magnetic Resonance [14, 15] is generally fairly insensitive except under certain favourable circumstances with high resolution N.M.R. spectroscopy of certain nuclides, usually only one isotope of an element, when absolute sensitivities of $<10^{-8}$g [15] have been achieved. However it does give an unambiguous identification of a nuclide. N.M.R. depends on the magnetic properties of atomic nuclei and involves magnetic dipole transitions between well defined energy levels. Many atomic nuclei possess small magnetic moments and behave like spinning bar magnets, only nuclei with both mass and atomic numbers even have zero spin and no moment. Two external fields are required for nuclear magnetic resonance analysis, a strong magnetic field H_o and a linear oscillating field H_1 perpendicular to H_o. In the presence of the magnetic field H_o a nucleus of non-zero spin can take up one of several levels (For Hydrogen, spin $I = \frac{1}{2}$ there are 2 levels, the spinning nucleus is either aligned in resonance with the field or flipped over so as to oppose it). It is possible to excite transitions between these levels by the application of energy of the appropriate frequency. The resonance condition at a fixed value of H_o will only have one corresponding oscillating frequency at which the system can absorb energy. The chemical environment of a nucleus affects its resonance frequency because variations in electron density alter the shielding experienced by the nucleus and thus the shift in field strength H_o needed to bring the nucleus back into resonance in different environments, gives information on the chemical environment of the nucleus. (This shift is thus often called the chemical shift).

Most instruments are of the high resolution type with parameters suited to detecting the resonance of one nuclei only. Notable progress has been made in developing high resolution techniques to allow the measurement of the molecular location of isotopes such as ^{13}C, ^{15}N and ^{17}O. However the highest resolution is only attained for liquid specimens, solid state spectra being somewhat broadened. Normally solids are dissolved in non protonated solvents. Again this is a destructive, bulk analysis technique. At the high resolutions only the fine structure in the resonance of the one nuclide is measured, isotopic ratios cannot be measured directly.

1.1.e Nuclear Methods

Nuclear Methods of stable isotope analysis depend on the interaction of nuclear particles with the nuclides of interest. These methods are readily applicable to isotopic analysis because the nuclear properties of the isotopes of an element are often widely different. For example in the nuclear reaction analysis of oxygen using the (p,α) reaction, because of reaction kinetics (explained in detail in section 3.1.b) a highly selective isotopic analysis is achieved for ^{18}O [16]. This arises because the energy of the α particles emitted from the $^{18}O\ (p,\alpha)^{15}N$ reaction is much greater than the corresponding energies from ^{16}O and ^{17}O. As discussed in Chapter 3 interference from isotopes of other elements may occur.

These methods fall into two main categories the first relying on delayed measurement of the induced activity in the product nucleus and the second using prompt methods of analysis which measure the scattered and emitted products immediately. Both of these two main categories can be adapted to provide spatial information on tracers. Tomographic examination with γ-detectors, of samples activated using neutrons or photons of γ-ray energies can provide three-dimensional information on the variation in concentration of the activated nuclides in a sample. However only moderate resolution has been achieved [17]. More commonly isotopes have been measured by autoradiographic techniques [18, 19] using different emulsions. However the nuclear technique with the greatest potential, and which is studied in this thesis, is sample interrogation with charged particle microbeams (or "ion microbeams") and the measurement of prompt emissions. Using these microbeam methods the spatial distribution of isotopes in materials can be determined from the particle groups, gamma-photons, neutrons, X-rays and scattered particles emitted from small regions interrogated with charged particle microbeams [20, 21].

The nuclear microprobe is a relatively new analytical tool in the field of ion beam analysis, which proffers the possibility of measuring fine spatial [22] distributions of elements and isotopes in materials. This opportunity arises because two of the analytical modes of the nuclear microprobe, namely nuclear reaction analysis and backscattering analysis, are isotopically sensitive. It also has the advantage of being essentially a non-destructive multi-mode technique

and can provide a wide variety of compositional information. Using the highly focused ion beams of a nuclear microprobe in conjunction with the two isotopically sensitive analytical modes, isotopic analysis at high spatial resolutions can be achieved, for instance 1μm resolution is attainable on the Oxford University microprobe. If required subsurface changes in composition to depths of ca. 3 μm [23] may also be measured using either Rutherford backscattering analysis or certain nuclear reactions [43]. Maximum advantage of the method is gained by utilising the maximum information provided by the interaction of the probe and target, thus another nuclear microprobe mode, ion beam induced X-ray analysis [24, 25] may prove useful. Although the X-ray analysis is not isotopically sensitive it could be used to measure total elemental concentration in order to obtain ratios of tracer to total elemental content. It would, additionally, readily indicate the presence of sample impurities. A detailed explanation of the nuclear microprobe is given in Chapter 2.

Very few stable isotopes have as yet been studied using the nuclear microprobe, in fact its use has been limited to $^{10}B/^{11}B$ [26] and to ^{18}O and ^{2}H [16, 27]. The advantages and limitations of both nuclear reaction analysis methods and backscattering analysis methods are examined in detail in this thesis and the range of isotopes for which the technique of stable isotope tracing using the microprobe is applicable is explored paying particular attention to selectivity and sensitivity.

1.2 COMPARISON OF THE AVAILABLE TECHNIQUES

With the growing number of surface and trace instrumental analysis methods it is important to ascertain the advantages and limitations of the techniques available. It is unlikely that any one technique alone will suit all purposes. In analysis it is always preferable to obtain as much information as possible about a sample, although time and finance may well curtail this ideal. In selecting the technique most applicable, selectivity and sensitivity are of utmost importance, although wide applicability and ease of operation of the technique are also desired. In the spatial determination of stable isotope tracers the latter two points may have to be compromised by the rigours of obtaining high sensitivity and selectivity. A comparison of the available techniques is given in Table 1.2 below.

TABLE 1.2: COMPARISON OF THE AVAILABLE TECHNIQUES

TECHNIQUE	COMMENTS	SPATIAL RESOLUTION AND SENSITIVITY
MASS SPECTROMETRY	Only S.I.M.S. and Laser probe mass spectrometry techniques can provide direct instrumental spatial measurements without prior tedious mechanical sample segmentation. Both suffer overlap of identical mass charge ratios especially as prior chemical separation cannot be used. Both rely on destructive sampling methods. Isotopic Tracer Method.	S.I.M.S. spatial resolutions <10μm, usually 70μm sensitivity $<10^{-8}$g (4). Laser probe spatial resolutions 1μM, Sensitivity (9) 10^{-18} to 10^{-20}g.
EMISSION SPECTROMETRY	Samples generally must be made conducting. Destructive Sampling. Bulk Analysis Method.	Sensitivity (12) 1×10^{-5}g - 4×10^{-9}g usually far poorer for isotopic measurements.
INFRARED SPECTROMETRY	Limited in sample type application. Bulk Analysis Method	Sensitivity (13) not for trace elements, usually > 1% ± 0.5%.
NUCLEAR MAGNETIC RESONANCE	Limited in sample type. High resolution N.M.R. important for molecular location of ^{13}C, ^{15}N, ^{17}O Bulk Analysis Method.	Under favourable high resolution N.M.R. sensitivities (15) $< 10^{-8}$g. Usually only for 1 isotope of an element.
NUCLEAR METHODS	Using nuclear microprobe. Good selectivity, of complex samples. Multi-mode for much simultaneous information. Sensitivity and interferences vary considerably for different isotopes. Particularly suited to elements of light to medium mass. Non-destructive sampling. Isotopic Tracer Method.	Spatial resolutions 1μm, usually 5-10μm. Sensitivity varies greatly with isotope Depth range usually only a few μm.

For the spatial analysis of stable isotope tracers one is only really left with a choice between the techniques based on the two probe modifications of mass spectrometry and that based on ion microbeam analysis. The mass spectrometry techniques may suffer extensively from overlap of identical mass/charge ratios. (Although when a high powered laser is used in the laser probe technique it should not suffer so actuely as S.I.M.S. This is because it should reduce the additional complications caused by the presence of molecular as well as atomic species. The likelihood of molecular species being present depends on the power of the laser used and the Z number of matrix elements present.) However when one uses ion microbeam analysis in conjunction with nuclear reactions one can usually circumvent any ambiguity and often by careful choice of reaction and experimental parameters one can obtain a highly selective analysis of the desired nuclide, even in very complex samples. Another disadvantage with both of the mass spectrometry techniques is that they rely on destructive sputter sampling and are affected by any nonuniformity in the sputter rate. Nuclear microprobe analysis is essentialy non-destructive. Thus the use of the nuclear microprobe for the non destructive spatial analysis of stable isotopes shows great promise. This thesis describes the investigation, development and application of the nuclear microprobe to the spatial analysis of stable isotopes.

CHAPTER 2

EXPERIMENTAL FACILITIES AND EQUIPMENT DESIGN

2.1 THE EXISTING NUCLEAR MICROPROBE FACILITY

The essential features of the Harwell nuclear microprobe are shown in Figure 2.1. A 3 MeV electrostatic generator, IBIS, accelerates a charged particle beam produced by an R.F. ion source. The vital feature of the nuclear microprobe is its ability to focus the accelerated charged particle beam to a very small intense beam spot. Initially microbeam work used collimated beams [28, 29], however these had low spatial resolutions and low ion beam intensities. The magnetic focusing system now used on IBIS is shown in Figure 2.2.

A small part of the accelerator beam passes through an aperture which acts as an object for the lens, a set of four quadrupole magnets in the form of a Russian quadruplet [30]. A demagnified image, demagnification factor 5.8, of the beam spot at the aperture is then produced 21cm beyond the last quadrupole as shown in Figure 2.2. The four quadrupole magnets are clearly seen in Figure 2.3 which shows a general picture of the chamber end of the nuclear microprobe. The beam spot, when incident on a viewing quartz, can be observed through the microscope placed at the back of the target chamber as seen in Figures 2.1 and 2.4. It is necessary to be able to see the beam in the chamber in order to ensure that it is the desired size and shape and to see its exact position. When a beam spot of approximately the required size and beam current is seen on the back viewing quartz one can watch as the position and current of the quadrupole lenses are altered to give the fine focusing needed to produce the extremely well defined small microbeams required. The position of the chamber itself can be moved in both the X and Y planes to centralize the position of the beam within the chamber. When measuring linear scans using nuclear reactions to detect light elements the permissible beam spot size is only tightly limited in one direction, that of the proposed scan. If one wishes to have as much beam current as possible for this type of scanning only three of the four magnetic lenses are required and typically the current density is 5 times that with all four lenses, the demagnification factors being 8.8 and 18.9. Several other types of focusing systems using electrostatic lenses, or variations on this magnetic quadrupole system have also been developed [31-35] producing beams down to a few microns in size. Although in the early 1970's the Harwell nuclear microprobe was the only ion microprobe there are

now more than 16[25] and most of these currently in use have a focusing system of the same general form as that shown in Figure 2.2. One of the limitations of the Harwell microprobe is a maximum mass-energy produce of 22 MeV-amu which dictates the range of beams and energies which can be successfully bent and focused onto the target.

The spatial information required can be obtained either by electrostatic scanning of the beam or by mechanical movement of the sample table using stepping motors. Elemental maps can be obtained by two dimensional scanning[36] using the electronic system shown in Figure 2.5. Generally mechanical scanning is most useful for linear scanning to obtain compositional information along a line. Long distances, up to 25mm across a sample can be measured by mechanical movement of the sample holder with respect to the beam using stepping motors. The distances between sampling points can be varied greatly, step sizes in the range 0.25 - 250 μm are available. There are three stepping motors in the chamber x, y and z. The z movement is only used to rotate the sample holder, seen in Figure 2.4, and locate the specimen in the beam path. Scanning may be carried out in the X and Y directions only. The side microscope can also be seen in Figure 2.4 and allows the front face of the sample to be viewed over the area of the sample to be scanned. A diagram of the mechanical scanning and data collection system[36] is seen in Figure 2.6. Electrostatic scanning is most useful for rapid continuous scanning over relatively small distances of about 500 μm. It is also useful to reduce beam damage when analysing sensitive samples by time averaging energy deposition. This type of scanning is achieved by passing a current from, for example, a sawtooth generator through the scan plates at either 50 or 500 Hz as shown in Figure 2.7. The same sawtooth can be used to simultaneously trigger the bright up on a cathode ray oscilloscope or to trigger a multichannel analyser working in dual parameter mode. This latter method of coincidence scanning data collection was used in Chapter 8 for the analysis of $^{15}N/^{14}N$ in all materials. A schematic diagram of the type of electronics used for dual parameter data collection is given in Figure 2.8, the energy spectrum and position of each event being stored in a canberra multichannel analyser operating in dual parameter mode. This typeof data is fully quantitative. For 2 dimensional (x,y) raster scanning, when the beam is scanned in synchronism with the electron beam of an oscilloscope the data obtained is only semi-quantitative.

The species emitted or scattered, on bombardment of the target by a charged particle beam, can be measured by a variety of detectors at different geometries and the standard detection systems are detailed below.

For nuclear reaction analysis the charged particles emitted are usually detected by a surface barrier detector at an angle of 135^{o} to the beam. Absorber foils are used to prevent scattered particles from reaching and saturating the detector. The electronic instrumentation typically consists of a preamplifier and main amplifier which feed the detector output signal to a multichannel analyser and often also to one or more single channel analysers with windows set to count over the peaks of interest. X-rays can be simultaneously detected with a silicon/lithium detector and used to indicate whether or not the beam is on the sample, as well as for elemental analysis. X-ray analysis may be used in conjunction with nuclear reaction analysis to determine isotope ratios, the former measuring total elemental concentration while the latter measures the concentration of an isotope.

A detailed view of the chamber facilities including the charged particle and X-ray detectors can be seen in Figure 2.4. The door of the chamber stands open and attached to the backplate are the back microscope used for viewing the beam, the stepping motion and the sample wheel. The sample wheel holds five sample mounts and a viewing quartz. On the right of the chamber one can see the copper cold finger and its dewar. The cold finger is used as a cryogenic trap for species (particularly carbon) present in the system which would otherwise be deposited on the sample surface during irradiation. Just above the copper cold finger one can see the microscope for viewing the front of the samples. The central hole allows the focused beam to pass through. In the chamber cone a surface barrier detector in its perspex holder sits top centre and the Si-Li X-ray detector can be seen on the left of the cone. The photograph in Figure 2.3 shows the modified backplate described later whereas Figure 2.4 shows the usual chamber backplate used for charged-particle detection analysis.

Isotope distributions are usually measured quantitatively by discontinuously scanning the ion beam across the sample and at each point on the scan, whilst the beam is stationary, collecting all the particles of interest. At the end of each irradiation the data from the counters is recorded and the ion beam automatically moved on. In order to ensure that each point in the scan receives the same irradiation dose, usually 1 μC, a beam current integrator (measuring the beam current falling on the sample) is used to control the counters and stepping motor. The entire electronic system used is shown in Figure 2.9.

2.2 MODIFICATIONS TO THE EXISTING NUCLEAR MICROPROBE FACILITY

Many modifications to and extensions of the existing nuclear microprobe detection systems were designed in order to carry out high resolution backscattering experiments and experiments requiring Ge(Li), NaI(Tl) or neutron detectors. These new detection systems are described below.

2.2.a High Resolution Backscattering Detection System

The rigours of high resolution backscattering analyses using silicon surface barrier detectors, necessitated the use of a low noise, high quality electronic system. The output from the detector is fed through an Ortec 142A preamplifier and an Ortec 471 spectroscopy main amplifier into a multichannel analyser. In order to reduce electronic noise a filtered, stabilised mains supply was installed (in conjunction with a clean earth) to run all the electronic instruments of the analysis system.

In order to optimise mass selectivity in high resolution backscattering analyses the angle of observation should be as high as possible, as explained in detail in section 3.1.a. The existing angle of collection was only 135^{o} thus it was necessary to design a holder for a small surface barrier detector at the highest possible observation angle. The confined chamber space posed geometrical problems but an observation angle of 170^{o} was achieved. One of the design drawings is given in Figure 2.10. The holder is held in place by a single watchmaker's screw which passes through the insulating and positioning perspex wedge. The thread was precision drilled into the chamber cone itself. The small 'T' mount surface barrier detector is inserted into the holder once the holder is in position in the chamber and the collimator is then pushed over the holder. Both collimator and holder are clearly seen in Figure 2.11 and the position of the assembly in the chamber is shown in Figure 2.12. An arc shaped collimator slit is required since the scattering angles fall in cones, and when one is working so close to the incident beam line the change in scattering angle subtended by a rectangular or circular slit would be significant.

The detector resolution obtained using the newly provided facility, with optimised electronics and a clean earth, was tested in an accelerator environment using α-spectrometry. The detector was positioned in the scattering chamber and a very thin high resolution

Cm-244 source placed in the chamber instead of a target. The beam stop prevented the accelerated beam from hitting the α source. The two main α peaks at 5.806 MeV and 5.763 MeV were used for energy calibration and the FWHM of the 5.806 MeV peak [37] used as the resolution check. The α-spectrum of Cm-244 is shown in Figure 2.13, typically the overall instrumental resolution obtained was about 13 to 13.5 KeV FWHM (Full Width at Half Maximum).

2.2.b Gamma-Ray Detection System

One of the facilities required for stable isotope analysis using certain nuclear reaction methods is a γ-ray detection system. Both a 76mm x 76mm NaI(Tl) detector and a 100cm^3, 17.4% efficient Lithium drifted Germanium detector with a 1.93 KeV FWHM @ Co^{60} 1.33 MeV γ, were aquired. The usual chamber arrangements had to be modified to decrease the detector to target distance. A special modified door shown in Figure 2.14 was designed which allowed the γ-detectors to within 14mm of the target. The detector 'hat' precluded the use of a z motion so a system was designed to allow maximum travel in the x and y directions. The sample plates and bracket are shown in detailed design in Figure 2.15. The NaI(Tl) detector is fairly light and was fairly readily supported in the detector 'hat' however the Ge(Li) detector with its 15 litre liquid Nitrogen dewar weighed 23Kg. The nuclear microprobe system is supported on vibration free concrete pillars some 6 metres high, however the rest of the working cabin remains subject to vibration with all its inherent microphony problems for Ge(Li) detection. A system was designed to support the Ge(Li) detector from the vibration free microbeam tube support.

Not only had the Ge(Li) detector support system to be substantial enough to take the weight expected, it also had to move in the x, y and z axes in order to follow the movement of the chamber when focussing different mass beams of various energies and also to allow removal of the detector from its position within the chamber to allow sample changing. Two of the design drawings are given in Figures 2.16 and 2.17 and a general overall view is shown in the photograph in Figure 2.18. The two thick support channels clearly seen in Figures 2.16 and 2.17 were attached to the vibration free beam line. The sliding support rail was made out of P.T.F.E. for ease of movement, likewise a thin P.T.F.E. sheet was placed between the 2 flat cryostat support plates for ease of

movement from side to side. The end stop plate attached to the frame ensured the correct repositioning of the detector within the detector chamber 'hat' after a sample change. The whole system was found to give free movement in the x, y, and z directions and thus one was easily able to follow the positions of the chamber. To allow use of the NaI(Tl) detector a small holder was provided which bolts onto the top moveable_dural plate.

Data collection was carried out by feeding the signal from the detector and preamplifier into an Ortec 571 spectroscopy main amplifier and then either straight into an 8100 Canberra Multichannel Analyser or through the 2d coincidence scanning electronics shown in Figure 2.8.

2.2.c The Neutron Detection System

The counting system for neutrons used a 51mm x 51mm Nuclear Enterprise liquid scintillant (type NE213) proton recoil detector placed at 0^{o} to the incident beam. The modified backplate shown in Figures 2.1 and 2.14 was used in order to decrease the target to detector distance. Figure 2.19 shows the electronics used. The output of the detector, which collects both neutrons and γ-rays, was fed after amplification into a pulse shape discriminator [38] which separated the neutrons and gammas by comparison of two weighted time integrals of the detector output. The shorter time integral represented the gamma yield, the longer one both neutrons and gammas. Data aquisition was carried out as described for charged particle analysis.

2.3 THE BUECHNER MAGNETIC SPECTROMETER

Another experimental facility used in an attempt to extend the mass limit of resolution for stable isotope analysis using backscattering analysis (as described in detail in Chapter 4) was a single focusing Buechner magnetic spectrometer. The Buechner spectrometer [39] is one of the earlier types of spectrometers, England's book [40] describes both this and several more recent spectrometers in detail.

A schematic diagram of the spectrometer facility used is shown in Figure 2.20. The accelerated charged particle beam impinges on the sample, is backscattered and passes through the magnetic spectrometer entrance slit. For this system the optimum resolution, typically 8-9 KeV F.W.H.M. was attainable at its highest scattering angle, 145^{o}, with a solid angle of 0.175 msr. The trajectory of the scattered particle M, charge q and energy E

in MeV (dictated by initial beam energy and backscatter kinematics) in a magnetic spectrometer field intensity B(MHz) is given in equation 2.1

$$\frac{q^2}{M} = \frac{2E}{(BR)^2} \qquad \text{... Equation 2.1}$$

where R cm is the radius of the particle trajectory. Inherently there is some ambiguity since different masses with different charge states could conceivably lead to the same value of q^2/M.

After passing through the magnet of the spectrometer the backscattered particles were detected using a 5cm long Ortec position sensitive surface barrier detector [41] (P.S.D.) for the simultaneous determination of charged particle energy and position. The P.S.D. was mounted in the focal plane of the magnetic spectrometer. A schematic diagram of the P.S.D. is given in Figure 2.21 along with the electronics used in conjunction with it for simultaneous energy and position measurement. The energy and position signals were processed after amplification by an Ortec 464/5 position sensitive analyser, displayed on a multichannel analyser and stored on magnetic tape. The maximum of the energy and position signals had to coincide thus extra delay had to be introduced when necessary. Only a small portion of the backscatter spectrum can be analysed by the P.S.D. for any given magnetic field setting. Whilst keeping all other parameters constant, a different energy range of the spectrum can be collected by altering the ~~frequency~~ magnitude of the field. For the convenient analysis of a sample it is desirable to choose an incident beam and beam energy such that given the correct choice of frequency the whole of the energy range containing the isotopes of interest can be collected on the length of the P.S.D.

In order to set up the magnetic spectrometer the P.S.D. was mounted on a support which holds it in position in the focal plane of the magnets and the whole system was then evacuated. The complete spectrometer was placed at the maximum backscatter angle of 145^0, dictated by the physical dimension of the magnets which at this angle only just avoid the beam line. An α-source, Cm-244, was placed in the chamber to simulate backscattered particles. The frequency required to collect the Cm-244 5.806 and 5.763 MeV α peaks in the middle region of the P.S.D. can be calculated using equation 2.1 and tabulations of R vs position on the P.S.D. for the system used. A typical calibration spectrum is seen in Figure 4.4.

In order to check the linearity of the P.S.D. a polished gold target was placed in the chamber and the backscatter from an impinging 5.8 MeV $^4He^+$ beam was recorded. The 5cm long P.S.D. was found to have a very good linearity except for an 8.5% increase in yield for 0.09 cm of its length at the high energy end of the spectrum. When collecting sample spectra the frequency was choosen preferably to position the spectral region of interest into the middle of the P.S.D. but always to avoid the non-linear region.

2.4 TARGET PREPARATION

Frequently positional information in the form of linear scans across a cross-section of a sample is required. The cross-section is cut and then must be polished to expose a flat, clean surface for interrogation. It is important to have flat surfaces for both backscattering and Nuclear Reaction analysis. Anomalous scattering from uneven samples will occur and make backscattering measurements very ambiguous, since the scattering of the incident beam by matrix nuclides at various angles from an uneven sample surface, could conceivably lead to a final energy which overlaps that from the nuclide of interest at the choosen detection angle. In Nuclear Reaction analysis differences in the trajectory path of the beam and reaction particle through an uneven sample surface, will lead to different final detected energies for the same reaction on a given nuclide within the sample. Thus making analysis very difficult. By placing the detector as close to 180^o to the beam as possible one can minimise the effects of topographical features. However from a consideration of reaction cross-sections and hence sensitivity, this may well not be the optimum detection position. In addition to ensuring that the sample surface is flat one must use a clean sample surface for interrogation. Sample surfaces may be contaminated by the presence of surface layers, such as carbon and oxide layers. These must be removed, using either ultrasonic cleaning and/or polishing, prior to interrogation with the beam in order to minimise the possibility of interference and also of attenuation of the incoming and outgoing particles by these surface layers.

A satisfactory method of preparing metallurgical samples has been found whereby one cuts the cross-section required, mounts it in Wood's alloy and then laps the surface with silicon carbide paper followed by diamond paste to a 1 micron finish. The sample is then cleaned using solvents in an ultrasonic bath using water, ethanol, acetone and ether in succession. This is satisfactory except when carbon analysis is to be carried out because the

sample surfaces polished using this method may be contaiminated with carbon. In these cases a final polish in gamma grade alumina is carried out and this has been found to adequately remove surface carbon.

Powder samples were prepared by pressing small pellets, 6mm in diameter and approximately 2mm thick, and then glueing them onto dural sample mounts. Very small amounts of silver dag were used to prevent chargeing up of the sample surface during irradiation. A thin sputtered layer of carbon over the surface may also be used to provide a conducting sample in those cases where carbon analysis is not required nor where carbon is likely to be a significant interference. Pressed powder samples are inevitably not very uniform and if a pressed powder sample is all that is available it is best to have the detector as close to the 180^{o} detection position as possible. Samples originally vacuum evapourated onto a substrate present a far better, more even surface.

With biological samples surface roughness cannot be removed without altering the sample to an unacceptable extent. This type of sample thus presents far more problems than those discussed above and the preparation of biological samples is described in detail in Chapter 8 as the preffered method evolved during the investigation of $^{15}N/^{14}N$ stable isotope ratios in barley root sections.

2.5 SOURCES OF MATERIALS USED

Wood's alloy - B.D.H. Chemicals Ltd., Poole, England.

Lapping products - silicon carbide papers - Carborundrum Company, Trafford Park, Manchester, England.

- Diamond lapping pastes and pads - Engis Ltd., Park Wood Trading Estate, Maidstone, Kent, England.
- Ultra Microid polishing alumina - Universal Abrasives Ltd., Doxey Road, Stafford, England.

Bismuth implanted silicon backscattering standard - H.V.L. Lab., A.E.R.E., Harwell, Didcot, Oxon., England.

^{26}Mg and ^{25}Mg enriched Magnesium - Chemistry Division, A.E.R.E., Harwell.

Magnesium, specpure - Johnson Matthey & Co. Ltd., 100 High St., Southgate, London, England.

Silicon, specpure - Johnson Matthey.

Cobalt - Goodfellow Metals, Cambridge Science Park, Cambridge, England.

Nickel, specpure - Johnson Matthey.

Silver - Goodfellow Metals.

Gold, specpure - Johnson Matthey.

Cm-244 α-source - Chemistry Division, A.E.R.E., Harwell.

$LiNbO_3$ - H.V.L. Lab., A.E.R.E., Harwell.

Be/Cu alloy - National Bureau of Standards, Washington D.C., U.S.A.

Boron, specpure - Johnson Matthey

Silicon Nitride - Materials Development Division, A.E.R.E. Harwell.

Silica, specpure - Johnson Matthey.

Strontium Fluoride, specpure - Johnson Matthey.

Sodium Chloride - B.D.H. Chemicals Ltd.

Aluminium, specpure - Johnson Matthey.

Indium Phosphide - Instrumentation & Applied Physics Division, A.E.R.E. Harwell.

Lead Sulphide - Chemistry Division, A.E.R.E. Harwell.

Silver Chloride, specpure - Johnson Matthey.

^{13}C enriched $BaCO_3$ - B.O.C. Ltd., Prochem, Deer Park Road, London, England.

^{12}C standards in steel - Inter Group Lab. of British Steel Corporation, Hoyle Street, Sheffield, England.

Nimonic alloy PE16 - Materials Development Division, A.E.R.E. Harwell.

316, standard steel - Materials Development Division, A.E.R.E. Harwell.

95% ^{13}C enriched CO_2 and 90% enriched CH_4 - B.O.C. Prochem Ltd.

Boron Carbide, specpure - Johnson Matthey.

^{15}N enriched urea - B.O.C. Prochem Ltd.

Barley Root sections - Letcombe Agricultural Laboratory, Letcombe, Nr. Wantage, Oxon., England.

CHAPTER 3

THEORETICAL APPRAISAL OF THE NUCLEAR MICROPROBE DETERMINATION OF THE SPATIAL DISTRIBUTION OF STABLE ISOTOPE TRACERS

The application of nuclear reaction and backscattering analyses to the determination of stable isotopes is governed by fundamental and practical factors. Their significance is highlighted by a detailed discussion of mass selectivity and sensitivity. The influence of nuclear microprobe operation and sample composition are selected for special consideration. The factors critically influencing mass selectivity in backscattering and nuclear reaction analysis differ and are thus discussed separately.

3.1 MASS SELECTIVITY

Stable isotope tracer methods are restricted to elements with more than one isotope, eliminating monisotopic elements from further consideration.

3.1.a Backscattering Analysis

Firstly the theoretical relationships and processes involved in backscattering analysis are outlined, followed by a more detailed examination of how each of the parameters involved affects mass selectivity.

In backscattering analysis the basic process involved is the scattering of a projectile ion by a target atom. When an incident particle beam of mass M_1, moving with constant velocity V_{o_1}, collides elastically with a stationary target nuclide of mass M_2, energy is transferred from the moving to the stationary particle. The particle cannot of course be backscattered if $M_1 \geq M_2$. The collision can be assumed to be purely elastic providing that:-

(a) The beam energy E_o >> the binding energy of the target atoms. (Chemical bonds are of the order of 10 eV thus E_o must be very much larger than this).

(b) Nuclear reactions and non Rutherford scattering do not occur. This imposes an upper limit on the projectile energy, the limit varies depending on the type of atoms involved and is discussed in detail later in this section.

By applying the principles of conservation of energy and momentum, the elastic scattering involved and presented diagrammatically in Figure 3.1 can be fully described. The equations governing the conservation of energy and momentum both parallel and perpendicular to the direction of incidence are given below:-

$$\tfrac{1}{2}M_1V_0^2 = \tfrac{1}{2}M_1V^2 + \tfrac{1}{2}M_2V_2^2 \qquad \text{... Eqn. 3.1}$$

$$M_1V_0 = M_1V \cos\theta + M_2V_2 \cos 0 \qquad \text{... Eqn. 3.2}$$

$$0 = M_1V \sin\theta + M_2V_2 \sin 0 \qquad \text{... Eqn. 3.3}$$

eliminating first $\emptyset$ then V_2 gives the following equation:-

$$V/V_0 = \left[\pm (M_2^2 - M_1^2 \sin^2\theta)^{\frac{1}{2}} + M_1 \cos\theta \right] / (M_2+M_1) \qquad \text{.. Eqn. 3.4}$$

this is + when $M_1 \leq M_2$.

The ratio of the scattered projectile energy, E, to the incident projectile energy, E_o, is given by the kinematic factor, K.

$$K = E / E_o \qquad \text{... Eqn. 3.5}$$

substituting in the values of V/V_o

$$K = \frac{V}{V_o}^2 = \frac{\left[1 - (M_1/M_2)^2 \sin^2\theta \right]^{\frac{1}{2}} + (M_1/M_2)\cos\theta}{1 + (M_1/M_2)}^2 \qquad \text{... Eqn. 3.6}$$

where θ = laboratory angle of scattering

M_1 = mass of the incident beam

M_2 = mass of the target

For a given scattering angle and incident energy the final scattered particle energy depends only on the kinematic factor which in turn (under these conditions) depends only on the ratio M_1/M_2. Hence in Rutherford backscattering analysis selectivity is truly based on mass and consequently, isobaric interference can occur. In reality the problem can often be circumvented since many elements have a large number of isotopes available for isotopic ratio analysis.

A mass resolution of 1 is defined as the ability to adequately resolve and measure signals from two nuclides of adjacent mass, i.e.

$\Delta M_2=1$. For stable isotope tracer work, an ability to measure adjacent masses is usually essential, although for certain elements a mass resolution of 2 would be adequate, for instance $^{35}Cl/^{37}Cl$ and $^{74}Ge/^{76}Ge$. Good mass resolution is dependent on good energy resolution of the charged particles scattered from adjacent masses. Consideration of the scattering kinematics shows that energy resolution is improved by:-

(a) Increasing incident particle energy.

(b) In most cases operating at high scattering angles where the rate of change of K with θ is minimal [42, 43]

(c) Increasing the incident mass (M_1). In fact it is the ratio of M_1/M_2 which is significant, this ratio should preferably be kept as high as possible.

The overall energy resolution also depends on:-

(d) the energy spread and scattering of the incident beam.

(e) the range of scattering angles subtended by the detector.

(f) the detector resolution.

These factors are discussed individually.

Incident Particle Energy

It can be seen from Equation 3.5 that increasing the beam energy, E_o, increases the mass resolution. However in practice E_o is limited by the accelerator facilities available and the need to minimise interferences caused by nuclear reactions and inelastic resonance scattering.

(i) The present generation of nuclear microprobes are associated with accelerators having maximum operating voltages of about 6 MV [44, 45]. The Harwell nuclear microprobe is limited to 3.5 MV and $^4He^+$ beams with energies of > 3 MeV are seldom attainable [22, 46].

(ii) In the Rutherford scattering region even incident particles undergoing close encounters with a target nucleus will be

deflected because of the enormous coulombic force. However interference by non-Rutherford scattering can occur whenever the incident beam energy is greater than the coulomb barrier of any target nucleus. Generally this occurs above 1 MeV for $^{1}H^{+}$ beams and about 2-3 MeV for $^{4}He^{+}$ beams. A compromise incident energy must be sought. Each case must be considered individually, the highest available beam energy being chosen which still avoids interference by nuclear reactions.

(iii) Resonance elastic scattering may also cause problems of interference if the projectile energy coincides with a particularly favoured excited state of a component in the sample matrix. This may be turned to advantage if the resonance peak is associated with the isotope to be investigated since the sensitivity will be increased.

An additional factor affected by incident energy is the scattering cross-section. This is discussed in the next section.

Scattering Angle

It can be seen from Equations 3.5 and 3.6 that for a given incident energy, E_o, the mass discrimination is, theoretically, wholly governed by the difference in the kinematic factors of the masses involved, ΔK. This is a function of the angle of scattering and, as discussed later in this section, the ratio of the target and beam masses.

The kinematic factors for a variety of incident beams, scattering angles, θ, and target masses were computed. It has been found [42, 43] that generally it is advantageous for θ to approach 180^{o}. Here the largest ΔK values for adjacent masses are obtained. The exception is when M_2 is very small and the ratio of M_2/M_1 approaches unity, in these cases the optimum θ can be found by comparing K values at different angles. Generally 180^{o} is the preferred location for the detector. This could almost be achieved by using an annular surface barrier detector, however the resolution of this type of detector is poor compared to the available planar surface barrier detectors. Since this leads to inferior mass resolution their use is precluded in this investigation. High scattering angles are also normally favoured as the rate of change of kinematic factor with angle is a minimum, this

diminishes problems of kinematic spread caused by the detector solid angle. The current Harwell microprobe has been designed to observe events at an angle of 135^{o} [21]. It is clear from Figure 3.2 that the kinematic spread for 3 MeV $^{4}He^{+}$ ions scattered from ^{24}Mg at 135^{o} is much greater than at 170^{o}. Despite the geometrical difficulties involved, namely fouling the microscope that observes the front of thick targets and intercepting the incident beam, an observation position with θ slightly greater than 170^{o} has been provided.

Although mass selectivity considerations favour the use of a high scattering angle it can be seen from Section 3 Equations 3.19 and 3.20 governing scattering cross-sections that increasing the scattering angle decreases the scattering cross-section. Clearly a compromise between the needs of mass selectivity and the conflicting needs of cross-section magnitude (mass sensitivity) must be made. The Rutherford backscattering cross-sections were computed at several beam energies for a variety of beam and target masses and scattering angles. It was found that increasing the scattering angle and to a lesser extent increasing the beam energy decreases the magnitude of the Rutherford cross-section, as theoretically predicted [42, 43]. However in most cases the cross-section is very high as shown in Figure 3.3 and generally the experimental conditions can be chosen to favour the optimum mass selectivity.

Incident Particle Mass

In principle notable increases in mass resolution can be obtained by using incident particles of high mass, for instance $^{14}N^{+}$ [42, 43]. However detection problems generally lead to losses in energy resolution that greatly outweigh any gain from increased mass. In addition in microbeam mode, increases in mass and energy make beam focusing more difficult.

The effects of heavier beam mass are studied in greater detail, in the context of the magnitude of deterioration of the detector resolution versus effective mass selectivity, later in this section.

In addition to the influence of these fundamental parameters on resolution, the overall energy and hence mass resolution also depends on factors which affect the energy analysis system. These additional factors are discussed in the following sections.

Energy Spread and Scattering of the Incident Beam

The amount of scattering of the beam through the slits is difficult to quantify but in practice is kept to a minimum by the following expedients in order to minimise any ultimate increase in the range of scattering angles subtended by the detector:-

(a) having the beam slit a large distance from the target. In the Harwell nuclear microprobe it is approximately 2 metres.

or (b) having a special double slit arrangement. The extra outer slit being shaped such that it affects and stops scattered beam only. Nobiling [35] describes the design and manufacture of specially shaped slits, two pairs of crossed stainless steel slits, which effectively suppress slit scattering for collimator diameters as small as 1 μm.

The voltage stability of the accelerator dictates the spread of beam energies delivered. In practice energy spreads of about 1 part in 10^3 are typical of conventional Van de Graaff accelerators, however modern pelletron machines are more stable to $\lesssim$ 0.5 kV at 3 MV. The latter type of machine not only has advantages in energy resolution but also decreases problems of chromatic aberrations in focusing systems [35]. The smaller the spread of incident beam energies the less the uncertainty as to the exact origin of the scattering particles detected.

The Range of Scattering Angles Subtended by the Detector

In normal Rutherford scattering the range of scattering angles subtended by the detector is influenced by the divergence of the incident beam, the size of the beam spot, the target to detector distance and the detector aperture. For microprobe work there are differences, namely the microbeam converges on the target and is focused to such a small size that its area has negligible influence if the ratio of in-focus to out-of-focus beam is as small as that of the Heidelberg system, 10^4:1 [34].

The effect of beam convergence on kinematic spread for a detector at 170°, with $^4He^+$ incident ions on a ^{24}Mg target is shown in Figure 3.4. For 3 MeV incident ions and the Harwell system, the

energy spread associated with the maximum half-angle of convergence of 0.285^{o} [22, 46] is of little consequence, the resultant energy spread at the detector being < 1 keV.

The influence of target to detector distance and detector aperture on kinematic spread is shown in Figure 3.2. If one assumes that a 5 keV kinematic spread is acceptable the need to decrease the aperture size with decreasing target to detector distance, is apparent. All those geometries with kinematic spread ≤ 5 keV are shown below the dotted line in Figure 3.2. With the Harwell system geometrical problems favoured the use of a relatively long target to detector distance and a wide aperture, 3.5 mm. The apertures used were arc shaped slits. When using rectangular or circular slits so close to the beam line any given scattering angle falls in a cone, thus if slits other than an arc shape are used problems of changing scattering angle would occur.

Generally the dimensions of commercially available planar detectors prevent their use at distances of less than 50 mm at $\theta = 170^{o}$. As mentioned previously the inferior energy resolution makes annular detectors unacceptable.

Sometimes electrostatic deflection of the beam is used to scan a larger area of material. The technique is of particular interest for the examination of sensitive biological samples as it effectively diminishes the sample damage in localised spots. The beam is scanned across a sample at a frequency of 50 Hz by applying a triangular waveform to a pair of parallel plates at the entrance to the target chamber. Although beam scanning changes the detector solid angle and also the observation angle, its influence is small. For the above system and a $\pm$ 1 mm beam deflection the detector solid angle changes by $\pm$ 0.5% and the observation angle by $\pm 0.9^{o}$. These changes in solid angle and scattering angle are acceptably small, consequently electrostatic scanning may be used when reduction in beam damage is essential. It is often preferrable to scan the beam in order to reduce beam damage rather than to use the alternative measure of reducing the beam current, which introduces an undesirable time penalty.

Detector Resolution

The inherent resolution of a detector, for a given set of operating conditions, is usually defined in terms of the smallest

attainable energy width for a given (usually Gaussian) peak from a reference source. This energy resolution is measured at half the maximum amplitude across the full width of the peak and is known as the Full Width at Half Maximum, F.W.H.M., value. Backscattering spectra most often display the integral of the Gaussian distribution, the error function. The F.W.H.M. of a Gaussian corresponds to the 12 to 88% range of the error function. Clearly if two peaks or back-scattered edges are closer in energy than the minimum F.W.H.M. measurable with a given detector they will not be resolved and the mass selectivity is lost.

Silicon surface barrier detectors are the most convenient for the detection of scattered particles. An interesting general paper discussing the spectral response of silicon surface barrier detectors to both light and heavy ions (up to ^{58}Ni) was given by Zabel et. al.[47]. Although F.W.H.M. values were not investigated.

For 5 MeV $^{4}He^{+}$ ions small planar detectors are available with resolutions of about 10 keV however electrical noise in an accelerator environment and overall operation factors including kinematic effects make resolutions of < 15 keV difficult to achieve. The detector resolution and the magnitude of this resolution degradation for our system was checked using α-spectrometry as discussed in Section 2.2.a. Typical overall instrumental resolutions obtained were about 13 to 13.5 keV F.W.H.M. for 5.8 MeV $^{4}He^{+}$ as seen in Figure 2.13. A Bismuth implanted silicon backscattering standard [48] was also used in order to obtain the overall experimental resolution, the most important additional factor included in this measurement is the degradation caused by kinematic broadening. With the 3 MeV $^{4}He^{+}$ beams available on the nuclear microprobe facility used, a mass resolution of one should be attainable up to mass 45 and a mass resolution of 2 up to mass 70. For 6 MeV $^{4}He^{+}$ beams the respective values should be mass 70 and mass 105.

Theoretically, as mentioned earlier, increasing the beam mass should extend the maximum masses resolved. However as the beam mass increases, the life and resolution of a silicon barrier detector deteriorates. There is some difference of opinion [49, 50] as to the exact magnitude of this degradation as can be seen by the spread of literative values shown in Figure 3.5. Muller [51] predicts a better

resolution for heavier beams than does Amsel [52], and Bergstrom [53] predicts an even worse resolution. Experiments were carried out using $^{14}N^{+}$ as the heavier ion beam. Backscattering spectra of Ni(58 to 64) and Co(59) with a 3.5 $^{14}N^{+}$ beam, Figure 3.6, do show the presence of nickel isotopes, the nickel spectrum crossing over the cobalt edge. However the resolution is poor. For 3 MeV $^{12}C^{+}$, $^{14}N^{+}$ and $^{16}O^{+}$ ions the resolution of silicon barrier detectors is between 50 to 70 keV. Consequently mass selectivity is poorer than for $^{4}He^{+}$ ions, since a mass resolution of 1 is attainable only up to mass 25.

Theoretically increasing the beam energy should also increase mass resolution. For $^{1}H^{+}$ and $^{4}He^{+}$ beams in the MeV range increased beam energy does lead to improved mass resolution as the energy resolution of silicon surface barrier detectors is almost independent [42] of energy in this range. However the same does not apply for heavier beams.

High resolution detectors, such as magnetic spectrometers and electrostatic analysers, are often avoided because of their low efficiency and operational inconvenience. However since the study of stable isotope distributions with surface barrier detectors requires the use of very small detector solid angles, their effective efficiency is comparable to that of magnetic and electrostatic analysers. Consequently the use of high resolution detectors appears worthwhile investigating.

Magnetic analysers improve system resolutions drammatically. The N.R.L. 180^{o} double focussing magnetic spectrometer [54] has a resolution of 1-2 keV for $^{4}He^{+}$ ions of a few MeV.

The improved energy resolution obtained with the magnetic analyser leads to correspondingly better depth and mass resolution. There are additional advantages with magnetic spectrometers, namely they avoid pulse pile up problems and also decrease interference from other particles of slightly different mass, although this is achieved by only looking at a small portion of the total energy spectrum with the analyser. Much available information is thus lost.

The reputed disadvantage of magnetic spectrometers is their extremely slow rate of data acquisition. This is a direct result of their small acceptance angle, only a small part of the spectrum being

measured at any one magnetic field setting, and also because the spectrometer accepts particles of only one charge state. The magnetic spectrometer at N.R.L. [54] has a variable solid angle of 0 to 25 msr. For high resolution work the angle must be on the lower part of the range but it is in fact of comparable magnitude to the solid angles dictated by the good mass resolution required of surface barrier detectors for stable isotope tracing. Even bearing in mind the slow rate of data acquisition the excellent resolution of these spectrometers suggests that their use in isotope tracer work may well be justified.

One can calculate the expected limit of mass resolution $\Delta M_2 = 1$ for magnetic analysers. The magnetic spectrometer analyses the momentum (energy) of the charged particles entering the input slit and focuses the dispersed charged particles, preferrably onto a position sensitive detector located in the image plane of the spectrometer. Particles of slightly different energies, E_o and $E_o + \Delta E$ traverse slightly different paths through the spectrometer and will be brought to a focus at different positions (X_o and $X_o + \Delta X$) along the image plane. In order to find the limit of mass resolution for $\Delta M_2 = 1$, one must find the final separation by the spectrometer, ΔE, between adjacent masses. For a magnetic spectrometer field intensity B, a non relativistic particle of momentum p and charge q has a curved deflection of radius R:-

$$R = p/Bq \qquad \text{... Eqn. 3.7}$$

The variation of path ΔR with momentum Δp is given by:-

$$\Delta R = \Delta p/Bq \qquad \text{... Eqn. 3.8}$$

Since $E = p^2/2M$ and $\Delta E = p\,\Delta p/M$ the variation E of E is:-

$$E/\Delta E = \frac{1}{2}\left(p/\Delta p\right) = \frac{1}{2}\left(R/\Delta R\right) \qquad \text{... Eqn. 3.9}$$

where $E = kE_o$, E_o being the incident beam energy (MeV), and ΔE is F.W.H.M. (MeV). Typical values of $R/\Delta R$ are $\hat{=}$ 2000 [42] hence $E/\Delta E = 1000$. For any ratio of $E/\Delta E = 1000$ and $\Delta M_2 = 1$, the maximum mass resolved using $^4He^+$ projectiles would be about 115 for a scattering angle $\hat{=}\ 180^o$ and about 85 for a scattering angle $\hat{=}\ 90^o$.

Electrostatic analysers have also been used to improve system resolution. Although Hage-Ali et al [55] describe one which operates up to 1 MeV, their application is usually limited to low energies (lower than the 1 MeV range). Electrostatic analysers are more commonly used, for instance by Honig and Harrington [56] and by Buck [57], below a few hundred keV. A schematic diagram of a backscattering detection system using an electrostatic analyser is given in Fig. 3.7.

An energy spectrum of scattered particles is built up by stepping or continuously scanning the voltage on the plates of the electrostatic analyser and collecting the impulses in the detector. Detectors for low energy ion scattering are usually electron multipliers of either the channel or Cu-Be dynode type.

An electrostatic analyser which operates at beam energies more pertinent to these studies is described by Hage-Ali [55]. The machine operates up to 1 MeV with an energy resolution of up to 0.4%.

The electrostatic analyser acts as an energy/charge filter. As the voltage on the plates changes scattered ions corresponding to E/q are transmitted through the analyser and counted. For a curved plate analyser as shown in Figure 3.7:-

$$E/q = \frac{V.R}{2d} \qquad \text{... Eqn. 3.10}$$

where E = kinetic energy of transmitted ions
q = charge of transmitted ions
V = potential difference between the plates
R = Mean radius of the plates
d = their separation

(N.B. Outer and inner plates are held at + V/2 and - V/2 respectively thus the trajectory through the analyser is at ground potential).

Energy resolution $E/\Delta E$ depends primarily on the ratio of the sum of the aperture widths, d, to the analyser radius, R, and on the selected energy itself. With a typical analyser of R = 10 cm, d = 0.5 cm, 100 eV singly charged particles would be collected when V = 10 volts. The energy resolution of electrostatic analysers is typically $\simeq$ 1 keV. Thus for a 250 keV $^4He^+$ incident beam the maximum mass resolved would be $\simeq$ 60.

It would thus appear that the use of the magnetic spectrometer for resolving isotopes in stable isotope tracer profile studies may well be worthwhile, the data acquisition rate being comparable to that attained by the very small acceptance angle surface barrier detectors required in these studies. Electrostatic analysers may well prove useful when running at lower energies but are limited in data collection rate because of their scanning mode of operation.

Energy Loss and Straggling

One of the important features of backscattering analysis is the ability to do depth analysis without recourse to sputtering or destruction of the sample. In the spatial determination of isotopes it is not intended to use this depth facility but, as will be seen in Section 3.3.a when studying complex samples containing surface inclusions, phase boundaries and heterogeneous thin layers, these effects must be taken into consideration. As the effects of energy loss and straggling affect the resolution of the backscattered spectrum it would seem apt to discuss them in this current section.

Under a given set of experimental conditions the energy of the scattered particle depends not only on the mass of the target nuclide (M_2) but also on the depth (X) of that target atom below the surface. Particles scattered from a depth of X loose energy both before and after scattering at a rate determined by the stopping power ε

$$\varepsilon = \frac{1}{N}\left(\frac{dE}{dX}\right) \qquad \text{... Eqn. 3.11}$$

where N = atomic density of the target

$\frac{dE}{dX}$ = average energy loss by all possible processes as the projectile passes through the target.

Figure 3.8 illustrates the scattering of a projectile through a sample thickness X. The final emergent energy E_1 is given by the following equation:-

$$E_1 = \left[E_o - \int_0^{X/Cos\theta s} \varepsilon_E \, d1_1 \right] K - \int_{X/Cos\theta s}^{0} \varepsilon_{E1} \, d1_2 \qquad \text{... Eqn. 3.12}$$

where ε_E and $\varepsilon_E 1$ are the stopping powers of the ingoing (1_1) and the outgoing (1_2) trajectories respectively.

E_o = incident surface energy

E = energy immediately before scattering

θs = laboratory scattering angle

The emergent particle energies can therefore provide detailed depth information, c.f. Eqn. 3.12, as well as information on the scattering mass, c.f. Eqns. 3.5 and 3.6. Thus in backscattering analysis the energy "scale" is simultaneously a mass "scale" and a depth "scale" and there can effectively be an overlap of masses. For instance the resultant energy of a particle scattered from a light nuclide near to the surface may be identical to the resultant energy from a heavy nuclide deeper into the target. There is some ambiguity of peak origin and this basic uncertainty leads to a loss of elemental specificity, i.e. a poorer mass resolution. Ambiguity is avoided in the preferred backscattering situation where there is a heavy dopant in a light matrix. Also the problem of loss of mass resolution is much reduced when the depth of sample interrogated is small. As in the spatial determination of isotopes where surface analysis rather than depth analysis is carried out. The maximum depth penetrated by the microprobe, if required, could be 3 μm (3 MeV, $^4He^+$) but in the studies carried out it was generally less than this, for instance using the microprobe to interrogate magnesium isotopes as described in Section 3.2.a it was $\triangleq$ 0.6 μm. For isotope work the energy region covered by the isotopes is very small, for instance for ^{25}Mg and ^{26}Mg (Section 3.2.a) ΔE = 37.7 keV and as the depth penetration is also small, the energy spread over the depth led in fact to an error of $<$ 1% which is of little consequence. Energy losses will become more significant in the more complex samples and this is discussed in Section 3.3.a.

Energy straggling is another process in backscattering which introduces uncertainty in target mass identification. It arises because a beam scattered at a depth X in the target is not mono-energetic. This would again smear the spectrum peaks or steps, however as the straggling is usually $\simeq$ 10% of the value of energy loss, for the spatial determination of isotopes the error is insignificant.

3.1.b Nuclear Reaction Analysis

When a charged particle beam interacts with a target an extensive range of radiations may be produced as illustrated in

Figure 3.9. The energy of the emitted radiation from a nuclear reaction may be determined from the reaction kinetics discussed in detail below.

Nuclear Reaction Kinetics

Nuclear reactions are usually represented in the form of a balanced equation:-

$$A + a \longrightarrow B + b + Q \qquad \text{... Eqn. 3.13}$$

where A = target nucleus
a = projectile
B = product nucleus
b = emitted particle(s)
Q = energy released or absorbed

Frequently nuclear reactions are presented in abbreviated form A(a,b)B.

The amount of energy released or absorbed by a nuclear reaction can be extremely large and must be accounted for to obtain the correct mass/energy balance.

Figure 3.10 represents a nuclear interaction resulting in a heavy product nucleus of mass M_4, the emission of a γ photon and a light emitted particle, M_3. A breakdown of the energy relationships (assuming that for this case an intermediate was formed) is given in Figure 3.11. Where:-

M_1 = mass of incident particle a, of energy E_1, velocity V_1.

M_2 = mass of target.

M_3 = mass of emitted light particle; energy E_3 (when product nucleus is in the ground state), velocity V_3 and if the emitted particle is in its ith excited state an energy E_{3i}.

E_γ = energy of γ produced on relaxation of particle B to the ground state.

M_4 = mass of product B. $E_4 = 0$

Q_o = energy released by reaction.

Q_i = the Q value for the reaction giving the ith excited state product.

Q_i is endoergic in Figure 3.12. $Q_i = E - Q_o$

By using the principle of conservation of total energy and mass:-

Total Energy $E_T = E_1 + Q_o = E_3 + E_4$ ... Eqn. 3.14

$$Q_o = (M_1 + M_2 - M_3 - M_4)c^2 \quad \text{... Eqn. 3.15}$$

and the information derived from the principle of conservation of momentum:-

$$M_3 V_3 \text{ Cos } \theta + M_4 V_4 \text{ Cos } \phi = M_1 V_1 \quad \text{... Eqn. 3.16}$$

$$M_3 V_3 \text{ Sin } \theta + M_4 V_4 \text{ Sin } \phi = 0 \quad \text{... Eqn. 3.17}$$

the kinetic relationships between the particles involved in the nuclear reaction, for the non-relativistic case, can be found. The energy of the prompt particle emitted, E_3, can be calculated:-

$$E_3 = E_1 \left[c \text{ Cos } \theta \pm (D - c^2 \text{ Sin}^2 \theta)^{\frac{1}{2}} \right]^2 = K_{(E_1)} E_1 \quad \text{... Eqn. 3.18}$$

where $c^2 = M_1M_3/(M_1+M_2)\ (M_3+M_4)$

$$D = M_2M_4 \left(\frac{E_T}{E_1} + \frac{M_1Q_o}{M_2E_T} \right) \Big/ (M_1+M_2)\ (M_3+M_4)$$

In order to find the excited state energy E_{3i};

$$E_{3i} = E_3 - E_\gamma \quad \text{... Eqn. 3.19}$$

Certain general features can be seen on consideration of these relationships:-

(1) The product particle energy decreases as the angle of observation increases away from the incident beam line.

(2) For negative Q values there is a threshold incident energy below which the reaction will not occur. This can be used to advantage to limit interferences. The threshold energy will in fact be slightly more than Q, to provide the required momentum for the product nucleus.

(3) The formation of excited states, as seen in Figure 3.11, reduces the product energy and thus a set of characteristic

discrete product particle energies will give characteristic spectral peaks.

These general features are used in order to help elucidate the best measuring conditions for the stable isotope of interest.

All nuclear reactions are isotopically sensitive because the nuclear properties of the isotopes of an element are frequently different. Isotopic sensitivity is generally optimised by choosing the most favourable reaction, irradiation energy and emitted radiation. While this may be relatively simple if the absolute concentration of the isotope tracer alone is to be measured, compromises may be necessary when measuring isotope ratios.

Choice of Reaction

An indication of the kinetic favourability of a nuclear reaction is given by its energy balance, commonly known as its Q-value. Generally reactions with high Q-values are favoured since the emitted radiations normally have higher energies than those from interfering reactions. For example the Q-values for the (α ,n) reaction on one of the stable isotopes of carbon, ^{13}C Q = 2.215 MeV, is only exceeded by that for ^{9}Be Q = 5.702 MeV, ^{25}Mg Q = 2.623 MeV and ^{21}Ne Q = 2.557 MeV, consequently measurement of the emitted neutrons should allow the highly selective measurement of ^{13}C [58]. However if $^{13}C/^{12}C$ isotope ratios need to be measured then the compromise of using the proton reactions $^{12}C(p,\gamma)^{13}N$ and $^{13}C(p,\gamma)N^{14}$ or the $^{12}C(dp)^{13}C$ and $^{13}C(d,p)^{14}C$ reactions may be necessary, despite the loss of selectivity attributable to the fairly large number of nuclides with higher Q-values [43] for both the (p, γ) and (d,p) reactions on ^{12}C and ^{13}C.

When measuring isotope ratios, the Q-value for the reaction with the tracer isotope should be greater than with the comparitor isotope. For example, using the (d,p) reaction to study the diffusion of tracer ^{25}Mg in magnesium, the Q values are Q = 8.86 MeV for ^{25}Mg and Q = 5.107 MeV for ^{24}Mg, allowing the ready measurement of the ^{25}Mg protons as can be seen by the peak separation in Figure 3.12 which shows two parts of the experimental spectrum obtained when interrogating natural magnesium using a 1.9 MeV deuteron beam and observing emitted particles at 135°.

The methods for determining the lowest abundance isotope are the most important, obviously the greatest possible change in the isotope ratio occurs when the two chosen isotopes of the element have the greatest initial difference.

In some cases more than one reaction will be required in order to obtain information about two isotopes. This does introduce the problem of ensuring that the sample volume interrogated is the same for each method, this is discussed in the sample constitution Section 3.3.a.

Irradiation Energy

Nuclear reaction analysis using low energy ion beams is ideal for the interference free determination of light elements in heavy matrices, due to the coulomb barrier suppression of heavy element reactions. Much of the work reported in the literature is concerned with light nuclides, due to the particular suitability of the technique for these cases coupled with the fact that great difficulties often arise when trying to measure light elements using other techniques.

However nuclear reaction techniques are not exclusively for light element analysis. 2.5 MeV protons undergo (p,γ) and $(p, p\gamma)$ reactions with a wide range of elements conceivably allowing measurement of ^{194}Pt and ^{195}Pt [59]. Also deuterons of about 3 MeV have been used to determine ^{52}Cr, ^{53}Cr, ^{54}Fe, ^{56}Fe and ^{87}Sr [60, 61]. Consequently nuclear reactions may be more suitable for the determination of very high mass isotope tracers than backscattering analysis, provided light element interference permits.

Selection of Emitted Radiation

Fundamentally, isotopic sensitivity is favoured by measurement of emitted particles rather than gamma-rays since the former are characteristic of the reaction, while the latter are characteristic of the residual nucleus. For instance, measurement of ^{24}Mg through the 1.368 MeV γ ray emitted by the reaction $^{24}Mg\ (p, p\gamma)\ ^{24}Mg$ is interfered with by ^{23}Na and ^{27}Al through the reactions $^{23}Na(p, \gamma)^{24}Mg$ and $^{27}Al\ (p, \alpha\gamma)^{24}Mg$ [59]. Particles also carry invaluable information on the sub-surface sample composition.

Much of the discussion of factors critically affecting energy resolution in scattering is irrelevant to the measurement of particles from nuclear reactions, since relatively poor energy resolution is normally adequate. Consequently factors such as beam convergence, and detector solid angle are of little importance. However, high observation angles are favoured to diminish the influence of sample topography and annular detectors may be used despite their inferior energy resolutions, where an increase in detector efficiency is desirable to improve sensitivity.

3.1.c X-Ray Production

Ion beam induced X-ray analysis [24, 62] is not isotopically sensitive, however if a nuclear reaction must be employed which allows only the measurement of the tracer isotope, the total elemental concentration may be measured simultaneously from its particle induced X-rays. The technique should be most readily applicable to elements of mass greater than sodium [21] when using proton or deuteron beams. X-ray cross-sections generally increase with increasing beam energy but decrease for ions of greater mass at any given energy.

In addition to providing total elemental concentrations for isotopic ratio measurements, ion beam induced X-rays may also prove invaluable to detect and identify sample impurities.

SUMMARY OF THE CONDITIONS REQUIRED TO GIVE OPTIMUM MASS SELECTIVITY FOR THE NUCLEAR MICROPROBE DETERMINATION OF STABLE ISOTOPE TRACERS USING NUCLEAR REACTION AND BACKSCATTERING ANALYSIS

Theoretical prediction and experimental investigation were used to elucidate the best conditions for the nuclear microprobe determination of the spatial distributions of stable isotopes. These have been discussed in detail in Sections 3.1.a - 3.1.c and are briefly summarised below.

BACKSCATTERING:-

(a) Bearing in mind the limit imposed on beam energy by the Q values of any interference nuclide present in the target, the highest beam energy available should be used for backscattering analysis. Resonance scattering may be useful for optimising the sensitivity of a particular isotope.

(b) Generally a scattering angle close to 180^{o} should be used, except when the ratio M_2/M_1 approaches unity. Careful consideration of K values at various scattering angles indicates the optimum detector observation angle when $M_2/M_1 \simeq 1$.

(c) Generally no advantage in mass resolution is obtained by using heavy ion beams eg ^{14}N, unless facilities are available to provide heavy ion beams at fairly high energies i.e. $\gtrsim$ 5 MeV and detectors other than silicon surface barrier detectors are used.

(d) The scattering of the incident beam must be minimised, for instance by using a double beam entrance slit arrangement in the scattering chamber. Another factor is beam energy stability, the accelerator used should deliver a fairly steady beam, typically spreads are in the order of 1 part in 10^3.

(e) The high resolutions required by isotope studies dictate very small detector acceptance angles.

(f) Electrostatic scanning (or "rastering") of the beam normally introduces insignificant error to the analysis.

(g) Annular detectors do not have acceptable resolutions. Small planar surface barrier detectors with high resolution are convenient to use and isotopes can be distinguished under careful experimental operation. The use of high resolution magnetic or electrostatic analysers would appear to be a justificable proposition.

NUCLEAR REACTIONS

(h) Many of the factors critically affecting energy resolution in scattering are irrelevant since relatively poor energy resolution is often adequate.

(i) The nuclear reaction must be chosen such that it gives the most selective determination of the isotopes required.

(j) The nuclear reaction cross-section data is used to find the energy which gives an optimum cross-section and hence sensitivity, bearing in mind possible interferences.

(k) A high observation angle is preferrable to decrease topographical effects.

The subsequent discussion of mass sensitivity (Section 3.2) takes account of the conditions required for good mass selectivity.

3.2 MASS SENSITIVITY

In stable isotope tracer analysis the sensitivity of a measurement method is best defined as the smallest change it can detect in the natural isotopic abundance of the tracer isotope, or, its absolute concentration, if the total elemental concentration is known. The highest sensitivities are achieved when using isotopes of low natural abundance. High sensitivity is desirable to reduce the consumption of enriched isotope tracers. Sensitivity for Backscattering and Nuclear reactions are discussed separately.

3.2.1 Backscattering Analysis

In backscattering analysis expected yields can be calculated fairly readily, the cross-sections (unlike nuclear reaction cross-sections) being readily predictable. For Rutherford scattering, within the confines stated at the beginning of Section 3.1.a, the differential scattering cross-section is given by Rutherford's formula [63]:-

$$\left(\frac{d\sigma}{d\Omega}\right)_c = \left[\frac{Z_1 Z_2\ e^2}{4E_c\ \mathrm{Sin}^2(\theta_{c/2})}\right]^2 \qquad \text{... Eqn. 3.20}$$

where the subscript c indicates that the values are given with respect to centre of mass co-ordinates. For the general case of Equation 3.20, transformation [64] from centre of mass to laboratory frame of reference yields equation 3.21

$$\left(\frac{d\sigma}{d\Omega}\right)\frac{cm^2}{sr} = \left(\frac{Z_1 Z_2 e^2}{4E}\right)^2 \frac{4}{\mathrm{Sin}^4\theta} \left\{\frac{\left[1 - ((M_1/M_2)\mathrm{Sin}^2\theta)^2\right]^{\frac{1}{2}} + \mathrm{Cos}\ \theta}{\left[1 - ((M_1/M_2)\mathrm{Sin}\ \theta)^2\right]^{\frac{1}{2}}}\right\}^2 \qquad \text{.. Eqn. 3.21}$$

where Z_1 = atomic no. of projectile atom with mass M_1

Z_2 = atomic no. of target atom with mass M_2

e = electronic charge in electrostatic units = 4.8×10^{-10} Stat C

E = energy of projectile immediately before scattering (in MeV)

θ = angle of scattering in the laboratory frame of reference.

It can be seen that $d\sigma/d\Omega$ varies in the following manner:-

(i) $d\sigma/d\Omega \quad \propto {}^{1}/_{E^2}$

(ii) $d\sigma/d\Omega \overset{\Omega}{\alpha} {}^{1}/_{(\text{Sin } \theta/2)^4}$ when $M_1 << M_2$, this dependence gives rapidly increasing yields as the scattering angle is decreased.

(iii) $d\sigma/d\Omega \propto Z_1^2$. The backscatter yield from a $^{12}C^+$ beam (Z=6) is nine times larger than for a $^{4}He^+$ beam (Z=2).

(iv) $d\sigma/d\Omega \propto Z_2^2$. Heavy atoms are far more efficient scatters of any given particle beam.

Clearly the restriction of detector solid angles to < 10 msr, to ensure good mass selectivity, adversely influences isotopic sensitivity. This is illustrated by a simple example. The isotopic sensitivity has been calculated for ^{26}Mg used as a stable isotope tracer for the hypothetical study of self-diffusion in magnesium metal. The measurement conditions assumed were those dictated by the Harwell nuclear microprobe chamber when observing scattering events at 170°, namely a detector solid angle of 6 msr. A 3 MeV $^{4}He^+$ ion beam was chosen, and an irradiation dose of 20 μ coulombs. Referring to Figure 3.13, the number of events characteristic of ^{26}Mg, has been taken as those arising from the centre third of the region between the ^{26}Mg and ^{25}Mg edges in an idealised spectrum. For natural magnesium, ^{26}Mg (11.17%), this is 2050 events. This is compared with events typical of the total magnesium content which arise from an identical region just below the ^{24}Mg edge, namely 18350 events. This leads to a standard deviation for the ^{26}Mg isotopic abundance, σ = 0.0026, and a coefficient of variation Cv_{26} = 2.3%. Consequently, despite the relatively high ion dose for a nuclear microprobe measurement, it is unrealistic to expect to measure changes of <5% in the natural isotopic abundance of ^{26}Mg, even for elemental magnesium. Isotopic sensitivity will be decreased by dilution with light elements and interference from heavy elements. This is discussed in Section 3.3. Heavier elements than Mg will have better isotopic sensitivities. Isotopic sensitivity is optimised by using the heaviest isotope as the tracer.

For the accurate calculation of isotopic composition the small differences in the scattering cross-sections for each of the different isotopes of an element must be taken into account. For an accurate

calculation when comparing total height ratios, for instance 24:26 as in Fig. 3.13, the number of events in the ^{26}Mg channel must be calculated under the ^{24}Mg peak using iterative steps to take into account the gradual changes in stopping power, cross-section, background and, if necessary, the contribution of the tails from adjoining steps or peaks beneath the area of interest.

The advantage of magnetic spectrometers in mass selectivity was mentioned earlier. Since instruments are available with apertures similar to those needed with silicon detectors, their use for stable isotope tracer measurement is further justified [65, 66].

3.2.b. Nuclear Reactions

Nuclear reaction cross-sections vary considerably and are fairly difficult to calculate. Generally experimental values reported in the literature are used [67-70]. Since there is a wide variation between cross-sections this can be used to advantage to enhance isotopic sensitivity by using a sensitive reaction for the tracer isotope of particular interest. Although reaction cross-sections for nuclear reactions are normally much lower than for Rutherford scattering this loss in sensitivity can often be more than compensated for by an increase in detector solid angle by a factor of 100.

The isotopic sensitivity that may be achieved using nuclear reactions is illustrated by the study of self-diffusion in magnesium. ^{25}Mg was used as tracer (natural abundance 10.13%) and compared with ^{24}Mg (abundance 78.7%) using the reactions $^{25}Mg(d,p)^{26}Mg$ and $^{24}Mg(d,p)^{25}Mg$. Deuteron energy = 1.9 MeV. Figure 3.12 shows the ^{25}Mg p_1 peak and the ^{24}Mg p_o peak from an experimental magnesium spectrum, as indicated the peaks are well separated. Their yields, for a 4 μC dose, were used to estimate the isotopic sensitivity for ^{25}Mg. For the isotopic ratio measurement:-

$$\text{Count ratio } {}^{25}Mg/{}^{24}Mg = 5.183 \times 10^{-2}$$

the variance of the count ratio = 7.847×10^{-4}.
This coefficient of variation of 1.51% suggests that a 3% change in isotopic abundance of ^{25}Mg, at the natural level for a 4 μC dose, should be measurable. This could be improved to 1% since a tenfold increase in detector efficiency is possible. However, it will be

degraded by decreases in Mg concentration and interference from light elements (see Section 3.3.2).

Although it has been demonstrated that good isotopic sensitivity can be obtained using nuclear reactions, wide variations are inevitable because of the numerous parameters involved.

3.3 THE INFLUENCE OF SAMPLE CONSTITUTION

Two aspects of the influence of sample constitution on nuclear microprobe measurements are considered. Firstly, bulk chemical composition. Secondly, sample heterogeneity. Backscattering and Nuclear Reaction Analysis will be considered in turn.

3.3.a Backscattering Analysis

The influence of bulk composition and sub-surface heterogeneity is complex. Of particular interest is the influence of these parameters in microbeam operation.

In backscattering analysis of stable isotopes it is preferrable that the tracer should be the heaviest mass present. This removes problems of interference by the presence of a high plateau from a heavier element, effectively acting as a high background under the tracer count region. It is not essential though, and indeed cannot be ensured since materials inevitably contain some heavy metal impurities. Therefore the influence has been calculated of 1% concentrations of Si, Co, Rb, Ag and Bi on the isotopic sensitivity for naturally abundant ^{26}Mg (see Table 3.1); the assumptions and conditions were identical to those used in Section 3.2.a.

Table 3.1

Coefficient of variation for the measurement of the natural abundance of ^{26}Mg in the presence of 1% Si, Co, Rb, Ag and Bi

IMPURITY	NIL	Si	Co	Rb	Ag	Bi
C_V	2.33%	2.42%	2.50%	2.54%	2.60%	2.82%

As might be expected the greatest influence is from bismuth. Even so, at the 1% level its influence on the isotopic sensitivity of ^{26}Mg is acceptable.

A general problem in ion beam analysis is the presence of surface impurities [58, 65, 71]. In the measurement of magnesium, both native oxide [65] and carbon deposited by the beam may be encountered. The experimental investigation of magnesium by backscattering is detailed in Chapter 4, however it is of interest to note that the simulation spectrum, shown in Figure 4.1, which allowed for the presence of oxide and carbon surface layers gave the best fit to experimental data. The use of simulations such as these are very useful in demonstrating the effects on spectra of different types and thicknesses of surface contaminants.

The influence of sample heterogeneity in microbeam operation is complex. For layer structures similar effects will be observed for micro and macro-beam operation [42]. However for multiphase systems, the observed scattering spectra will depend on the scale of dispersion of the phases relative to the beam size. When inclusions are large with respect to the beam, their composition will be accurately represented by the scattering spectra except at boundaries. There overlap effects occur, namely the analysis of both phases simultaneously and the passage of scattered particles from one phase through the second en route to the detector. As the inclusions decrease in size spectra become almost uninterpretable, until the particles become so small that a true solution is effectively formed. The same considerations apply to multilayered structures except that the penetration depth of the beam relative to the layer thickness is the important factor [42].

Topographical effects are also complex. Metallic samples do not present quite so much of a problem as other sample types and may undergo sequential polishing (using silicon carbide paper, diamond pastes to 1 or $\frac{1}{4}$ μm, alumina to remove residual silicon contamination and then diamond paste again) in order to try to remove topographical features. One must be cautious though because excessive polishing can affect distributional as well as topographical features.

Pressed powder samples are inevitably not very uniform, samples originally vacuum evaporated onto a substrate present a far better surface, avoiding topographical problems. With powder samples and particularly with biological samples surface roughness cannot be removed without altering the sample to an unacceptable extent. However, by using an observation angle very close to 180^{o} errors caused by

surface topography can be minimised. Its effect is two-fold firstly the incident and exit trajectories will be as near as possible the same thus avoiding, or at least minimising, the effects of exit through inclusions, phase boundaries or just through a thicker part of an uneven surface. Secondly this is the minimum path length within the target thus diminishing errors introduced by changes and inaccuracies in stopping powers and straggling. Additional information about complex structures should be obtained for other sources, for instance optical microscopy.

Whilst considering biological samples it is useful to consider the effects of sample damage [72, 73]. Although by using stable isotope tracers one avoids the effects of radiation damage caused by the presence of radioactive tracers in a sample, some beam damage during analysis is almost inevitable. When an energetic charged particle beam impinges on a target, large amounts of energy are dissipated into the target and some ionisation occurs. Much of the deposited energy causes thermal damage which may be reduced by lowering the dose rate. This may be achieved by using a low beam current or preferably, as it does not increase the analysis time, continuous electrostatic scanning can be used as discussed in Section 2.3. Usually nuclear reaction and backscattering experiments are carried out in vacuum, however if the chamber is filled with air or an inert gas this medium can help dissipate some of the heat generated. The experimental arrangements used and the problems related to gas filled target chambers are discussed in (74, 75). The advantages of using an inert gas are two fold as it also allows easier preparation of biological samples. Vacuum samples can be prepared but the technique is fairly difficult and often water loss damages samples irreparably.

3.3.b Nuclear Reaction Analysis

The influence of sample composition and heterogeneity in analysis by nuclear reactions is far less predictable than for backscattering analysis because of the resonant nature of cross-sections and the variety of emitted radiations. In general the measurement of emitted particles is preferred since they carry information on subsurface composition and surface contamination, while emitted gamma-rays are less informative. For heterogeneous materials, differences between the cross sections of tracer and comparison isotopes will create problems. Similar difficulties will ensue if X-ray measurements are

used to determine the total elemental concentration. Analysis of two phase systems may prove virtually impossible except when inclusions are much larger or smaller than the beam.

In isotope measurement by nuclear reaction analysis isotopic sensitivity may be influenced adversely by light element interference. This is illustrated for a ^{25}Mg tracer, as used in Section 3.2.b. The influence of the concentrations of B, N, Al, Si and S (having higher Q values than magnesium, these nuclides are the most likely interferences) on the isotopic sensitivity for ^{25}Mg has been assessed experimentally.

In calculating the coefficient of variation for the $^{25}Mg/^{24}Mg$ isotopic ratio it was assumed that the statistical influence of the interfering elements was directly proportional to their count contributions in the region of the ^{25}Mg p_1 peak and the ^{24}Mg P_o peak. The influence of the impurities is shown in Table 3.2.

Table 3.2

The influence of impurities on the coefficient of variation for the $^{25}Mg/^{24}Mg$ isotope ratio, at their natural abundances

IMPURITY	NIL	B	N	Al	Si	S
$C_{V25/24}$	1.51%	2.90%	2.10%	1.51%	1.60%	1.52%

The lightest elements, B and N, clearly have the greatest influence. In general the influence of light element interference must be assessed for every analytical problem.

3.4 SUMMARY OF THE APPRAISAL OF THE NUCLEAR MICROPROBE DETERMINATION OF THE SPATIAL DISTRIBUTION OF STABLE ISOTOPES

The distribution of stable isotope tracers may be determined using the nuclear microprobe by nuclear reaction or backscattering analysis. In some cases ion beam induced X-rays may be used in order to obtain the ratio of tracer isotope to the total elemental concentration. Both nuclear reactions and backscattering are largely confined to elements of light to medium mass. Microbeam operation allows the attainment of spatial resolutions approaching 2 μm with little adverse affect on mass selectivity or isotopic sensitivity. The highest isotopic sensitivities, ca 1%, appear to be achievable using

nuclear reactions. The two techniques are somewhat complementary, for nuclear reaction analysis isotopic sensitivity is degraded mainly by light element interference whereas in backscattering analysis the converse applies, heavy element interferences cause the problems. Difficulties may occur with complex samples, for instance in two phase systems microbeam operation permits only the examination of inclusions larger than the beam. The summary of the conditions for optimal mass selectivity in nuclear reaction and backscattering techniques for stable isotope tracing is given at the end of Section 3.1.

Although the rival technique, ion-probe mass-spectrometry can achieve isotopic sensitivities of 0.1% at spatial resolutions of $< 10\ \mu m$, its range of application can be severely limited by mass interferences and the formation of molecular species [8].

The nuclear microprobe technique for the spatial determination of stable isotope tracers would be most suitable for the study of corrosion mechanisms, self-diffusion and possibly biological processes if beam damage can be minimised. For complex materials the selectivity of nuclear reactions may prove invaluable.

In the following chapters the nuclear microprobe in conjunction with each of its two mass sensitive modes is applied to the measurement of stable isotope abundances and tracers in a variety of materials.

CHAPTER 4

BACKSCATTERING TECHNIQUES FOR THE MEASUREMENT OF STABLE ISOTOPE ABUNDANCES AND TRACERS

Several examples illustrating the use of backscattering for the absolute quantitative analysis of stable isotopes are detailed in this chapter and an appraisal is made of the possible extension of the technique to allow spatial analysis. The use of both surface barrier detectors and a magnetic analyser was investigated.

4.1 STABLE ISOTOPE ANALYSIS USING SURFACE BARRIER DETECTORS

Silicon surface barrier detectors, as discussed in Section 3.1.1f, are the most convenient for scattered particle measurement and their use was investigated first. A 3 MeV $^{4}He^{+}$ beam was produced by the nuclear microprobe and focussed onto the chosen targets. The scattered particles were detected by a high resolution solid state detector placed either initially at the usual particle collection position of 135^{o} or at the new 170^{o} position. The active surface of the detector was covered by a tantalum shield with a slit cut into it as shown in Figure 2.7. This slit reduces the angle subtended by the detector and hence reduces kinematic spread and its consequent spectrum degradation. An arc shaped slit was used to ensure collection at the correct angle. As detailed in Chapter 2 the rigours of high resolution backscattering spectrometry necessitated the use of a low noise high quality electronic system.

The stable isotopes of magnesium were investigated using a planar detector with an energy resolution $\simeq$ 11.5 keV FWHM. Part of the experimental spectrum obtained using a 3 MeV $^{4}He^{+}$ beam, the original collection angle of 135^{o} and a 1mm x 2mm slit placed 37mm from the sample, is shown in Figure 4.1. Although this detail shows only the two low abundance ^{26}Mg and ^{25}Mg stable isotopes all three were clearly visible. Figure 4.1 also shows spectra generated by a simulation programme.

The computer programme, used in order to help analyse backscattering spectra, was an adaptation of the large simulation programme written by Ziegler, Lever and Hirvonen [65, 76]. Basically the programme sets up an idealised spectrum and then convolutes in factors which degrade this idealised spectrum, producing a simulation of an experimental spectrum. A few iterations comparing calculated simulated spectra with the experimental

data are made and so that by a process of successive simulations one arrives at the best simulation of the data and has effectively "deconvoluted" the spectrum. This type of simulation method has been shown to be much more successful to the application of a wide range of data than the far more difficult approach of direct deconvolution (i.e. the removal of equipment resolution and other factors which degrade the resolution) of the experimental data. The problem with direct deconvolution lies in the inherent differences in the statistical processes used. In deconvolution one normally obtains the transform of the data and the resolution function, divides them and then obtains the inverse transform. When the Poisson statistics of the data (which contains significant high frequency components) is divided by the resolution function (which has practically zero high frequency component) the resultant high frequency component is unrealistically magnified and hence the inverse transform contains excessive oscillations.

The idealised spectra are based on coulombic scattering and on the Ziegler-Chu[77] energy loss polynomials. The programme calculates, by detailed numerical integration, the energy loss into the target, the elastic scattering of the projectile and the energy loss back out of the target. Using Bragg's rule one can attempt to deal with multi-element layers. The effects of detector resolution, the energy loss of projectiles in the detector surface metal layer and the interdiffusion of two or more layers are also included in the calculated simulation spectrum. The equations used to simulate the spectra are given in Appendix A. In high resolution backscattering each isotope may appear separately and isotope effects must be accounted for. In the original Ziegler programme the isotope effects were removed, being treated as another factor degrading the spectrum resolution. In the adapted programme used, the isotopes were retained each being treated separately taking into account the differences in kinematics, scattering cross-section and the different stopping powers. Some of the simulated spectra obtained are given in the Figures illustrating this chapter and can be compared with experimental data. It is worth noting that for visual impact the isotope steps in some of the Figures are marked as flat. The steps are not in fact absolutely flat owing to changes in scattering cross-section and, to a lesser extent, stopping power as the incoming particle energy decreases. Over very small energy changes the differences are slight and within the accuracy of the programme and the graphs one does apparently see "plateaus".

Figure 4.1 shows two simulations calculated using the computer simulation programme described. The two shown allow for magnesium with a 70 Å oxide layer, with and without 80 Å of carbon. The spectrum simulated assuming the presence of both oxide and carbon layers gives the better fit with the experimental data, particularly at the leading edges of the "plateau" regions. The experimental data was used to calculate the isotopic composition of magnesium. The counts used were those in the centre third of the ^{26}Mg and ^{25}Mg steps and a similar region in the ^{24}Mg region. The corrected ^{26}Mg, ^{25}Mg and impurity contributions to the region under the ^{24}Mg step were calculated using an iterative method incrementing stopping power and cross-section at each energy interval in order to obtain the ^{24}Mg contribution by difference. The resulting abundances are given in Table 4.1 below.

TABLE 4.1: EXPERIMENTALLY DETERMINED ABUNDANCES OF MAGNESIUM AND SILICON USING A SURFACE BARRIER DETECTOR

DETECTION CONDITIONS	SAMPLE	ISOTOPES INVESTIGATED			
135°, 1 x 2.2mm slit. 37mm from sample 40 µc Kinematic spread ≃ 11 keV	Mg	Isotope	Mg^{24}	Mg^{25}	Mg^{26}
		abundance expected	78.7	10.13	11.17
		abundance determined	78.8 ± 1.46 C_V = 1.84%	10.3 ± 0.24 C_V = 2.45%	10.8 ± 0.26 C_V = 2.42%
170°, 3.0mm arc slit 60mm from sample 16 µc Kinematic spread ≃ 4.5 keV	Mg	Isotope	Mg^{24}	Mg^{25}	Mg^{26}
		abundance expected	78.7	10.13	11.17
		abundance determined	78.7 ± 1.48 C_V = 1.88%	9.9 ± 0.39 C_V = 3.98%	11.4 ± 0.42 C_V = 3.68%
170°, 3.0mm arc slit 60mm from sample 4 µc Kinematic spread ≃ 4.5 keV	Si	Isotope	Si^{28}	Si^{29}	Si^{30}
		abundance expected	92.2	4.7	3.1
		abundance determined	92.7 ± 3.2 C_V = 3.45%	4.12 ± 0.49 C_V = 12%	3.2 ± 0.44 C_V = 13.6%

As mentioned in Section 3.1 it is desirable to collect backscattered particles at the highest possible angles thus reducing kinematic spread. The 1 by 2 mm slit used at 135° (Ω = 0.6 msr) has a kinematic broadening of

≃ 11.5 keV. At the 170° maximum collection angle, 60 mm from the sample, the same slit would subtend 0.22 msr with a kinematic spread of ≃ 2 keV. As the sensitivity is greatly reduced at the new position it is advantageous to use the largest arc slit which still ensures an acceptable kinematic spread, <5 keV. A 3.0 mm arc slit, 60 mm away from the target was used. Part of the spectrum of magnesium obtained under these conditions is given in Figure 4.2. Again the isotope steps are visible and the abundances obtained are given in Table 4.1. While use of the higher observation angle improves mass resolution through reducing kinematic degradation of the spectrum, in practice the overall resolution was not improved since the transmission mount detector available had a relatively poor resolution, about 13.5 keV (FWHM).

Figure 4.3 shows the silicon steps obtained from the spectrum of a bismuth implanted silicon backscattering standard. This standard is usually used to check the overall resolution of the various systems used. The abundances found are listed in Table 4.1.

The abundances found for both magnesium and silicon are in good agreement with the expected abundances although for the latter the statistics are poor because of the low dose used. These results demonstrate the ability of backscattering to quantitatively determine stable isotope abundances. Since the method is an absolute one it has the advantage that no calibration standards are needed, providing that the scattering approximates closely to pure Rutherford scattering.

4.2 STABLE ISOTOPE ANALYSIS USING THE MAGNETIC SPECTROMETER

To extend the limit of mass resolution a Buechner magnetic spectrometer was used to analyse the backscattering particles. At present there is no magnetic spectrometer facility available on the nuclear microprobe thus these feasibility experiments were carried out on the Tandem Van de Graaff accelerator which has a single focussing Buechner magnetic spectrometer but unfortunately no microprobe focussing. The single focussing Buechner spectrometer is described in detail in Chapter 2. As discussed there, the optimum resolution was attainable at the highest backscattering angle of 145°, with a solid angle of 0.175 msr. Using a position sensitive detector and a very thin ^{244}Cm alpha source (6×10^{-5} d.p.s.) in the place of a target, a practical resolution of 8.5 ± 0.2 keV FWHM was achieved. The relevant calibration curve is shown in Figure 4.4. It should be noted that the resolution obtained

with the Harwell single focussing Buechner is considerably poorer than that obtained by the N.R.L. double focussing facility as described in Chapter 3.

The mass resolution of the silicon surface barrier detector and the magnetic spectrometer is compared in Table 4.2 for a variety of ions with a range of energies.

TABLE 4.2: OPTIMISTIC THEORETICAL MAXIMUM LIMITS OF MASS RESOLUTION CALCULATED FOR OUR DETECTION SYSTEMS

INCIDENT BEAM	NOMINAL BACKSCATTERING ANGLE	OPTIMUM OVERALL RESOLUTION & DETECTOR TYPE	THEORETICAL MASS LIMIT FOR $\Delta M = 1$
3.0 MeV $^4He^+$	135^o	Silicon surface barrier detector ≃ 15 keV	≃ 45
3.0 MeV $^4He^+$	170^o		≃ 48
5.8 MeV $^4He^+$	170^o		≃ 70
3.0 MeV $^4He^+$	170^o	Magnetic spectrometer ≃ 9 keV	≃ 64
3.0 MeV $^4He^+$	145^o		≃ 62
5.8 MeV $^4He^+$	145^o		≃ 88
5.8 MeV $^{16}O^{+4}$	145^o		≃ 158
20.0 MeV $^{16}O^{+4}$	145^o		> 200

The table clearly shows that the magnetic spectrometer has the better mass/energy resolution and also has the capability of successfully analysing heavier and more energetic beams. It would have been interesting to examine magnesium using a 3 MeV $^4He^+$ beam and the magnetic analyser in order to get a direct comparison with the isotope resolution of the surface barrier detectors. Unfortunately this was impractical because of the extreme difficulty in obtaining low energy, low mass beams from the Tandem accelerator that were sufficiently stable for our purposes. A good beam was obtained at 5.8 MeV $^4He^+$. The maximum theoretical limit of resolution $\Delta M = 1$ at the available angle 145^o was ≃70 thus a nickel sample provided a convenient target. The spectrum obtained with a 5.8 MeV $^4He^+$ beam at 145^o is shown in Figure 4.5. The isotopes are clearly evident and again the data was used to obtain stable isotope abundances. The results are shown in Table 4.3.

TABLE 4.3: EXPERIMENTALLY DETERMINED ABUNDANCES OF SILVER AND NICKEL USING A MAGNETIC SPECTROMETER

SAMPLE	ISOTOPE ABUNDANCES		EXPERIMENTAL. CONDITIONS
	EXPERIMENTAL	EXPECTED	
NICKEL 58	67.6 ± 4.01%	67.88%	
60	26.6 ± 2.07%	26.23%	5.8 MeV $^4He^+$ BEAM
61	1.24 ± 1.17%	1.19%	$\theta = 145^\circ$
62	3.45 ± 0.81%	3.66%	Ω = 0.175msr
64	1.04 ± 0.37%	1.08%	
SILVER 107	51.63 ± 2.6%	51.83%	20 MeV $^{16}O^{+4}$ BEAM
109	48.3 ± 1.55%	48.17%	$\theta = 145^\circ$
			Ω = 0.175msr

Heavier mass beams were also available on the Tandem and the higher energy and higher charge state beams provided the most convenient beam currents and the most stable beams. A 20 MeV $^{16}O^{+4}$ beam was used to obtain the backscatter spectrum of silver shown in Figure 4.6. An analysis time of 70 minutes was required to collect a satisfactorily defined spectrum. This was a consequence of the low beam current (ca 50 namps) low solid angle (0.175 msr) and the inherent problem of charge state fractionation. This latter problem arises because whenever charged particles pass through a target, orbital electrons are captured and lost and hence the beam fractionates between the available charge states. The fractionation values, which are in fact energy dependent, have been tabulated by Marion and Young [68]. The problem of spectrum interpretation when several charge states are present is somewhat simplified by the fact that usually only one charge state of a given mass appears on the detector at any given frequency. Obviously in order to shorten analysis times, improvements in beam current and solid angle are possible cf. the solid angle range available on the N.R.L. magnetic spectrometer [54]. Collection of the scattered ions with the highest abundance charge state optimises sensitivity. Despite limitations isotope steps were resolved and the abundances found are given in Table 4.3. The abundances found for both the silver and nickel spectra are in good agreement with the expected values and clearly demonstrate the ability of the magnetic spectrometer to quantitatively determine stable isotope abundances and greatly extend the mass limit of resolution of the backscattering technique.

4.3 APPRAISAL OF THE ADAPTATION OF THE BACKSCATTERING TECHNIQUE FOR SPATIAL ANALYSIS

The great advantage of the nuclear microprobe is its capability to allow spatial measurements to be carried out. Thus the possibility arises for one to measure the spatial distributions of stable isotopes in a system which has been treated with a stable isotope.

Although it has been shown by the examples studied in this chapter that backscattering can be used successfully to measure stable isotope abundances even at relatively high mass when employing magnetic spectrometers, its extension to nuclear microprobe analysis will be severely restricted by sensitivity as implied by the results in Tables 4.1 and 4.3 which indicate that even at high doses for pure elements the isotopic sensitivity (i.e. coefficient of variation from standard deviation) is low. In spatial analysis a scattering spectrum must be collected at each analysis point, increasing the analysis time in proportion to the number of points examined. This will be time consuming since the analysis of an individual point will normally exceed 5 minutes and could take as long as 1 hr. Although in theory analysis times can be decreased by increasing incident beam currents it is often not possible to exceed a few nano-amps because of beam damage and pile up phenomena particularly when using silicon surface barrier detectors. Solid angle limitations on mass resolution ultimately control analysis speed when using either silicon surface barrier detectors or magnetic spectrometers. While the latter have a fundamental advantage in energy resolution, their sensitivity is affected by charge state fractionation whereas silicon detectors are unaffected since they collect all charge states.

Because of these limitations backscattering will only be employed to measure isotope abundances with the nuclear microprobe in exceptional circumstances*. In all probability $^{4}He^{+}$ irradiation with measurement of scattered particles using a silicon detector will be selected because of its convenience, and mass resolution will be adjusted by optimising the irradiation energy. For many light elements nuclear reaction methods will be preferred for isotope measurement despite the need for calibration which is not essential when using scattering because of its fundamental basis.

4.4 CONCLUSIONS

Backscattering analysis has been successfully used to quantitatively determine the absolute abundances of stable isotopes and the use of the magnetic spectrometer to extend the mass limit of resolution of the technique has been successfully demonstrated. It would appear that the lack of sensitivity will severely limit the application of the technique for spatial analysis.

*The development of a new detector [143] for heavy ion backscattering analysis may perhaps modify these conclusions.

CHAPTER 5

NUCLEAR REACTION METHODS FOR THE SPATIAL ANALYSIS OF STABLE ISOTOPES, IN PARTICULAR ^{13}C AND ^{12}C

It was apparent from the detailed theoretical investigation of the two isotopically sensitive modes of the nuclear microprobe discussed in Chapter 3, that nuclear reaction methods were particularly well suited to light element analysis [78]. In this chapter, sensitive and selective nuclear reaction methods have been sought for the nuclear microprobe measurement of the spatial distributions of ^{13}C and $^{13}C/^{12}C$ ratios as an example of the application of nuclear reaction methods to stable isotope analysis.

The behaviour of carbon in biochemical, biomedical and physicochemical systems is of widespread interest. Whilst ^{14}C is commonly used as an isotope tracer in mechanistic studies it is not always suitable, for instance where the introduction of a radioactive tracer might be barred or where it might be overwhelmed by the inherent radioactivity of the specimen. Furthermore, as mentioned earlier, in the investigation of many processes isotope ratio values are far more informative than the tracer concentrations alone. Consequently, ^{13}C can be an attractive alternative to ^{14}C in tracer studies, providing a spatially sensitive method is available to measure ^{13}C and $^{13}C/^{12}C$ ratios.

A comprehensive investigation was undertaken of the ^{13}C and ^{12}C reactions that could be induced by the various beams, of up to 3 MeV, available on the nuclear microprobe to find the most promising reactions for the measurement of ^{13}C and $^{13}C/^{12}C$ ratios. The conditions governing the use of these reactions, particularly light element interferences, are detailed.

5.1 PRELIMINARY SURVEY OF POSSIBLE REACTIONS SUITABLE FOR THE SPATIAL DETERMINATION OF ^{13}C and $^{13}C/^{12}C$ RATIOS

In selecting reactions suitable for use on the nuclear microprobe, good sensitivity is of paramount importance because of the inherently low beam currents available, < 25 nA, and the large number of analyses per specimen. Good selectivity is also highly desirable to simplify data resolution. Whilst certain nuclear reactions, such as the (p,γ) [79-87] reaction, are satisfactory for the determination of $^{13}C/^{12}C$ ratios in bulk specimens their suitability for application to the nuclear microprobe was

questionable on the grounds of sensitivity so experimental examination of this was undertaken.

Although the (p,n) [88-91] reaction has been used to measure ^{13}C the threshold energy (in the region of 3.23 MeV) and the resonance energies (6.7, 7, 8.8 MeV) are too high for the Harwell nuclear microprobe. Even if the most favourable irradiation conditions could be used the sensitivity for measuring ^{13}C is barely acceptable for nuclear microprobe application [91]. In addition only ^{13}C and not ^{12}C can be measured as the Q value for the $^{12}C(p,n)^{12}N$ reaction is -18.13 MeV. The Q value of the $^{13}C(p,n)^{13}N$ reaction -3.03 MeV is also rather unfavourable. As ^{7}Li, ^{9}Be, ^{11}B, ^{18}O and ^{37}Cl all have more positive reaction Q-values extensive interference is possible. Experience with the determination of ^{9}Be [58] suggests that the (α,n) reaction has considerable potential for the highly selective determination of ^{13}C with significant interference being limited to that by beryllium. The use of the (α,n) reaction for the measurement of ^{13}C in thick targets of 89% enriched $^{*}CH_3I$ deposited onto a tantalum backing has been reported by Ramström [92]. He was primarily interested in the astrophysical application of the $^{13}C(\alpha,n)^{16}O$ reaction as a neutron source during star evolution and the use of the reaction for the determination of the spatial distribution of ^{13}C tracers does not appear to have been carried out. The remaining alpha induced charged particle reactions show little promise for ^{13}C determinations as all have high reaction thresholds. With the deuteron energies available on the Harwell microprobe both the $^{13}C(d,n)^{14}N$ and the $^{12}C(d,n)^{13}N$ nuclear reactions will occur. The neutrons emitted have been measured using the time of flight technique, however this is incompatible with the present nuclear microprobe facility since the long pulse width, 20ns, leads to unacceptably poor energy resolution. Neutron measurement methods with exception of the (α,n) method are unattractive because of the high probability of interference from the many (p,n) and (d,n) reactions on nuclides which emit relatively high energy neutrons [93]. Consequently the only reaction suitable for carbon analysis using neutron detection in conjunction with the nuclear microprobe appeared to be the $^{13}C(\alpha,n)^{16}O$ reaction, therefore this reaction was investigated experimentally.

The (d,p) [20, 94] reaction is used routinely for the nuclear microprobe determination of ^{12}C and sensitivities of ca. 1ppm [94] are now attainable. Obviously it would be convenient if these techniques could be extended to allow simultaneous analysis of spatial distributions of ^{13}C. Cross-section studies [95, 96] indicate that the po particle group emitted

by the reaction $^{13}C(d,p_o)^{14}C$ is measurable for ^{13}C enriched targets. In addition the deuteron induced gamma producing reactions do show some promise [97] for the analytical measurement of ^{12}C and ^{13}C and thus were investigated.

The (^{3}He, p) and (^{3}He,α) reactions have been used by several groups [98, 104], mainly to analyse bulk ^{12}C. Most workers have carried out their measurements by utilising the resonance γ-rays emitted from the product nuclides. Kaim and co-workers [105] did measure the proton groups from the $^{12}C(^3He, p)^{14}N$ reaction although a consideration of the charged particle product energies suggests that interference may well occur in both ^{12}C and ^{13}C analysis by this reaction, thus limiting the sensitivity attainable. The sensitivity of the method and the extent of interference were investigated.

The details of the investigations of the most promising reactions are described and the probable value of the various techniques for the nuclear microprobe measurement of ^{13}C and $^{13}C/^{12}C$ ratios is discussed.

5.2 EXPERIMENTAL INVESTIGATION AND DISCUSSION OF THOSE REACTIONS CONSIDERED MOST APPLICABLE TO $^{13}C/^{12}C$ STABLE ISOTOPE ANALYSIS

The experimental investigation was carried out using the nuclear microprobe and the counting systems described in detail in Chapter 2. ^{12}C and ^{13}C standards were prepared as pressed powder discs from $BaCO_3$ enriched up to 90% in ^{13}C. Interference studies were undertaken for Li, Be, B, N, O, F, Na, Mg, Al, Si, P, S and Cl using targets of $LiNbO_3$, Be/Cu alloy, B, SiN, SiO_2, SrF_2, NaCl, Mg, Al, Si, InP, PbS and AgCl as polished solids or pressed powder discs. For the $BaCO_3$ samples very careful measurement conditions were required in order to minimise any loss of ^{13}C as $^{13}CO_2$ due to heat damage by the beam. A 1.6nA rastered beam was used stepped after each 0.1 μC dose of charge.

5.2.1 The (α,n) Reaction

Sensitivity and selectivity in the measurement of ^{13}C by the (α,n) reaction were optimised through choice of irradiation energy and by neutron energy discrimination.

Consideration of ^{13}C and in particular the $^9Be(\alpha,n)$ reaction cross-sections at 0^o indicated that irradiation with 2.8 MeV $^4He^+$ ions

would optimise the yield of neutrons from ^{13}C (106). Few nuclides produce neutrons of greater or comparable energy to those emitted by the reaction $^{13}C(\alpha,n)^{16}O$ as can be seen in Table 5.1.

TABLE 5.1 EMITTED NEUTRON ENERGIES FROM POSSIBLE INTERFERENCES TO ^{13}C ANALYSIS USING THE (α,n) REACTION

$E_o{}^4He^+ = 2.8$ MeV, $\theta = 0^o$

TARGET NUCLIDE	EMITTED NEUTRON ENERGY (MeV)
^9Be	8.486
^{25}Mg	5.416
^{21}Ne	5.312
^{13}C	4.936
^{10}B	3.704
^{17}O	3.269
^{11}B	2.754
^{26}Mg	2.734
^{22}Ne	2.179
^{18}O	1.919

Assuming Neon to be absent, the neutron yield obtained for various neutron energy threshold settings of the pulse discrimination system was determined for targets of boron, 1.89% beryllium in copper, silica, ^{13}C enriched $BaCO_3$ and magnesium. Since the maximum energy of neutrons emitted by ^9Be, ^{25}Mg, ^{21}Ne, ^{13}C, ^{10}B, ^{17}O, ^{11}B, ^{26}Mg, ^{22}Ne and ^{18}O are those shown in Table 5.1 a series of threshold settings were found which successively eliminated neutrons from those targets. The values found and the related neutron energies are shown in Figure 5.1. By choosing a ^{10}B cut-off point, 3.704 MeV, only neutrons from ^9Be, ^{25}Mg and ^{13}C can be collected. For these conditions 1 wt % of ^{13}C in a $BaCO_3$ matrix gave 885 counts/μ coulomb and the relative responses for ^9Be, ^{25}Mg and ^{13}C were found to be 13.7 : 0.001 : 1.0. A far greater sensitivity, 4300 counts/μ coulomb, was obtained for ^{13}C by reducing the neutron energy threshold to just above that of ^{18}O, 1.919 MeV. While this leads to additional interference from ^{26}Mg and $^{10/11}B$ none was measurable for ^{17}O at its natural abundance in SiO_2.

Calibration curves for the two measurement conditions are shown in Figure 5.2. Since on a weight basis the relative responses for ^{9}Be, $^{25/26}Mg$, ^{13}C and $^{10/11}B$ were 3.9 : 0.001 : 1.0 : 0.007 the choice of the lower discrimination energy has the advantage of enhancing sensitivity with little loss in selectivity. For matrices containing little or no beryllium and minor amounts of $^{25/26}Mg$ and $^{10/11}B$ the (α,n) reaction is virtually specific for the measurement of ^{13}C with a sensitivity of ca. 100 ppm.

5.2.2 The (d,p) and (d,α) reactions

Carbon distributions are frequently measured on the Harwell nuclear microprobe by the $^{12}C\ (d,p)^{13}C$ reaction with a 1.3MeV deuteron beam [20, 94], thus these conditions were choosen initially to study the possible extension of the technique to measure ^{13}C. The particle energy spectra obtained for natural and enriched $BaCO_3$ targets are shown in Figure 5.3. The p_o particle groups from both ^{12}C and ^{13}C clearly stand out. Straight line calibration graphs, Figure 5.4, were obtained for both ^{12}C and ^{13}C by measuring their p_o peak areas over channels 60 to 68 and 115 to 135 respectively. For a $BaCO_3$ matrix sensitivities were obtained of 40900 and 3250 counts/μC/1 wt. % ^{12}C and ^{13}C respectively giving direction limits of 5 and 60 ppm respectively were obtained.

Extensive interference with the determination of ^{12}C and ^{13}C through their emitted p_o groups [93] may occur since many light elements react with deuterons. Consequently the extent of interference by elements from Li to Cl was studied with the exception of Neon. The charged particle energy spectra of some of the interferences are given in Figures 5.5 to 5.8 and the interference levels of the 4 worst interferences Li, B, F and N are given in Figure 5.9. The interference by boron to ^{13}C is due to the very high background levels from the $^{10}B_{p_1}$ and also from the tails of the higher energy $^{10}B_{p_o}$ and $^{10}B_{\alpha_1}$ peaks. The $^{10}B_{p4}$ and the very high background levels from other higher energy boron peaks cause the interference to ^{12}C analysis. The broad $^{7}Li_{\alpha o}$ peak causes interference to $^{13}C_{p_o}$ analysis and the very high background levels from the $^{7}Li_{\alpha o}$, $^{6}Li_{p_o}$ and $^{6}Li_{p_1}$ peaks all hinder $^{12}C_{p_o}$ analysis. The high background levels from the $^{14}N_{p_o}$ and $^{14}N_{\alpha o}$ groups cause interference to $^{13}C_{p_o}$ analysis and general high levels of background from high energy Nitrogen peaks causes the interference to $^{12}C_{p_o}$ analysis.

The tail of the higher energy $^{19}F_{\alpha_o}$ peak causes some interference to ^{13}C analysis and the $^{19}F_{p_6}$ peak causes some interference to ^{12}C analysis.

The effect of varying the incident beam energy both on the yield of ^{13}C and also the degree of interference from Li, B, F and N are given in Figures 5.10 and 5.9 respectively. The greatest sensitivities, ca. 6300 and 108,600 counts/μC giving detection limits of 30 and 2ppm for 1 wt. % ^{13}C and 1 wt. % ^{12}C in $BaCO_3$ respectively, were obtained with 1.5 MeV deuterons. However although increasing the irradiation energy can reduce the degree of interference from some isotopes, the interference of lithium on ^{13}C is reduced by almost two orders of magnitude, in some cases the degree of interference increases above 1.4 MeV. The choice of bombarding energy would thus depend to some degree on which interferences were likely to be present but clearly for matrices containing even limited amounts of Li, N, B and F considerable caution must be exercised in applying the (d,p) reaction. While interference from other light elements was found to be lower, the measured R values (where R is the ratio of the yield of 1 wt. % interference nuclide to the yield of 1 wt. % ^{13}C or ^{12}C all measured per μC) indicate that few can be ignored completely as can be seen in Table 5.2 below.

TABLE 5.2 INTERFERENCE TO THE MEASUREMENT OF ^{12}C AND ^{13}C USING THE (d,p_o) NUCLEAR REACTIONS.
$E_o d$ = 1.3 MeV, θ = 135°

NUCLIDE	R VALUE (^{12}C)	R VALUE (^{13}C)
Li	0.49	4.7
Be	0.16	0.008
B	0.009	0.073
O	0.005	< 0.0001
N	1.3	0.18
F	0.067	0.0155
Na	0.0001	0.001
Mg	0.001	0.008
Al	0.0007	0.006
Si	0.0002	0.006
P	0.0008	0.0008
S	0.012	0.001
Cl	0.009	0.0002

$$R = \frac{\text{(Yield of 1 wt. \% Interference Nuclide/μC)}}{\text{(yield of 1 wt. \% } ^{13}C \text{ or } ^{12}C/\mu C)}$$

For materials containing insignificant amounts of interfering elements the (d,p) reaction will allow the nuclear microprobe determination of $^{13}C/^{12}C$ ratios with a reasonably high sensitivity. The inferior sensitivity for ^{13}C reduces the possibility of measuring small enrichments of the tracer isotope.

The (d,α) reaction was found to be of no use for the determination of ^{13}C and ^{12}C. As can be seen in Figure 5.3 the $^{13}C_{\alpha_o}$ peak sits under the $^{16}O_{p_o}$ group and also on the edge of the low energy tail of the $^{12}C_{p_o}$ peak, thus interference would be unacceptably high. The $^{12}C_{\alpha_o}$ peak is totally absorbed by the absorber foils needed to prevent scattered deuterons reaching the active detector layer.

5.2.3 The (^{3}He,p) and (^{3}He,α) Reactions

The cross-section [104, 105] for the $^{13}C(^3He,p)^{15}N$ nuclear reaction rises slowly with increasing energy. Good sensitivity for the measurement of ^{13}C will therefore be favoured by choosing an irradiation energy close to the 3 MeV maximum of the Harwell nuclear microprobe. Consequently, initial studies used 2.8 MeV ^{3}He ions and the emitted particle spectra, shown in Figure 5.11, were produced by irradiating natural and enriched $BaCO_3$ targets. Since the $^{12}C_{p_o}$ peak suffers interference from the $^{13}C_{p2}$ and $_{p3}$ groups clearly seen in Figure 5.11, on the basis of the known ^{13}C and ^{12}C concentrations of the standards a linear least squares fitting procedure was employed to obtain the best values for the response of 1 wt. % ^{12}C and 1 wt. % ^{13}C interference within the $^{12}C_{p_o}$ region. For a sample the ^{13}C concentration is obtained directly from the $^{13}C_{p_o}$ particle group, this is then used to correct the ^{12}C value. The calibration curves obtained for both ^{13}C and ^{12}C are given in Figure 5.12. Sensitivities of 320 and 840 counts/μC for 1 wt. % ^{13}C and 1 wt. % ^{12}C in $BaCO_3$ respectively were obtained, giving limits of 630 and 240 ppm respectively.

A wide range of light elements react with $^3He^+$ [30] ions and again the interference level of all the elements up to $Z \leq 17$ with the exception of H, He and Ne was investigated. The four most serious interferences were found to be beryllium, lithium, boron and nitrogen and the relevent particle spectra are given in Figures 5.13 to 5.16.

The very high degree of interference from the beryllium to the $^{13}C_{p_o}$ peak is due to the $^9Be_{p_o}$ and $^9Be_{p_1}$ peaks while the interference to the $^{12}C_{p_o}$ peak is due to the presence of the $^9Be_{p_3}$ peak and (to

some extent) the $^{9}Be_{p_2}$ low energy tail. The interference to the $^{13}C_{p_o}$ peak analysis caused by Lithium is due to the $^{7}Li_{p_o}$ whilst the $^{7}Li_{p_4}$ and general high background level from high energy Lithium peaks causes the interference for $^{12}C_{p_o}$ analysis. As can be seen from Figure 5.15 several ^{10}B and ^{11}B proton peaks cause interference to both $^{13}C_{p_o}$ analysis and $^{12}C_{p_o}$ analysis. The $^{14}N_{p_1}$ and $_{p_2}$ peaks interfere with $^{13}C_{p_o}$ analysis and several nitrogen peaks cause interference to $^{12}C_{p_o}$ analysis. Figure 5.17 shows the variation in ^{13}C yield with increasing energy. The highest sensitivity of 460 counts/μC for 1 wt. % ^{13}C in $BaCO_3$ was obtained at 3 MeV $^{3}He^{+}$, the energy limit of the machine. The yield of the $^{12}C_{p_o}$ group also increases with increasing beam energy and a sensitivity of 1400 c/μC was obtained at 3 MeV $^{3}He^{+}$. The effect of increasing the beam energy on the relative interference levels of the four worst interferences was investigated and the results are given in Figure 5.18. Again the effect on the levels of interference varies but it can be seen that to work at 3 MeV is advantageous both with regard to sensitivity and the degree of interference. The inverse proportionality of the R value and energy is partly attributable to the increase in sensitivity for both ^{12}C and ^{13}C with increasing energy. The remaining elements cause less interference and the R values obtained at 2.8 MeV are listed in Table 5.3.

TABLE 5.3 INTERFERENCE TO THE MEASUREMENT OF ^{12}C AND ^{13}C USING THE $(^{3}He,p_o)$ NUCLEAR REACTIONS

$E_o {}^{3}He^{+}$ = 2.8 MeV, θ = 135°

NUCLIDE	R VALUE (^{12}C)	R VALUE (^{13}C)
Li	12.0	7.3
Be	28.0	18.5
B	0.122	0.97
N	0.015	0.51
O	< 0.001	0.001
F	0.06	0.04
Na	0.01	0.004
Mg	< 0.001	< 0.0001
Al	0.005	< 0.0001
Si	< 0.001	< 0.0001
P	0.004	0.013
S	< 0.001	0.002
Cl	< 0.001	< 0.0001

$$R = \frac{\text{(Yield of 1 wt. \% Interference Nuclide/μC)}}{\text{(Yield of 1 wt. \% } ^{13}C \text{ or } ^{12}C/\mu C)}$$

The (^{3}He,α) peaks were found to be of no value for ^{12}C and ^{13}C measurement. The $^{13}C_{\alpha_0}$ to α_4 peaks were barely discernable and although the α_5 and α_6 are just visible they lie very close to the $^{13}C_{p_1}$ and p_2 peaks. The $^{12}C_{\alpha_0}$ peak was entirely absorbed by the thickness of detector mylar absorber foil used to prevent scattered $^3He^+$ ions entering the active detector.

Although the (^{3}He,p) reaction may be used for the nuclear microprobe determination of $^{13}C/^{12}C$ ratios this reaction tends to be less attractive than the (d,p) reaction because of its lower sensitivity and wide suseptibility to interference. For the Harwell nuclear microprobe irradiation with 3 MeV $^3He^+$ ions optimises sensitivity and selectivity.

5.2.4 $^2H^+$ Induced Gamma Reactions

A major disadvantage of the (d,p) method for the determination of $^{13}C/^{12}C$ ratios is its relatively high susceptibility to interference. Measurement of prompt gamma-rays emitted during deuteron bombardment, with a high resolution Ge(Li) detector, offers a possible means of retaining the good sensitivity of the (d,p) method while discriminating more successfully against interferences.

Gamma-ray spectra of enriched and natural $BaCO_3$ targets bombarded with a 1.5 MeV deuteron beam are given in Figure 5.19 and the assignment of peak origins are tabulated in Table 5.4.

TABLE 5.4 IDENTIFICATION OF THE GAMMA-RAYS EMITTED BY IRRADIATING ^{12}C AND ^{13}C WITH 1.5 MeV DEUTERONS AND OBSERVED IN THE SPECTRA SHOWN IN FIGURE 5.19

Peak Number	Reaction	Gamma-ray Energy (MeV)	Gamma-ray Transition (MeV)
1	$^{13}C(d,p\gamma)^{14}C$	6.09	6.09 → 0
2	$^{13}C(d,n\gamma)^{14}N$	5.685	5.685 → 0
3	(1 se)		
4	(2 se)		
5	(1 de) ^{13}C $(d,\alpha\gamma)^{11}B$	5.03	5.03 → 0
6	^{13}C $(d,n\gamma)^{14}N$	4.910	4.910 → 0

/Table Continued ..

TABLE 5.4 (Continued)

Peak No.	Reaction	Gamma-ray Energy (MeV)	Gamma-ray Transition (MeV)
7	(2de)		
8	(5se)		
9	(6se)		
10	(5de)		
11	(6de)		
12	$^{13}C(d,n\gamma)^{14}N$	3.373	$5.685 \longrightarrow 2.312$
13	$^{12}C(d,p\gamma)^{13}C$	3.085	$3.085 \longrightarrow 0$
14	(13se)		
15	$^{13}C(d,n\gamma)^{14}N$	2.312	$2.312 \longrightarrow 0$

se and de denote the single and double escape peaks.

Only the 3.085 MeV γ-ray from the reaction $^{12}C(d,p\gamma)^{13}C$ is produced for ^{12}C and must be used for its measurement. Although six gamma-rays produced by the reactions $^{13}C(d,p\gamma)^{14}C$, $^{13}C(d,n\gamma)^{14}N$ and $^{13}C(d,\alpha\gamma)^{11}B$ have been identified that at 3.373 MeV was preferred for the measurement of ^{13}C on the grounds of sensitivity. Using these two γ-rays and a simple base line subtraction method to calculate their associated peak areas, straight line calibration graphs were obtained for ^{12}C and ^{13}C which are given in Figure 5.20. Sensitivities of 1800 and 3100 counts per μC, giving detection limits of 640 and 440 ppm were found for 1 wt. % ^{13}C and 1 wt. % ^{12}C in $BaCO_3$ respectively. The poorer sensitivities are partly a consequence of the reaction cross-sections involved and partly a consequence of gamma-ray detection efficiency. The poorer detection limits also reflect the adverse influence of the high compton background on counting statistics.

Again since so many gamma peaks are produced when bombarding samples with deuteron beams all possible interferences up to Z = 17 with the exception of H, He and Ne were investigated. Gamma-ray detection was found to give poorer discrimination against light

element interference than expected. Although direct interference can occur from reactions that lead to the production of ^{13}C and ^{14}N, namely, $^{15}N(d,\alpha)^{13}C$ and $^{16}O(d,\alpha)^{14}N$, interference studies on nitrogen and oxygen indicate that they are of little or no consequence. Interference through gamma-ray overlap can, however, occur. The 3.373 MeV peak is poorly separated from the 3.368 MeV gamma-ray produced by the reaction $^{9}Be(d,p\gamma)^{10}B$, the 3.368 MeV emission from $^{32}S(d,p\gamma)^{33}S$ and the 3.385 MeV and 3.364 MeV emissions from $^{24}Mg(d,p\gamma)^{25}Mg$ and $^{24}Mg(d,\alpha\gamma)^{22}Na$ respectively. Fortunately, these problems can be circumvented by chasing other gamma-rays for the measurement of ^{13}C, but with some loss of sensitivity. The 3.085 MeV peak is overlapped by gamma-rays emitted by 9 of the 13 light elements tested. The interfering gamma-rays involved are the 3.09 MeV emission from $^{19}F(d,p\gamma)^{20}F$, the 3.07 MeV emission from $^{23}Na(d,\alpha\gamma)^{21}Ne$, the 3.082 MeV emission from $^{24}Mg(d,p\gamma)^{25}Mg$, the 3.10 MeV and 3.057 MeV emissions from $^{27}Al(d,p\gamma)^{28}Al$, the 3.069 MeV emission from $^{31}P(d,\alpha\gamma)^{29}Si$, the 3.098 MeV emission from $^{32}S(d,p\ )^{33}S$, the 3.11 MeV emission from $^{32}S(d,p\gamma)^{33}S$, and less well authenticated emissions from $^{9}Be(d,n\gamma)^{10}B$ and $^{7}Li(d,\alpha\gamma)^{5}He$. Quantitatively the degree of interference can be seen from the measured R values which are tabulated below in Table 5.5.

TABLE 5.5 INTERFERENCE TO THE MEASUREMENT OF ^{12}C AND ^{13}C USING THE $^{12}C(d,p\gamma)^{13}C$ $E\gamma$ = 3.085 MeV AND THE $^{13}C(d,n\gamma)^{14}N$ $E\gamma$=3.373 MeV REACTIONS

$E_o d$ = 1.5 MeV, $\theta = 0^o$

NUCLIDE	R VALUE (^{12}C)	R VALUE (^{13}C)
Li	0.015	< 0.066
Be	0.054	0.016
B	< 0.006	< 0.008
N	< 0.0008	< 0.0001
O	< 0.0001	< 0.00003
F	0.028	< 0.069
Na	0.020	< 0.002
Mg	0.006	0.004
Al	0.0017	< 0.014
Si	< 0.00006	< 0.00006
P	0.007	< 0.00002

/Table continued ...

TABLE 5.5
(Cont'd)

NUCLIDE	R VALUE (^{12}C)	R VALUE (^{13}C)
S	0.022	0.0013
Cl	0.013	< 0.001

$$R = \frac{\text{(Yield of 1 wt. \% Interference Nuclide/}\mu C)}{\text{(Yield of 1 wt. \% } ^{13}C \text{ or } ^{12}C/\mu C)}$$

The limit values indicate the measurement limitations imposed by the presence of a Compton continuum rather than a gamma-ray peak. This limitation is highly significant for some elements, notably lithium and fluorine. For certain elements, particularly boron and nitrogen the degree of interference is much less than for the (d,p) method, and gamma-ray measurement might be used with advantage for the examination of materials containing those elements. Although deuteron induced gamma-rays may be used for the nuclear microprobe determination of ^{13}C and $^{13}C/^{12}C$ ratios, the method is less sensitive than the (d,p) method, and its use will be limited by the presence of a wide range of light elements.

5.2.5 $^{3}He^{+}$ Induced Gamma Reactions

Measurement of prompt gamma-rays emitted during $^{3}He^{+}$ ion bombardment offers a means of circumventing some of the light element interferences encountered when determining ^{13}C and ^{12}C by measuring emitted particles. Gamma-ray spectra of enriched and natural $BaCO_3$ bombarded with a 2.8 MeV $^{3}He^{+}$ beam are given in Figure 5.21 and the assignments of peak origins are tabulated in Table 5.6 below.

TABLE 5.6 IDENTIFICATION OF THE GAMMA-RAYS EMITTED BY IRRADIATING ^{12}C AND ^{13}C WITH 2.8 MeV $^{3}He^{+}$ ION, AND OBSERVED IN THE SPECTRA SHOWN IN FIGURE 5.21

Peak No.	Reaction	Gamma-ray Energy (MeV)	Gamma-ray Transition (MeV)
1	$^{13}C(^{3}He,p\gamma)^{15}N$ $^{13}C(^{3}He,n\gamma)^{15}O$	7.572 7.56	7.572 → 0 7.56 → 0
2	(1, se)		

/Table continued ...

TABLE 5.6
(Cont'd)

Peak No.	Reaction	Gamma-ray Energy (MeV)	Gamma-ray Transition (MeV)
3	(1,de)		
4	$^{12}C(^{3}He,p\gamma)^{14}N$	5.685	5.685 → 0
5	$^{13}C(^{3}He,p\gamma)^{15}N$	5.305	5.305 → 0
6	$^{13}C(^{3}He,p\gamma)^{15}N$	5.276	5.276 → 0
7	$^{12}C(^{3}He,p\gamma)^{14}N$	5.104	5.104 → 0
8	(5,se)		
9	(6,se)		
10	(7,se)		
11	(5,de)		
12	(6,de)		
13	(7,de)		
14	$^{12}C(^{3}He,p\gamma)^{14}N$	3.945	3.945 → 0
15	(14,se)		
16	$^{12}C(^{3}He,p\gamma)^{14}N$	2.792	5.104 → 2.312
17	$^{13}C(^{3}He,p\gamma)^{15}N$	2.734	9.06 → 6.33
18	$^{12}C(^{3}He,p\gamma)^{14}N$	2.598	4.91 → 2.312
19	$^{12}C(^{3}He,p\gamma)^{14}N$	2.312	2.312 → 0
20	(19,se)		
21	$^{12}C(^{3}He,p\gamma)^{14}N$	1.634	3.945 → 2.312
22	$^{13}C(^{3}He,n\gamma)^{15}O$	1.41	7.56 → 6.15

se and de denote the single and double escape peaks.

The 5.305 MeV gamma-ray emitted by the reaction $^{13}C(^{3}He,p\gamma)^{15}N$ was chosen for the quantitative determination of ^{13}C because of its superior sensitivity. While the 2.311 MeV gamma-ray from the reaction $^{12}C(^{3}He,p\gamma)^{14}N$ is apparently the most sensitive for the measurement of ^{12}C, we confirmed a previous observation that it is unsuitable for prompt measurements because it is also fed by the decay of ^{14}O, $t_{\frac{1}{2}}$ = 17s, produced by the reaction $^{12}C(^{3}He,n)^{14}O$ (97).

Consequently, the next most sensitive gamma-ray at 1.634 MeV was chosen for the quantitative determination of ^{12}C. These gamma rays gave straight line calibration curves which are shown in Figure 5.22. For a $BaCO_3$ matrix sensitivities at 1 wt. % were 360 and 100 counts/μ coulomb for ^{12}C and ^{13}C respectively giving detection limits of 4100 and 3500 ppm. The reduction in sensitivity obtained for gamma-ray detection compared to particle detection parallels our experience with deuteron irradiation. Because of its low sensitivity the method will only be suitable for the examination of materials containing high carbon concentrations.

The degree of interference found for the light elements examined is indicated by the measure R values. For the 1.634 MeV and 5.305 MeV gamma-rays the R values obtained for ^{12}C and ^{13}C respectively are given in Table 5.7 below.

TABLE 5.7 INTERFERENCE TO THE MEASUREMENT OF ^{12}C AND ^{13}C USING THE $^{12}C(^3He,p\gamma)^{14}N$ E_γ=1.634 MeV AND THE ^{13}C $(^3He,p\gamma)^{15}N$ E_γ=5.305 MeV REACTIONS

NUCLIDE	R VALUE (^{12}C)	R VALUE (^{13}C)
Li	< 0.045	0.057
Be	0.042	< 0.043
B	< 0.0008	< 0.0006
N	< 0.0008	< 0.001
O	< 0.001	< 0.0002
F	0.64	0.016
Na	< 0.004	< 0.0004
Mg	0.024	< 0.0003
Al	< 0.0002	< 0.0002
Si	< 0.0002	< 0.0002
P	< 0.0007	< 0.0008
S	0.083	< 0.003
Cl	0.016	< 0.0003

$$R = \frac{\text{(Yield of 1 wt. \% Interference Nuclide/}\mu C)}{\text{(Yield of 1 wt. \% } ^{13}C \text{ or } ^{12}C/\mu C)}$$

The limitation imposed by a Compton continuum, as opposed to an overlapping gamma-ray, is indicated by a less than value. Interfering reactions which could produce ^{14}N and ^{15}N were found to be of no consequence for the selected gamma-rays. However, several elements cause interference through gamma-ray overlap. The 5.305 MeV gamma-ray is poorly separated from the 5.300 MeV emission from $^{19}F(^{3}He,\alpha\gamma)^{18}F$, and a broad line close to 5.36 MeV emitted by the reaction $^{7}Li(^{3}He,p\gamma)^{9}Be$. The 1.634 MeV gamma-ray is overlapped by a 1.63 MeV emission from $^{9}Be(^{3}He,p\gamma)^{11}B$, an unassigned 1.632 MeV emission from ^{19}F, a 1.623 MeV emission from $^{24}Mg(^{3}He,p\gamma)^{26}Al$, a 1.611 MeV emission from $^{35}Cl(^{3}He,\alpha\gamma)^{34}Cl$, and several gamma-rays close to 1.63 MeV from $^{32}S(^{3}He,p\gamma)^{34}Cl$ and $^{32}S(^{3}He,\alpha\gamma)^{31}S$. Although, these interferences may be largely overcome by selection of alternative gamma-rays for the determination of ^{12}C and ^{13}C, the already low sensitivity of the method is reduced further. Consequently, the circumstances in which advantage can be taken of the good selectivity of the method will be strictly limited to samples with high carbon contents.

5.2.6 $^{1}H^{+}$ Induced Gamma Reactions

The sensitivity of the (p,γ) reaction for the measurement of ^{12}C and ^{13}C was checked by irradiating a $BaCO_3$ target 90.7% enriched in ^{13}C with a 0.8 MeV proton beam. The irradiation energy was choosen as it falls within the optimum range, 0.6 - 0.8 MeV, recommended for the determination of $^{13}C/^{12}C$ ratios [81, 84, 87]. Under these conditions the gamma-rays at 8.061 MeV from ^{13}C and at 2.366 MeV from ^{12}C were barely discernable for an incident charge of 25 μC. The very poor sensitivity is consistent with that found by Engelmann et al. [84] where 1000μC and 1500μC doses were required for $^{13}C/^{12}C$ analyses. Such doses are totally unacceptable in spatial analyses because analysis times become excessively long due to the large number of analysis points. Extrapolating the sensitivities obtained by Engelmann to the nuclear microprobe measurement conditions acceptable for spatial analysis, <0.2 and <1 counts/μC can be expected from 1 wt. % ^{13}C and 1 wt. % ^{12}C in $BaCO_3$ respectively. Although the use of our 7.5 x 7.5 cm NaI(Tl) detector would raise the sensitivities by approximately an order of magnitude, they would remain impractically low for nuclear microprobe analysis.

5.3 CONCLUSIONS

Sensitive and selective nuclear reaction methods have been sought for the nuclear microprobe measurement of the spatial distributions of ^{13}C and $^{13}C/^{12}C$ ratios and a summary of the reactions and measurement conditions used is given in Table 5.8 below.

TABLE 5.8 SUMMARY OF REACTIONS USED FOR ^{13}C AND $^{13}C/^{12}C$ ANALYSIS USING THE NUCLEAR MICROPROBE

REACTION	INCIDENT BEAM (MeV)	DETECTOR	DETECTED RADIATION (MeV)	SENSITIVITY* IN $BaCO_3$ C/1 wt. %	PPM*
$^{13}C(d,p_o)^{14}C$	1.3 $^2H^+$	Surface Barrier	6.216 $^1H^+$	3300	60
$^{12}C(d,p_o)^{13}C$			3.255 $^1H^+$	41000	5
	1.5 $^2H^+$	"	6.344 $^1H^+$	6300	30
			3.384 $^1H^+$	108600	2
$^{13}C(^3He,p_o)^{15}N$	2.8 $^3He^+$	Surface Barrier	11.2401 $^1H^+$	320	630
$^{12}C(^3He,p_o)^{14}N$			5.852 $^1H^+$	840	240
	3.0 $^3He^+$	"	11.365 $^1H^+$	460	440
			5.969 $^1H^+$	1400	150
$^{13}C(\alpha,n)^{16}O$	2.8 $^4He^+$	NE 213 Scintillant	^1_0n 2 MeV	4300	100
$^{13}C(dn\gamma)^{14}N$	1.5 $^2H^+$	Ge(Li) NaI(Tl)	3.373 γ	1800	640
$^{13}C(d\alpha\gamma)^{11}B$					
$^{13}C(dp\gamma)^{14}C$					
$^{12}C(dp\gamma)^{13}C$			3.085 γ	3100	440
$^{13}C(^3He,p\gamma)^{15}N$	2.8 $^3He^+$	"	5.28 γ	100	3500
$^{13}C(^3He,n\gamma)^{15}O$					
$^{13}C(^3He,\alpha\gamma)^{12}C$					
$^{12}C(^3He,p\gamma)^{14}N$			1.634 γ	360	4100
$^{13}C(p,\gamma)^{14}N$	0.8 $^1H^+$	"	8.061 γ	< 0.2	
$^{12}C(p,\gamma)^{13}N$			2.366 γ	< 1	

* concentration required for 50% reliable error

Within the limitations imposed by the Harwell nuclear microprobe, four techniques have been found to be suitable for the simultaneous determination of the spatial distribution of ^{12}C and ^{13}C. For applications which demand

high sensitivity the first choice is deuteron irradiation with detection of emitted protons. However, the technique must be applied with caution since serious light element interference can occur, notably from Li, N, B and F. Substitution of gamma-ray for proton detection may circumvent this problem, particularly for B and N, but at a considerable loss in sensitivity. Although, $^{3}He^{+}$ ion irradiation using proton detection is an additional alternative, it will rarely merit selection because its susceptibility to light element interference is similar to that for the (d,p) method, while its sensitivity is inferior by a factor of at least ten. Although $^{3}He^{+}$ ion irradiation with gamma-ray detection is the least sensitive method, the wide choice of gamma-rays for the detection of both ^{12}C and ^{13}C offers a means of circumventing most interferences, and it may find application in the examination of materials rich in carbon. Proton irradiation with gamma-ray detection is particularly insensitive and is clearly unsuitable for nuclear microprobe analysis, despite finding favour for the determination of $^{13}C/^{12}C$ ratios in bulk specimens.

For ^{13}C analysis alone the (α,n) reaction is particularly attractive as it is both highly selective and reasonably sensitive.

CHAPTER 6

THE SPATIAL ANALYSIS OF THE STABLE ISOTOPE ^{13}C USED AS A TRACER DURING THE OXIDATION OF PE16 BY CO_2

A problem of considerable importance at the present time is the oxidative/carburization corrosion of many alloys at high temperatures in a variety of gases. Carbon dioxide in particular has been found to cause corrosive carburization of a number of alloys, greatly affecting their mechanical properties.

Carbon dioxide is used as the coolant for Magnox reactors and their successors, the Advanced Gas Cooled Reactors (A.G.R.'s). Thus its corrosive interaction behaviour with other reactor materials is of great concern (especially because of the potential radiation hazards). A simple schematic diagram Figure 6.1 shows the flow of coolant through an A.G.R. The reactor core consists of fuel elements containing fuel pellets of uranium oxide enriched in U-235, clad in stainless steel and surrounded by a graphite moderator. The whole of the fuel element assembly is supported by tie bars made out of the nimonic alloy PE16. The heat produced in the reactor core by normal fission processes is removed by circulating high pressure carbon dioxide gas and is then transferred via heat exchangers to steam generating plant in the power station. The carbon dioxide coolant is a mixture of CO_2, CO, CH_4 and water vapour. The methane is used to inhibit the attack on the graphite moderator by CO_2, producing CO, a process which effectively corrodes away the moderator. Other reactor components are corroded by the carbon dioxide based coolant. A critical component is the PE16 tie bar as its failure would allow the fuel element assembly to fall with profound consequences. The behaviour of PE16 in CO_2 at elevated temperatures has been studied previously [107]. In this chapter CO_2 labelled with the stable isotope tracer ^{13}C, in conjunction with spatial nuclear microprobe methods, is used to study the oxidative carburization processes, cf. in PE16 tie bar material, to improve our understanding of the mechanisms involved.

The development of sensitive, selective methods for the spatial analysis of ^{13}C and $^{13}C/^{12}C$ ratios was discussed in detail in Chapter 5. Some of the methods described, namely those based on the (d,p) and (α,n) nuclear reactions can be applied to investigate the carburization corrosion of a fuel cladding material, nimonic alloy PE16, treated at 800°C in carbon

dioxide isotopically labelled in ^{13}C. Profiles of ^{12}C, ^{13}C, $^{13}C/^{12}C$ and oxygen across PE16 samples are presented. Previous experiments [107] have found the oxidation kinetics of CO_2 on PE16 to be pseudoparabolic, the penetration increasing parabolically with time and temperature. Intergrannular oxidation and carburization were both observed. However, there is some ambiguity as to the exact origin of the carbon in the carburization profiles observed. The intention of this work was to distinguish between carbon originally present in the alloy and carbon introduced during the intergrannular oxidation of the alloy by carbon dioxide, thus facilitating a deeper understanding of the processes involved.

6.1 SAMPLE PREPARATION AND EXPERIMENTAL PROCEDURE

The ^{13}C standards used throughout the investigation to establish the most suitable method for measuring ^{13}C and $^{13}C/^{12}C$ ratios, described in Chapter 5, were pressed powder pellets of ^{13}C labelled $BaCO_3$. These provided an adequate calibration for that purpose, although because they are so sensitive to beam damage a large rastered beam of very low beam current was used whenever they were interrogated. Thus the acquisition of data was relatively slow compared to the rate of data acquisition possible when measuring metallic material such as the PE16 samples which can withstand small and quite intense beams (20-40 nA; at spatial resolutions as high as 5 μm). Ideally when one measures high spatial resolution profiles which contain many points, one requires a standard which may be analysed, under as nearly identical conditions to the sample as possible and preferably in between each sample run in order to monitor any changes in analysis conditions. The powdered $BaCO_3$ standards could not fulfil these requirements in an acceptably short analysis time and so the preparation of a suitable ^{13}C standard in steel was required. A ^{12}C standard in steel was readily available.

In order to improve the likelihood of producing a high ^{13}C content standard in steel, a sample of the steel must initially be decarburized to remove the ^{12}C already present before carburizing with a labelled ^{13}C reagent. PE16 is notoriously difficult to decarburize since it contains one of the most stable of all carbides, titanium carbide. However samples of 316 standard steel were successfully decarburized by heating in a silica vessel lined with tantalum, at 800°C for 6 weeks in 1 atmosphere pressure of hydrogen. The tantalum acts as a "getter" for both carbon and oxygen. Oxidation would produce a protective barrier on the sample which would hinder decarburization. The carbon content of the 316 sample was analysed

using the Harwell nuclear microprobe and a nuclear reaction method dependant upon the $^{12}C(d,p_o)^{13}C$ reaction. The decarburized 316 sample was found to contain 0.00036 ± 0.00018 wt. % ^{12}C on average, compared with the untreated archive 316 sample which contained 0.032 ± 0.0038 wt. % ^{12}C. The decarburized 316 material was then placed in another silica vessel and connected to a resevoir of 90% ^{13}C labelled methane and heated at 800°C for six weeks. The extent of ^{13}C labelling was then quantified. A calibration curve for the ^{13}C content in $BaCO_3$ enriched standards was obtained using the $^{13}C(d,p_o)^{14}C$ reaction in conjunction with the Harwell nuclear microprobe. The ^{13}C content of the 316 sample was then found to be 3.29 ± 0.036 wt. % ^{13}C using this calibration surve and the pertinent stopping power corrections. Since the ratio of $^{13}C/^{12}C$ in the methane was known one could calculate the wt. % ^{12}C expected. The ^{12}C content of the 316 standard measured simultaneously with the ^{13}C agreed well with the expected value.

The ^{13}C labelled nimonic alloy samples were prepared as follows. Nimonic alloy PE16 sample discs, 14.3mm in diameter and 1mm thick, were placed individually in silica cruicibles as shown in Figure 6.2. The composition of PE16 is given in Table 6.1 below.

TABLE 6.1 SPECIFICATION OF THE NIMONIC ALLOY PE16

ELEMENT	STANDARD wt. % COMPOSITION
C	0.08
Mn	0.05
B	0.0003
Al	1.3
Ti	1.2
Zr	0.03
Cr	17.1
Ni	42.5
Mo	3.1
Balance as Fe	

The CO_2, enriched to 95% ^{13}C, was introduced into the vessel such that at 800°C, the usual test temperature for highly alloyed reactor materials, it attained 1 atmosphere pressure. In each vessel the sample was placed on a

silica support which ensured that the sample was held within the strictly controlled temperature region when the whole vessel was suspended within a furnace. The copper oxide, seen at the top of the vessel, is effectively an oxygen resevoir such that the carbon and carbon monoxide produced during the oxidation/carburization processes could readily combine with the oxygen from the copper oxide to regenerate carbon dioxide. Samples of PE16 were treated in the labelled gas, at 800^{o}C for various lengths of time and then removed and cooled. Cross-sectional pieces of each sample were mounted in Woods metal as described in Section 2.4, ready for interrogation with the nuclear microprobe.

The ^{13}C and ^{12}C in the treated PE16 samples, the standards and archive PE16 were initially measured using the $^{13}C(d,p_o)^{14}C$ and $^{12}C(d,p_o)^{13}C$ reactions with a 1.3 MeV incident deuteron beam from the Harwell nuclear microprobe as described in Chapter 5. The respective p_o groups required were detected using a silicon surface barrier detector placed at an angle of 135^{o} to the incident beam. Initially a ^{13}C calibration curve was obtained using both the $BaCO_3$ standards containing various enrichments of ^{13}C, and the ^{13}C/316 steel standard. A typical calibration curve is shown in Figure 5.4. The ^{13}C standard in steel was then used throughout the experimental run to monitor and correct for any change in conditions between each sample which could affect ^{13}C measurement. A ^{12}C calibration curve was obtained by using ^{12}C standards in steel, for example that shown in Figure 6.3. The 1% ^{12}C standard was used throughout the run to monitor and correct for any changes in conditions which affect ^{12}C measurement. Not only did the use of the ^{12}C standard in steel allow faster analysis times in an analogous fashion to the use of the ^{13}C in steel standard, it also overcomes a serious interference problem caused by oxygen. Since the oxygen content in $BaCO_3$ is about four times greater than that of ^{12}C in natural abundance $BaCO_3$, the interference from the $^{16}Op_o$ peak (positioned just on the lower energy edge of the $^{12}Cp_o$ peak) can cause considerable interference. As the ^{13}C content increases the magnitude of the interference increases, this decreases the reliability of the ^{12}C measurement and calibration curve. By using ^{12}C in steel standards, which contain only trace quantities of oxygen, this problem is circumvented.

An X-ray detector was used to locate the edge of the PE16 samples in order to spatially relate the profile obtained to the edge of the sample. This was achieved by mechanically moving the sample relative to the beam and monitoring for the iron and chromium X-rays. These elements are present

in the steel samples but not in the Wood's metal sample mounting material. The profile data obtained, as particle group yield for ^{13}C and particle group yield for ^{12}C for each scan point across the sample, can then be converted to profiles of ^{13}C and ^{12}C weight % against distance from the sample edge.

Since the process being investigated was an oxidative/carburization process it was useful to measure the oxygen profiles across the PE16 samples as well. This was achieved by measuring the oxygen p_1 group in an exactly analogous manner to that used for measuring the ^{12}C p_o and ^{13}C p_o groups. A 1.1 MeV deuteron beam from IBIS was used to induce the charged particle reaction $^{16}O(d,p_1)^{17}O$ and a silicon surface barrier detector (with two 9 mg/cm^2 mylar absorber foils) was placed at 135^o to the beam line to measure the emitted p_1 particle group. Oxygen standards of zirconium metal, oxidised to different oxygen levels, and also ZrO_2 were used. The calibration curve, Figure 6.4, was obtained by a polynomial least squares method. Using the calibration curve profiles of oxygen weight % against distance from the sample surface were obtained.

Although measurements of the ^{13}C profiles were planned, using the highly selective $^{13}C(\alpha,n)^{16}O$ method, they have been prevented by time limitations. The desirability for such measurements to ensure that the (d,p) results have not been disturbed by a minor aluminium interference is discussed later.

6.2 RESULTS AND DISCUSSION

The penetration of the labelled ^{13}C into the PE16 samples treated for different periods of time at 800^{o}C is shown in Figures 6.5 to 6.12. All of these figures each show profiles of the weight percentages obtained of ^{12}C, ^{13}C, and $^{13}C/^{12}C$. The first three figures show profiles through the complete cross-sections of samples PE16/21, PE16/23 and PE16/24 at a spatial resolution of 25 μm. The remaining five figures give measurements into the samples from either the bottom or top sample surfaces at a 5 μm spatial resolution.

The wt. % ^{12}C was found directly from the ^{12}C p_o group using the usual techniques [108] with wide and narrow measurement groups to remove the affects of surface carbon contamination. The wt. % ^{13}C was found from the ^{13}C p_o group however there was some interference from the Alp_o peak, the energy of which is almost identical to the ^{13}C p_o peak. The level of aluminium interference within the ^{13}C p_o region was obtained by measuring

the archive PE16 material, the expected counts from natural ^{13}C in PE16 can be calculated and although only just significant can be subtracted from the count observed in this region for archive PE16. The average residual count was then taken to be the aluminium interference. Collaborative evidence was obtained from particle spectra of the ^{13}C standard, archive PE16 and aluminium. Each of the ^{13}C counts/μC were corrected for the average aluminium contribution. Obviously it would be interesting to unequivocably verify that the aluminium interference was adequately corrected for. This could probably be achieved using the $^{13}C(\alpha,n)^{16}O$ reaction method. However measurements would be relatively imprecise because of the inferior sensitivity of the (α,n) method, as discussed in Chapter 5, hence the accuracy of the profile data would be severely affected. Alternatively X-ray analysis might be used to look for any significant alterations in aluminium concentration in a given region during the experiment which may effect the ^{13}C result. The $^{13}C/^{12}C$ ratio was obtained by dividing the average ^{13}C wt. %, obtained from up to 8 scans across a given sample, by the average ^{12}C wt. % obtained simultaneously. The ingress of ^{13}C tracer can be seen through the enhancement of the $^{13}C/^{12}C$ ratio above the natural value.

Figures 6.5 to 6.7 show the carbon isotope profiles of the complete sample widths at a 25 μm spatial resolution for material treated for 1096, 4029 and 4601 hours. All three profiles i.e. ^{12}C, ^{13}C and the $^{13}C/^{12}C$ ratio were needed to interpret the carbon behaviour in these extremely inhomogeneous samples as apparent inconsistences often occur as a result of the inhomogeneity. The ^{12}C profiles show several anomalously high points. Where the ^{12}C concentration is high without a correspondingly high ^{13}C concentration, this probably indicates the persistence of a large carbide precipitate which was present in the original material. The ^{12}C profiles throughout probably reflect both the original carbon distribution in the PE16 samples and some redistribution of ^{12}C by diffusion or displacement by oxygen. A typical ^{12}C original distribution is that of archive PE16 shown in Figure 6.13. The distribution is quite scattered and precipitates certainly appear to be present. Generally the ingress of ^{13}C into the samples is far more clearly seen from the ^{13}C wt. % profiles than those of the ratios because the latter have more scatter as a result of the original inhomogeneous distribution of carbon. Using the three profiles for each of the PE16 samples one can clearly distinguish the ^{13}C ingress into the samples from the carbon originally present and by using the ^{13}C tracer one largely overcomes the problem of confusion due to diffusion of

carbon originally present when using CO_2 of natural abundance to follow the oxidative/carburization processes in PE16.

It can be seen in the profiles that the amount of carburization from the two surfaces in towards the centre is asymmetric. This is because the bottom of the PE16 samples rested against the silica support whereas the top of the samples were freely exposed to the CO_2 oxidant and hence greater changes were observed as expected. As the period of carburization increases the amount of ^{13}C penetration and build up very clearly increases. Indeed the degree of penetration of ^{13}C is very high even quite early on in the carburization period and for example in the PE16/24 ratio profile at a depth of 250 μm below the top surface the ^{13}C content is over 25% of the total carbon present compared to the natural level of 1.11%. A fast mechanism for the transfer of carbon deep into the samples is needed to explain these observations. It is thought that a 'crevice' type corrosion mechanism may provide an explanation [107]. In the crevice corrosion mechanism it is thought that oxidation opens up the alloy structure by internal attack and crevices appear. As the gas goes down the crack it experiences changing carbon and oxygen potentials. At the mouth of the crack oxygen is preferentially removed from the gas whilst at the base of the crevice carbon is the predominant species removed from the gas. By this crevice corrosion mechanism carbon can penetrate very long distances fairly rapidly.

Previous results [107] have shown a complex behaviour of carburization and decarburization at the outer edges of the sample within approximately a 90 μm region from the surface. Consequently higher spatial resolution, 5 μm, scans were obtained for the first ≈ 250 μm into each sample surface. Figures 6.8 to 6.10 show ^{12}C, ^{13}C and $^{13}C/^{12}C$ profiles measured inwards from the bottom, less exposed, sample surface. Again as the period of carburization increases the amount and degree of penetration of ^{13}C increases. However rather than just a carbon peak towards the sample edge followed by a roughly exponential diffusion into the alloy one can see a more complex behaviour at this higher spatial resolution. Looking both at the ^{13}C and $^{13}C/^{12}C$ profiles, one sees a small ^{13}C peak about 10-15 μm (on average) from the outside edge followed by a region of about 20 μm width with a very low ^{13}C concentration and then a second far larger and broader carburized region peaking between 50-100 μm from the surface and extending roughly from 35 to 200 μm in from the surface. It should be noted that the outer

^{13}C peak in specimen PE16/21 ^{13}C profile (Figure 6.8) is obscured by the anomalously high ^{12}C concentration near this surface however it can be clearly seen in the $^{13}C/^{12}C$ ratio profile. The high ^{12}C concentration at this surface may be due to redistribution but could be due to a residual surface precipitate, especially since the other samples PE16/23 and PE16/24 show evidence of redistribution of ^{12}C inwards into the material.

Figures 6.11 and 6.12 show the ^{12}C, ^{13}C and $^{13}C/^{12}C$ profiles measured inwards from the top sample surfaces of specimens PE16/21 and PE16/24 respectively. As expected this surface showed increased carburization compared to that of the bottom surface, in accordance with the effects seen in the low spatial resolution scans. A very marked increase in the overall amount and degree of penetration of ^{13}C was observed with increasing carburization period. Again evidence of original ^{12}C precipitates was observed. In Figure 6.12 it can be seen that the $^{13}C/^{12}C$ profile presents a clearer picture of ^{13}C ingress than many of the other $^{13}C/^{12}C$ profiles mainly because of the small scatter on the ^{12}C region corresponding to the second large ^{13}C peak region. The complex picture of ^{13}C distribution is similar to that shown by the high resolution scans on the bottom surface except that there is little evidence of a first ^{13}C peak near the surface in the highly carburized PE16/24 sample. All the ^{13}C appears to have ingressed deeper into the material.

Since PE16 contains both titanium and chromium it forms both carbides and oxides of high thermodynamic stability. To help interpret the carburization information the oxidation profiles across the PE16 samples were also obtained. Examples of the oxygen profiles are given in Figures 6.14 and 6.15. The former shows the oxygen profile corresponding to the carbon profiles in Figure 6.10, those of PE16/24 measured inwards from the bottom surface. There is a very narrow region of high oxidation, c.a. 7.7 wt. % down to 1 wt. % of oxygen, over the first 12 μm from the surface and then the oxidation falls to 0.1 wt. % oxygen after the first 30-40 μm from the surface. Figure 6.15 shows the oxygen profile corresponding to the carbon profiles in Figure 6.12, those of PE16/24 measured inwards from the top surface. Figure 6.15 shows the far higher degree of oxidation from the top side of PE16/24, ca. 15.6 wt. % down to 1 wt. % oxygen over the first 60 μm and then falling to <0.1 wt. % oxygen approximately 80-90 μm from the bottom edge. This difference between top and bottom was expected due to the shielding of the bottom edge from CO_2 oxidant during the experiments.

On examining the extent of oxidation for each alloy sample and correlating these results with the requisite carburization scans from the top and bottom sample edges the outer high carbon peak is found to correspond roughly with the very high oxygen content, the outer oxide scale. The carbon uptake increases across the outer scale to a maximum near the oxide/alloy interface. In the underlying intergrannular oxide region there appeared to be little ^{13}C present until the carburization again increased to a maximum in the vicinity of the boundry of the intergrannular oxide/unoxidised alloy. From here the carbon level tends to fall in a typical exponential diffusion profile towards the centre of the sample. This behaviour is given in diagrammatic form in Figure 6.16. It is clear that the carburization even a couple of hundred microns in from the surface mainly origionates from the carbon in the CO_2 gas and not from migration of carbon originally present in the material.

Careful consideration of the relative carbon and oxygen potentials, detailed in Figure 6.17, [107] is needed in order to gain some understanding of the technical and mechanistic significance of the data. In the outer scale carbon could be precipitated in the region of the TiO_2/Ti_3O_5 boundry by the deposition of carbon on catalytic surfaces (those containing iron) from carbon monoxide. This is known as the Boudard reaction:-

$$2CO \longrightarrow CO_2 + C \qquad \text{... (Eqn. 6.1)}$$

Although as can be seen in Figure 6.17 [107], this does require the improbably high partial pressures of 0.88 and 0.12 atmospheres for carbon monoxide and carbon dioxide respectively. In addition this reaction can be inhibited by oxide films and hence this reaction should be expected to be somewhat restricted by the highly stable oxides formed with the PE16. Previous work [109] has shown that carbon which is deposited by the Boudard reaction remains mainly at the surface of the oxide film thus this could be the origin of the first smaller ^{13}C peak. Subsidiary reactions which may be relevant [110] are those based upon oxidation by CO_2 and H_2O:-

$$2M + CO_2 + H_2O \longrightarrow 2MO + CO + H_2 \qquad \text{... (Eqn. 6.2)}$$

At the boundry between the outer oxide scale, Ti_3O_5, and the intergrannular oxide Ti_2O_3, additional reactions can contribute to carburization:-

$$3Ti_2O_3 + CO \longrightarrow 2Ti_3O_5 + C \qquad \text{... (Eqn. 6.3)}$$

$$\text{and} \quad Cr + CO \longrightarrow \underset{\text{(most probably } Cr_3C_2)}{Cr_x\,Cy} + Cr_2O_5 \qquad \ldots \text{(Eqn. 6.4)}$$

thus either depositing carbon or forming chromium carbides. With reference to Figure 6.17 [107] within the metal itself titanium carbide can only co-exist with Ti_2O_3 along line AB. Previous experimental evidence [107, 110] namely the absence of TiC in association with the intergrannular Ti_2O_3 implied that the oxygen and carbon potentials varied along a course above AB (B′) passing across this line at either B or B′ along to BC or B′C′ to D and D′. Within the purely metal region only TiC can exist since neither Al_4C_3 nor $Cr_{23}C_6$ would be stable at equilibrium. Using the information available in Figure 6.17 [107] one can detail the regions found experimentally and given diagrammatically in Figure 6.16 [107].

6.3 CONCLUSIONS

Nuclear microprobe analysis and ^{13}C tracer experiments have been successfully applied to the investigation of the high temperature corrosion of the Nimonic alloy PE16 by $^{13}CO_2$.

The $^{13}C(d,p_0)^{14}C$ and $^{12}C(d,p_0)^{13}C$ reactions were used to measure the ^{13}C and ^{12}C profiles over their respective ranges, of 0.0005 - 0.17 wt. % and 0.05 - 1.1 wt. %, within the PE16 samples. $^{13}C/^{12}C$ ratio profiles were also obtained from the data.

The addition of carbon to the alloy from $^{13}CO_2$, was followed through measurement of the ^{13}C in the specimens exposed at 800°C for times between 1096 hours and 4601 hours. The use of the ^{13}C stable isotope tracer allowed clear distinction between carbon added from the gas phase and carbon initially present in the alloy. The distribution of the latter was based on the measurement of ^{12}C, the major component of natural carbon. PE16 normally contains relatively large carbide precipitates, and high resolution measurements of carbon distributions are characterised by the presence of extensive scatter. While corrosion experiments undertaken in natural CO_2 are complicated by difficulties in distinguishing between added and archive carbon, those conducted with CO_2 highly enriched in ^{13}C are not. The ^{12}C profiles proved that much of the archive distribution of carbon persists, even at the longest exposure time.

The presence of oxide films increases corrosion resistance of alloys and since PE16 contains some very highly stable oxides and carbides one

would expect the penetration of carbon to be hindered somewhat. In fact although a proportion of the carbon, the first carbon peak, is apparently located at the surface of the intergrannular oxide region of the alloy, a considerable proportion penetrates very deeply into the intergrannular region. It is thought to do so via the crevice corrosion mechanism [107]. Most of the carbon build up in the alloy was found to come from the CO_2 gas rather than relocation of carbon originally present in the alloy.

Further work should be carried out using the (α,n) reaction to measure the ^{13}C profiles again, to unequivocably verify that the aluminium interference has been adequately corrected.

CHAPTER 7

THE SPATIAL ANALYSIS OF ^{10}B BURN-UP IN IRRADIATED B_4C USING THE STABLE ISOTOPE TRACER ^{7}Li CREATED IN SITU.

In Fast Reactors the neutron absorber assemblies are made out of boron carbide either in its natural state or enriched in ^{10}B. ^{10}B has a particularly high neutron absorption cross-section, hence its suitability as an absorber material. Typical Fast Reactor core designs allocate approximately 10% of the core positions to absorber assemblies although by increasing the enrichment of ^{10}B, at some expense, this could be reduced to about 8% thus leaving more space for fuel elements and hence increasing the breeding ratio. During the normal working of a fast reactor boron "burn-up" occurs in the B_4C absorber assemblies i.e. the ^{10}B is converted into lithium via the $^{10}B(n,\alpha)^{7}Li$ reaction. Since the efficiency of the absorber assembly depends on the amount of ^{10}B present it is important to quantify the extent of this burn-up. Some of the ^{7}Li is used up in the $^{7}Li(n,n\alpha)^{3}H$ reaction but as it has a neutron threshold energy of 1.2 MeV[111] the reaction occurrence is very low, [112] probably about three orders of magnitude lower than the rate of production of lithium. Also the lithium profiles in their own right are important because the formation of lithium affects the structure of the B_4C and it is thought [113] that lithium bonding is responsible for the mechanisms of ^{3}T retention in the absorber assemblies. Some of the lithium and tritium produced in the assemblies is lost and this is to some extent dependent on the initial porosity in the B_4C pellets. It should be noted that although the efficiency of the absorber assembly depends on the amount of ^{10}B present, usually the actual "life-time" of the absorber assemblies in the reactor tends to be dictated by engineering design, as during irradiation the B_4C swells and radiation creep occurs causing distortion of the assemblies. Obviously there is a maximum movement after which the distortion hinders the removal of the absorber assemblies in and out of the core.

A method capable of spatial measurement has been developed to follow the "burn-up" of ^{10}B in B_4C assemblies since the "burn-up" in different assembly rods or even within the same rod is not necessarily expected to be uniform because of the variations in neutron flux experienced. In fact measurements of "burn-up" within the assemblies provides a very useful additional check on neutron flux variations at different positions in the reactor core.

7.1 CHOICE OF REACTION FOR THE SPATIAL MEASUREMENT OF "BURN-UP" IN FAST REACTOR ABSORBER RODS

If one wishes to follow this "burn-up" one can either measure the disappearance of the ^{10}B or the formation of ^{7}Li, where ^{7}Li is effectively a stable isotope produced in situ. The $^{10}B(d,p)^{11}B$ reaction has been used [114] to determine ^{10}B in metals and both ^{10}B and ^{11}B have been simultaneously analysed [26] using the $^{10}B(\alpha,p)^{13}C$ and $^{11}B(\alpha,p)^{14}C$ nuclear reactions. However ^{25}Mg, ^{14}N and ^{29}Si are possible interferences to the ^{10}B determination using the (d,p) reaction and ^{27}Al a possible interference to the determination of ^{10}B using the (α,p) reaction. If one chooses to follow the formation of ^{7}Li rather than the disappearance of ^{10}B, the $^{7}Li(p,\alpha)He^{4}$ reaction offers the possibility of a highly selective determination. The Q value for the reaction is Q = 17.347 MeV which is considerably higher than the next largest $^{11}B(p,\alpha)^{8}Be$ Q = 8.59 MeV. Another advantage of following the formation of ^{7}Li is that one is measuring a small quantity on theoretically a zero background whereas when measuring the disappearance of ^{10}B one is looking for a small difference on a large signal. If the spatial determination of lithium using the $^{7}Li(p,\alpha)\alpha$ reaction is to be used to follow the boron burn-up which occurs during the normal running of a reactor, it is first necessary to verify that the position of the ^{7}Li is a true indication of the position of the ^{10}B. The ^{7}Li may move away from the ^{10}B site because of one or more of the following processes; transmutation recoil, diffusion under the influence of the high reactor temperatures, relocation during sample preparation for analysis and movement during sample interrogation by the microbeam.

In the transmutation $^{10}B(n,\alpha)^{7}Li$, Q = 2.79 MeV, the ^{7}Li will be produced with recoil energy, [115, 116] thus moving away from the original ^{10}B site. The distance it travels can be calculated and its significance will depend on the spatial sensitivity required. For the measurements of B_4C samples, which are several mm across, a spatial resolution > 20 μm should be adequate.

From the law of conservation of momentum, when the α particle is ejected from the reaction nucleus with an energy E_α, the resultant nuclide recoils backwards with a momentum P_{Li} such that:-

$$P_{Li} = -P_\alpha \qquad \text{... Eqn. 7.1}$$

$$P_\alpha = M_\alpha V_\alpha \qquad \text{... Eqn. 7.2}$$

$$E_\alpha = \frac{M_\alpha V_\alpha^2}{2} \quad \text{... Eqn. 7.3}$$

where M_α = mass of alpha particle

V_α = velocity of alpha particle

Assuming the peak of the distribution of neutron energies in a fast reactor to be about 1 MeV then from kinematics E_α = 1.96 MeV. There will in reality be a spread of values but taking this peak value:-

$$P_\alpha = \sqrt{2E_\alpha M_\alpha} = - P_{Li} \quad \text{... Eqn. 7.4}$$

$$E_{R_{Li}} = \frac{P^2_{Li}}{2M_{Li}} = \frac{2E_\alpha M_\alpha}{2M_{Li}} = \frac{E_\alpha M_\alpha}{M_{Li}} \quad \text{... Eqn. 7.5}$$

$$\therefore \quad E_{R_{Li}} = (4/7)\ 1.96 = \underline{1.12 \text{ MeV}}$$

Using the stopping power and range tabulations of Northcliffe and Schilling [117] and Bragg's rule, the distance travelled by the ^{7}Li nuclei through the B_4C, ρ = 2.332 gcm^{-3}, can be calculated and was found to be just over 2.1 µm. Thus on average the movement of the lithium nuclei from the original boron site can be described as being within a sphere of radius 2.1 µm. This is well within the minimum spatial resolution of > 20 µm and thus the errors introduced by recoil effects will be insignificant.

Loss of lithium by diffusion out through the fairly porous B_4C absorber assemblies, within the reactor, could be verified by making use of an alternative technique of directly measuring the ^{10}B and ^{11}B as already mentioned. One could then use the ^{10}B/^{11}B data to calculate the amount of ^{7}Li expected and then compare it with the value of ^{7}Li directly obtained from the ^{7}Li(p,α)α reaction. One would thus be using the two measurement techniques in a somewhat complementary fashion.

Any movement of the ^{7}Li by diffusion under the influence of the micro-beam will be seen by bombarding a given sample location for a period of time during which the ^{7}Li concentration changes, if any, are monitored.

One of the main difficulties which may arise is the possible relocation or loss of the lithium during sample preparation. The B_4C absorber assemblies are made up of cylindrical pellets of B_4C stacked end on end.

In order to measure the radial distribution of lithium in B_4C pellets it will be necessary to take a slice of material from the centre of each pellet by means of a diamond slitting wheel. Although the lithium will lay within the crystal structure of the B_4C and may be relatively firmly bound, since the nuclear microprobe measures only to a depth of a few μm, loss or movement of lithium in this small area is critical. Some indication of lithium loss should be obtainable from the comparison of the nuclear microprobe results with bulk lithium measurements obtained from material taken from the same pellets. One could perhaps also obtain some indication of the subsurface variation of ^7Li, in the first few microns, from the energy distribution of the emitted alpha particles.

7.2 EXPERIMENTAL

The absorber assembly pellets of interest were first mounted in epoxy resin. The sample slices were then obtained by cutting a slice from the centre of each pellet using a diamond cutting wheel. The slices were then polished, on the surface to be interrogated by the beam, in the usual manner using diamond lapping products. The basic procedure is described in Chapter 2 although because these samples were active all polishing was carried out within glove boxes. In addition in order to help minimise any further loss of lithium during polishing, oil based rather than water based lapping products were used in conjunction with carbon tetrachloride as solvent.

The ^7Li profiles were measured by the $^7Li(p,\alpha)\alpha$ reaction using the nuclear microprobe, a silicon surface barrier detector and single channel and multichannel analysis systems as described in Chapter 2. Mylar absorber foils were placed in front of the detector in order to prevent any scattered particles entering the detector. When analysing active samples one sometimes has to place a tantalum shield (with a slit cut into it exposing the area for interrogation) over the sample face. This helps reduce background levels caused by the target β radiation. For these samples the radiation levels were low, about 10 mr/hr β on contact, and no radiation problems occurred.

7.3 RESULTS AND DISCUSSION

An initial investigation was carried out to elucidate the optimum incident beam energy for these analyses. The cross-section for the $^7Li(p,\alpha)\alpha$ reaction increases with increasing beam energy, however the energy gap between the α groups produced by the ^7Li and ^{11}B reaction (most likely interference)

decreases. Thus although the sensitivity does increase it may not necessarily be advantageous to work at the higher energy.

Samples containing lithium and the most likely interferences, boron and fluorine (Q. values 17.347, 8.59 and 8.115 MeV respectively), were bombarded with various energy proton beams from the nuclear microprobe. The results obtained are given in Figure 7.1. At the higher energies, 2.0 MeV and above, so many absorber foils were required to remove scattered particles that the reaction groups of interest were totally absorbed before reaching the detector. The highest sensitivity was obtained at 1.5 MeV were the two most likely interferences are negligible. Using the ratio value R, i.e. the yield of 1 wt. % interference nuclide per microcoulomb divided by the yield of 1 wt. % ^{7}Li per microcoulomb, one finds that for boron R = 0.0001 and for fluorine R = 0.00008. Although the sensitivities for 1.0 and 1.5 MeV $^{1}H^{+}$ beams are very similar it is advantageous to work at the slightly higher energy because surface effects become less dominant the further the beam penetrates into the sample.

The circular B_4C samples were interrogated first across one diameter and then across the diameter at right angles to the first. Since these samples were over 1 cm in diameter a spatial resolution of 250 μm was choosen as giving adequate data in an acceptable analysis time. The counts/μC/1 wt. % ^{7}Li in the $LiNbO_3$ standard were converted into counts/μC/1 wt. % ^{7}Li in a B_4C matrix using the relevant stopping power corrections [118] for the attenuation, particularly of the outgoing α's, over the energy range resulting in product α's of an energy within the effective energy window of the detector. The counts at each scan point can then be converted to a ^{7}Li concentration profile. The profiles obtained are given in Figures 7.2 to 7.5. The perpendicular diametric scans across pellets 197, 185 and 172 agree very closely, implying that the neutron flux in the x and y directions across a given horizontal plane within the absorber assembly is fairly uniform. As sample 160 was broken one scan is incomplete. Even so the differences observed between scans possibly indicate slight variations in the neutron flux in the x and y directions at this extremity of the absorber assembly. These four pellets come from different vertical locations in one absorber assembly, pellet 197 was located towards one end and pellet 160 towards the other. The amount of neutron flux variation across each pellet from these different locations does vary slightly as seen in Table 7.1 below. This could be due to self-shielding or temperature effects.

TABLE 7.1: VARIATION IN THE MAXIMUM AND MINIMUM ^{7}Li CONCENTRATIONS ACROSS PELLETS FROM DIFFERENT VERTICAL LOCATIONS IN AN ABSORBER ASSEMBLY

PELLET NUMBER	APPROX. MAX^{M} ^{7}Li wt. %	APPROX. MIN^{M} ^{7}Li wt. %	DIFFERENCE IN MAX^{M} AND MIN^{M}
197	1.29	0.67	0.62 (48%)
185	1.68	0.80	0.88 (52.4%)
172	2.16	1.03	1.13 (52.3%)
160	2.17	1.15	1.02 (47%)

Generally the degree of burn-up in the centre of the pellets is only half of that in the outside edge. Also as one moves vertically along the absorber assembly from pellet 197 to pellet 160 the degree of burn-up increases greatly. Bulk analysis obtained from pieces of the same absorber pellets have been carried out using an alternative method. After high pressure dissolution of the B_4C in nitric acid the lithium content was determined using flame photometry [119]. In order to compare the bulk analyses obtained by flame photometry, to the effective mean bulk analyses obtained from these diametric scans across the cylindrical B_4C pellets, the spatial values must be weighted with respect to their distance from the pellet centre. This weighting is necessary because the value obtained in the outermost scan point is representative of a far larger quantity of material than the value from the central point. Therefore the spatial point values were weighted by a factor equal to the difference in the relevant inner and outer band radii squared. On dividing the sum total of these weighted values by the total weighting factors one then obtains a representative mean bulk value for each pellet. These values are compared with those found by flame photometry in Table 7.2. Also included for comparison are the values of ^{7}Li calculated knowing the ^{10}B and ^{11}B concentrations in the absorber assemblies before and after irradiation and the reasonable assumptions that each of the ^{10}B atoms lost are transmuted to a ^{7}Li atom which reacts no further.

TABLE 7.2: COMPARISON OF ^{7}Li BULK ANALYSES

PELLET NUMBER	NUCLEAR MICROPROBE BULK VALUES wt. %	BULK VALUES BY FLAME PHOTOMETRY wt. %	BULK VALUES CALCULATED FROM ^{10}B AND ^{11}B DATA wt. %
197	0.96	1.16	1.15
185	1.24	1.39	1.55
172	1.55	1.62, 1.68, 1.72, 1.76	1.91
160	1.50	1.47	1.71

A point to note when comparing these values from the nuclear microprobe and flame photometry is that the nuclear microprobe data was obtained from the slice in the centre of the pellet whereas those for the flame photometry method were obtained from the edge slice of the pellets. However the variation from the edge to the centre of a pellet is not usually very large and the results obtained from the spatial measurements are lower than expected. This very likely represents a loss of ^{7}Li during the preparation procedure, in particular the cutting of the pellet slice by the diamond wheel. B_4C is an extremely hard material, difficult to cut and at the temperatures involved it is quite likely that the fairly mobile ^{7}Li was released by the B_4C. The more porous the B_4C the more readily release occurs. There did not appear to be any significant movement of ^{7}Li within the sample whilst being interrogated by the microbeam. This was found by bombarding the same position for ten times the normal does of 1μC per scan point and recording the counts for each 1 μC dose period. No change in counts were observed. Thus the ^{7}Li would appear to be lost during the cutting and polishing. One can sometimes use the shape of the spectra obtained from both standards and sample in order to verify surface losses. The whole shape of the curve can change. If all the ^{7}Li was lost from the surface leaving only subsurface ^{7}Li, the high energy point of the spectrum would have moved to lower energy. Unfortunately because of the extremely poor energy resolution of the detection system with so many nickel absorber foils causing a high degree of spectral degradation, any small changes in energy due to the depth origin of the emitted alpha particle were smeared out and the spectra were of little help in interpreting the data.

Comparing the ^{7}Li bulk values obtained from both the nuclear microprobe and flame photometry methods one can clearly see that as one goes

from pellet 197 to pellet 160 the ^{7}Li concentration appears to be increasingly lower than theoretically predicted. This could well indicate loss of ^{7}Li by diffusion during reactor irradiation. Perhaps the application of the $^{7}Li(p,\alpha)\alpha$ method to follow boron burn-up may be limited to those cases where ^{7}Li loss is negligible, for instance in relatively low temperature irradiations of that experienced by pellet 197 (temperature $\simeq 720^{o}C$).

7.4 CONCLUSIONS

^{7}Li distributions across B_4C absorber assembly pellets have been obtained by the $^{7}Li(p,\alpha)\alpha$ reaction in conjunction with the nuclear microprobe. Quite marked profiles were obtained and generally only about a half the boron burn-up occurs in the centre of the pellets compared to that at the pellet edges. Although these profiles provide very good relative data the absolute values obtained were somewhat lower than expected. This may well be due to loss of ^{7}Li during sample preparation, in particular during the cutting of the B_4C slices. It may also partly be attributed to some error introduced using the $LiNbO_3$ single crystal as calibrator, for instance inaccuracies in existing stopping power data. It may also be caused by loss of ^{7}Li by diffusion processes during reactor irradiation as discussed. This very fundamental problem may well limit the application of the $^{7}Li(p,\alpha)\alpha$ reaction method to boron burn-up measurements where the irradiation temperature is low causing negligible loss of lithium during irradiation.

It would be very interesting to measure ^{7}Li distributions across a material which is far less likely to loose ^{7}Li during preparation for analysis, for instance a material which is easier to cut than B_4C. If one wished to regard the bulk values obtained by the alternative technique as absolute values, the spatial data could be normalized with respect to them by application of the normalization factor between the bulk values from the two techniques and the weighting factors to correct for bulk cylinder to diametric scan data.

CHAPTER 8

THE APPLICATION OF ^{15}N AS A STABLE ISOTOPE TRACER IN BARLEY ROOTS

To date very little work has been carried out on the application of the nuclear microprobe to biological samples. The opportunity arose to work in collaboration with the nearby Agricultural Research Council Letcombe Laboratory on the application of the stable isotope ^{15}N as a tracer, in the investigation of the uptake of nitrogen by a segment of intact barley plant roots. The uptake of plant nutrients is of considerable importance in improving crop yields, not only with respect to finding the best nutrient types but also in finding variations of nutrient uptake under different conditions. The uptake of several plant nutrients such as phosphate, potassium and calcium by different parts of the root system had been investigated [120, 121] in detail at Letcombe using radioactive tracers. Usually the techniques used to investigate the biological specimens are micro-autoradiography and electron probe microanalysis. Of course the latter is of no use in isotopic tracer measurements since the technique is not isotopically sensitive and micro-autoradiography cannot be carried out for nitrogen since there is no suitable radioactive tracer. Methods using the stable isotope ^{15}N provided a reasonable alternative. Experiments had been carried out in which bulk root measurements of ^{15}N had been obtained using conventional mass spectrometry after combustion of the root, followed by purification of the gaseous products. However the extension of the investigation to include lateral spatial measurements of the ^{15}N across the barley roots was required in order to follow the nitrogen distribution across the root, from the labelling solution outside the root, to the centre of the root which conducts the nutrients and water to the plant shoot. It was therefore proposed to try to develop a technique allowing lateral spatial measurement of ^{15}N and $^{15}N/^{14}N$ ratios across barley roots using the nuclear microprobe.

8.1 SURVEY OF NUCLEAR REACTIONS SUITABLE FOR ^{15}N, ^{14}N ANALYSES

Several nuclear reactions have been reported as suitable for ^{15}N and/or ^{14}N measurements, these include the following:-

$^{14}N(d,p)^{15}N$ and $^{14}N(d,\alpha)^{12}C$ (Refs: 122-125)

$^{14}N(p,\gamma)^{15}O$ and $^{15}N(p,\alpha\gamma)^{12}C$ (Refs: 79, 82, 84, 126-130)

$^{14}N(d,p\gamma)^{15}N$ and $^{14}N(d,n\gamma)^{15}O$ (Refs: 131-133)

$^{14}N(p,n\gamma)^{14}O$ (Ref. 134)

$^{15}N(p,p)^{15}N$ (Ref. 135)

$^{14}N(n,\gamma)^{15}N$ (Ref. 136)

$^{14}N(n,2n)^{13}N$ (Refs. 137, 138)

The latter two are incompatible with the focussed charged particle microprobe facility.

Sundqvist et. al. [123] have successfully used the (d,p) and (d,α) reactions for the analysis of ^{14}N in single grain samples of wheat and barley. The ^{14}N content being related to the protein content. The beam was only collimated by slits to 1.5 mm^2 and low beam currents were used, however the beam energy used, 6 MeV $^2H^+$, exceeds the energy limit available to the focussing microprobe. Although the technique has proved successful for ^{14}N determination it will not allow the simultaneous measurement of ^{15}N because of the likelihood of interference. The Q value for the $^{15}N(d,p)^{16}N$ reaction is only 0.265 MeV and although that of the $^{15}N(d,\alpha)^{13}C$ reaction is +7.69 MeV, interference is highly likely since so many other nuclides have an even higher reaction Q value.

The $^{14}N(d,p)^{15}N$ reaction is used routinely for the analysis of ^{14}N in metallurgical samples [139] on the nuclear microprobe using focussed 1.9 MeV $^2H^+$ beams. A sensitivity of approximately 1630 C/μC/1% ^{14}N in metallurgical samples is obtained giving a sensitivity limit of ≏ 0.002%.

Both Bodart et. al. [132] and Chen et. al. [131] have successfully used the (d,nγ) and (d,pγ) reactions for the measurement of $^{14}N/^{12}C$ ratios in various biological samples although again only ^{14}N rather than $^{15}N/^{14}N$ ratios can be measured. Bodart used a 2.3 MeV $^2H^+$ beam of large diameter, 5-20mm, to induce the reactions and measured the emitted γ's ($^{14}N(d,n\gamma)O^{15}$ E_γ = 7.286 MeV) using both a 10% efficient Ge(Li) detector and a NaI(Tl) detector. Chen made similar measurements using a 12.7 x 12.7 cm^2 NaI(Tl) detector but made use of the $^{14}N(d,p\gamma)^{15}N$ E_γ 5.3 MeV peak in addition to the peak at the higher energy. Relatively large doses were used, 10-500 mA for 10 minutes. At the lower end of this range 6 μC may be acceptable when analysing microtome sections of barley root however from previous experience with rather beam sensitive powder samples the higher end of the range, towards the ca. 300 μC dose, is unlikely to be acceptable.

Matsumato et. al. [135] have used proton elastic scattering to measure ^{15}N and ^{18}O in various biological samples. A 6.7 MeV $^{1}H^{+}$ beam was used to investigate very thin samples, prepared by evaporation of 5-10 μ litres, measuring the backscatter at an angle of 165^{o}. The scattering yield from ^{15}N was found to be extremely small so the following suggestions to improve sensitivity were made: use beam currents up to 100 nA, increase the detector solid angle and utilise an annular detector. Some increase in detector solid angle, 1.74 msr was that used, could be utilised without detriment to the spectral resolution bearing in mind the solid angle restrictions discussed in Chapter 3, however an increase in yield of several orders of magnitude was required for adequate sensitivity and increasing the solid angle certainly could not provide that. The damage done to barley cells at beam currents even approaching 100 nA is totally unacceptable in small spatial scans, many cell walls being completely broken. Annular detectors are not currently available with the resolution required, i.e. better than 15 KeV FWHM. Thus the sensitivity would probably remain rather poor. In addition Kelly et. al. [126] found that in biological samples, for thicknesses of more than 0.25 μm, the low energy end of the oxygen overlaps the high energy end of the nitrogen. Thus computerised resolution enhancement methods are required.

The $^{14}N(p,n\gamma)^{14}O$ reaction was used to measure ^{14}N content in grain by Standing et. al. [134] with a 16 MeV $^{1}H^{+}$ beam, which greatly exceeds the energy limit of the focussed microprobe. The nitrogen content was calculated from the ^{14}O decay E_{γ} = 2.31 MeV. However if ^{12}C and ^{13}C were present in the sample, interference to the nitrogen measurement would be likely from the $^{12}C(p,\gamma)^{13}N$ E_{γ} = 2.366 MeV and the $^{13}C(p,\gamma)^{14}N$ E_{γ} = 2.313 MeV reactions.

The most popular method for the analysis of ^{15}N and $^{15}N/^{14}N$ ratios in biological materials involves the use of proton induced gamma reactions; the $^{14}N(p,\gamma)^{15}O$ E_{γ} = 3.042 MeV and the $^{15}N(p,\alpha\gamma)^{12}C$ E_{γ} = 4.439. Generally lower energy $^{1}H^{+}$ beams, in the region of 1 MeV, have been favoured in order to reduce the number of possible interfering reactions although Xenonlis et. al. [129] discussed the application of high voltage accelerators for this type of nitrogen analysis. They used 4.3 MeV $^{1}H^{+}$ beams and measured the $^{14}N(p,p\gamma)^{14}N$ 2.313 MeV E_{γ} and the $^{15}N(p,\alpha\gamma)^{12}C$ 4.439 MeV E_{γ}. Of course with the focussed microprobe the lower energy beams are preferable not only to minimise interference but also because they are far easier to focus to the extremely small dimensions required for reasonable spatial resolution. Both a 100 cm^{3} Ge(Li) detector and a 10.2 x 10.2 cm^{2} NaI(Tl) detector have been used to measure the emitted gammas. The ^{15}N 4.439 MeV peak is fairly sensitive

especially when using NaI(Tl) detectors however the sensitivity for ^{14}N determination is considerably lower.

Available information indicated that measurement of deuteron and proton induced gamma-rays and deuteron induced protons might be suitable for the nuclear microprobe measurement of ^{15}N and ^{14}N. Consequently the value of these techniques was assessed experimentally.

8.2 EXPERIMENTAL EVALUATION OF THE MOST SUITABLE NUCLEAR REACTIONS FOR THE SPATIAL ANALYSES OF ^{15}N AND ^{14}N

Initial feasibility studies were carried out using each of the chosen reactions in turn. Pressed powder targets of urea, NH_2CONH_2, containing different enrichments of ^{15}N were placed in the nuclear microprobe chamber and interrogated using focussed beams from the nuclear microprobe.

Investigating the $^{15}N(p,\alpha\gamma)^{12}C$ and $^{14}N(p,\gamma)^{15}O$ reactions first, in order to choose the optimum incident energy, it was necessary to consider the reaction resonances tabulated in Table 8.1.

Table 8.1: GAMMA-EMISSION ENERGIES FROM THE $^{1}H^{+}$ INDUCED γ REACTIONS ON ^{14}N AND ^{15}N

RESONANCE ENERGY KeV	NUCLEAR REACTION	(mb)	RESONANCE WIDTH (KeV)	E_γ EMITTED KeV	COMMENT ON RESONANCE
360	$^{15}N(p,\alpha\gamma)^{12}C$	0.03	94	4.439	
429	$^{15}N(p,\alpha\gamma)^{12}C$	200	0.9	4.439	fairly strong
429	$^{15}N(p,\gamma)^{16}O$	0.001	0.9	6.46	
700	$^{14}N(p,\gamma)^{15}O$	-	100	8.0	
710	$^{15}N(p,\gamma)^{16}O$	-	40	6.72	
898	$^{15}N(p,\alpha\gamma)^{12}C$	800	2.2	4.439	strong
1040	$^{15}N(p,\alpha\gamma)^{12}C$	15	130	4.439	strong
1040	$^{15}N(p,\gamma)^{16}O$	1	130	13.09	
1059	$^{15}N(p,\gamma)^{16}O$	-	4	8.34	
				5.27	
				3.04	
1210	$^{15}N(p,\alpha\gamma)^{12}C$	600	22.5	4.439	very strong
1544	$^{14}N(p,\gamma)^{15}O$	-	34	8.8	
1640	$^{15}N(p,\alpha\gamma)^{12}C$	340	68	4.439	very strong

Table Continued ...

TABLE 8.1 (Continued)

RESONANCE ENERGY KeV	NUCLEAR REACTION	(mb)	RESONANCE WIDTH (KeV)	Eγ EMITTED KeV	COMMENT ON RESONANCE
1742	$^{14}N(p,\gamma)^{15}O$	-	5	9.0	
1807	$^{14}N(p,\gamma)^{15}O$	-	5	9.0	
1979	$^{15}N(p,\alpha\gamma)^{12}C$	35	23	4.439	fairly strong

It can be seen from Table 8.1 that there were several very strong resonance energies for the ^{15}N reaction leading to the emission of the 4.439 MeV gamma ray. The variation in yield using different beam energies was investigated using the nuclear microprobe and a 100 cm^3 "17% efficient" Ge(Li) detector. One of the spectra obtained is shown in Figure 8.1. The $^{15}N(p,\alpha\gamma)^{12}C$ E_γ = 4.439 MeV and its single and double escape peaks were all clearly seen. The variation in yield of the NH_2CONH_2 sample fully enriched in ^{15}N (i.e. 95.1 atom % ^{15}N; 44.5 wt. % ^{15}N in urea) at different energies is shown in Figure 8.2. The sensitivity of the measurement increased with increasing incident beam energy as each successive resonance was included. The 4.439 MeV gamma transition is extremely strong and the ^{15}N content could have been evaluated directly from the peak intensity of the 4.439 MeV line. However the 5.242 and 8.283 MeV gamma transitions which can be used for ^{14}N analysis have very low yields, especially when compared to the strong ^{15}N transition. In order to enhance the chances of successfully measuring the ^{14}N, for the $^{15}N/^{14}N$ ratio values required, it appeared preferable to work at lower proton beam energies, below the 1.21 MeV resonance. This was verified by Engelmann et. al. [84, 127] who found that for $^{15}N/^{14}N$ measurements when the ^{15}N isotopic concentration was above the natural abundance (0.36%) the optimum incident $^1H^+$ energy was 1.1 MeV, whilst 1.25 - 1.75 MeV was preferable when the ^{15}N level was below the natural level. Once the ^{15}N enrichment was above 5% it was extremely difficult to measure the ^{14}N at all. As these $^{15}N/^{14}N$ tracer experiments were such that the ^{15}N level of enrichment rose above the natural level, a bombarding energy of 1.1 MeV was choosen in order to see if the sensitivities were adequate for both ^{15}N and ^{14}N measurement under nuclear microprobe conditions. Even after 35 μC of charge had been collected, whilst bombarding NH_2CONH_2 containing the natural abundances of the nitrogen isotopes, the peak yields in the region of the 5.242 MeV and 8.283 MeV γ's from the ^{14}N reaction were insignificant. In fact typically irradiation doses of about 100 μC in conjunction with a 10.2 x 10.2 cm^2 NaI(Tl) detector and

about 1000 μC in conjunction with a 100 cm^2 Ge(Li) detector were used by Engelmann et. al. [84, 127]. Comparing these results and scaling down to the beam doses acceptable for spatial microprobe analysis, from the point of view of both beam damage and spatial analysis time, the counts expected for 1 μ C/1% ^{14}N were in the region of 0.05 counts using the optimum conditions of a NaI(Tl) detector and the resolved 5.242 MeV γ peak. Thus under the conditions required for spatial analysis using the nuclear microprobe only ^{15}N rather than $^{15}N/^{14}N$ ratio values could be successfully measured. For ^{15}N analysis only, the constraints on incident energy were somewhat diminished. An incident $^1H^+$ energy may be choosen such that all the large resonances of the $^{15}N(p,\alpha\gamma)^{12}C$ reaction leading to the 4.439 MeV prompt γ transition could be utilised, the only constraint being the level of interference from other light elements encountered. The interference levels from all elements with $Z \leq 17$, with the exception of H, He and Ne, were obtained at the optimum incident energy of 1.69 MeV and are given in Table 8.2. A 10.2 x 10.2 cm^2 NaI(Tl) detector was used in order to achieve the highest sensitivity.

TABLE 8.2: MAGNITUDE OF THE INTERFERENCE TO THE MEASUREMENT OF ^{15}N USING THE $^{15}N(p,\alpha\gamma)^{12}C$ REACTION. E_γ = 4.439 MeV

INTERFERENCE	R	POSSIBLE ORIGIN
SULPHUR	0.098	$^{34}S(p,\gamma)^{35}Cl$ 4.17 MeV ⟶ t.g. (60%) branch + several other transitions. e.g. 7.601 ⟶ 3.16. E_γ = 4.441 (8%)
FLUORINE	0.063	$^{19}F(p,\gamma)^{20}Ne$ 4.969 and 4.248 MeV ⟶ t.g. + many observed transitions. e.g. 13.55 ⟶ 9.11 MeV. E_γ = 4.401 MeV.
LITHIUM	0.0155	$^6Li(p,\gamma)^7Be$ 4.53 MeV ⟶ t.ground.
CHLORINE	0.0027	$^{35}Cl(p,\gamma)^{36}Ar$, 4.44 MeV ⟶ t.g. (60%)
BORON	0.002	$^{11}B(p,\gamma)^{12}C$. Same residual nucleus, same but lower abundance peaks.
BERYLLIUM	0.0019	$^9Be(p,\gamma)^{10}B$, 4.75 and 4.45 ⟶ t.g.

where $R = \frac{\text{(Yield of 1 wt. \% interference nuclide/ μ C)}}{\text{(Yield of 1 wt. \% } ^{15}N \text{ in Urea/μ C)}}$

this notation should be used throughout this chapter with ^{15}N being replaced by ^{14}N where appropriate.

Although none of the worst interferences gave even a tenth of the yield from ^{15}N, the application of the technique may be of very limited application

when samples contain appreciable quantities of sulphur, fluorine and lithium. However for the barley plants no significant interference was expected.

A typical spectrum obtained using the NaI(Tl) detector is given in Figure 8.3, the main and single escape peaks from the $^{15}N(p,\alpha\gamma)^{12}C$ E_γ = 4.439 MeV transition are clearly visible. A typical calibration curve is given in Figure 8.4 and a sensitivity of 4,240 counts/μC/1 wt. % N^{15} in urea was obtained.

Although it was obviously preferable to analyse both ^{15}N and ^{14}N simultaneously the sensitivity required for spatial analysis at these low beam doses necessitated the use of the (d,p) or the (d,nγ) reactions for the ^{14}N analysis.

For the $^{14}N(d,p)^{15}N$ and the $^{14}N(d,\alpha)^{12}C$ reactions an incident beam of 1.9 MeV $^2H^+$ was used and an annular detector was choosen to collect the resultant charged particles in an attempt to achieve better sensitivity. An 150 mm^2 active area detector with 300 μm depletion depth was available. From Kinematics the resultant energy of the $^{15}Np_o$ group under these conditions was 8.89 MeV and that of the $^{14}N_{\alpha\ o}$ group was 9.84 MeV. In order to detect the 8.89 MeV proton group, detector absorber foils were required to degrade its energy prior to entering the detector surface. Approximately 90 μm of nickel foil was used and this totally absorbed the $^{14}N_{\alpha\ o}$ group. In addition to the $^{14}Np_o$ group only the $^{33}Sp_o$ and p_1 groups and the $^{25}Mgp_o$, $^{29}Sip_o$ and $^{10}Bp_o$ groups could be detected and were therefore the only potential sources of interference. The levels of interference found from each of these is listed in Table 8.3 with the exception of ^{29}Si which wasn't measurable.

TABLE 8.3: MAGNITUDE OF INTERFERENCE TO THE MEASUREMENT OF ^{14}N USING THE $^{14}N(d,p_o)^{15}N$ REACTION

INTERFERENCE NUCLIDE	SILICON SURFACE BARRIER DETECTOR AT 135° R	SILICON SURFACE BARRIER DETECTOR AS CLOSE TO 0° AS POSSIBLE R
Boron	0.54	0.088
Sulphur	0.0062	0.0224
Magnesium	0.004	0.00144

A typical spectrum for a NH_2CONH_2 sample is shown in Figure 8.5 only the $^{14}N(d,p_0)^{15}N$ group being seen since 90 μm of Nickel detector foils attenuated lower energy proton and alpha groups as previously described.

A typical calibration curve is given in Figure 8.6, and a sensitivity of 1150 counts/μC/1 wt. % ^{14}N in urea was achieved. Although a higher sensitivity could be achieved using a larger surface area annular detector this sensitivity proved adequate for these ^{15}N tracer experiments.

A 1.9 MeV $^2H^+$ beam was used to investigate the analytical potential of deuteron induced gamma reactions. (The radiation hazard prevented the use of higher energy deuteron beams on the nuclear microprobe.) The strongest de-excitation gammas from the products of the deuteron induced gamma reactions are given below:-

$^{14}N(d,\alpha\gamma)^{12}C$	E_γ = 4.43	very weak peak
$^{14}N(d,p\gamma)^{15}N$	E_γ = 5.28, 5.31	very strong peak
$^{14}N(d,n\gamma)^{15}O$	E_γ = 6.82	weak peak
	E_γ = 7.3	strong peak
	E_γ = 8.3	less strong peak
$^{15}N(d,n\gamma)^{16}O$	E_γ = 6.14	weak peak

The sensitivity of the ^{15}N analysis was extremely low, even with the fully ^{15}N enriched urea targets (44.5 wt. % N^{15} in NH_2CONH_2) the $^{15}N(d,n\gamma)^{16}O$ $E\gamma$ = 6.14 MeV transition was only just discernable. A sensitivity of 90 c/μC/1 wt. % ^{15}N in urea at best, with a sensitivity limit in the region of 7700 ppm was found. For the barley experiments the maximum amount of ^{15}N was in the region of 1.8 - 2 wt. % ^{15}N in the root and since it was likely that the cell structure would only withstand very low dose rates, sensitivity was of the utmost importance. The sensitivity offered by the $d \longrightarrow \gamma$ reaction was totally inadequate and compared very unfavourably with that of the $^{15}N(p,\alpha\gamma)^{12}C$ reaction namely 4,240 counts/μC/1 wt. % ^{15}N in urea. The γ-ray spectrum obtained by deuteron irradiation of a natural NH_2CONH_2 sample using the Ge(Li) detector is given in Figure 8.7. Three of the ^{14}N induced transitions at 8.3, 7.3 and 5.3 MeV were seen although the double escape of the 8.3 MeV peak fell very close to the 7.3 MeV γ peak. The sensitivity obtained using the 5.3 MeV γ main peak was approximately 140c/μC/1 wt. % ^{14}N in urea and for the weaker peak at 8.3 MeV a sensitivity of ≃ 80c/μC/wt. % ^{14}N

in urea was obtained. As the $^{14}N(d,p)^{15}N$ reaction was far more sensitive it was prefered for ^{14}N analysis. For ^{15}N the prefered method was that based on the $^{15}N(p,\alpha\gamma)^{12}C$ reaction.

8.3 THE LABELLING OF BARLEY ROOTS WITH A ^{15}N TRACER

Barley seeds were soaked in distilled water for 6 hours, the water being continually aerated. The seeds were then spread evenly over a double layer of Whatmans No. 1 filter paper on a sterile tray. The filter paper was moistened and the tray then covered with black polythene sheet to make it light-proof and sufficiently airtight to prevent excess drying of the filter paper. The tray was then maintained at 20°C for the seeds to germinate. This usually takes about 48 hours and the seeds were planted out when the first seminal root was approximately 2-3mm long. Uniformly germinated seeds were placed onto a stainless steel mesh suspended in a black polythene tank of nutrient solution A. (Table 8.4).

TABLE 8.4: NUTRIENT CULTURES USED TO GROW BARLEY ROOT AND SUBSEQUENTLY LABEL THEM WITH A ^{15}N TRACER

COMPOUNDS	CONCENTRATION m moles/litre	
	A	B
$Ca(NO_3)_2.4H_2O$	0.15	1.5
$K\ NO_3$	0.50	5.0
$Na\ NO_3$	0.20	2.0
$K\ H_2\ PO_4$	0.10	1.0
$MgSO_4.\ 7H_2O$	0.15	1.5
$H_3\ BO_3$	9.22×10^{-3}	9.22×10^{-3}
Fe EDTA	9.22×10^{-3}	9.22×10^{-3}
$CuSO_4.5H_2O$	0.16×10^{-3}	0.16×10^{-3}
KC1	14.10×10^{-3}	14.10×10^{-3}
$MnSO_4.4H_2O$	3.60×10^{-3}	3.60×10^{-3}
$(NH_4)_6Mo_7O_{24}.$ $4H_2O$	0.016×10^{-3}	0.016×10^{-3}
$ZnSO_4.7H_2O$	0.77×10^{-3}	0.77×10^{-3}

During labelling the 3 nitrates in Culture B are all replaced by the requisite amount of KNO_3 enriched to 99% ^{15}N.

The seeds were left in the dark, in a controlled temperature of 20°C, for two days prior to replanting uniform plants into individual jars containing 500 mls of solution B (in Table 8.4). All solutions were gently aerated at all times. After nine days growth the seedlings were placed over the labelling culture solution which was identical to culture B except that all three nitrates were replaced by potassium nitrate enriched to 99% in ^{15}N. The pattern of uptake was established by leaving the seedlings in the labelling culture for various periods. When similarly treated roots were left in the unlabelled ^{14}N culture for similar periods of time to that in the ^{15}N culture, i.e. "chaser" experiments were carried out, a different pattern of accumulation emerged. Differences should indicate those regions which readily exchange the nitrogen and those which do not.

After growing and labelling the barley seedlings in the desired sequence of cultures the roots of the barley plants were prepared for sectioning. There are two basic requirements in the preparation of plant tissue for sectioning namely, (a) to freeze the root immediately after treatment to stop redistribution of tracer within the tissue (rapid freezing reducing the size and growth rate of ice crystals [140, 141] which cause severe cellular disruption) and (b) to support the tissue in a suitable matrix to prevent it being ruptured during sectioning. Methyl cellulose was used for these experiments since it is fairly easy to use and good quality sections can be obtained above 5 μm. Immediately after the root segments were removed from the plants they were dipped first into distilled water and blotted to remove surface contamination of ^{15}N, then into a viscous solution of methyl cellulose (at 2°C) and then were immersed in liquid nitrogen. The selected portion of the frozen root was severed from the remainder of the root system and mounted onto a microtome chuck, with the methyl cellulose cooled in liquid nitrogen and then allowed to warm to cryostat temperature (-20°C) before sectioning to the required thickness. An excellent detailed account of basic mounting and sectioning techniques is given by Sanderson [142]. Individual sections were transferred from the microtome knife, with the aid of a wooden handled needle, to a piece of mylar film in the base of the cryostat. The last cut face of the section was placed against the mylar film.

The method used for mounting the microtomed freeze dried root sections ready for nuclear microprobe analysis evolved during the series of experiments. However ultimately 100 μm sections were placed, with the lower face of the freeze dried section (i.e. the one in contact with the mylar during

freeze drying) uppermost, onto Nickel mounts and held in place by strips of double sided sticky tape which adhered to the cellulose matrix leaving the root region itself clear for microprobe interrogation.

The barley plants were grown, labelled, freeze dried and sectioned by Mr. J. Sanderson in collaboration with Dr. D. Clarkson, both of the Agricultural Research Council Letcombe Laboratory.

8.4 EXPERIMENTAL INVESTIGATION OF ^{15}N AS A STABLE ISOTOPE TRACER IN BARLEY ROOT SECTIONS

The ^{15}N and ^{14}N levels in the treated barley root sections were analysed using first the $^{15}N(p,\alpha\gamma)^{12}C$ and then the $^{14}N(d,p)^{15}N$ reactions in conjunction with the nuclear microprobe. One of the main problems, when analysing these extremely thin root sections, is that of beam damage. Low beam currents, the continuous electrostatic scanning method and special sample mounting techniques were used in order to help minimise beam damage.

8.4.a Sample handling techniques used during root cell analysis

The first sample mounting technique tried involved the use of a small air cell in an attempt to more readily conduct away the heat deposited in the barley cells by the beam. The air was trapped between two small perspex plates sealed with a perbunam "rubber" 'O' ring, the beam hole in the front plate being sealed with a mylar window onto the back of which the root section was placed. Mylar was used rather than the more radiation damage resistant kapton because the former contains no nitrogen other than that absorbed by the film from the atmosphere. The second mounting method was very simple and involved placing the root sections directly onto nickel sample blocks (nickel being highly unlikely to introduce any interference to the analyses) and then to cover the root sections with a 6.3μm mylar film to prevent the cells being sucked off the nickel blocks during the evacuation of the microprobe chamber. Root sections were mounted using either of the two methods and were bombarded for different beam doses, in the range 20μC to 0.5μC, under the conditions detailed earlier for ^{15}N and ^{14}N analysis. The root sections placed in the air cells were very badly damaged, the chamber vacuum pressure rather suggested that the air cells were leaking thus the root sections were effectively being bombarded in vacuum. Although the simple expedient of placing the root cells in good contact with nickel blocks, proved more successful there was still evidence of

beam damage. The higher incidence of beam damage in sections partially damaged during freeze drying suggested that radiation shrinkage of the overlaying mylar film was the cause, rather than the direct interaction with the beam. While improvements to the gas cell method might have been implemented, including the use of helium to increase heat dissipation, this option was not pursued as the problem of radiation damage to the mylar window would have remained. Consequently, improvements to the nickel block method were sought. A sample preparation technique which is often used in electron microscopy, primarily to prevent sample surface charging up during bombardment, is to deposit a very thin film of carbon over the section to be examined. Thus a third sample mounting technique was tried out. Barley root sections were placed on Nickel blocks, each section being held in place by two thin strips of double sided sticky tape which contact the cellulose matrix surrounding the barley root sections. The whole of the nickel block surface was then covered by a 0.02 μm layer of carbon, prior to interrogation using charged particle beams. This undoubtably appeared to be the most satisfactory method of sample mounting and was used for all subsequent measurements on barley root sections. Figure 8.8 shows two photographs of a barley root section before and after bombardment with 1.9 MeV deuterons. The beam was electrostatically scanned over the desired pathway across the cell and a total of 2 μC of charge were deposited over the area of the beam. Figure 8.8, Photograph i has the different regions of the root section clearly marked where (a) denotes the cellulose matrix to support the section when cutting frozen sections in the cryostat at -20°C, (b) is the outer region of the root segment consisting of the epidermis and cortex. The epidermis is an outer rank of small cells. The cortex has larger cells with few air spaces between the cells. (c) is the stele, a region of much smaller cells bounded by a single rank of small thick walled cells, the endodermis, which acts as a semi-permeable barrier between the cortex and stele and xylen vessel. (d) shows the central xylen vessel. Low beam doses were preferred to minimise the amount of damage; 20 μC of charge completely destroyed most of the cell walls. Very little damage was incurred by a maximum of 5 μC charge spread over an area of ≃ 50 x 350 μm in a cell, or slightly more when a proton beam is used because it produces less damage than the same dose of deuterons. A 2 μC dose of deuterons produced no visible damage as can be seen in Figure 8.8 Photograph ii. Generally when examining sections from the tracer experiments the dose was restricted to 2 μC but was increased to

a maximum of 5 μC for those cells treated for the shortest periods with ^{15}N.

8.4.b Spatial measurement methods used for root cell measurement

When spatially analysing samples using the nuclear microprobe there are two alternative methods, firstly one could mechanically move the sample whilst keeping the beam position static, and secondly one could electrostatically scan the beam continuously across the sample whilst keeping the sample static. This latter method was used for the $^{15}N/^{14}N$ analyses in order to help minimise beam damage on these sensitive samples by minimising the dose rate. The beam was electrostatically scanned continuously across the required distance, just larger than the radius of the root section. The coincidence scanning data collection system used is described in detail in Chapter 2. Effectively the scan is split into a choosen number of data collection blocks. Instead of collecting a single spectrum across the whole radius of the barley root, 32 or 16 spectra were collected over approximately 15 or 30 μm sections of the barley root respectively. The actual number of collection blocks choosen depends on a compromise between spatial resolution and sensitivity requirements. The method of spatial analysis is clearly seen by looking at Figures 8.9 and 8.10. Figure 8.9 shows some of the 16 gamma ray spectra obtained using the NaI(Tl) detector and the $^{15}N(p\alpha\gamma)^{12}C$ reaction on a urea sample enriched in ^{15}N (44.5 wt. % ^{15}N in urea). The main and single escape peaks of the 4.439 MeV γ are clearly seen in each block. Figure 8.10 shows some of the 16 proton spectra obtained using an annular detector and the $^{14}N(d,p_0)^{15}N$ reaction on a natural urea target. The $^{14}Np_0$ (8.888 MeV) group is clearly visible, broadened somewhat by the Nickel detector absorber foils.

8.5 RESULTS AND DISCUSSION

The first batch of barley roots spatially analysed comprised of root sections of a variety of thicknesses in the range 30 - 100 μm, mounted some with the lower face of the freeze dried section (which had been in contact with the mylar) uppermost and some with the lower face of the freeze dried section against the Nickel block, as illustrated in Figure 8.11. The roots were treated in the labelling culture for either 48 hours or for only 5 minutes. An example of the two parameter spectrum of the highly enriched barley root section treated for 48 hours is shown in Figure 8.12. The 4.439 MeV main peak and its single escape peak are clearly visible in each section

of the root scan(with a 17 μm spatial resolution in this case). Also it can be clearly seen that the ^{15}N builds up at the endodermis which acts as a barrier to the movement of ions. This was expected from the behaviour of ^{14}N profiles in roots treated with natural abundance nitrogen cultures. The position of the central region is also clearly seen in Figure 8.13 which shows a ^{14}N profile where a larger spatial resolution was used to allow the beam to extend across the xylen vessel in the root. The position of the centre is much easier to locate than the boundry between the root section epidermis and the cellulose matrix. In order to find the representative $^{15}N/^{14}N$ ratio profile, many scans were obtained across the radii of roots treated for each period in the cultures, these were combined to find the average $^{15}N/^{14}N$ ratio at each point. The combining of the scans was always carried out from the centre outwards because of the difficulty in locating the outside edge. When combining the different scans it is important to use only good sections. During freeze drying and the other root handling processes parts of the cell may be distorted, only those scans across undistorted regions could be used in order to combine scans and get good lateral spatial accuracy since the radii of distorted regions could vary significantly from the average undistorted radius. Photographs of the root sections, taken before and after bombardment of each section, helped considerably in the sorting and combination of data.

The most consistent results were obtained from the thickest root sections with the freeze dried layer at the top of the root section directly under the carbon deposit. This is probably a result of several factors which are discussed below.

It can be seen in Figure 8.11 that after freeze drying the root section consists mainly of hollow space, cell walls and an extremely thin layer (in the region of 1 or 2 μm) of the frozen cell contents which contains most of the nitrogen. In the thicker sections more of the nitrogenous material may have adhered to some of the cell walls rather than drop to the bottom, thus effectively presenting a "thicker" nitrogen layer to the beam. This can then interact with more of the ^{15}N resonances to improve sensitivity and quantitation. Another very important factor is that the thicker sections were far more regular, with less cell walls collapsed, thus they presented a more uniform pathway for the beam to traverse.

It is advantageous to have the nitrogenous layer uppermost since one can control the initial beam energy entering the sample whereas, as shown in

Figure 8.11, there are several different pathways for the beam to traverse when the nitrogenous layer is placed at the bottom. It is highly likely that the incident beam energy, when it hits this layer, will vary. Quantitation will thus be extremely difficult. For all subsequent barley root sample batches 100 μm sections, flashed with 0.02 μm of carbon, mounted with the nitrogenous layer uppermost were used.

Although the movement of ^{15}N after 48 hours was clearly seen, the spatial analysis method was too insensitive to detect the ^{15}N movement after the 5 minute exposure experiment. Consequently root sections were treated for various, longer times in the labelling culture. In addition sections from nearer the tip (1 cm from the tip) of the root were used since the outer root cells of this part of the root have a higher nitrogen status, i.e. there is more unused nitrate, and thus the labelled ^{15}N from the culture can exchange with it very easily. In addition the cell diameters at the tip tend to be smaller and thus were less susceptible to damage during sectioning and freeze drying.

The tracer experiments, where the roots were exposed to the labelling culture for periods of 2 hours and 24 hours, produced measurable $^{15}N/^{14}N$ ratio profiles. The resultant $^{15}N/^{14}N$ ratio profiles obtained from averaging many root section scans from each of the two periods are given in Figures 8.14 and Figure 8.15 respectively. The two have similar patterns but after 2 hours the $^{15}N/^{14}N$ ratio was still fairly low whereas after 24 hours considerable exchange between the ^{15}N labelling culture and the outer cortical cells (which act as a storage 'larder') had occurred. As expected those cells closer to the centre had a much lower $^{15}N/^{14}N$ ratio because they do not have as a high a nitrogen status and the ^{15}N cannot so easily exchange with ^{14}N already present. A very good lateral spatial picture of the ^{15}N movement was obtained clearly verifying the importance of the 'larder' cells of the root section where ^{15}N exchange had occurred to a high degree. From this type of data one might work out kinetic information on the uptake and exchange of ^{15}N by the cells, in different lateral positions across the root section, with time. One would have to treat many batches of roots in the ^{15}N labelling culture for periods between 2 and 24 hours, measure the spatial $^{15}N/^{14}N$ profiles and then calculate the rates. Sufficient time was not available for the quantity of data required to be obtained but quite clearly the evidence obtained to date strongly indicates that this type of information could be acquired.

Further experiments were carried out to elucidate how quickly the high ^{15}N status cells lose the accumulated ^{15}N. Some plants take up and lose nitrogen at different rates since enzymatic conversion of nitrate to protein fixes and diminishes the amount of nitrogen which can be lost. To this end these further experiments of the "chaser" type were carried out by removing the young plants from the labelling culture B after a given period of time and subsequently allowing the young plants to continue growing in the unlabelled culture B for an additional period of time.

Figure 8.16 shows the $^{15}N/^{14}N$ profile obtained by labelling barley plants for 24 hours followed by growth in the unlabelled culture for 24 hours. Figure 8.16, of the 24 hour chaser experiment, clearly shows a very similar pattern to that of Figure 8.15 where the plants were just labelled for 24 hours. Although it should be noted that in Figure 8.16 the electrostatic scan did not cover the outside edge of the samples and further work should be carried out to ensure the outside edge is also measured. However it can be seen that a considerable portion of the ^{15}N in the high nitrogen status cell region, or "larder cell" region, had readily re-exchanged with ^{14}N when the plants were placed in the unlabelled culture. However the concentration of ^{15}N in the smaller cells of the stele is practically unchanged, the nitrogen in this region is thus far less susceptible to exchange which may indicate some degree of fixation of the nitrogen as protein. Due to time limitations further "chaser" experiments have not been carried out, however from Figure 8.16 it can be seen that the rate of loss of ^{15}N from various radial positions across a root section and hence the degree of fixation of nitrogen across the section could be obtained by measuring the average $^{15}N/^{14}N$ profiles across many sections after a variety of chaser treatment periods.

Considering the results obtained throughout the accuracy of the quantitative $^{15}N/^{14}N$ data was inevitably affected by the inherent problems of sample irregularities and inhomogenity in freeze dried sections. The incomplete knowledge of the exact material traversed by the beam within the freeze dried sections affects the nuclear reaction kinematics, cross-sections and stopping powers used in data interpretation when comparing responses in standards and responses in the root sections. The experiments have been designed, as described in detail within this chapter, to minimise this inherent difficulty. However if one could work using a cryogenic stage this problem could be largely overcome. The use of the cryogenic stage would ensure that the nitrogenous material remains in solution through the whole

CHAPTER 9

SUMMARY OF CONCLUSIONS AND FURTHER WORK

The use of the nuclear microprobe, in conjunction with backscattering and nuclear reaction analysis, has been successfully demonstrated for the spatial determination of stable isotope tracers in a variety of materials. Fundamental assessment of the applicability of both backscattering and nuclear reaction analysis for these lateral spatial isotopic measurements indicated that microbeam operation had no specific disadvantages.

Although backscattering analysis has been successfully used to quantitatively determine the absolute abundances of stable isotopes, the lack of sensitivity (which imposed unacceptably long analysis times) severely limited the application of the technique for spatial analysis. However the use of nuclear reaction analysis has provided sensitive and selective methods capable of measuring high lateral spatial resolution profiles of stable isotopes and isotope ratios of light elements. Compared to conventional nuclear microprobe analysis, selection of the measurement conditions was often complicated by several factors. For example because stable isotope ratios were often preferred, simultaneous measurement of more than one isotope was required and a compromise of measurement conditions almost inevitable. Since high tracer sensitivity was vital to optimise the detection of any changes in tracer isotope abundance and since enriched stable isotope tracers are expensive, the conditions choosen were usually optimised for the tracer isotope.

The potential of the nuclear microprobe for stable isotope tracer analysis has been demonstrated by the successful application of the technique in ^{13}C, ^{7}Li and ^{15}N stable isotope experiments, which serve as illustrative examples. They were choosen to provide as wide a spectrum of sample types as possible.

The detailed investigation of reactions capable of measuring ^{13}C and ^{12}C allowed a full appreciation of the capabilities and limitations of the various reactions for different applications. Four techniques were found to be suitable for the simultaneous determination of ^{13}C and ^{12}C. For applications requiring the highest sensitivity the (d,p) reactions were preferred although serious light element interference could limit its use in certain cases. The use of γ rather than proton detection circumvented interference problems but at considerable loss of sensitivity and the ^{3}He induced γ reactions provided

a useful alternative method but only for carbon rich samples. For ^{13}C analysis alone the (α,n) reaction was particularly attractive, it being both highly selective and reasonably sensitive. A good understanding of corrosion is important because of its widespread occurrence and generally detrimental effects. The $^{13}C(d,p)^{14}C$ and $^{12}C(d,p)^{13}C$ nuclear reactions were successfully used to provide ^{12}C, ^{13}C and $^{13}C/^{12}C$ ratio profiles in a study of the mechanism of the oxidative carburization corrosion of the nimonic alloy PE16 treated in ^{13}C labelled CO_2. The use of the ^{13}C stable isotope tracer clearly distinguished between the carbon added from the gas phase and the carbon initially present in the alloy, the latter being based on ^{12}C measurement. It was clearly shown that the majority of carburization occurring was due to ingress of carbon from the CO_2, whilst the original carbon distribution remained practically unaltered. Further work utilising the method based on the $^{13}C(\alpha,n)^{16}O$ reaction would provide useful collaborative information. The need for both ^{13}C, ^{12}C and $^{13}C/^{12}C$ ratios would argue in favour of nuclear microprobe analysis as opposed to S.I.M.S. analysis. The fact that ^{12}C and ^{13}C concentrations were to some degree phase dependent would have made even the $^{13}C/^{12}C$ values obtained by S.I.M.S. of dubious value. Further applications in the field of corrosion and in the field of materials compatability in general, where the system components include light elements, would be expected.

A special area of application is to materials in which the natural abundance of an isotope has been disturbed, for example in a material which had been subjected to nuclear transmutation either artificially or naturally. Such disturbances may act as indicators or tracers of those processes involved. Hence the example of the formation of ^{7}Li in B_4C fast reactor control material, by the reaction $^{10}B(n,\alpha)^{7}Li$ was investigated. The ^{7}Li distributions were measured using the $^{7}Li(p,\alpha)\alpha$ reaction and although good relative spatial information was successfully obtained there was still uncertainty as to the exact quantitation of the ^{7}Li data. This could be due to a very fundamental problem, that of lithium loss during reactor irradiation or could be due to loss of lithium during preparation for analysis or to standardization errors. Further investigation to improve the quantitation is required. When following the formation of a species by nuclear transmutation great care in translating the data is necessary, to avoid confusing nuclear and non-nuclear processes. Hence $^{10}B/^{11}B$ ratios as well as ^{7}Li distributions would have been valuable. Indeed, measurement of other isotopes formed during the transmutation of the boron isotopes (e.g. T or He) may have given further valuable information on

the nuclear processes and associated physico-chemical processes involved.

The applicability of nuclear microprobe methods to radiation sensitive materials was investigated by a study of the mechanism of nitrogen exchange in barley roots using ^{15}N labelled nitrate. The avoidance of specimen damage during the preparation and examination of root sections was critically important and acceptable procedures have been developed. $^{15}N/^{14}N$ ratio profiles across barley root sections were successfully obtained with insignificant damage to the cellular structure. The $^{15}N(p,\alpha\gamma)^{12}C$ and the $^{14}N(d,p)^{15}N$ reactions were used to measure the ^{15}N and ^{14}N respectively. The movement of ^{15}N across the root sections was clearly seen and the different regions of the section were clearly identifiable, the measured behaviour correlating very well with the expected physiological behaviour. By carrying out additional labelling experiments (for more varied labelling periods) the rate of nitrogen uptake and loss across the root sections could be measured accurately. Also by carrying out additional "chaser" experiments kinetic information on the rate of exchange and loss of ^{15}N from different lateral positions across the barley root sections could be obtained. This would also give information about the amount of nitrogen fixation as protein. Examination of frozen sections on a cryogenic stage might decrease errors caused by the sample distortion and inhomogeneity inherent in freeze dried samples.

In addition to the further work emanating directly from the stable isotope experiments there is much scope for the development of nuclear microprobe techniques capable of analysing other stable isotopes with good lateral spatial resolution. During this study the detection and sampling handling facilities have been considerably extended but there are still many further improvements, particularly on computerised data handling facilities, which would be very useful.

LIST OF PUBLICATIONS

1. "The Nuclear Microprobe Determination of the Spatial Distribution of Stable Isotope Tracers", P.M. Hirst, J.W. McMillan, D.J. Malcolme-Lawes.
   Nucl. Inst. Meth. 168 (1980) 203-209.
   Presented at 4th International Conference on Ion Beam Analysis, Aarhus, June 1979.

2. "Backscattering Techniques for the Measurement of Stable Isotope Abundances and Tracers", P.M. Pollard, J.W. McMillan, D.J. Malcolme-Lawes.
   In. Press. Journal of Radioanal. Chem.
   Presented at the Modern Radiochemical Methods Conference, York, September 1980.

3. "The Development of Nuclear Microprobe Techniques for the Spatial Determination of ^{13}C and $^{13}C/^{12}C$ Ratios", P.M. Pollard, J.W. McMillan, D.J. Malcolme-Lawes.
   A.E.R.E. Report R10136
   Presented at the 6th Modern Trends in Activation Analysis Conference, Toronto, June 1981. To be Published in the Journal of Radioanalytical Chem.

APPENDIX: THE EQUATIONS USED TO CALCULATE SIMULATION BACKSCATTER SPECTRA

Simulations of backscatter spectra, utilised in Chapter 4, were generated using the following method. The simulation spectra are based upon coulombic scattering theory and on the Ziegler-Chu [Zi75] energy loss polynomials. The Ziegler-Chu tables provide polynomial coefficients $a_{\alpha i}$ such that the energy loss per unit areal density of element a is given by:-

$$\varepsilon_{\alpha} = \sum_{i=o}^{5} a_{\alpha_i} E^i \qquad \text{... Eqn. A1}$$

where ε is in units of $eV/10^{15}$ atoms cm^{-2}

E is in keV

Considering a multielement layered system, the composition matrix is input and is then converted into a matrix of atom fractions F_α for each atomic species present. Assuming Bragg's rule to be valid the composite energy loss in $eV/10^{15}$ atoms cm^{-2} is given by Equation A2:-

$$\sum_{\alpha} F_\alpha \varepsilon_\alpha \ (E) \qquad \text{... Eqn. A2}$$

For a given incident energy E_o the energy of the incident beam E_r is calculated as follows as it exists from each layer, r, of a multilayered sample:-

$$E_r = E_o - \sum_{r} \sigma_r \qquad \text{... Eqn. A3}$$

$$\sigma_r = N_r \ \text{Sec}\ \phi \ \Sigma \ F_\alpha \varepsilon_\alpha \ (E_{r-1}) \qquad \text{... Eqn. A4}$$

where ϕ is an angle between the incoming beam and the perpendicular to the layer surface.

The energy loss values for a layer r are than calculated for the incident energy E_{r-1}. The set of energies E_r then serve as collision energies for the subsequent calculations of backscatter from the different species in a layer, e.g. from a nucleus of type at the bottom of a layer r with incident energy E_r. On the outward trajectory the particle looses energy and emerges from the top of a layer 1 at an angle of θ.

The initial backscatter energy $E_{r,\ r+1,\alpha}$ is calculated as follows:-

$$E_{r,\ r+1,\alpha} = K_\alpha E_r \qquad \text{... Eqn. A5}$$

and $K_\alpha^2 = \left[m \cos\theta + (M_\alpha^2 - m^2 \sin^2\theta)^{\frac{1}{2}} \right] / \left[m + M_\alpha \right]$ ... Eqn. A6

where m is the mass of the incident beam, and

M_α is the mass of species

Let $E_{rs}\alpha$ denote the energy of a particle exiting from the top of a layer s having previously backscattered from the bottom of layer r, then:-

$$E_{rs\alpha} = K_\alpha E_r - \sum_{\gamma=o}^{\gamma=r-s} \sigma_{r,\ r-\gamma} \quad \text{... Eqn. A7}$$

where

$$\sigma_{rs} = -N_s \sec(\theta - \phi) \sum F_\alpha \varepsilon_E (E_{r,\ s+1, \alpha}) \quad \text{... Eqn. A8}$$

The energy loss ε_α being calculated as in Equation A1.

For light element isotopes, where the energy differences between isotopes can be relatively large, each isotope is treated as a separate 'element' having the same Z but a different mass M_α and different ε_α values.

One now has to calculate the number of counts at the detector in the energy range $E_{r1\alpha}$ to $E_{r-1,\ 1,\alpha}$ from an atomic species α using the following:-

$$n = 6.25 \times 10^{24}\ Q\Omega\sigma\ F_{r\alpha}\ N_r \quad \text{... Eqn. A9}$$

where Q (μC) = charge

Ω (msr) = solid angle

σ ($cm^2\ sr^{-1}$) = cross-section. This is assumed to be constant for each layer and characteristic of its average i.e. the cross-section at an energy = $\frac{1}{2}(E_{r-1} + E_r)$

and $F_{r\alpha}$ is the fraction of atoms of type α in layer r

At this point the yield for each species α present in each layer has been found along with the corresponding exit energies. In order to arrive at a simulation of the experimental spectrum, the various partial spectra are summed over the experimental channel width e.g. 3 keV/Channel. This final spectrum is obtained by summing the total counts in each spectrum from the high energy end, performing a linear interpolation on this sum at e.g. 3 keV intervals and then differentiating the result to give the number of counts

per channel. A stopping power correction is often required to take into account the variation of σ and hence yield with varying collision energy. Since the yield has been calculated using cross-section values at the collision energy E_o giving final energies E_{rlx} one must correct to the collision energies corresponding to the final channel energies E_{out}. One knows the final channel energies E_{out} thus one can interpolate to find the corresponding collision energy E_{BC} given the table of already calculated values of E_{rlx} and E_r for each element. The correction factor (Eo/E_{BC}^2) must be used to multiply the calculated counts/channel.

The additional factors which degrade the spectrum e.g. detector resolution and the energy loss of projectiles in the detector surface metal layer are also convoluted into the calculated spectrum in order to obtain the final simulation spectrum.

REFERENCES

(1) N.A. Matwiyoff, M.J. Reisfield, T.R. Mills, B.B.M. McInteer, M. Goldblatt, "Isot. and Rad. Techniques in Soil Phy. and Irrigation Studies". I.A.E.A. Vienna (1974) 11.

(2) N.C. Dyer, A.B. Drill, "Nucl. Act. Techniques in the Life Sciences" I.A.E.A., Vienna (1972).

(3) N. Onuma, R.N. Clayton, T.K. Maynary, Geochim . Cosmochim . Acta., 36(2) (1972) 157.

(4) J.A. McHugh, "Methods of Surface Anal." (Editor A.W. (Zandema) Chapter 6. (1975) Elsevier Press.

(5) J. Roboz, "Intro. to Mass. Spec. Instr. and Techniques" (1968) Interscience.

(6) T. Mulvey, R.K. Webster (Eds.) "Mod. Physical Techniques in Material Techn." (1974) Oxford University Press.

(7) J.W. Mayer, A. Turos, Thin Solid Films 19 (1973) 1.

(8) H. Liebl, J. Phys. E8 (1975) 797.

(9) R. Kaufmann, F. Hillenkamp, R. Wechsung, Europ. Spec. News, 20 (1978) 41.

(10) F. Hillenkamp, E. Unsold, R. Kaufmann, R. Nitsche, Appl. Phys. 8 (1975) 341.

(11) M. Pinta, "Mod. Meths. for Trace Element Anal." (1978) Arbor Science.

(12) G. Morrison (Ed.) "Trace Anal. Physical Methods" (1965) Wiley.

(13) H. Szymanski, "Prog. in I.R. Spec." V1/2/3 (1966) Plenum Press.

(14) B. Pesce, "N.M.R. in Chemistry" (1965) Academic Press.

(15) M.G. Hecht, "Magnetic Res. Spec." (1967) Wiley.

(16) J.F. Singleton, N.E.W. Hartley, Journal of Radioanal. Chem., 48 (1979) 337.

(17) T.B. Pierce, J. Huddleston, I. Hutchinson, "Proc. 6th Mod. Trends in Activ. Anal.", Toronto (1981) to be published.

(18) A.W. Rogers, "Techniques in Autoradiog." (1967) Elsevier.

(19) M.R. Louthan, D.E. Rawl, R.T. Huntoon, Corrosion - N.A.C.E., V28 No. 5 (1972) 172.

(20) T.B. Pierce, J.W. McMillan, P.F. Peck, I.G. Jones, Nucl. Instr. Meth. 118 (1974) 115.

(21) J.A. Cookson, J.W. McMillan, T.B. Pierce, Journal of Radioanal. Chem., 48 (1979) 337.

(22) J.A. Cookson, A.T.G. Ferguson, F.D. Pilling, Journal of Radioanal. Chem., 12 (1972) 39.

(23) I.V. Mitchell, Phys. Bulletin, 30 (1979) 23.

(24) W. Hink, Revue de Physique Appliquee, 11 (1976) 31.

(25) J.A. Cookson, A.E.R.E. R-9273 (1979).

(26) C. Olivier, J.W. McMillan, T.B. Pierce, Journal of Radioanal. Chem., 31 (1976) 515.

(27) C.R. Allen, G. Dearnaley, N.E.W. Hartley, "Proc. Int. Conf. on Ion Beam Surface Anal." (Editors O. Meyer, G. Linker, F. Kappler) (1976) 901. Plenum Press.

(28) T.B. Pierce, P.F. Peck, D.R.A. Cuff, Nature 211 (1966) 66.

(29) B.K. Mak, I.R. Bird, T.M. Sabine, Nature 211 (1966) 738.

(30) J.A. Cookson, Nucl. Instr. Meth., 165 (1979) 477.

(31) W.M. Augustyniak, D. Betteridge, W.L. Brown, Nucl. Instr. Meth., 149 (1978) 669.

(32) M. Suter, H. Jung, W. Wolfi, G. Bonai, G. Stoller, "Annual Rep. of Lab. fur Kemphysik", E.T.H. Zurich (1974).

(33) P. Krejcik, J.C. Kelly, Nucl. Instr. Meth., 168 (1980) 247.

(34) R. Nobiling, K. Traxek, F. Bosch, Y. Civelekoglu, B. Martin, B. Povh, D. Schwalm, Nucl. Instr. Meth. 142 (1977) 49.

(35) R. Nobiling, Y. Civelekoglu, B. Povh, D. Schwalm, K. Traxel, Nucl. Instr. Meth., 130 (1975) 325.

(36) J.W. McMillan, "Analysis of Non-Metals in Metals", (Editor G. Kraft), (1981), Gruyter.

(37) R.N. Chanda, R.A. Deal, I.N. - 1261 (1970).

(38) G. White, "2nd I.S.P.R.A. Nucl. Electronic Symposium", Stresa, Italy (1975).

(39) C.P. Browne, W.W. Buechner, Rev. of Sci. Instr. 27 (1956) 899.

(40) J.B.A. England, "Techniques in Nucl. Structure Phys. Part 2" (1974) Chapter 4, MacMillan Press.

(41) E. Laesgaard, Nucl. Instr. Meth., 162 (1979) 93.

(42) N. Chu, J. Mayer, M.A. Nicolet, "Backscattering Spec." (1978) Academic Press.

(43) J.R. Bird, B.L. Campbell, P.B. Price, Atomic Energy Review, 12(2), (1974) 275.

(44) F. Bosch, A.E. Goresy, B. Martin, B. Povh, R. Nobiling, D. Schwalm, K. Traxel, Science, 199 (1978) 765.

(45) D. Brune, U. Lindh, J. Lorenzen, Nucl. Instr. Meth., 142 (1977) 51.

(46) J.A. Cookson, F.D. Pilling, A.E.R.E. R-6300 (1970).

(47) T.H. Zabel, M.P. Fewell, D.C. Kean, R.H. Spear, A.M. Baxter, Nucl. Instr. Meth., 174 (1980) 459.

(48) I.V. Mitchell, H.L. Eshback, Nucl. Instr. Meth., 149 (1978) 727.

(49) F. Abel, Journ. of Radioanal. Chem., 16 (1973) 567.

(50) R. Hart, H. Dunlap, A. Mohr, O. Marsh, Thin Solid Films, 19 (1973) 137.

(51) P. Muller, W. Szymczak, G. Ischenko, Nucl. Instr. Meth., 149 (1978) 239.

(52) G. Amsel, C. Cohen, A. L'hoir, "Proc. Int. Conf. Ion Beam Surface Layer Anal." (Eds. O. Meyer, G. Linker, F. Kappler),(1976) Plenum Press.

(53) I. Bergstrom, K. Bjorkqvist, B. Domeij, G. Fladda, Canad. Journal of Phys., 46 (1968) 2679.

(54) J.K. Hirvonen, G.K. Hubler, "Proc. Int. Conf. Ion Beam Surface Layer Anal.", (Eds. O. Meyer, G. Linker, F. Kappler) (1976) Plenum Press.

(55) M. Hage-Ali, P. Siffert, Nucl. Instr. Meth., 166 (1979) 412.

(56) R.E. Honig, W.L. Harrington, "Ion Beam Surface Layer Anal." (Eds. J.F. Ziegler, J.W. Mayer) (1975) Elsevier.

(57) T.M. Buck, "Meth. of Surface Anal." (Ed. A.W. Czandema) (1975) Elsevier.

(58) J.W. McMillan, P.M. Hirst, F.C.W. Pummery, J. Huddleston, T.B. Pierce, Nucl. Instr. Meth., 149 (1978) 83.

(59) G. Deconninck, G. Demortier, "Nucl. Techniq. in Basic Metal Inds." Proc. of an I.A.E.A. Symp. Vienna (1973) 573.

(60) C. Olivier, M. Peisach, Journ. of Radioanal. Chem., 5 (1970) 391.

(61) C. Olivier, M. Peisach, Journ. of Radioanal. Chem., 11 (1972) 105.

(62) F. Folkmann, J. Phys. E8 (1975) 429.

(63) E. Rutherford, Phil. Mag., 21 (1911) 669.

(64) J.F. Ziegler, R.F. Lever, Thin Solid Films, 19 (1973) 291.

(65) J.F. Ziegler, R.F. Lever, J.K. Hirvonen, I.B.M. RC-5619 (1975).

(66) J.K. Hirvonen, G.K. Hubler, "Proc. Int. Conf. on Ion Beam Surf. Layer Anal." (Eds. O. Meyer, G. Linker, F. Kappler) V.I. (1976) Plenum Press.

(67) T. Lauritsen, F. Ajzenberg-Selove, Nucl. Phys., 78 (1966) 1.

(68) J.B. Marion, F.C. Young, "Nucl. React. Anal. Graphs and Tables", (1968) North Holland.

(69) Landolt-Bornstein, "Nucl.Data and Functional Relationships in Sci. and Tech." New Series I/V56 (1973) Springer Verlag.

(70) D. Brune, J.J. Schmidt, (Eds.) "Handbook on Nucl. Act. Cross-Section Technical Report Series", 156, I.A.E.A., Vienna (1974).

(71) J.F. Ziegler (Ed.) "New uses of Ion Accelerators" (1975), Plenum Press.

(72) R.E. Shroy, H.W. Kramer, K.W. Jones, Nucl. Instr. Meth., 149 (1978) 313.

(73) B.J. Seigel, D.R. Beaman, "Phy. Aspects of Electron Microscopy and Microbeam Anal." (1975) Wiley & Sons.

(74) J.A. Cookson, F.D. Pilling, Phys. Med. Biol., 21 (1976) 965.

(75) G. Kraft, H.W. Daves, B. Fisher, U. Kopf, H. P. Liebold, D. Quis, H. Stelzer, J. Kiefer, F. Schofer, E. Schnieder, U. Weber, H. Wulf, H. Dertinger, Nucl. Instr. Meth., 168 (1980) 175.

(76) J.R. Morris, Ph.D Thesis, Lancaster University (1978).

(77) J.F. Ziegler, W.K. Chu, Atom. & Nucl. Dat. Tab., 13 (1973) 463.

(78) P.M. Hirst, J.W. McMillan, D.J. Malcolme-Lawes, Nucl. Instr. Meth., 168 (1980) 203.

(79) E. Ricci, Anal. Chem., V43 No. 13 (1971) 1866.

(80) D.A. Close, A.E. Evans, J.J. Malanify, C.J. Umbarger, LA-DC-72 (1971) 1414.

(81) D.A. Close, J.J. Malanify, C.J. Umbarger, Nucl. Instr. Meth., 113 (1973) 561.

(82) E. Ricci, Nucl. Instr. Meth., 94 (1971) 565.

(83) E. Ricci, J. Radioanal. Chem., 9 (1971) 273.

(84) C. Engelmann, M. Loevillet, I.E.E.E. Trans. on Nucl. Sci., VNS-26, 1 (1979) 1539.

(85) S. Fiarman, G. Schneier, Enviro. Sci. & Tech., 6 (1972) 79.

(86) W.S. Lyon (Ed.), ORNL-4636 (1971) 25.

(87) C. Engelmann, "Nucl. Activ. Techniq. in Life Sciences", I.A.E.A. Vienna (1978) 47.

(88) G. Cabane, C. Engelmann, Revue de Phys, Appliq., 3 (1968) 365.

(89) M. Peisach, Chem. Communic., 18 (1966) 632.

(90) M. Peisach, E.U.R. 3896 d-f-e (1968) 65.

(91) M. Peisach, R. Pretorius, P.J. Strebel, Anal. Chem., 40 (1968) 850.

(92) E. Ramstrom, T. Wielding, Nucl. Phy., A272 (1976) 259.

(93) E. Everling, L. Koenig, J. Mattauch, H. Wopstra (Eds.), "Nucl. Data Tables, Part 1 (1960) 24,27. U.S. Gov. Printing Office, Washington.

(94) F.C.W. Pummery, J.W. McMillan, Nucl. Instr. Meth., 168 (1980) 181.

(95) P.H. Liebenauer, Thesis, Univ. Microfilm No. 70-25888 (1970).

(96) S.K. Datta, G.P.A. Berg, P.A. Quinn, Nucl. Phy., A312 (1978) 1.

(97) T.B. Pierce, P.F. Peck, Proc. S.A.C. Conf., Nottingham (1965) 159, W. Heffer and Sons Ltd.

(98) Hsin-Min Kuan, T.W. Bonner, J.R. Risser, Nucl. Phy., 51 (1964) 481.

(99) N.G. Puttaswamy, Thesis, Stanford University (1966).

(100) C. Engelmann, "Uses of Cyclotrons in Chem., Metal and Biol." (1970) 328. Butterworths.

(101) E. Ricci, R. Hahn, E.U.R. 3896 d-f-e (1968) 15.

(102) G. Deconninck, G. Demortier, "Nucl. Techn. in Basic Metal. Ind." I.A.E.A. Vienna (1973) 573.

(103) T.B. Pierce, E.U.R. 2957 (1966) 47.

(104) D. Bromley, E. Almqvist, Rep. on Prog. in Phys., XXIII (1960) 544.

(105) R.E. Kaim, D.W. Palmer, J. Radioanal. Chem. 48 (1979) 295.

(106) J.B. Marion, J.L. Fowler, "Fast Neutron Phys." VI (1960) 102, New York, Interscience.

(107) M.J. Bennett, M.R. Houlton, J.W. McMillan, C.F. Knights, R.M. Haves, F.C.W. Pummery, Oxidation of Metals, V15, N3/4 (1981) 231.

(108) J. Huddleston, I.G. Hutchinson, T.B. Pierce, A.E.R.E. - R9457 (1980).

(109) W.B. Jepson, J.E. Antill, J.B. Warburton, Brit. Journ. of Corrosion 1 (1965) 15.

(110) J.E. Antill, K.A. Peakall, J.B. Warburton, "Proc. Int. Conf. on Corrosion", B.N.E.S., July (1979) 187.

(111) G.W. Hollenberg, H.E.D.L. - SA - 1164 (1977).

(112) J.C. McGuire, T.A. Renner, Atomic Energy Review, V16, N4 (1978) 657.

(113) C.C. Miles, S. Wexber, E.R. Ebersole, A.N.L. - 8107 (1974).

(114) C. Olivier, M. Peisach, J. Radioanal. Chem., 12 (1972) 313.

(115) G. Harbottle, A.G. Maddock, "Chemical Effects in Nuclear Transformations in Inorganic Systems", (1979), North Holland Press.

(116) H.J. Emeleus, A.G. Maddock, "Radiochem. Inorganic Chem." Series 2V8 Chapter 6 (1978) Butterworths, University Park Press.

(117) L.C. Northcliffe and R.F. Schilling, Nucl. Data. Tables, V7A, No. 3 and 4 (1970).

(118) H.H. Anderson, J.F. Ziegler, "The Stopping Powers and Ranges of Ions in Matter" V3 and V4 (1977) Pergamon.

(119) J.W. McMillan, S.J. Firkin, Chem. Div., A.E.R.E. Harwell, Private Communication (1981).

(120) R.S. Russell, J. Sanderson, Expt. Bot. 18 (1967) 491.

(121) D.T. Clarkson, J. Sanderson, Agricultural Research Council, Letcombe Laboratory Annual Report 1970 (1971) 16.

(122) C. Olivier, J.W. McMillan, T.B. Pierce, Nucl. Instr. Meth., 124 (1975) 289.

(123) B. Sundqvist, L. Gonczi, R. Bergman, U. Lindh, Int. Journ. of App. Radiation and Isot., 25 (1974) 277 and 27 (1976) 273.

(124) B. Sundqvist, L. Gonczi, R. Bergman, U. Lindh, I.B. Koersner, "Proc. Int. Conf. on Ion Beam Surface Anal." (Eds. O. Meyer, G. Linker, F. Kappler) (1976) Plenum Press.

(125) L. Gonczi, H. Berggen, R. Didriksson, B. Sundqvist, U. Lindh, Nucl. Instr. Meth., 149 (1978) 337.

(126) B.V. King, J.C. Kelly, J.R. Bird, "2nd Australian Conf. Nucl. Techniq. of Anal." (1978) 45.

(127) C. Engelmann, I.A.E.A. - SM - 227/92 (1979) 47.

(128) I. Golicheff, M. Loeuillet, C. Engelmann, J. Radioanal. Chem., 12 (1972) 233.

(129) A.C. Xenoulis, C.E. Douka, J. Radioanal. Chem., 54 (1979) 205.

(130) J.J. Malanify, D.A. Close, Nucl. Instr. Meth., 118 (1974) 293.

(131) N.S. Chen, J.H. Fremlin, Radiochem. Radioanal. Lett., 4 (1970) 365.

(132) F. Bodart, G. Deconninck, J. Mengeot, I.A.E.A. - SM - 227/98.

(133) C. Olivier, "Proc. 19th Nucl. and Atomic Act. Anal. Conf." Gatlinburg, Tennesse (1975) 71.

(134) K.G. Standing, D.A. Dohan, "Application of Small Acc." Denton (1975) 76CH1175-9NPS, 549.

(135) S. Matsumoto, Y. Hashimoto, H. Yamashito, I. Yamane, Nucl. Instr. Meth., 174 (1980) 189.

(136) L. Andras, A. Balint, A. Csoke, A.Z. Nagy, KFKI-1978-38.

(137) D.E. Wood, "Activ. Anal. with 14 MeV Neutron Gen.", Advances in Activ. Anal. 2, (1972) Academic Press.

(138) D.A. Dohan, K.G. Standing, Cereal Chem., 53 (1976) 91.

(139) J.W. McMillan, F.C.W. Pummery, Journal of Radioanal. Chem. V38 (1977) 51.

(140) A. Sakai, K. Otsuka, Plant Physiol., 42 (1967) 1680.

(141) H.T. Meryman, Science, 124 (1956) 515.

(142) J. Sanderson, Journ. of Microscopy, 96 (1972) 245.

(143) A. Chevarier, N. Chevarier, S. Chiodelli, Nucl. Instr. Meth. 189 (2,3) (1981) 525.

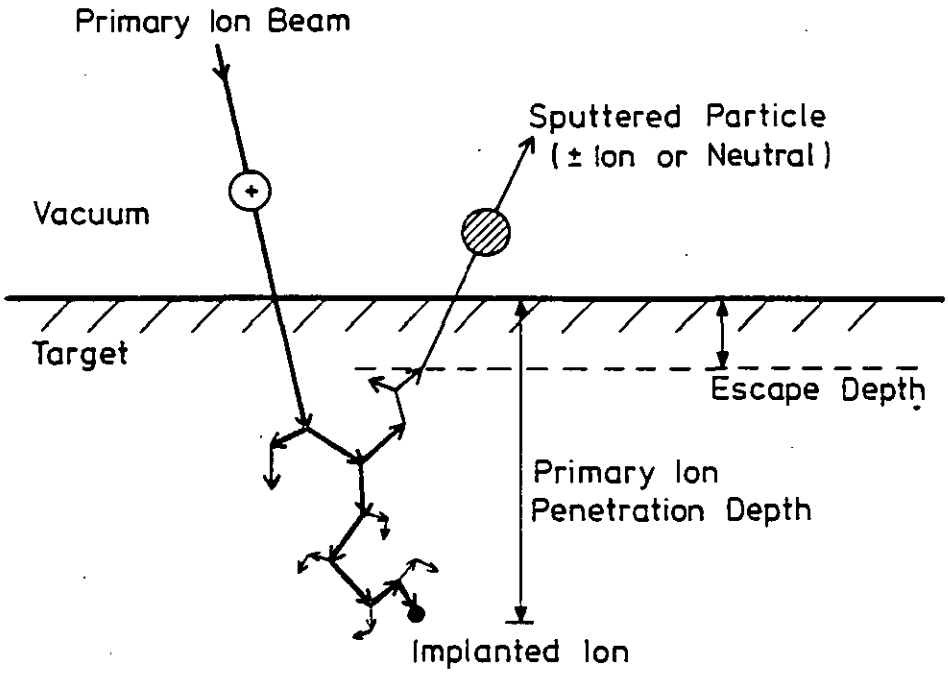

FIG. 1·1 SCHEMATIC REPRESENTATION OF THE COLLISION CASCADE PROCESS OF ENERGY LOSS AND ION EJECTION INVOLVED IN THE ION SPUTTERING.

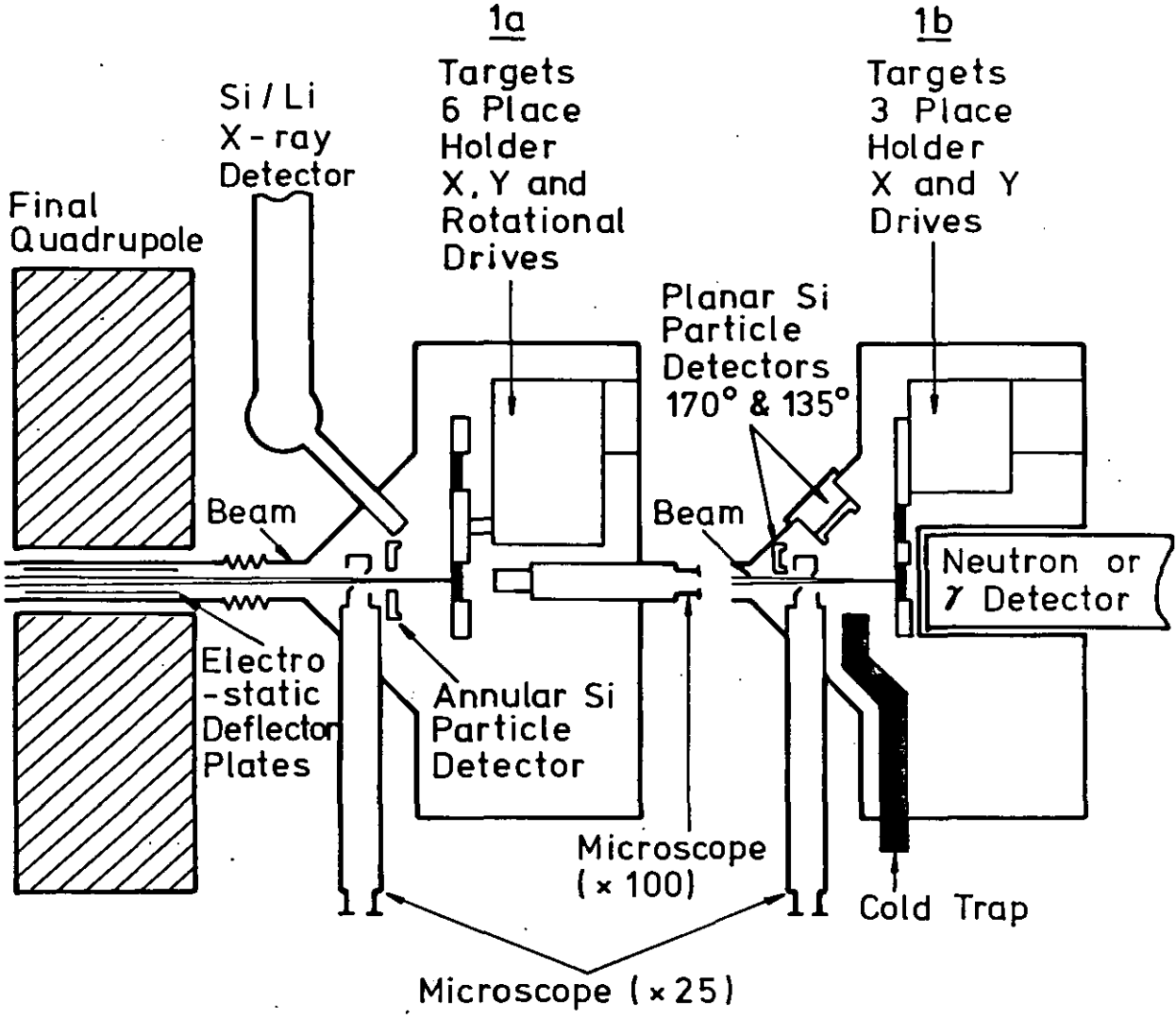

FIG. 2·1 DIAGRAM OF THE NUCLEAR MICROPROBE CHAMBER FACILITIES.

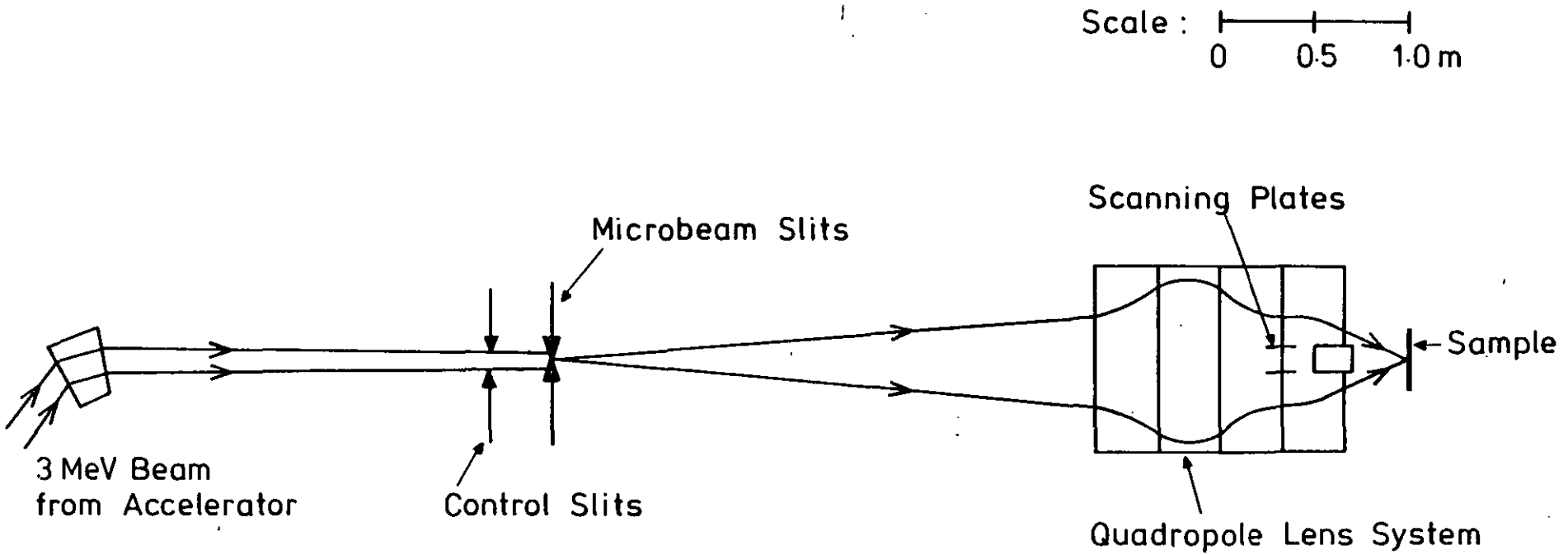

FIG. 2·2 SCHEMATIC REPRESENTATION OF THE FOCUSSING MICROBEAM SYSTEM [25]

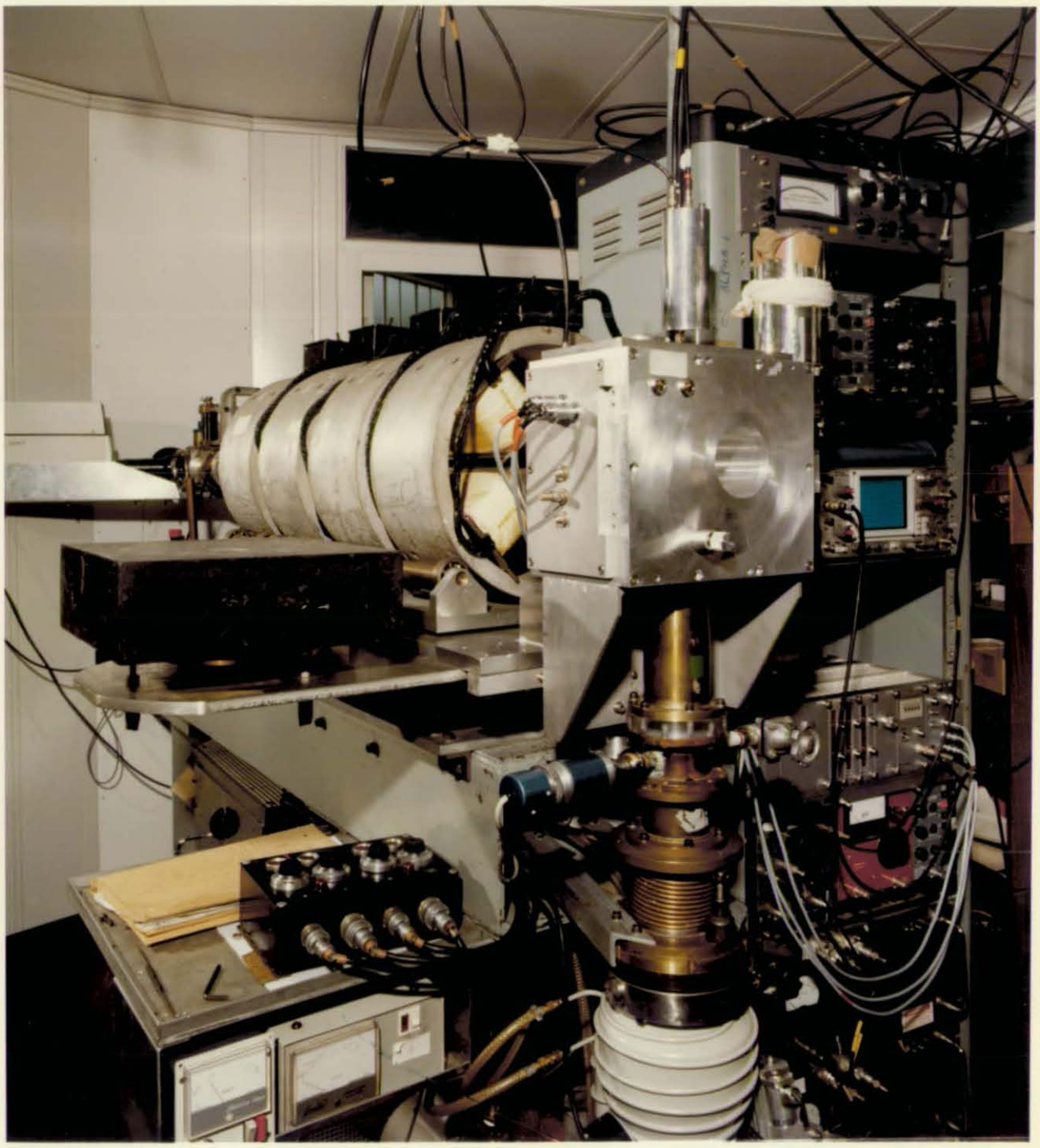

Figure 2.3. General view of the nuclear microprobe showing the quadropole magnets and chamber.

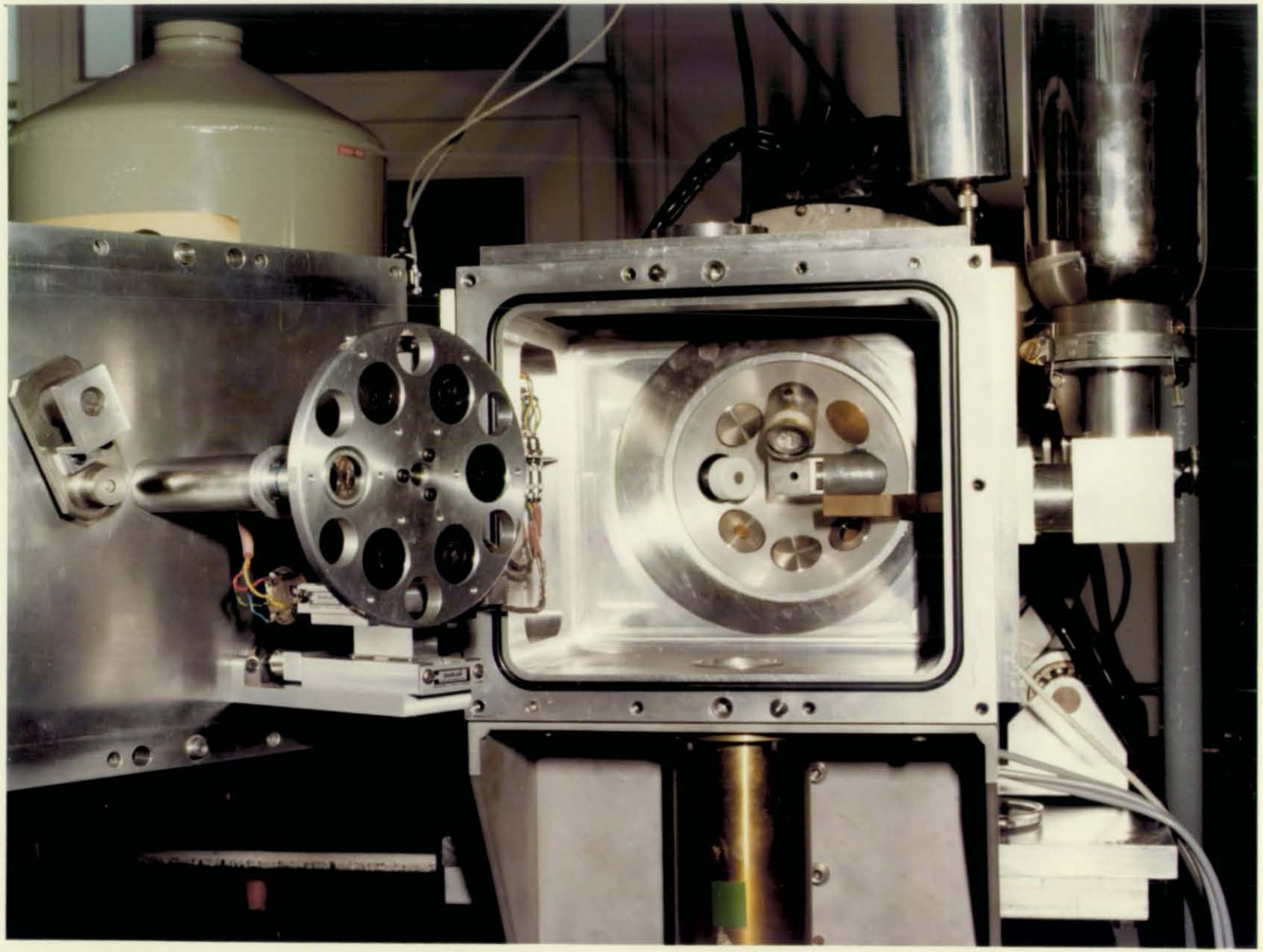

Figure 2.4. Detailed view of the chamber facilities used for charged particle and X-ray analysis.

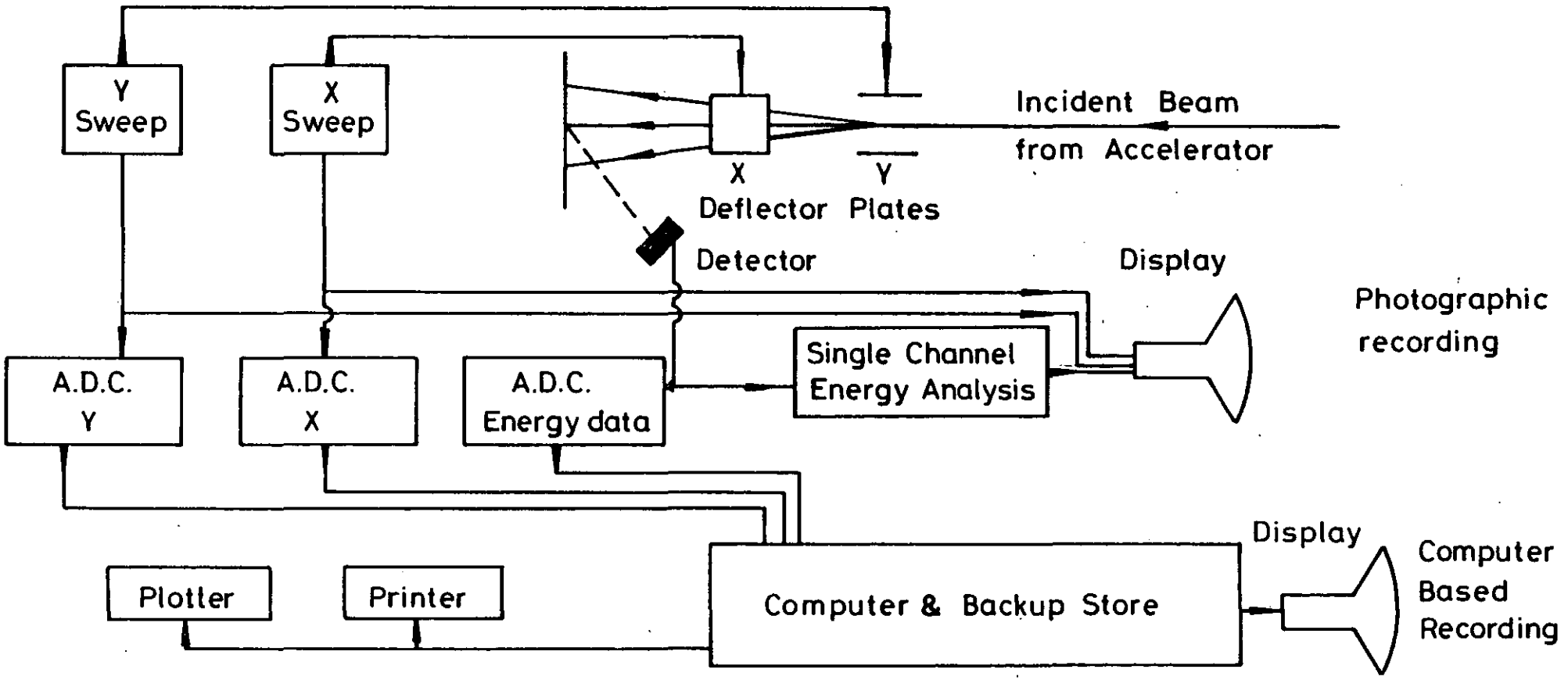

FIG. 2·5 TWO DIMENSIONAL 'RASTER-SCANNING' AND DATA COLLECTION.

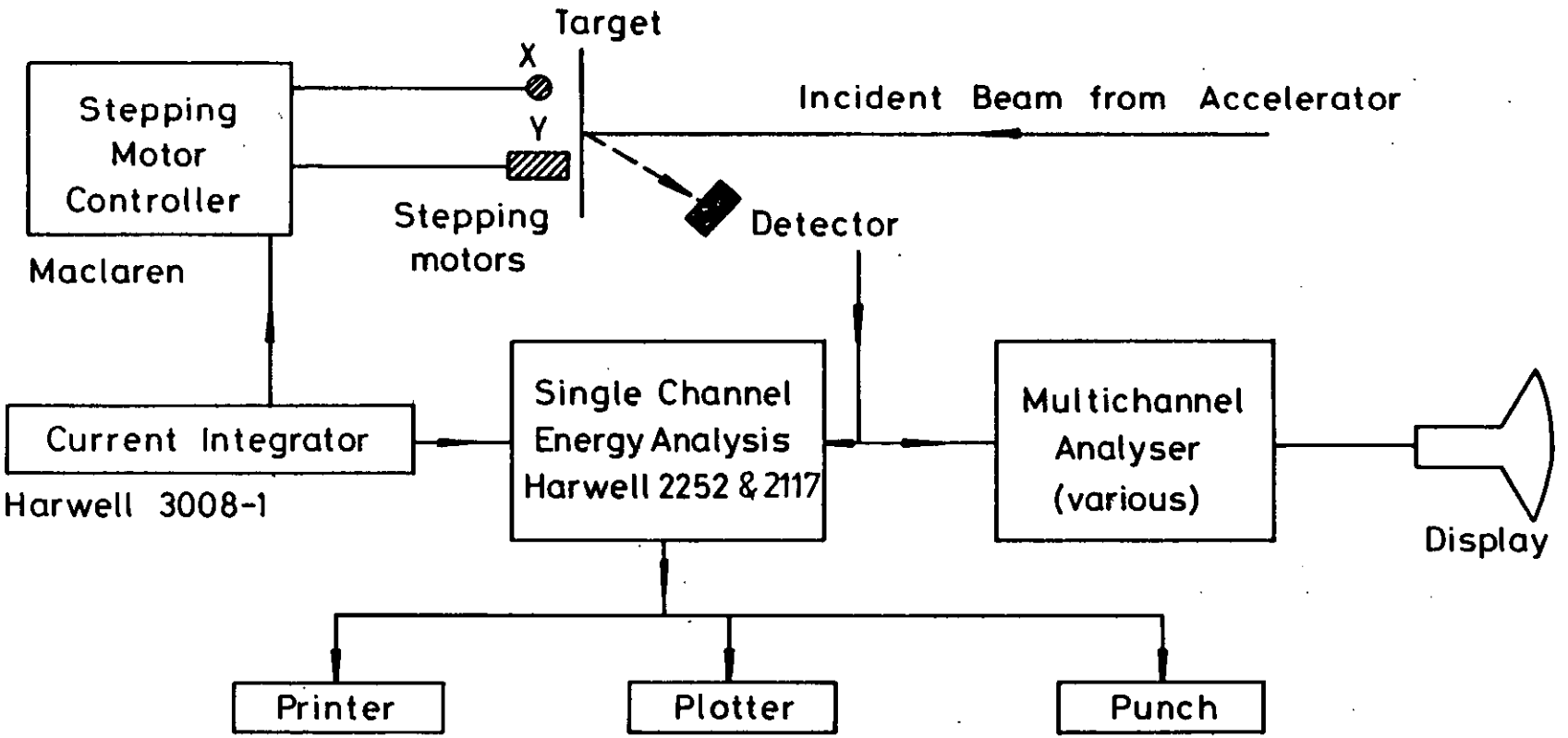

FIG. 2·6 THE MECHANICAL SCANNING AND DATA COLLECTION.

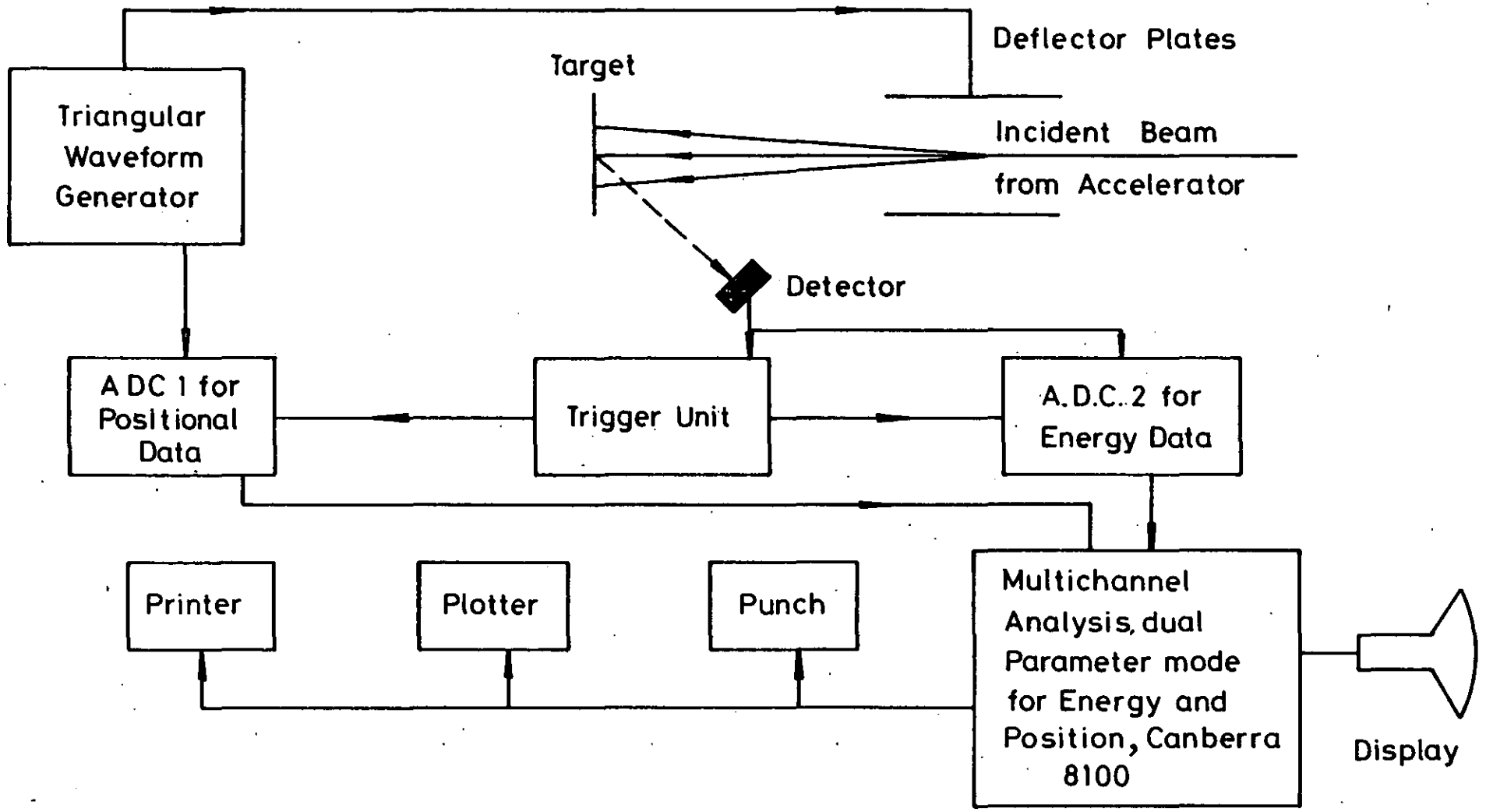

FIG 2·7 LINEAR ELECTROSTATIC SCANNING AND DATA COLLECTION.

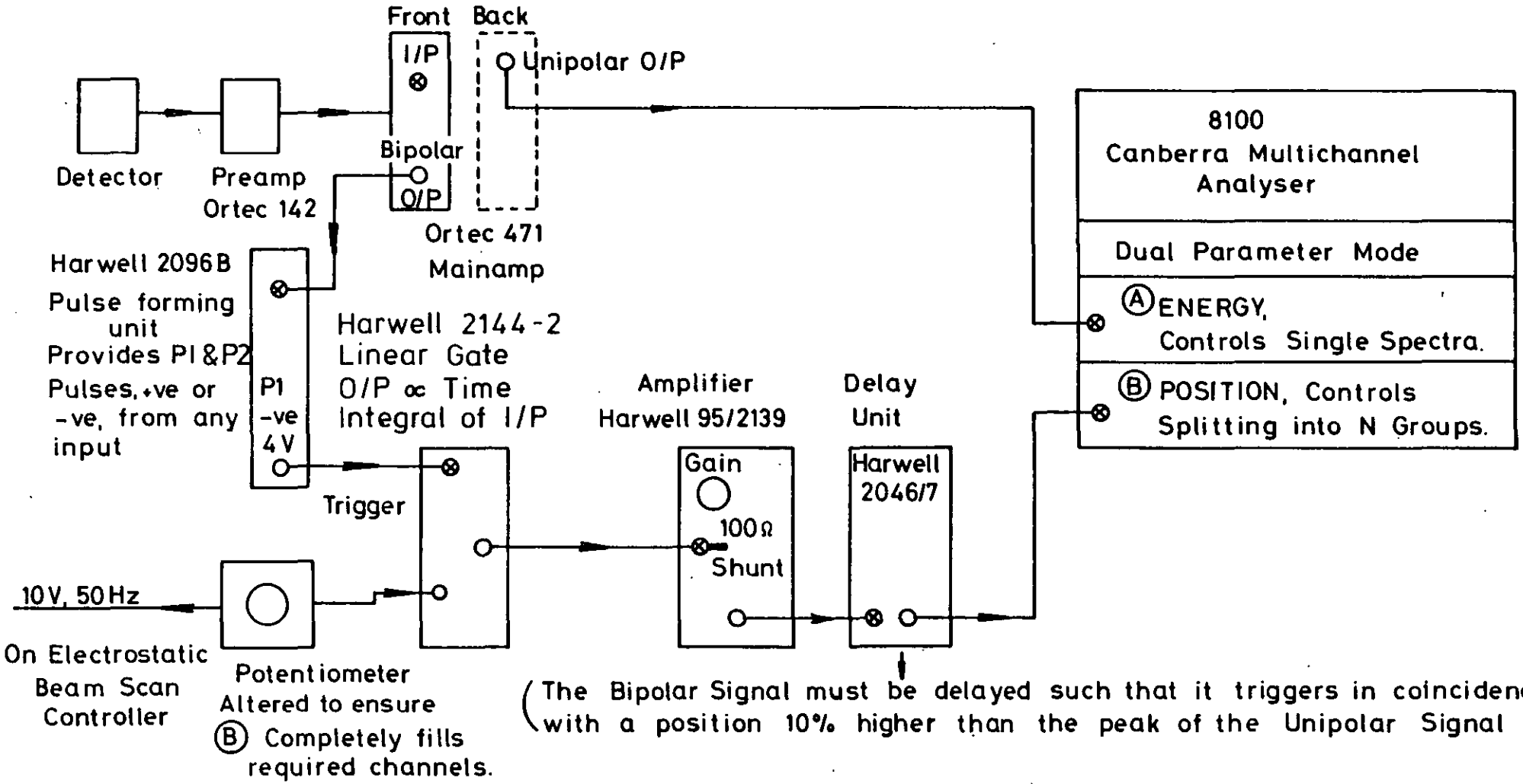

FIG. 2·8 SCHEMATIC DIAGRAM OF THE ELECTRONICS USED FOR DUAL PARAMETER (Energy & Position) SCANNING DATA COLLECTION.

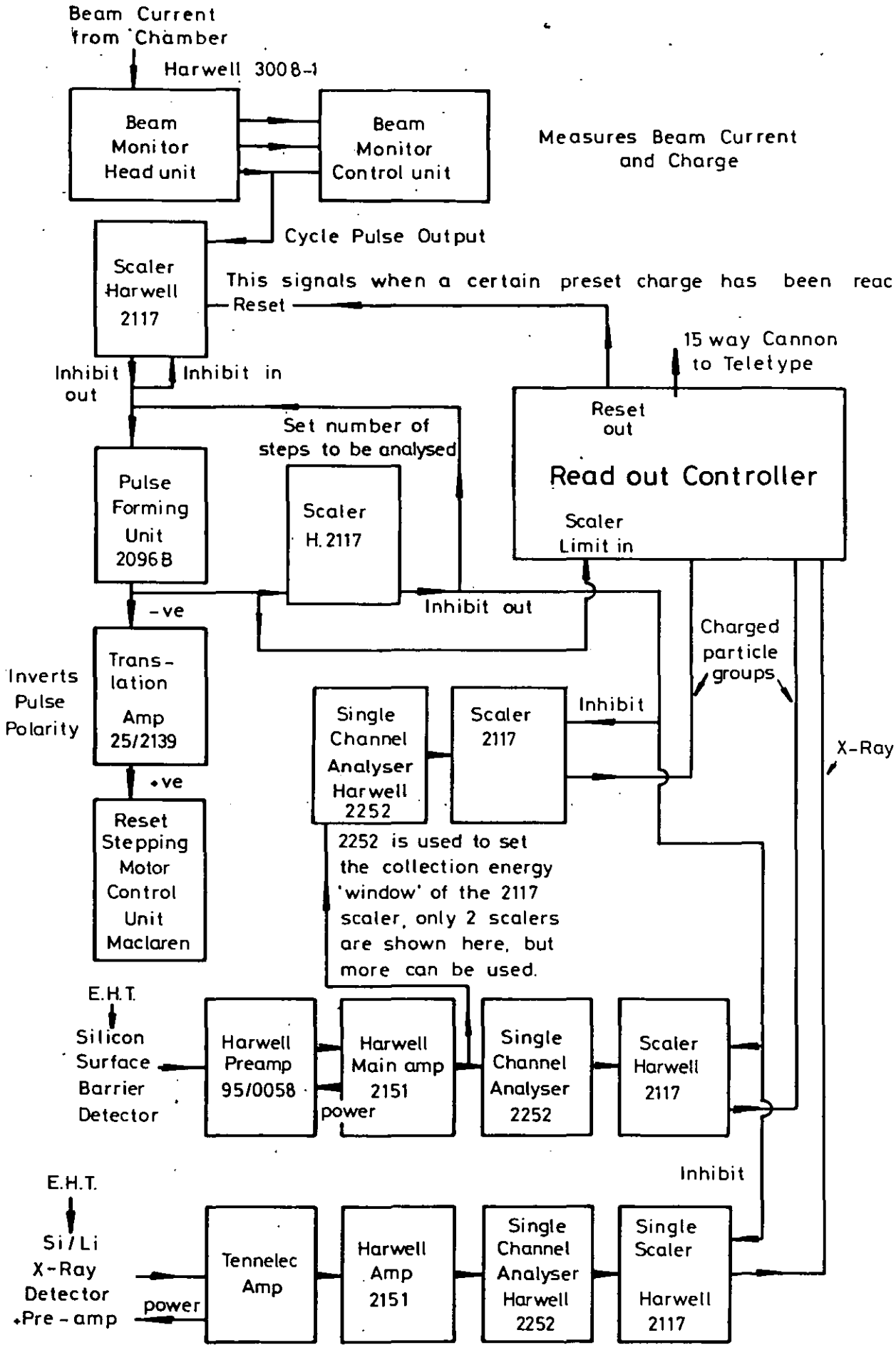

FIG. 2·9. EXISTING DATA COLLECTION SYSTEM USING SILICON SURFACE BARRIER AND X-RAY DETECTORS

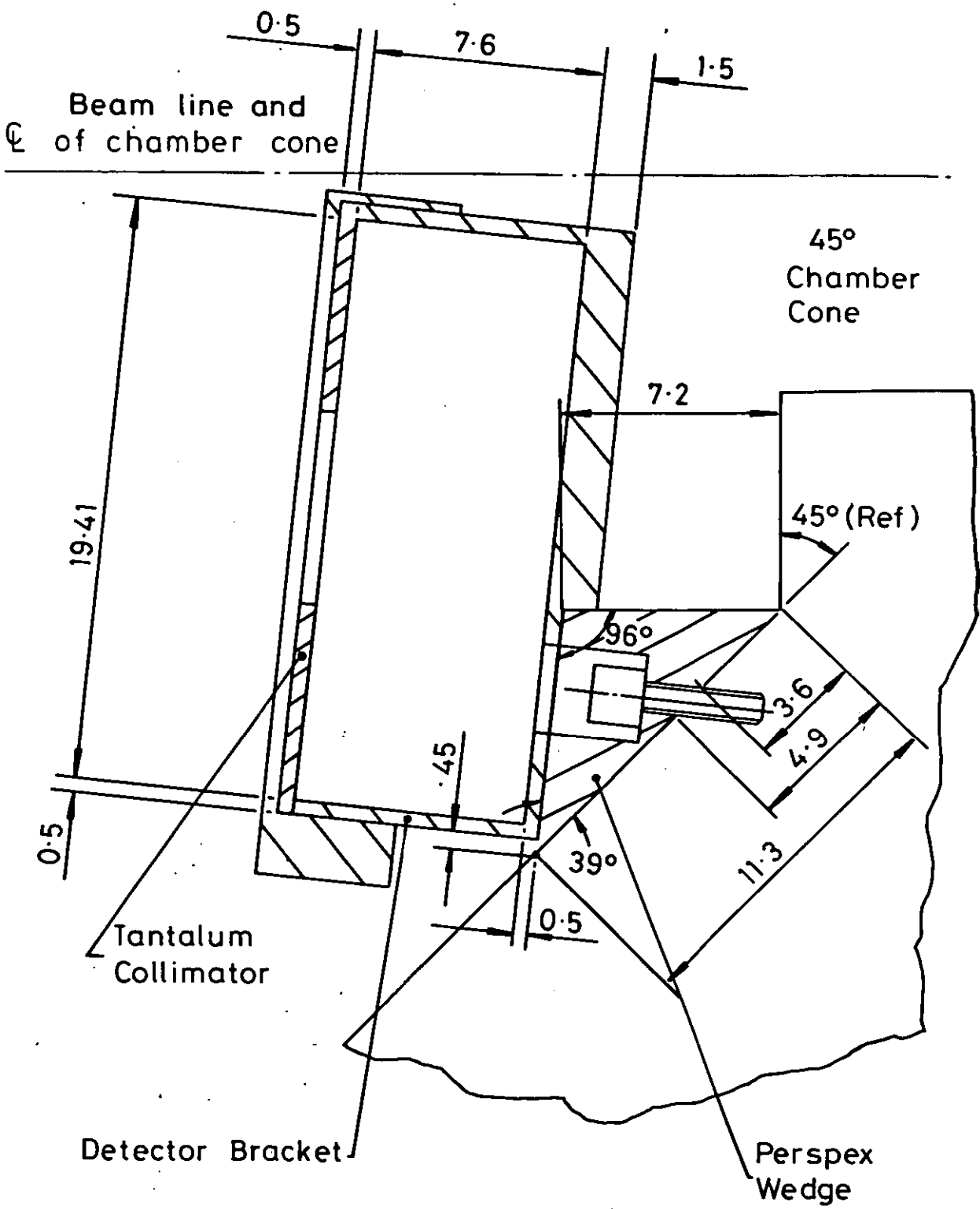

FIG. 2·10 SECTIONAL VIEW OF DETECTOR HOLDER AND COLLIMATOR ASSEMBLY IN HORIZONTAL PLANE OF THE BEAM.

0 1 2 3 4 5 6 7 8 9 10

Scale in millimetres

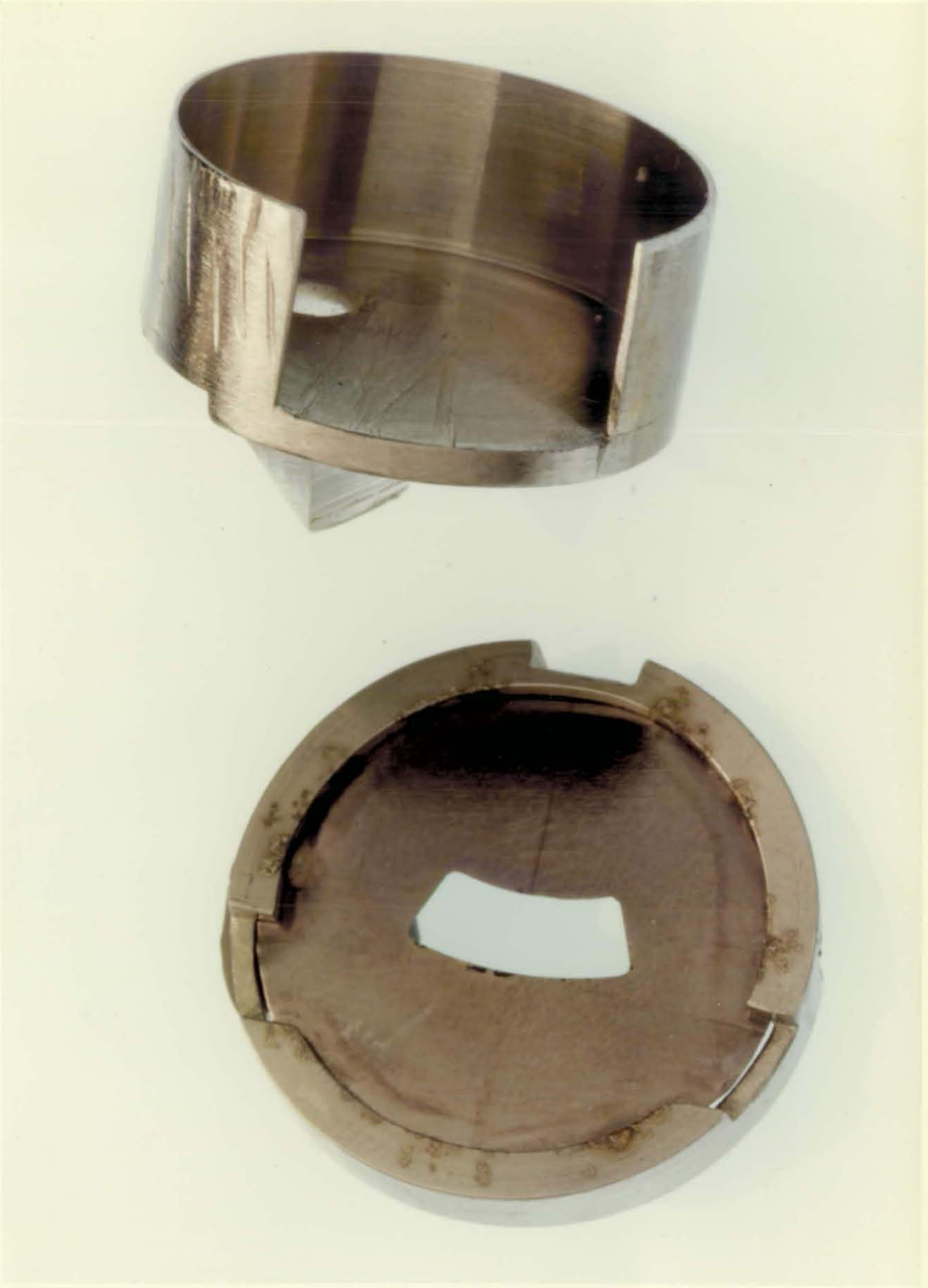

Figure 2.11. Magnified view of detector holder (O.D. = 20.4 mm) and collimator assembly used in backscattering analysis.

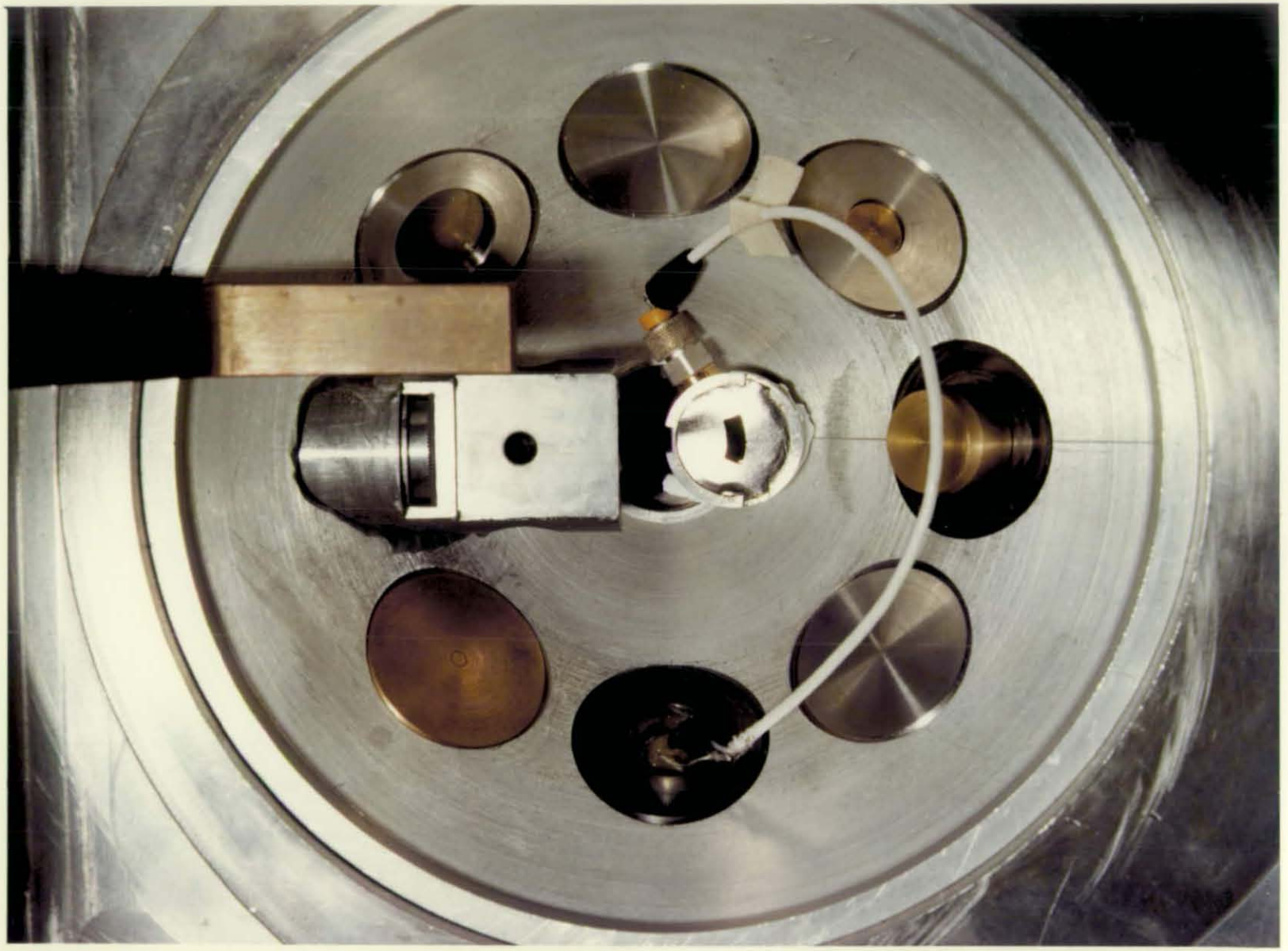

Figure 2.12. View of the chamber cone showing the position of the detector holder and collimator assembly used in backscattering analysis.

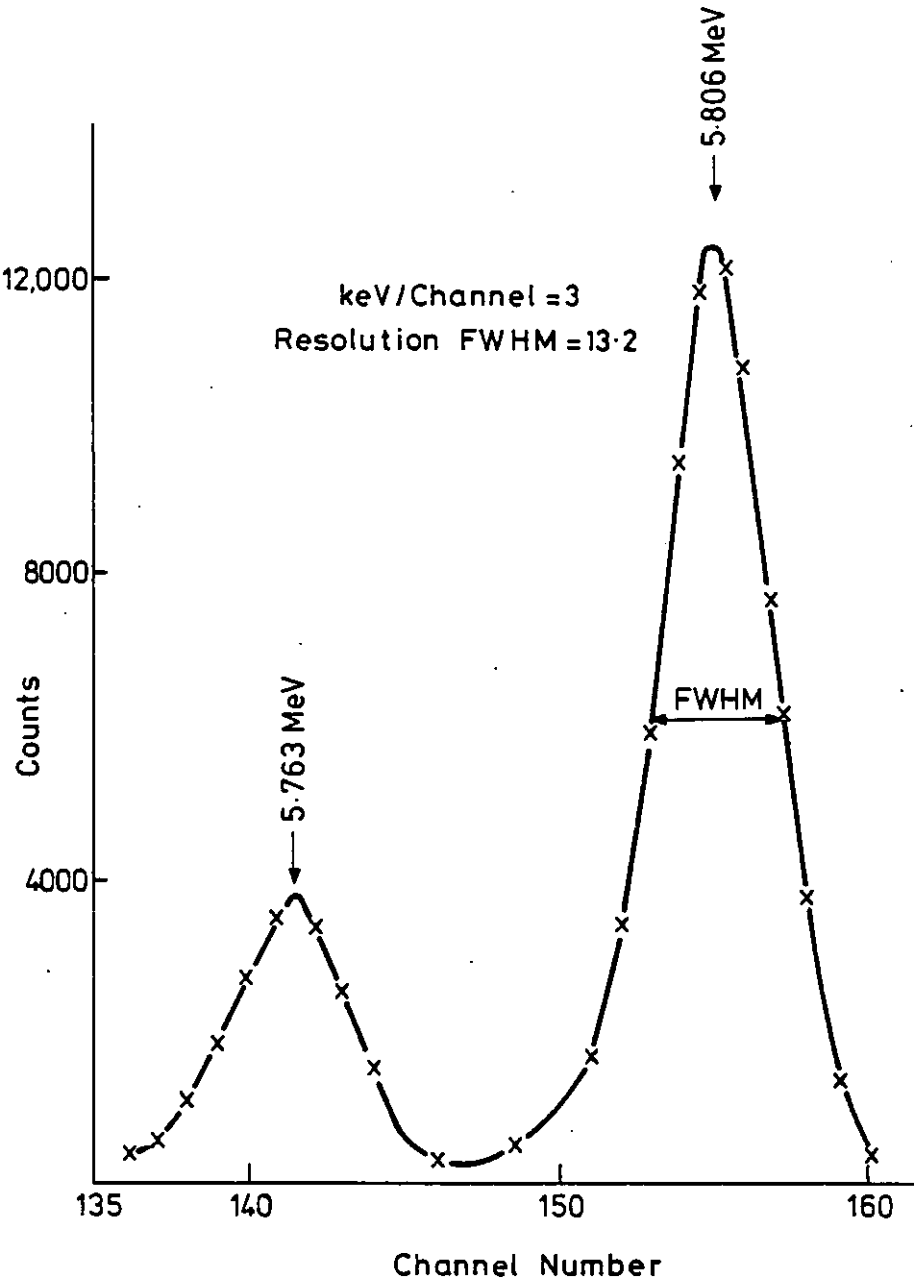

FIG. 2·13 ENERGY CALIBRATION USING A CM-244 SOURCE.

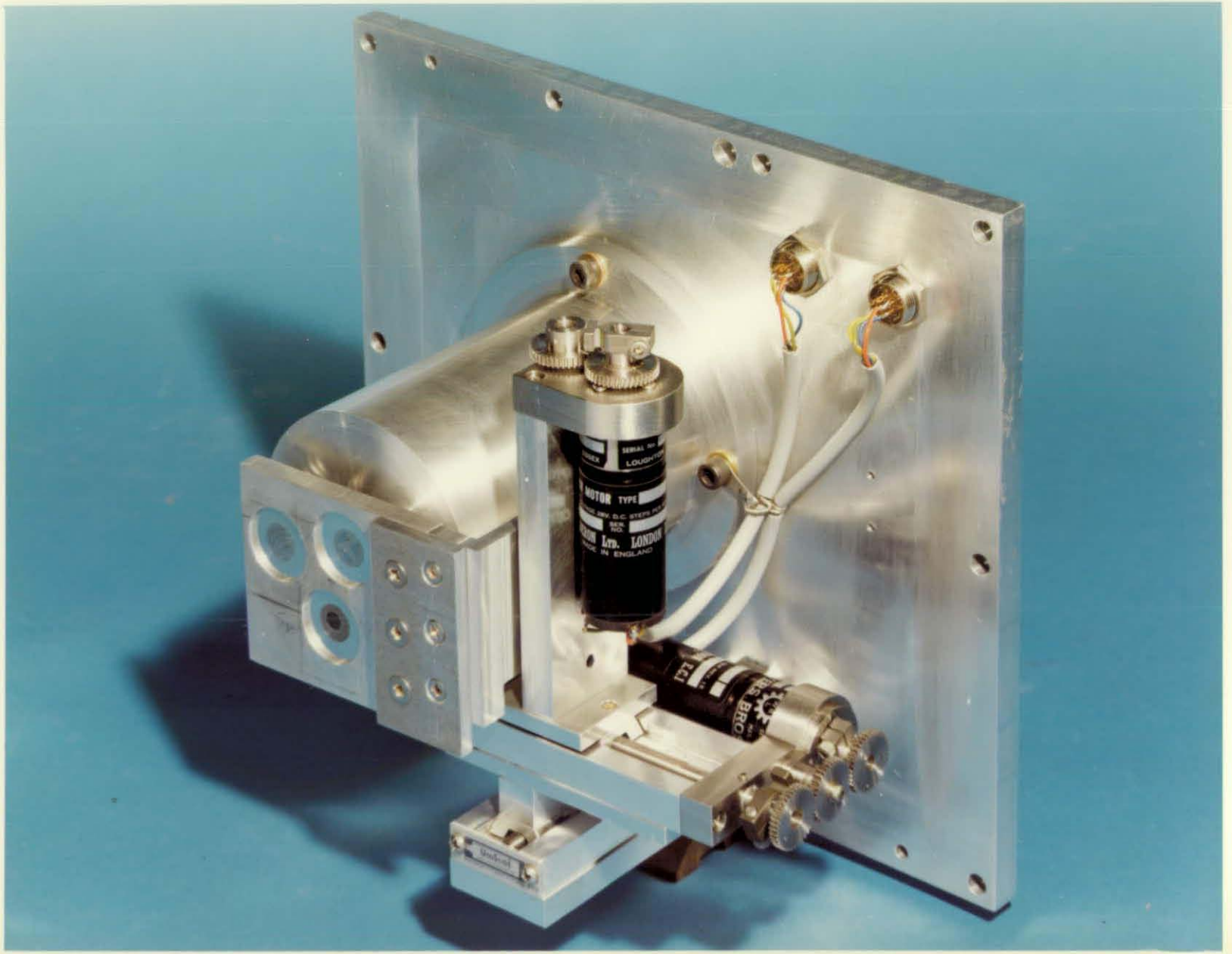

Figure 2.14. The modified backplate, sample holder and motion used in X-ray and neutron detection.

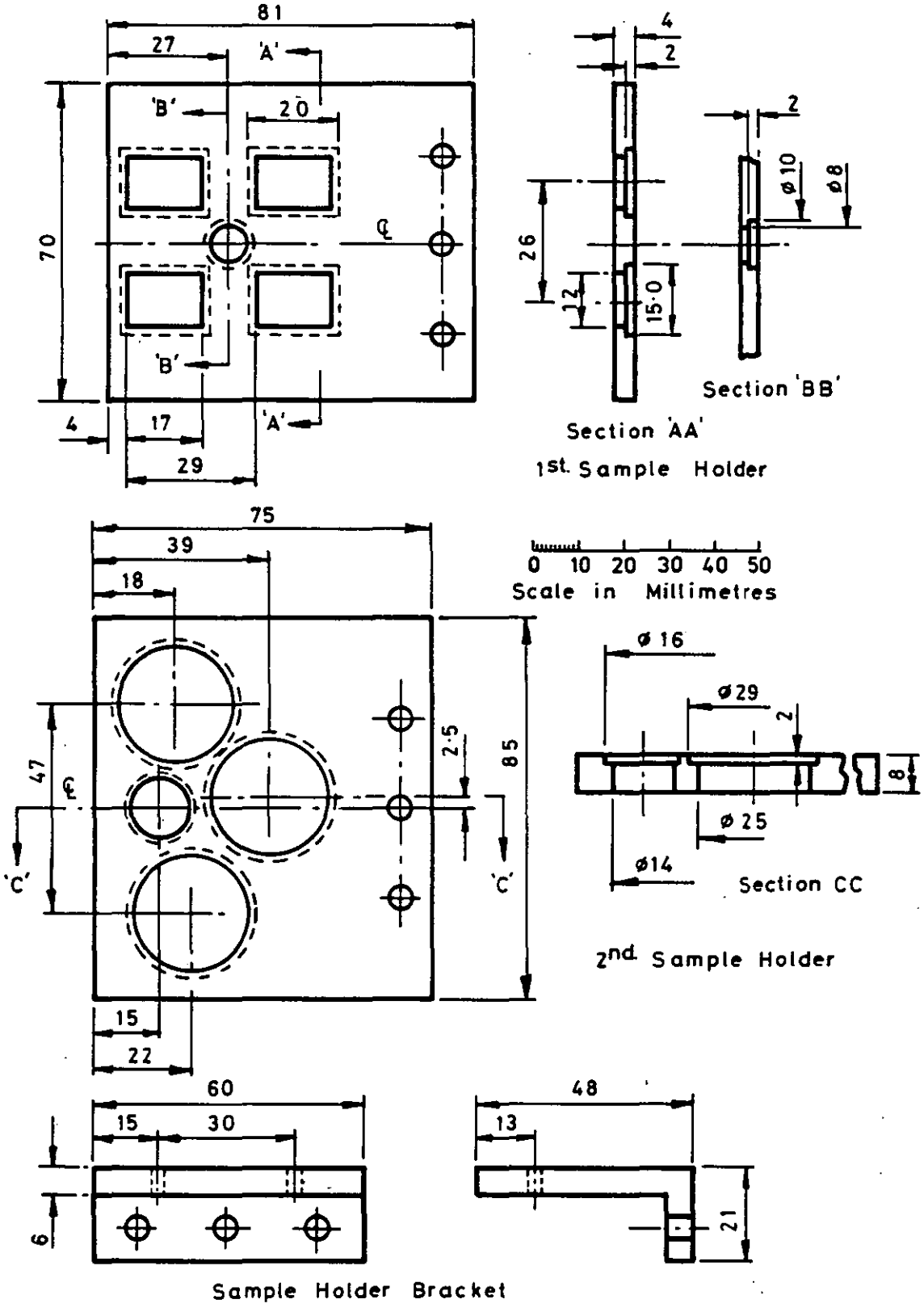

FIG. 2·15. SAMPLE HOLDERS AND BRACKETS USED TO MOUNT VARIOUS TYPES OF SAMPLES IN THE NUCLEAR MICROPROBE CHAMBER MODIFIED FOR X-RAY AND NEUTRON DETECTION.

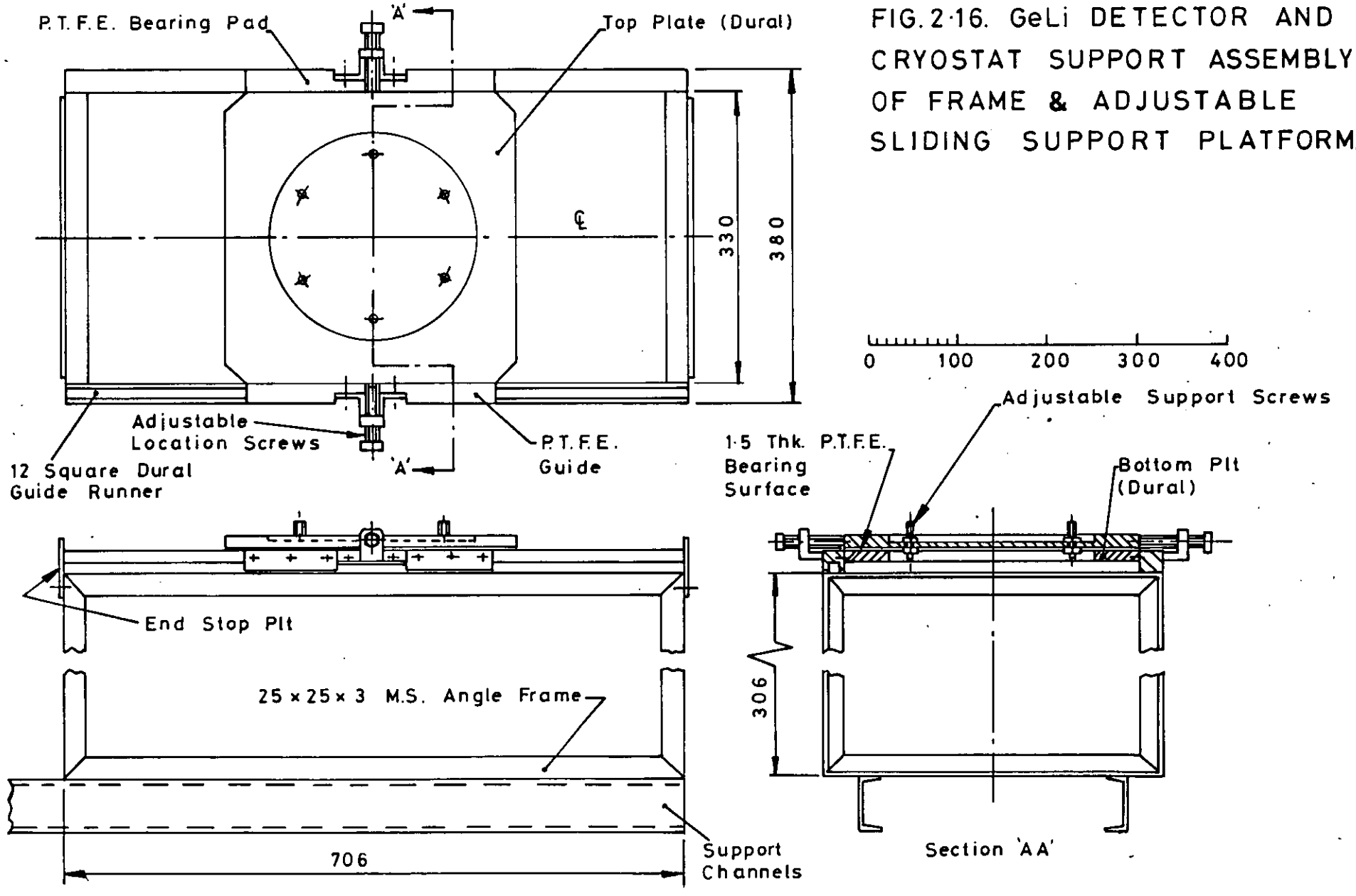

FIG. 2·16. GeLi DETECTOR AND CRYOSTAT SUPPORT ASSEMBLY OF FRAME & ADJUSTABLE SLIDING SUPPORT PLATFORM.

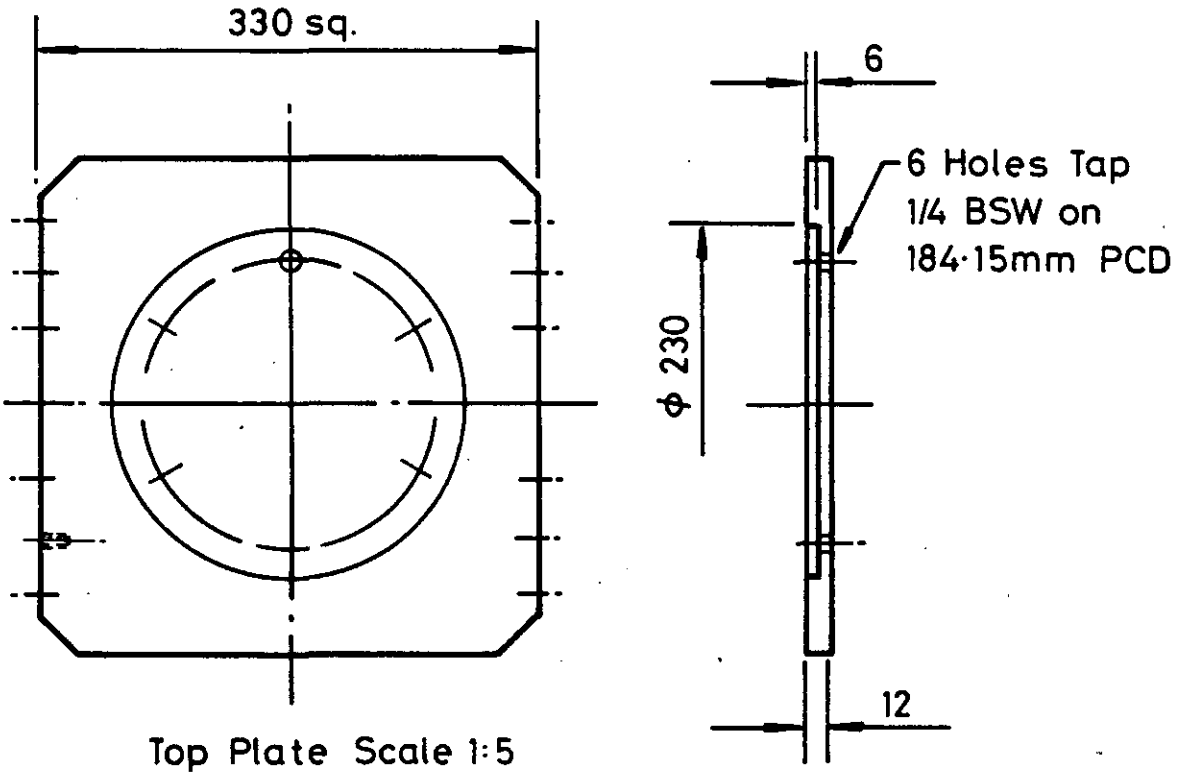

FIG. 2·17 DETAIL OF PLATES SHOWN IN FIG. 2·16

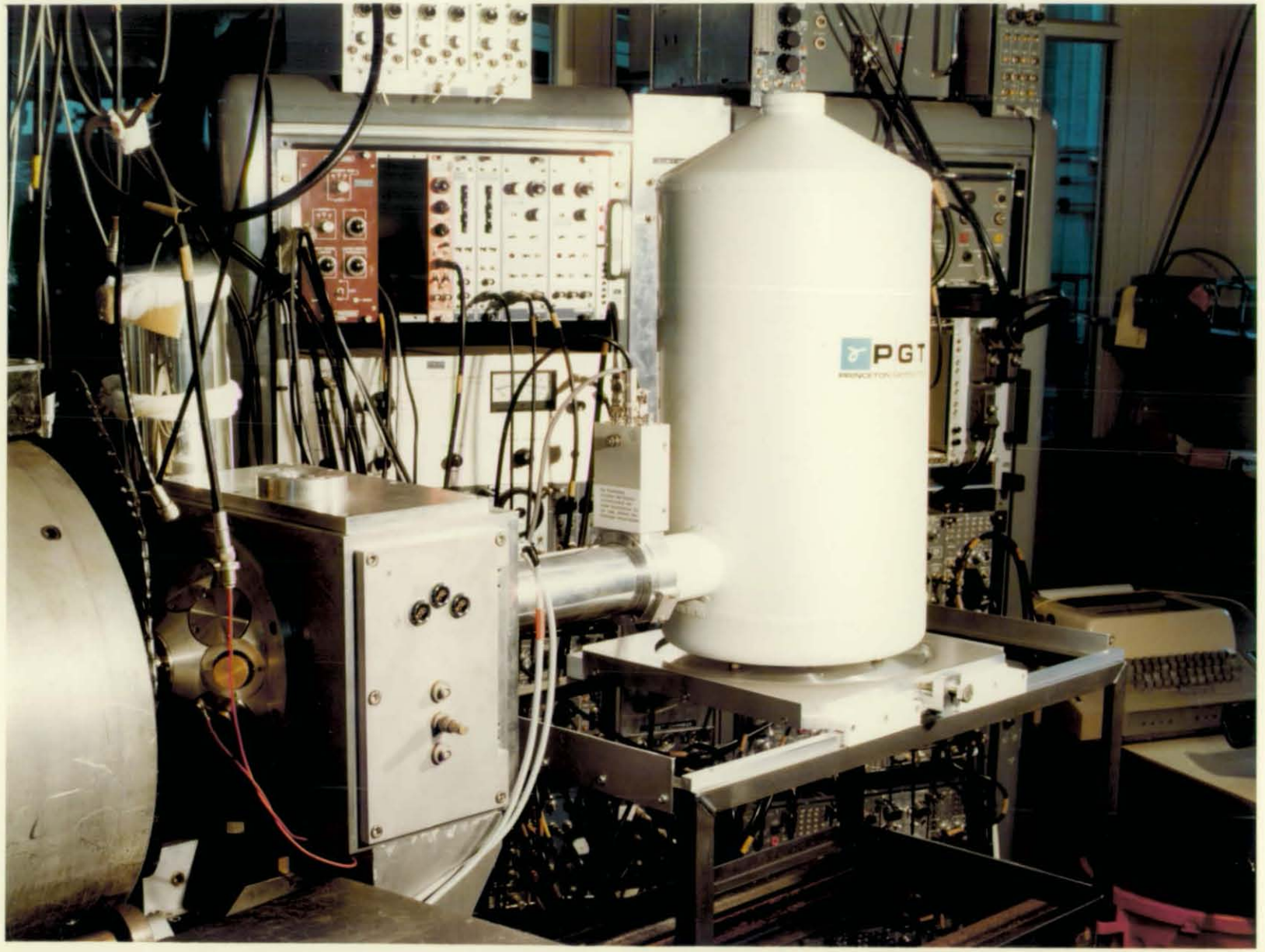

Figure 2.18. General view of the GeLi detector and cryostat support assembly.

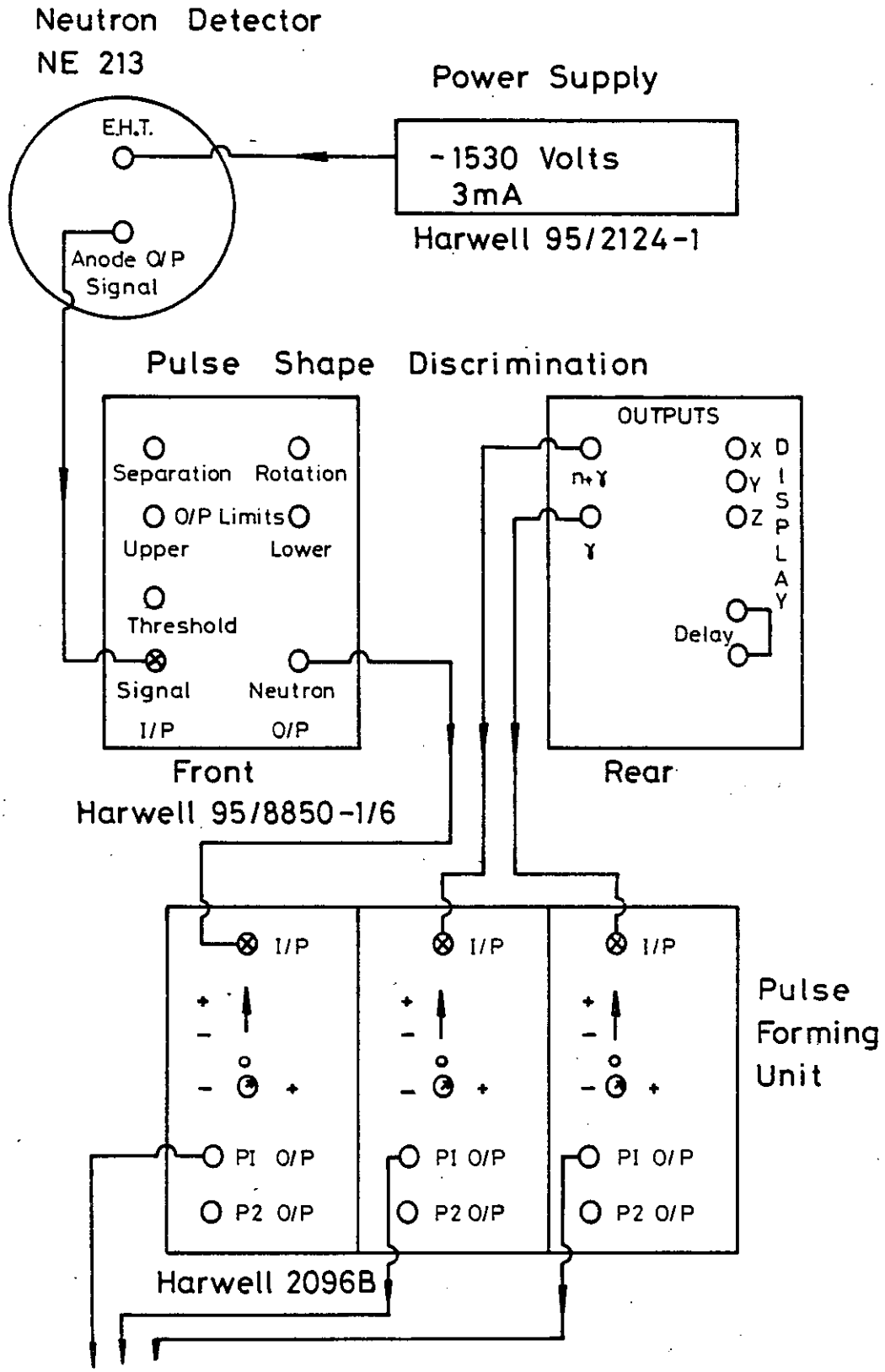

FIG. 2·19 ELECTRONIC DIAGRAM FOR THE NEUTRON DETECTION SYSTEM.

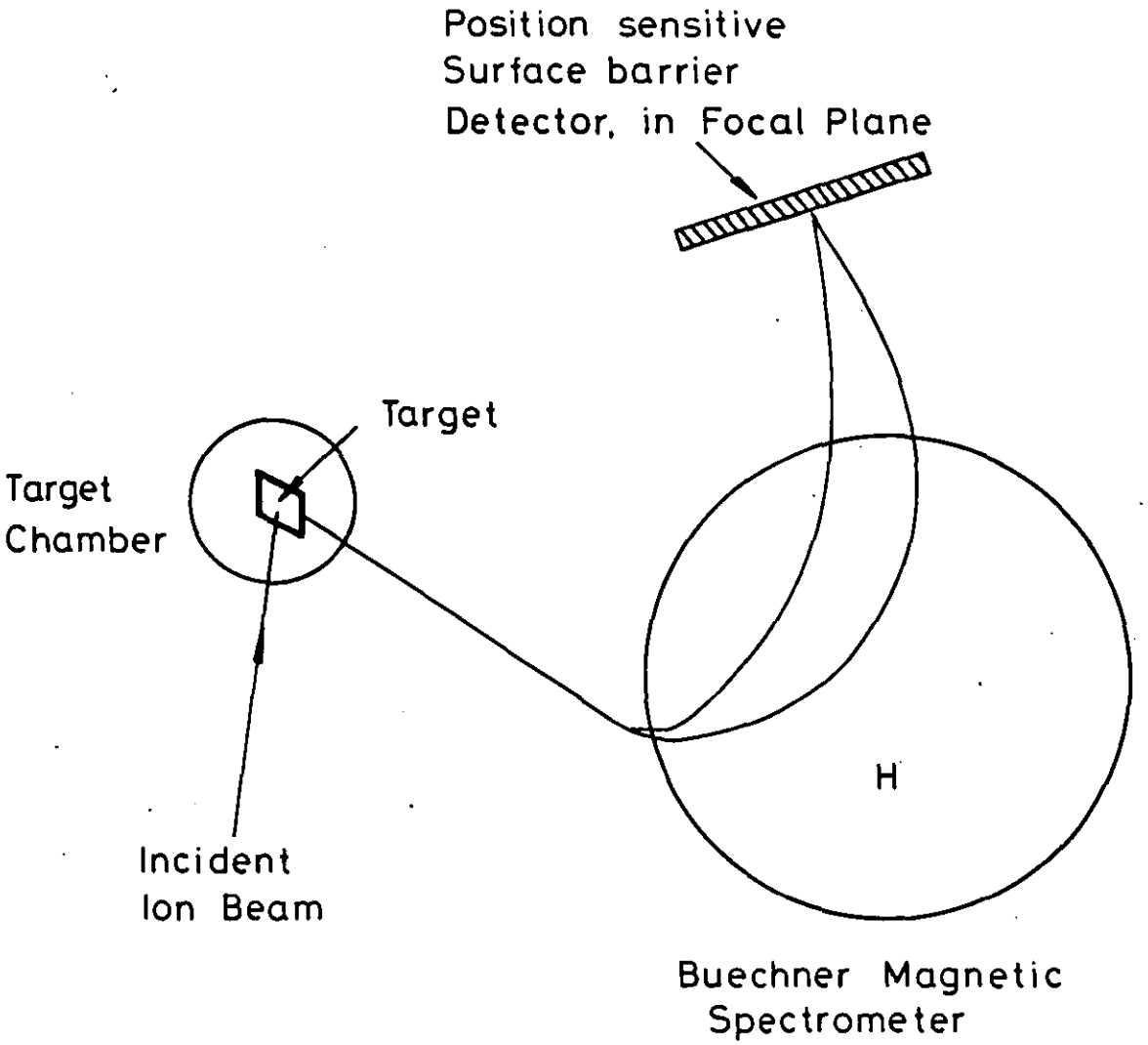

FIG. 2·20 SCHEMATIC DIAGRAM OF THE BUECHNER MAGNETIC SPECTROMETER.

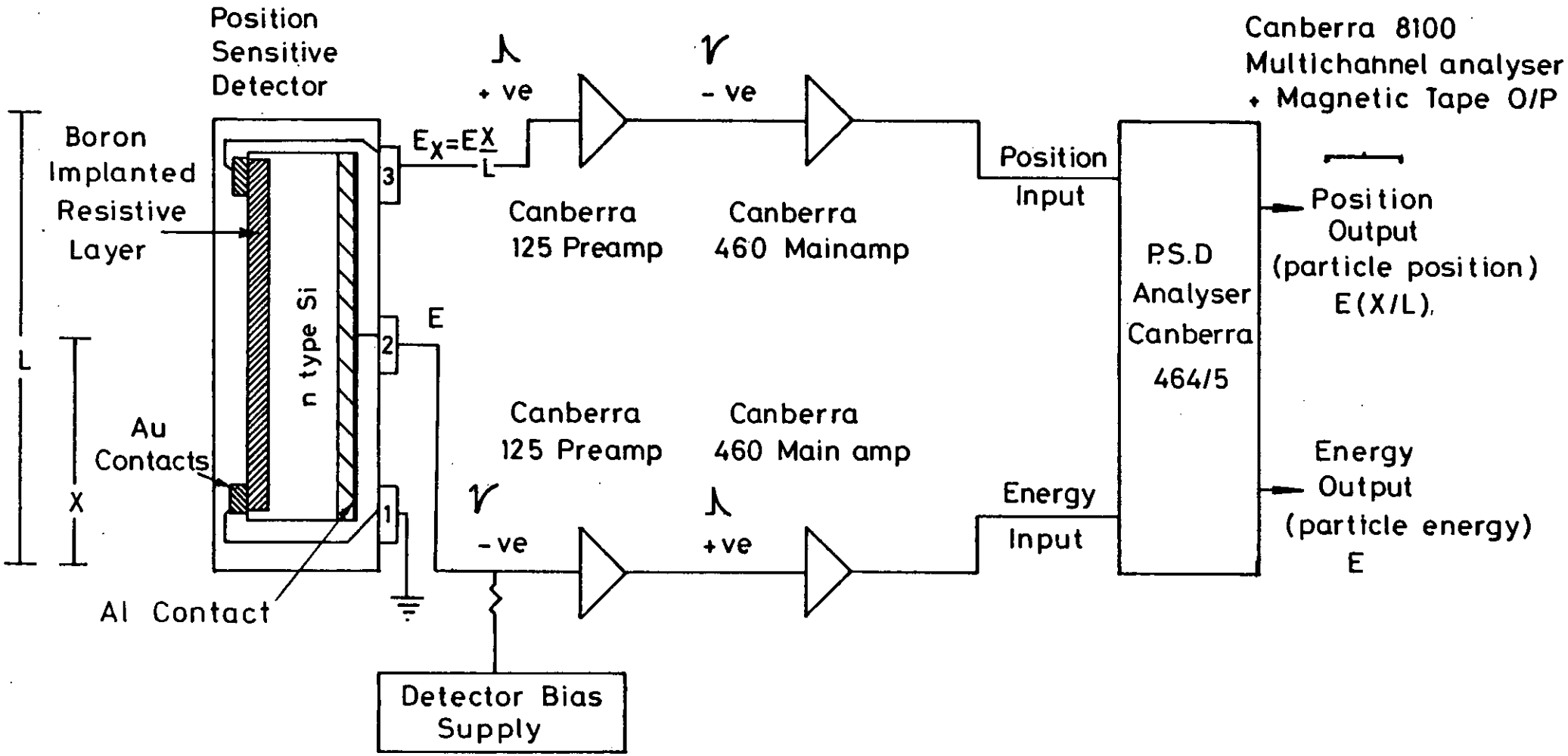

FIG. 2·21 SIMULTANEOUS MEASUREMENT OF ENERGY AND POSITION BACKSCATTER SPECTRA USING A POSITION SENSITIVE DETECTOR

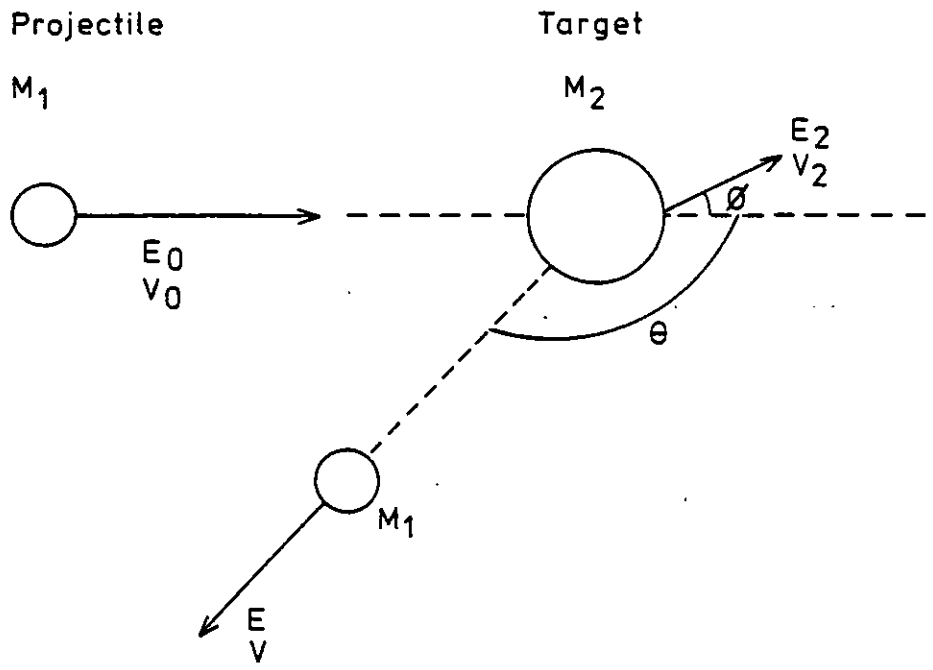

FIG. 3·1 SCHEMATIC DIAGRAM OF AN ELASTIC COLLISION (all in laboratory frame of reference).

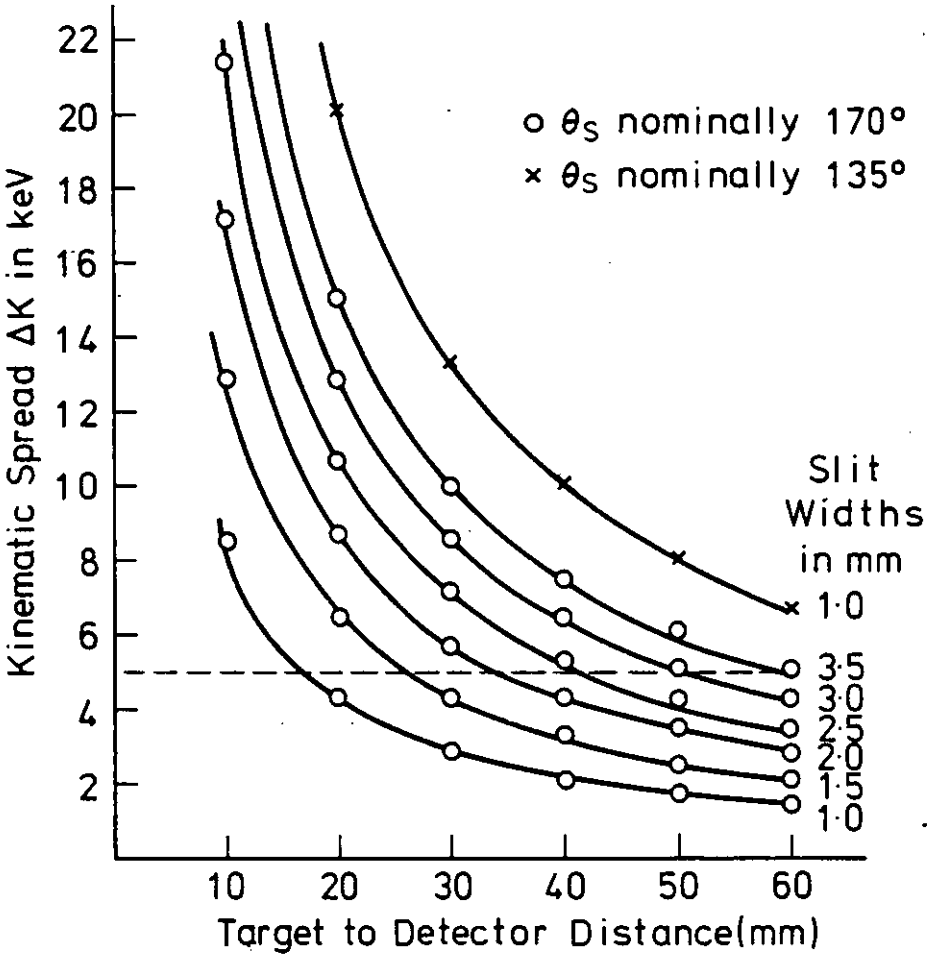

FIG 3·2 THE VARIATION OF KINEMATIC SPREAD WITH TARGET TO DETECTOR DISTANCE AND SLIT WIDTH AT TWO SCATTERING ANGLES. $E_{o\alpha} = 3\,MeV$, Mg^{24} TARGET. GEOMETRIES BELOW THE DOTTED LINE HAVE $\Delta K \leq 5\,KeV$.

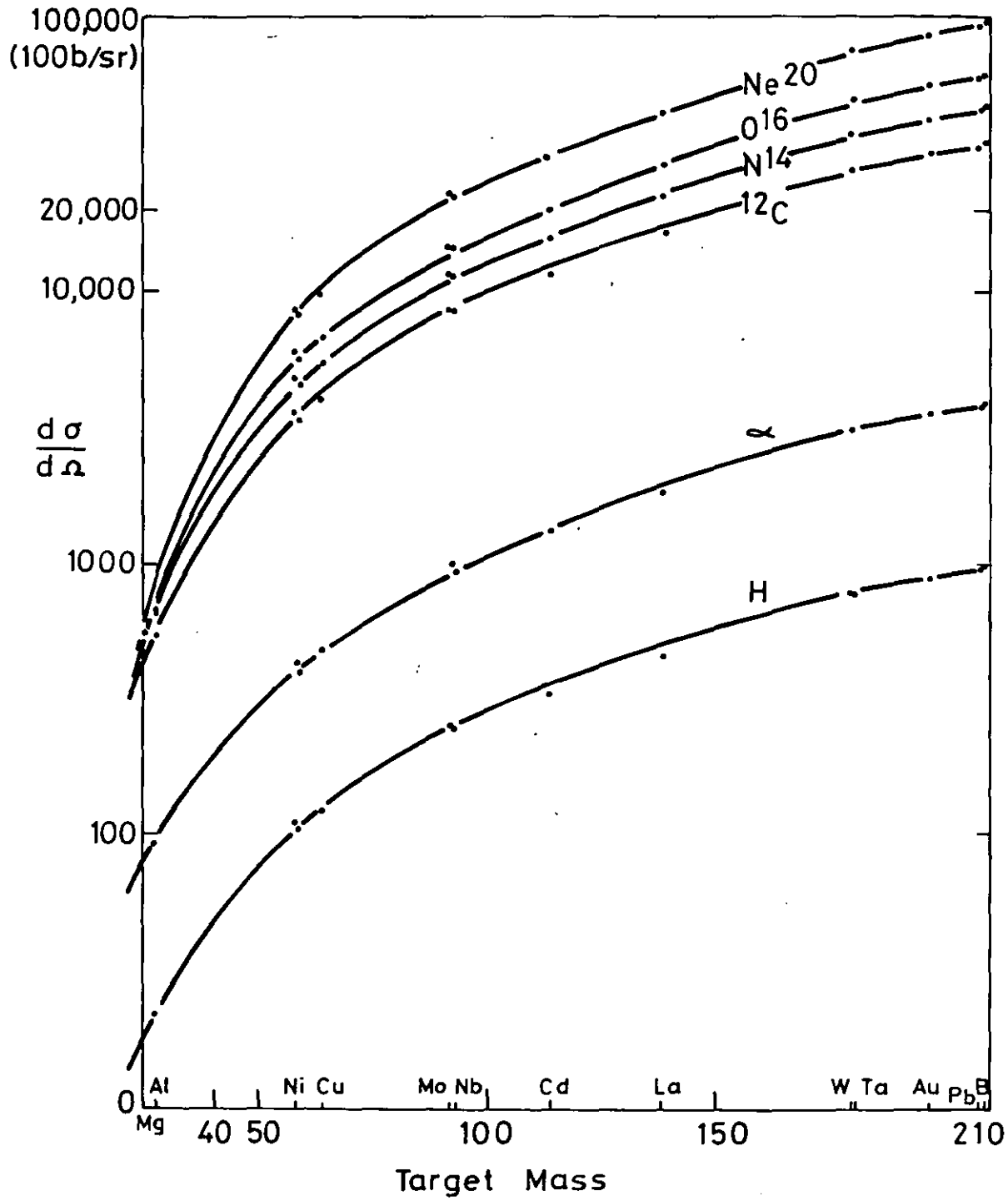

FIG. 3·3. CALCULATED RUTHERFORD CROSS-SECTIONS
$\theta = 175°$; $E_{beam} = 3{\cdot}0$ MeV.

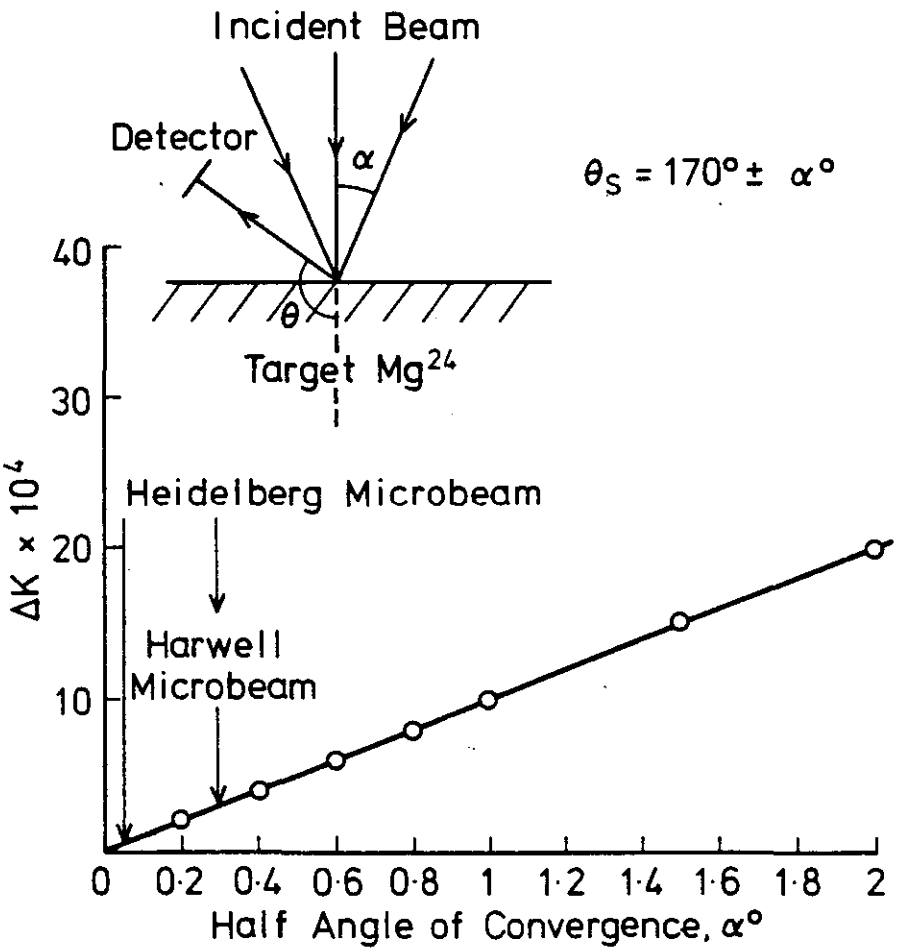

FIG. 3·4 THE EFFECT OF BEAM CONVERGENCE ON KINEMATIC SPREAD

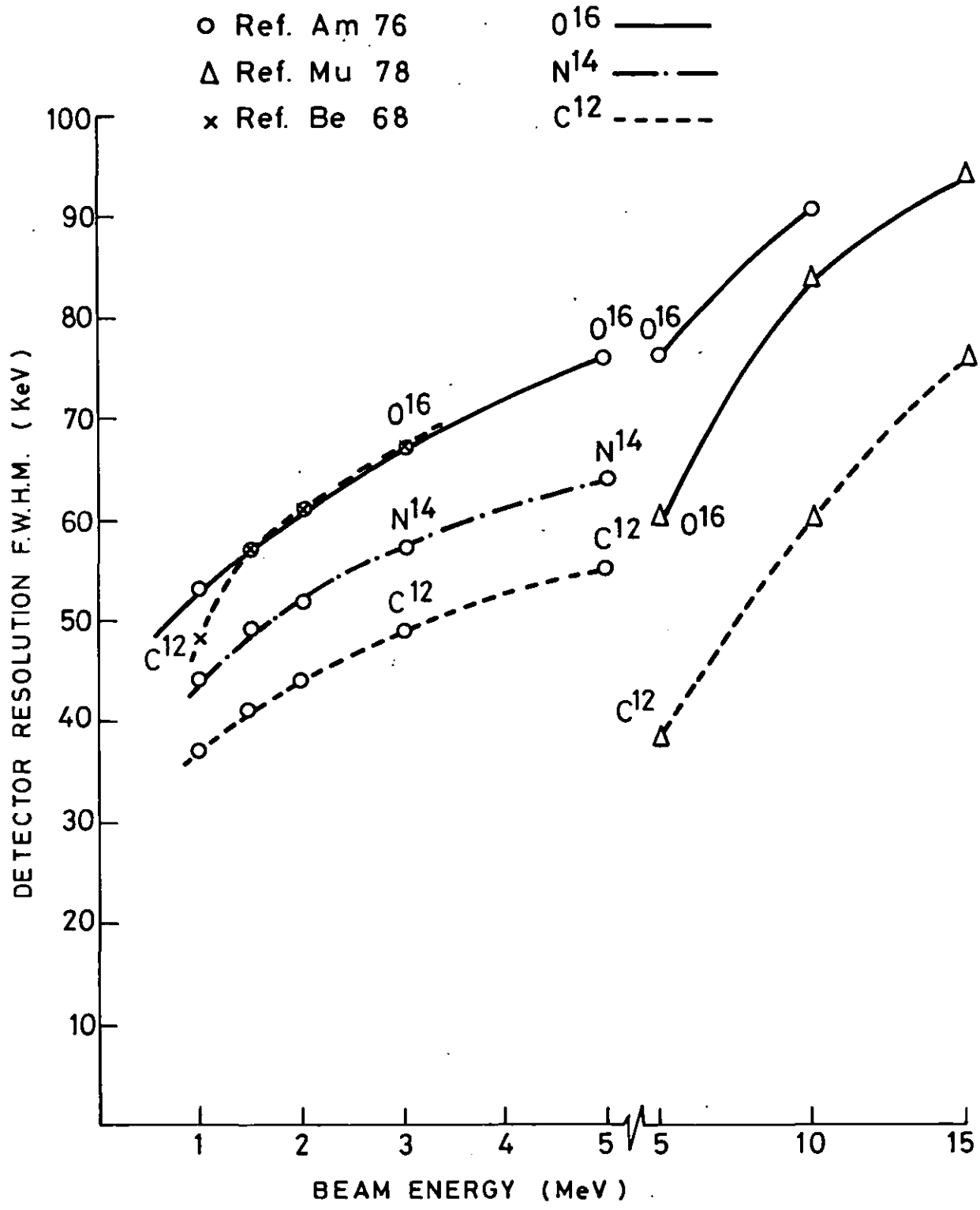

FIG 3.5 COMPARISON OF THE LITERATURE VALUES OF DETECTOR RESOLUTIONS USING VARIOUS ION BEAMS.

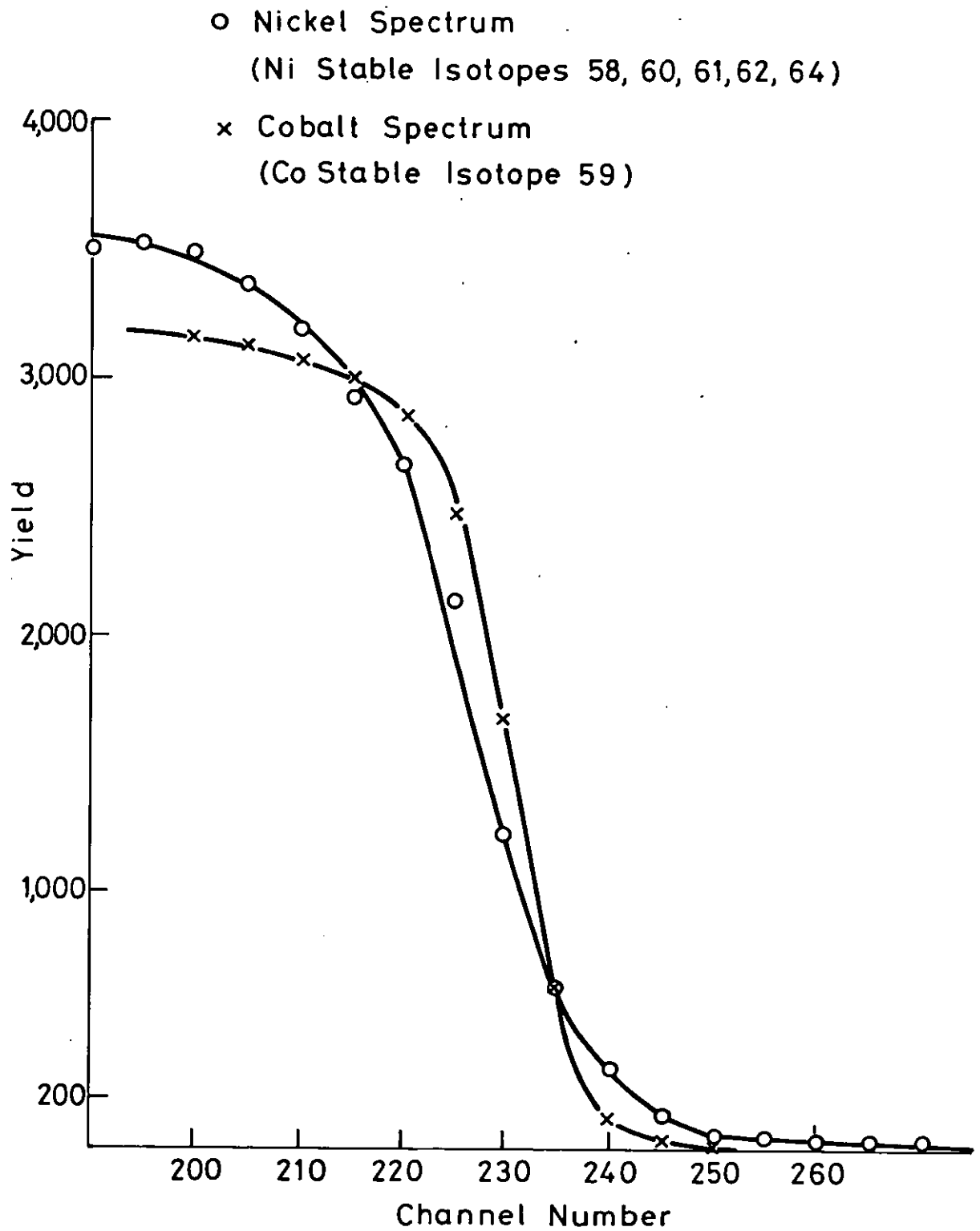

FIG. 3·6. BACKSCATTER SPECTRA OF COBALT AND NICKEL, $\theta = 164°$, $E_0 = 3{\cdot}5$ MeV, $^{14}N^{+}$ BEAM.

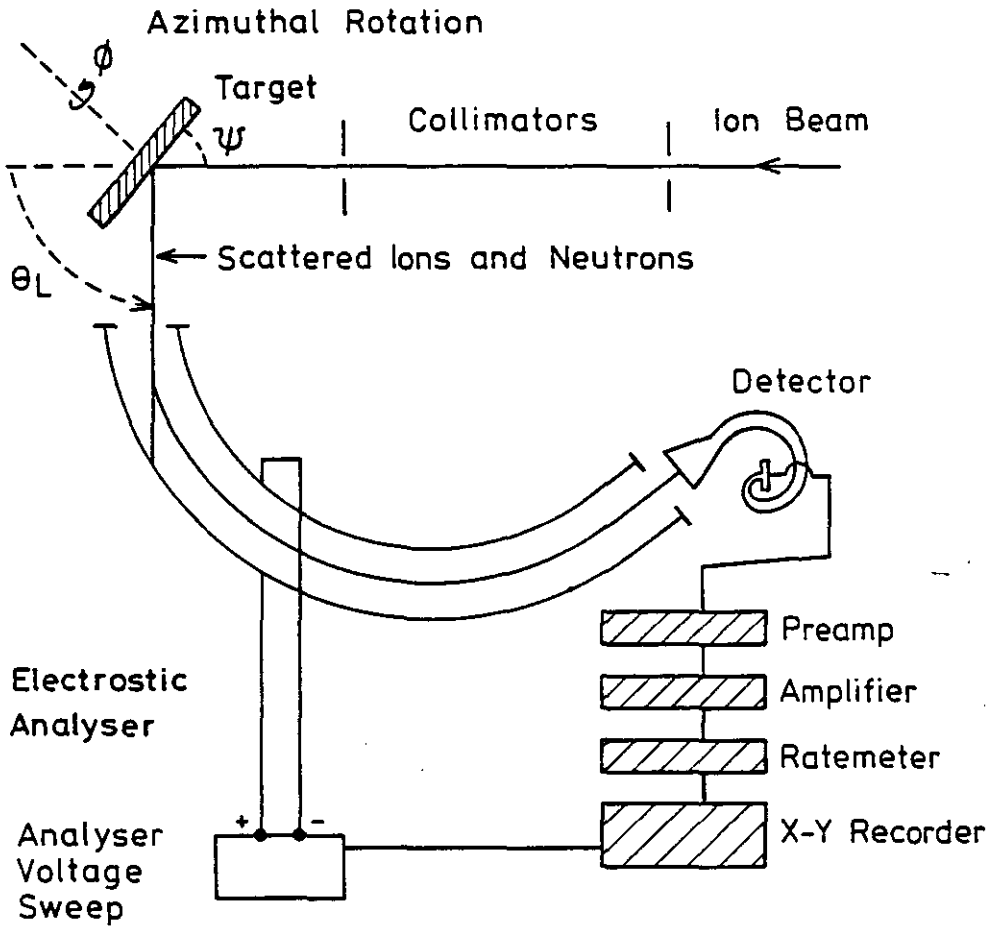

FIG. 3·7 SCHEMATIC DIAGRAM OF AN ELECTROSTATIC BACKSCATTERING ANALYSIS SYSTEM.

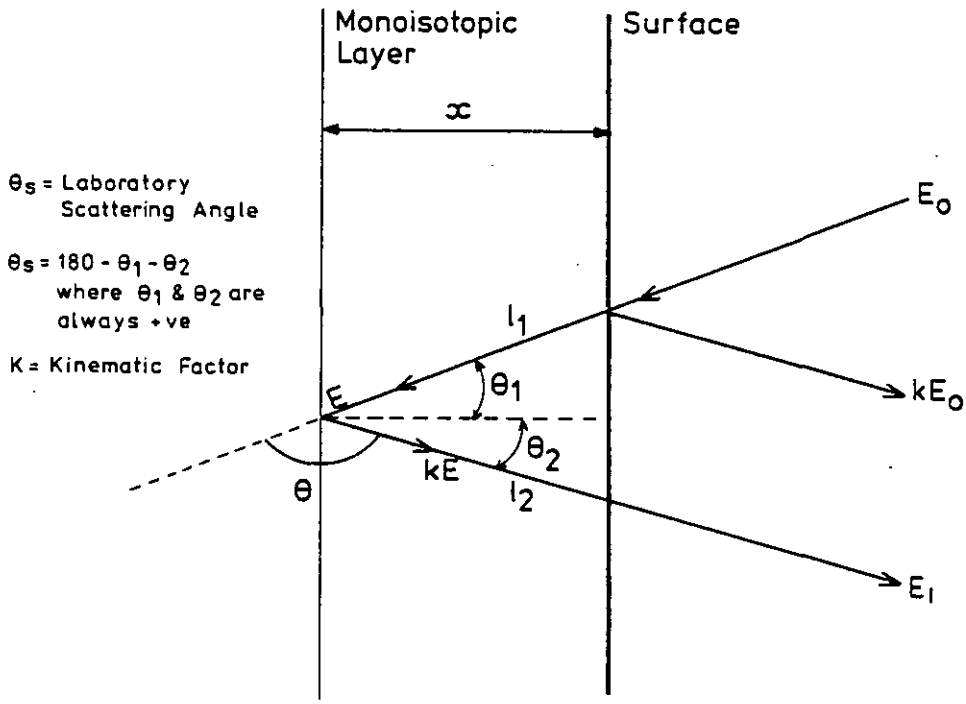

FIG. 3·8 DIAGRAMMATIC REPRESENTATION OF THE PRINCIPLE OF ELASTIC SCATTERING THROUGH A SAMPLE OF THICKNESS x.

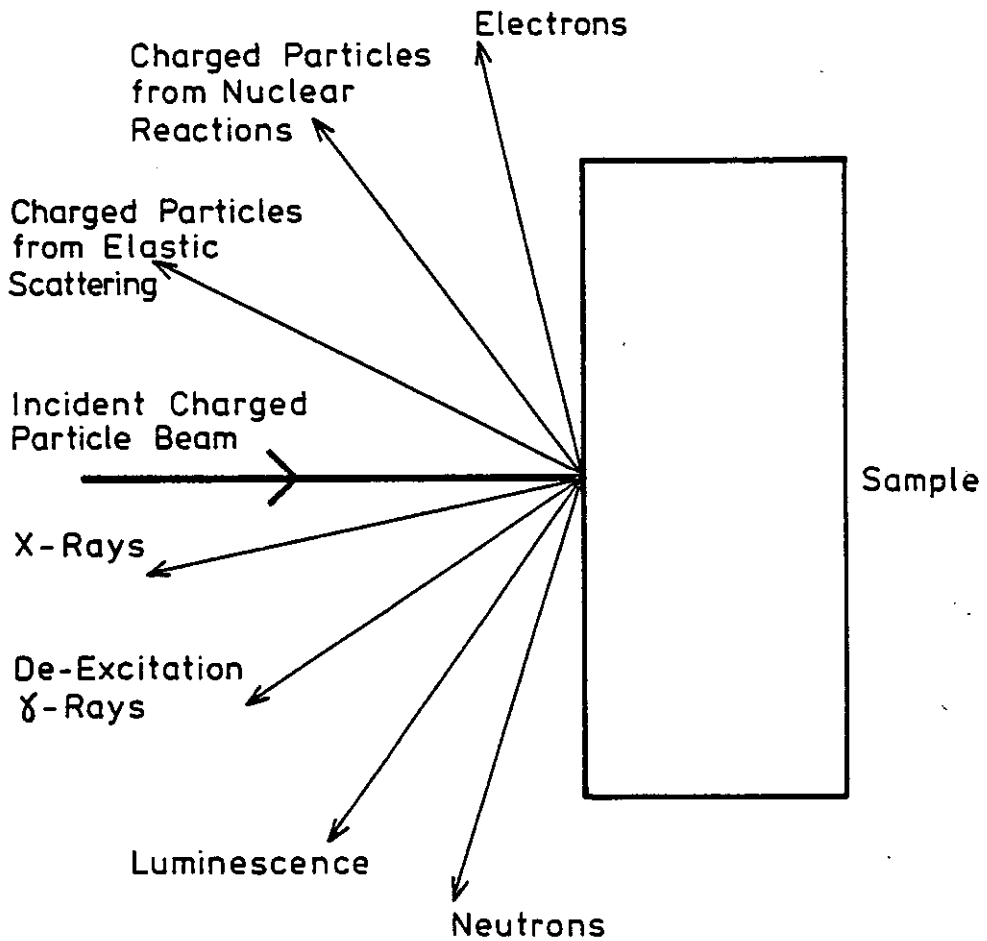

FIG. 3·9. SCHEMATIC·DIAGRAM SHOWING SOME OF THE EMITTED RADIATIONS, RESULTING FROM CHARGED PARTICLE BOMBARDMENT.

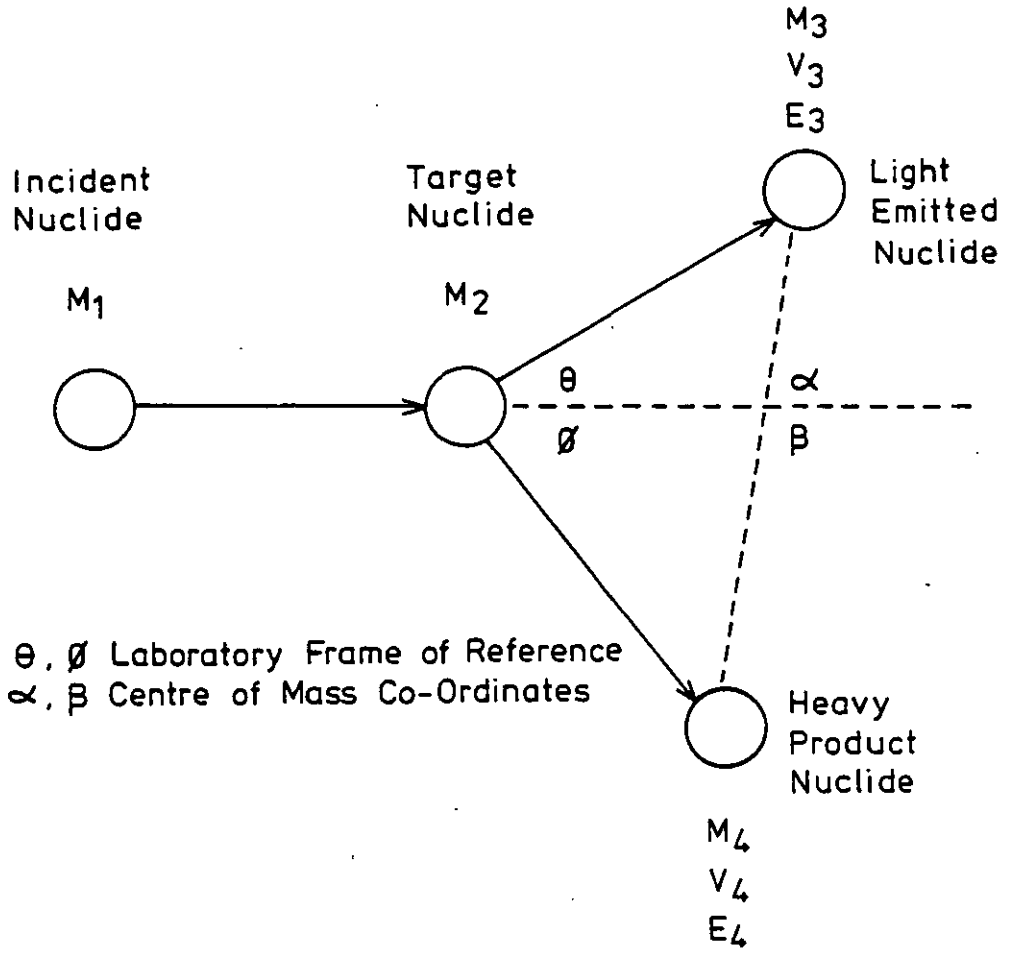

FIG. 3·10 INTERACTION OF NUCLIDES UNDERGOING NUCLEAR REACTION.

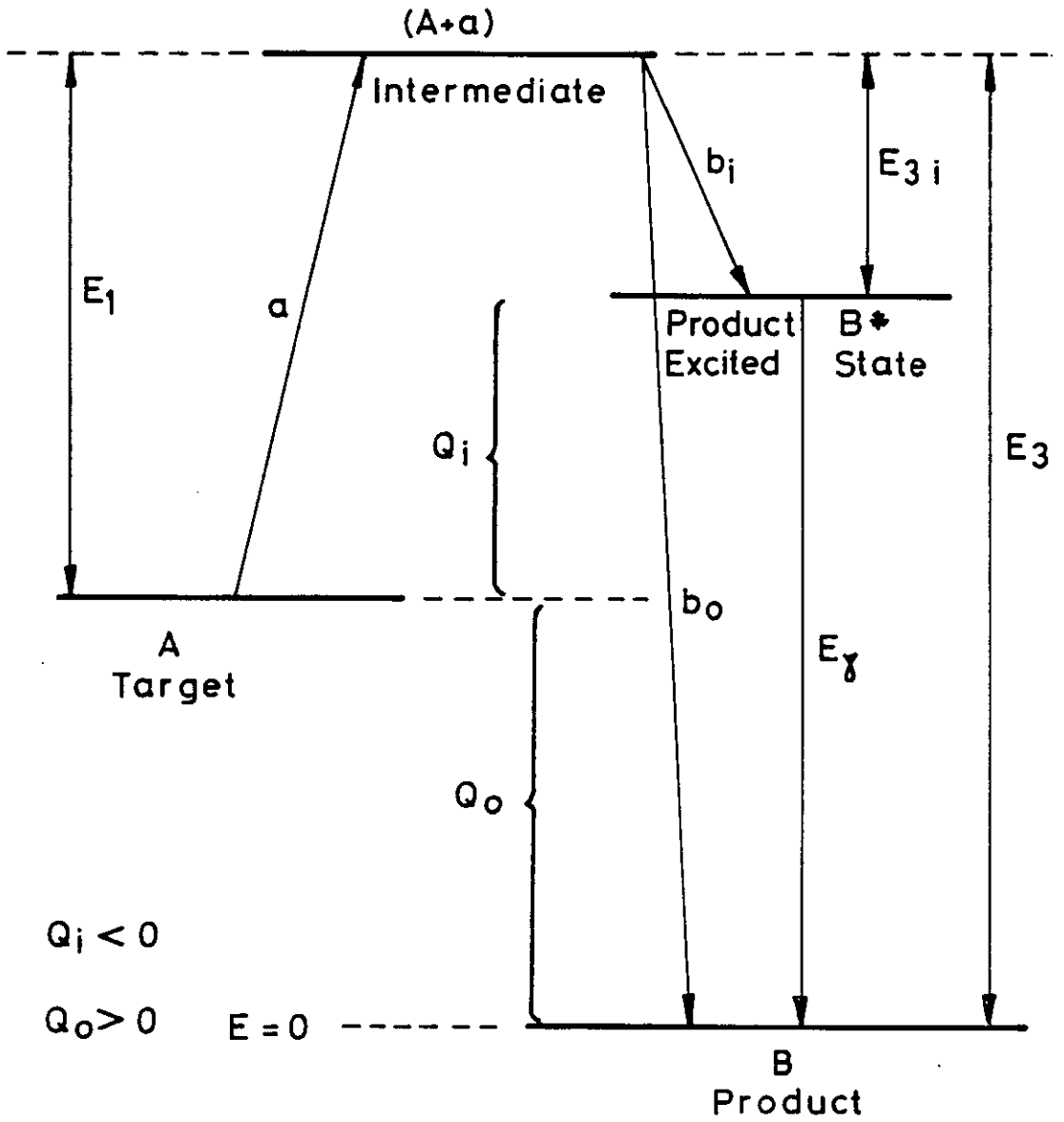

FIG. 3·11. ENERGY RELATIONSHIPS OF A NUCLEAR REACTION.

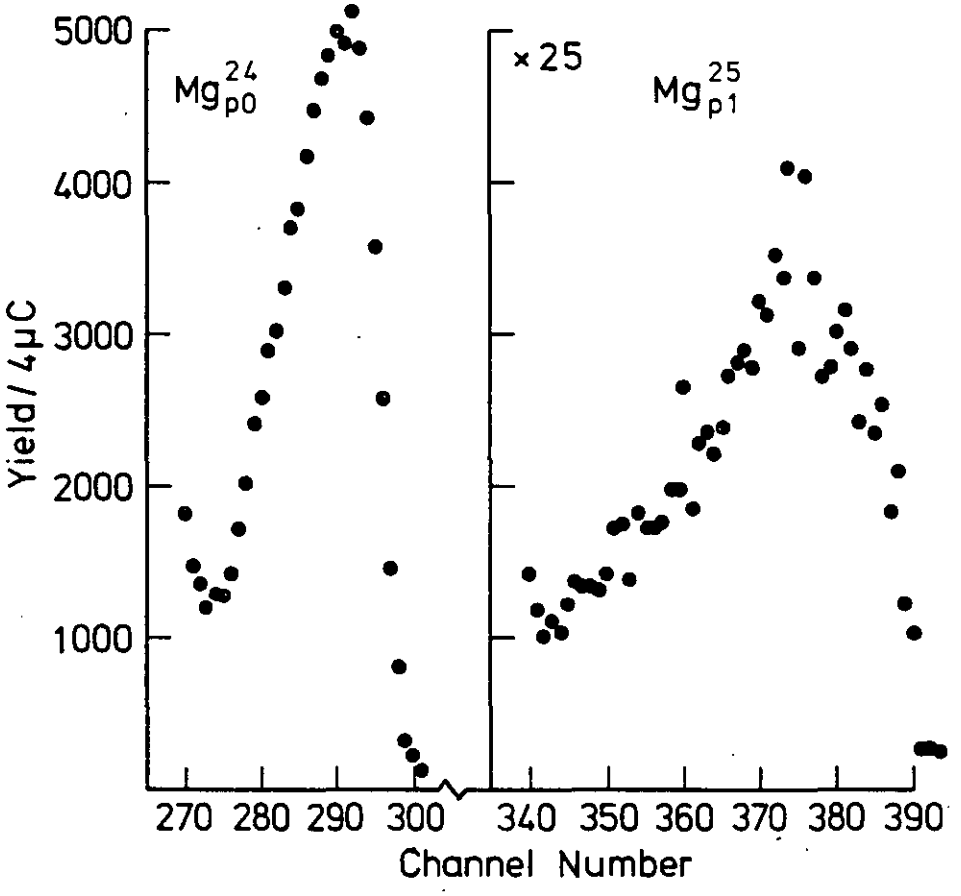

FIG. 3·12 MAGNESIUM ISOTOPE PEAKS FROM THE CHARGED PARTICLE SPECTRA OF MAGNESIUM E_{od}=1·9 MeV, θ =135°

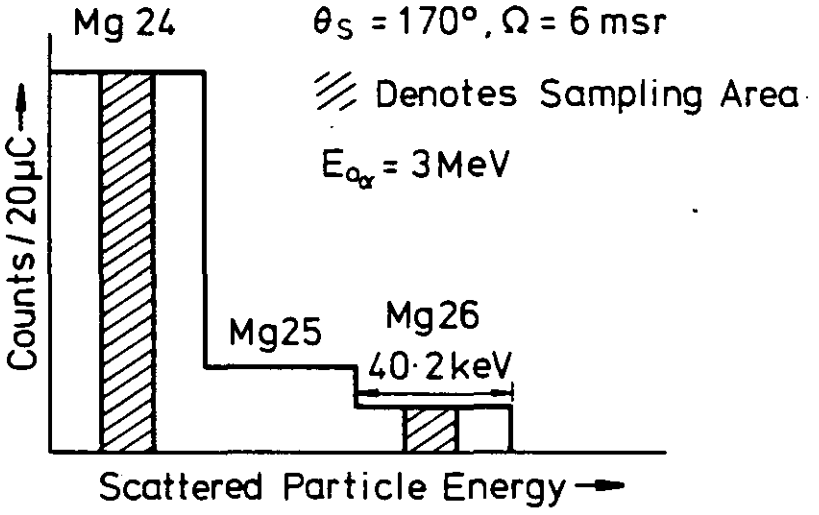

FIG. 3·13 IDEALISED CONDITIONS FOR THE DETERMINATION OF ISOTOPIC SENSITIVITY

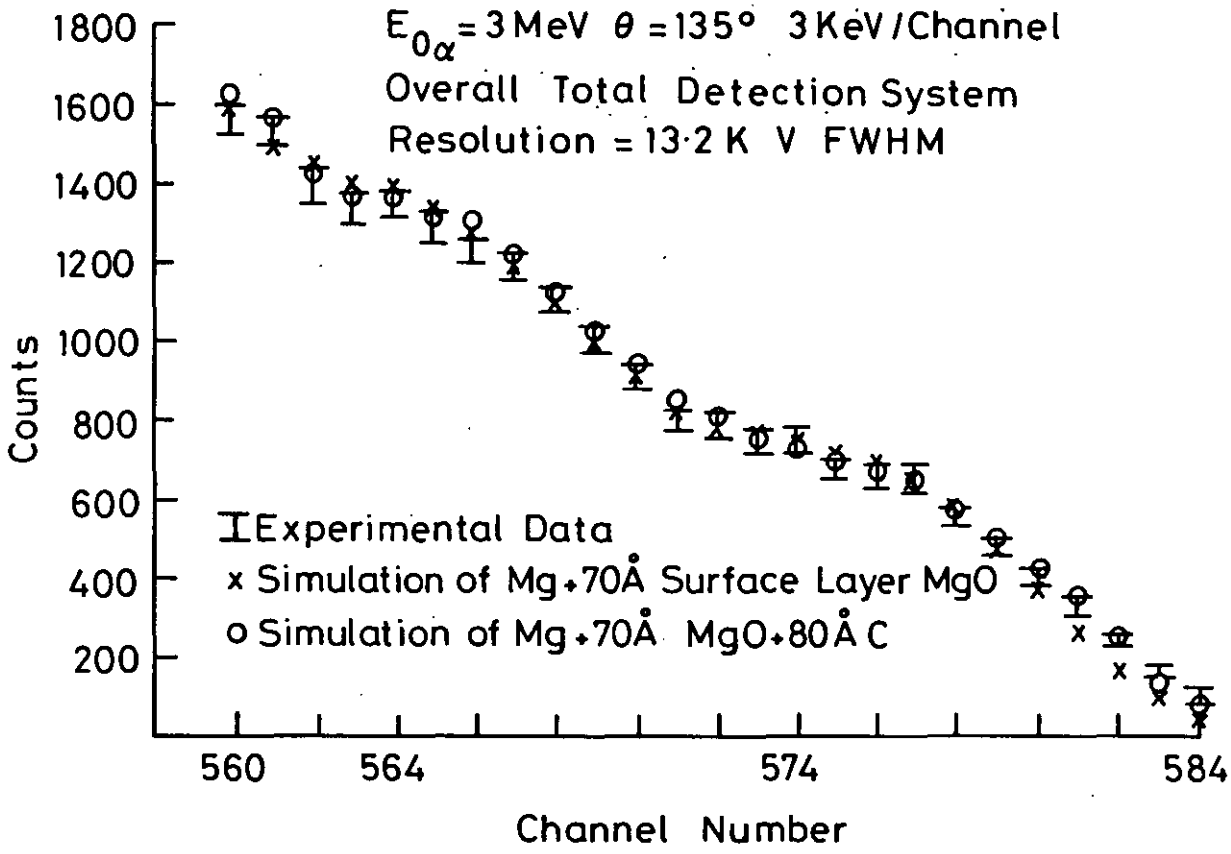

FIG. 4·1 THE MAGNESIUM 25 AND 26 ISOTOPE STEPS OF THE BACKSCATTERING SPECTRUM OF NATURAL MAGNESIUM, COMPARING EXPERIMENTAL DATA AND SIMULATIONS.

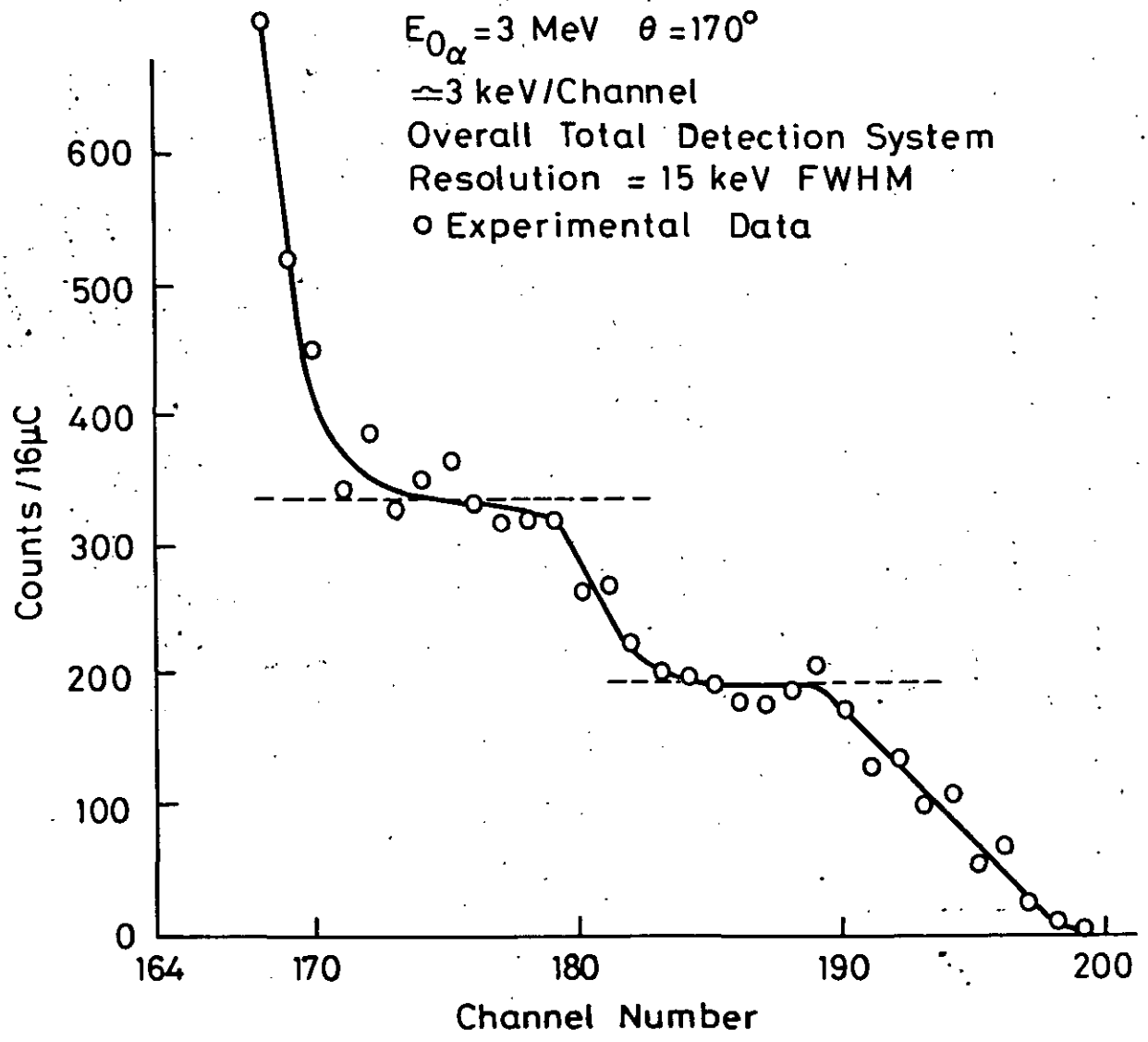

FIG. 4·2 PART OF THE BACKSCATTERING SPECTRUM OF NATURAL MAGNESIUM.

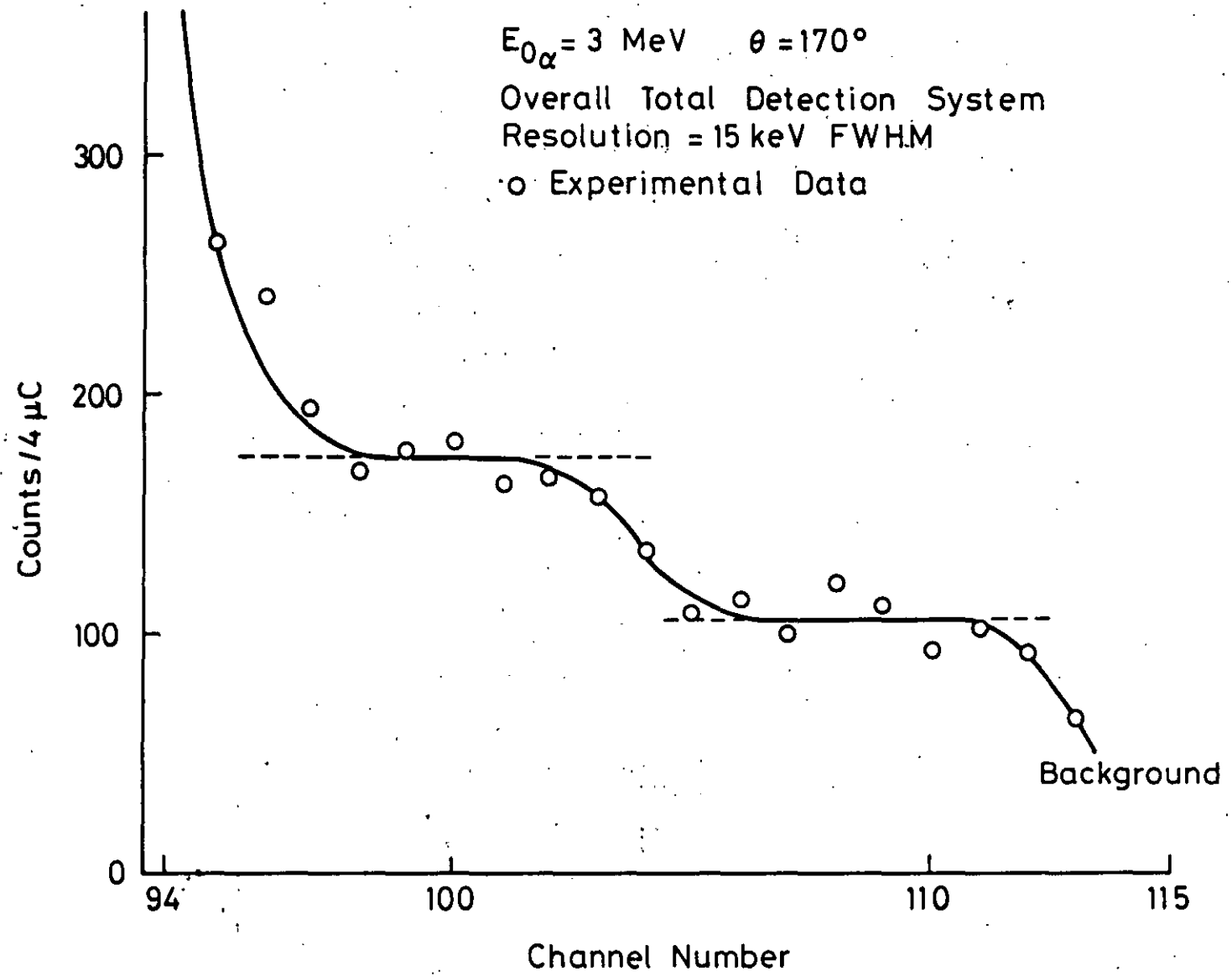

FIG. 4·3 PART OF THE BACKSCATTERING SPECTRUM OF BISMUTH IMPLANTED SILICON SHOWING THE SILICON ISOTOPES OF MASS 29 AND 30.

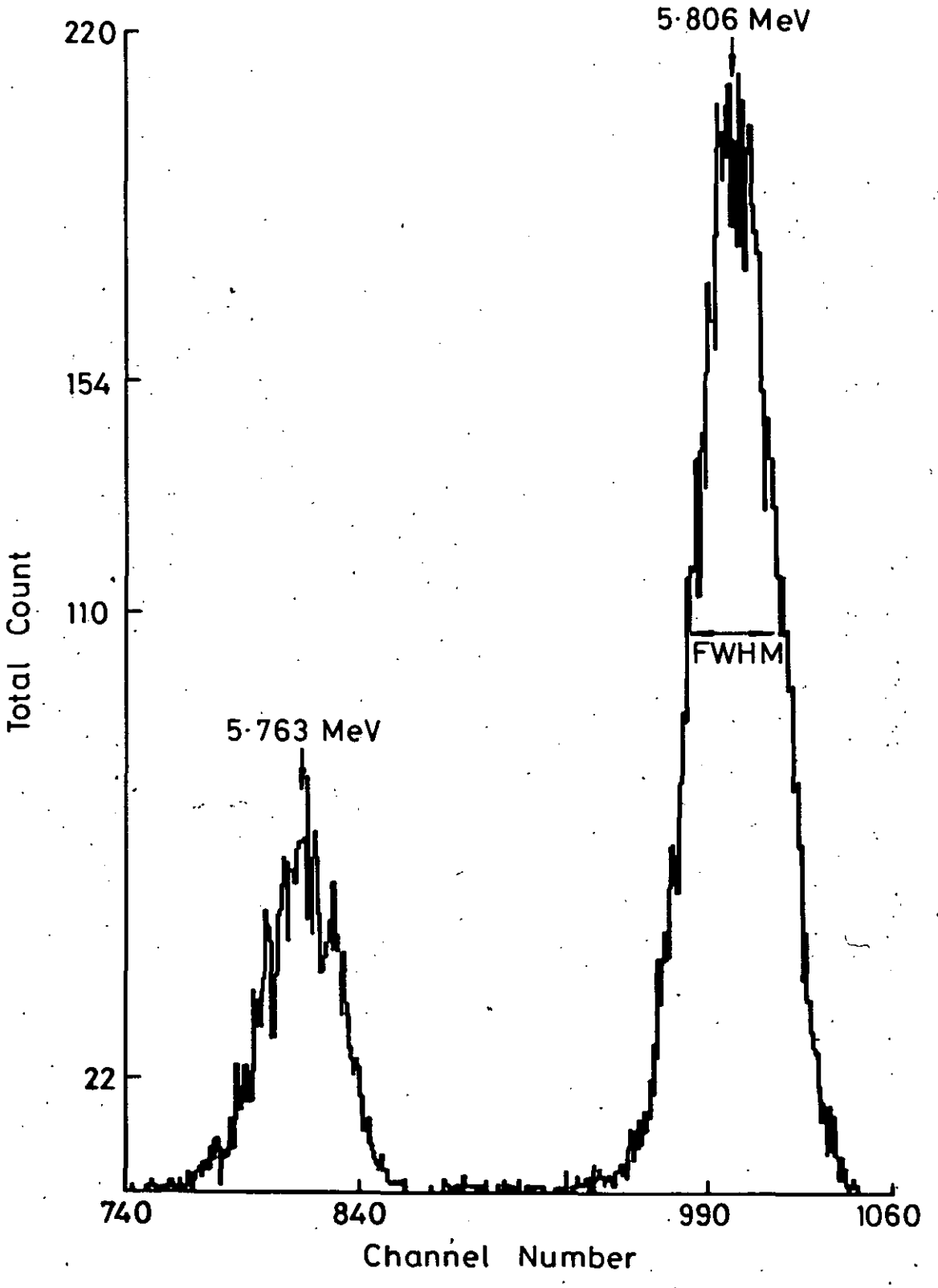

FIG. 4·4 MAGNETIC SPECTROMETER POSITION SPECTRUM OF A CM=244 SOURCE f = 29·5 MHz

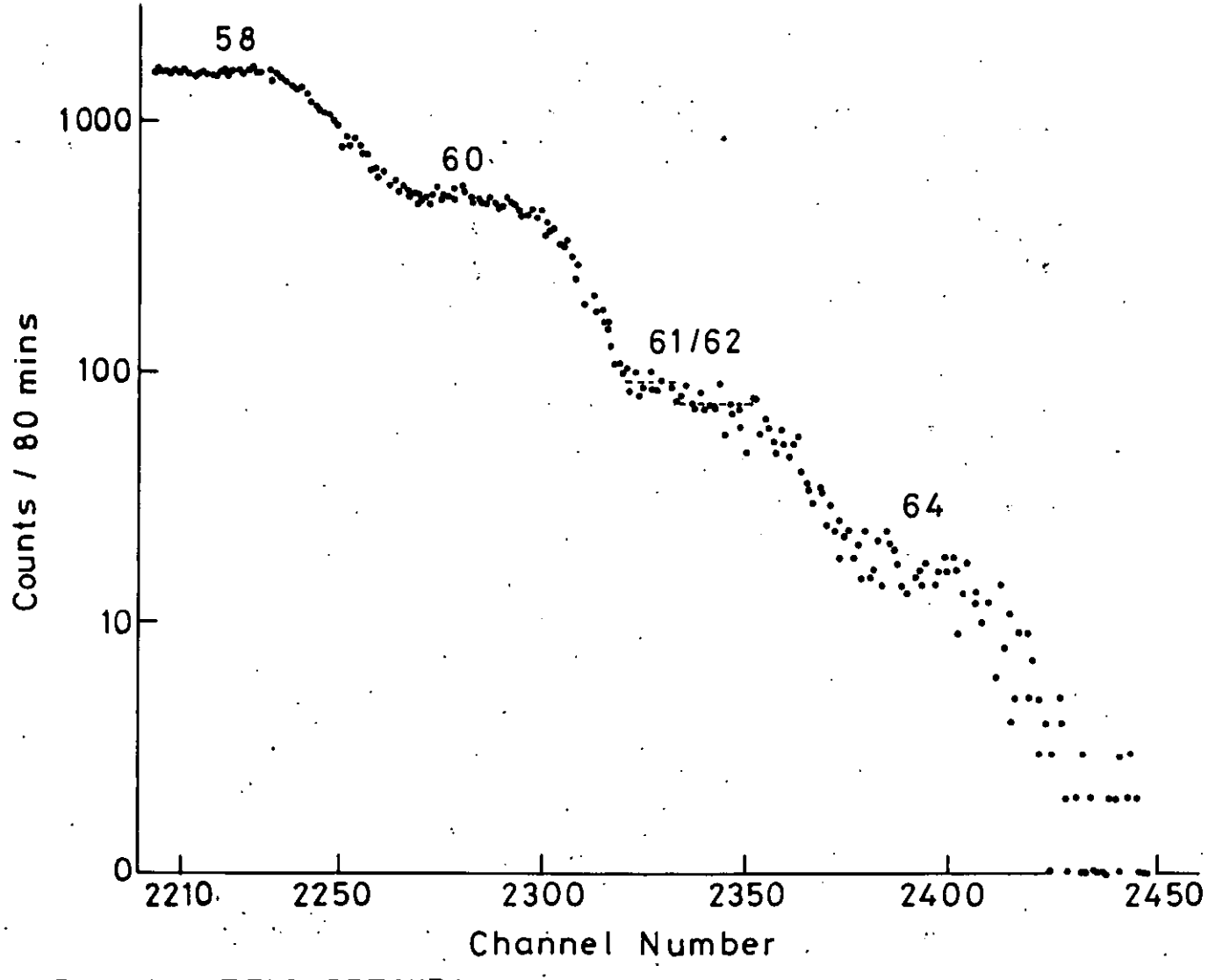

FIG.4·5 MAGNETIC SPECTROMETER POSITION SPECTRUM OF NICKEL
$\theta_B = 145°$, 5·8 MeV $^4He^+$ BEAM, $\Omega = 0·175$ msr, f=26·1 MHz.

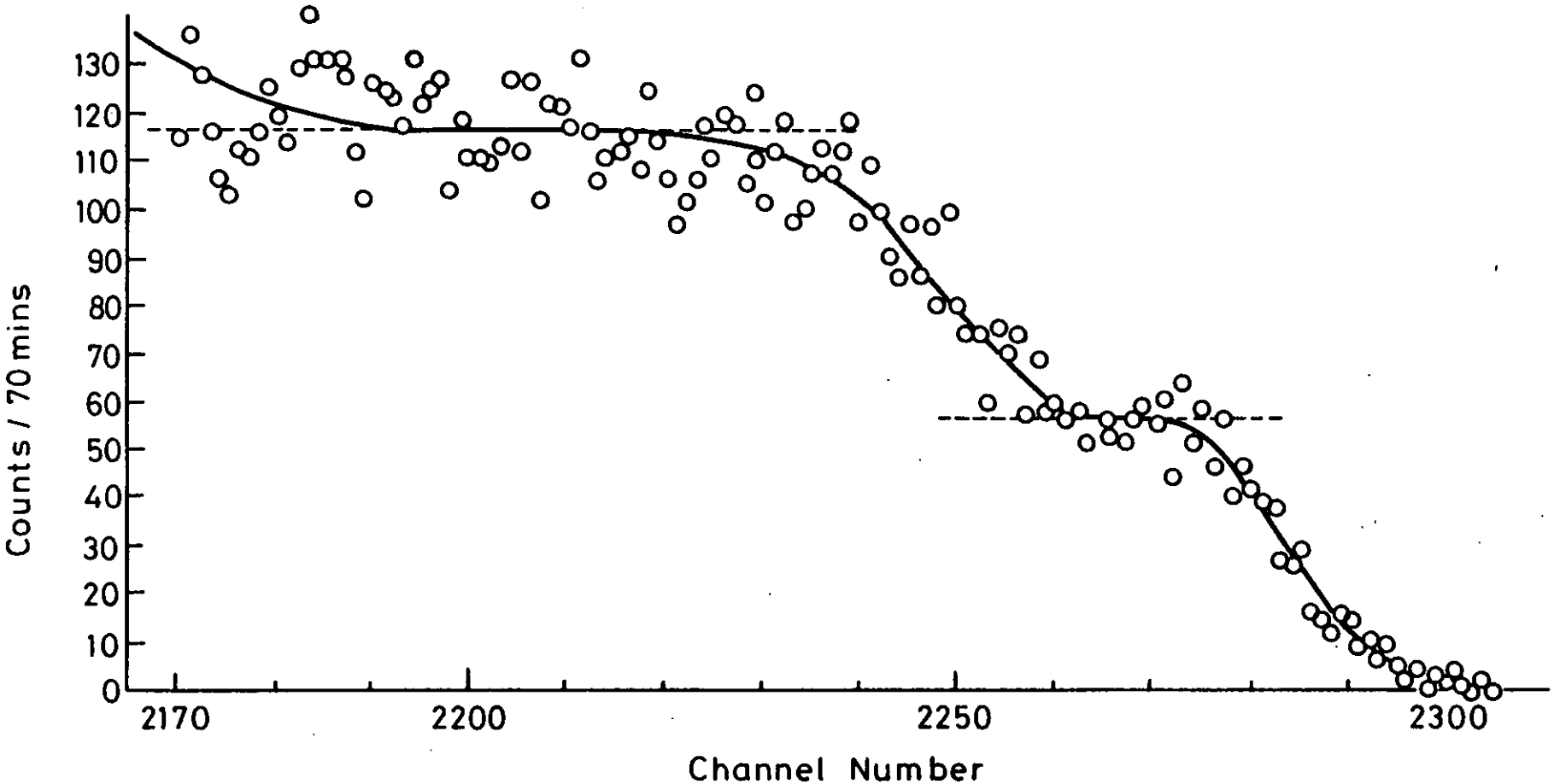

FIG. 4·6 MAGNETIC SPECTROMETER POSITION SPECTRUM OF SILVER $\theta_B = 145°$, 20 MeV $^{16}O^{+4}$ BEAM, $\Omega = 0{\cdot}175$ msr, $f = 32{\cdot}8$ MHz

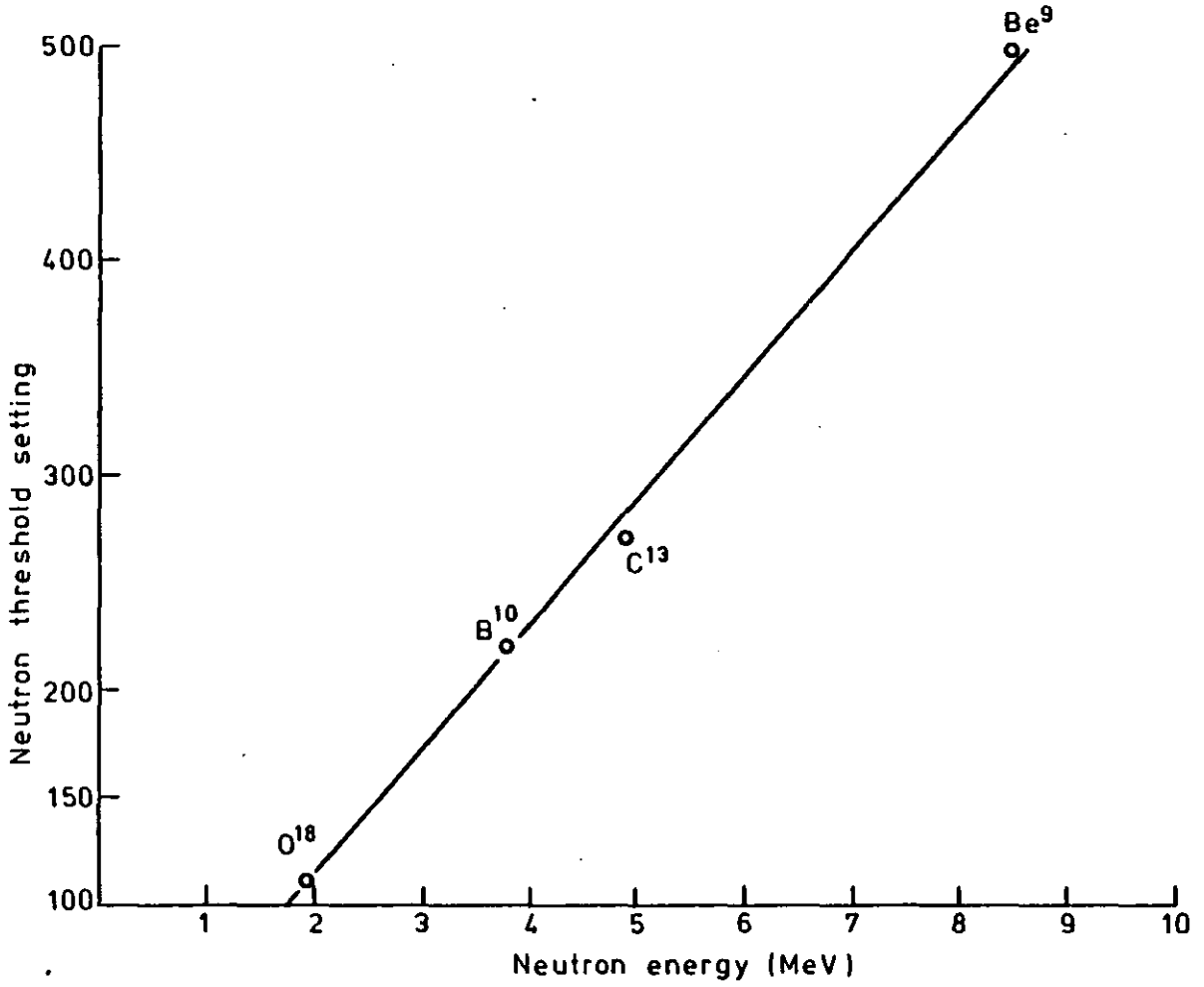

FIG.5·1.(α,n) CALIBRATION CURVE OF NEUTRON ENERGY AGAINST THRESHOLD SETTING.

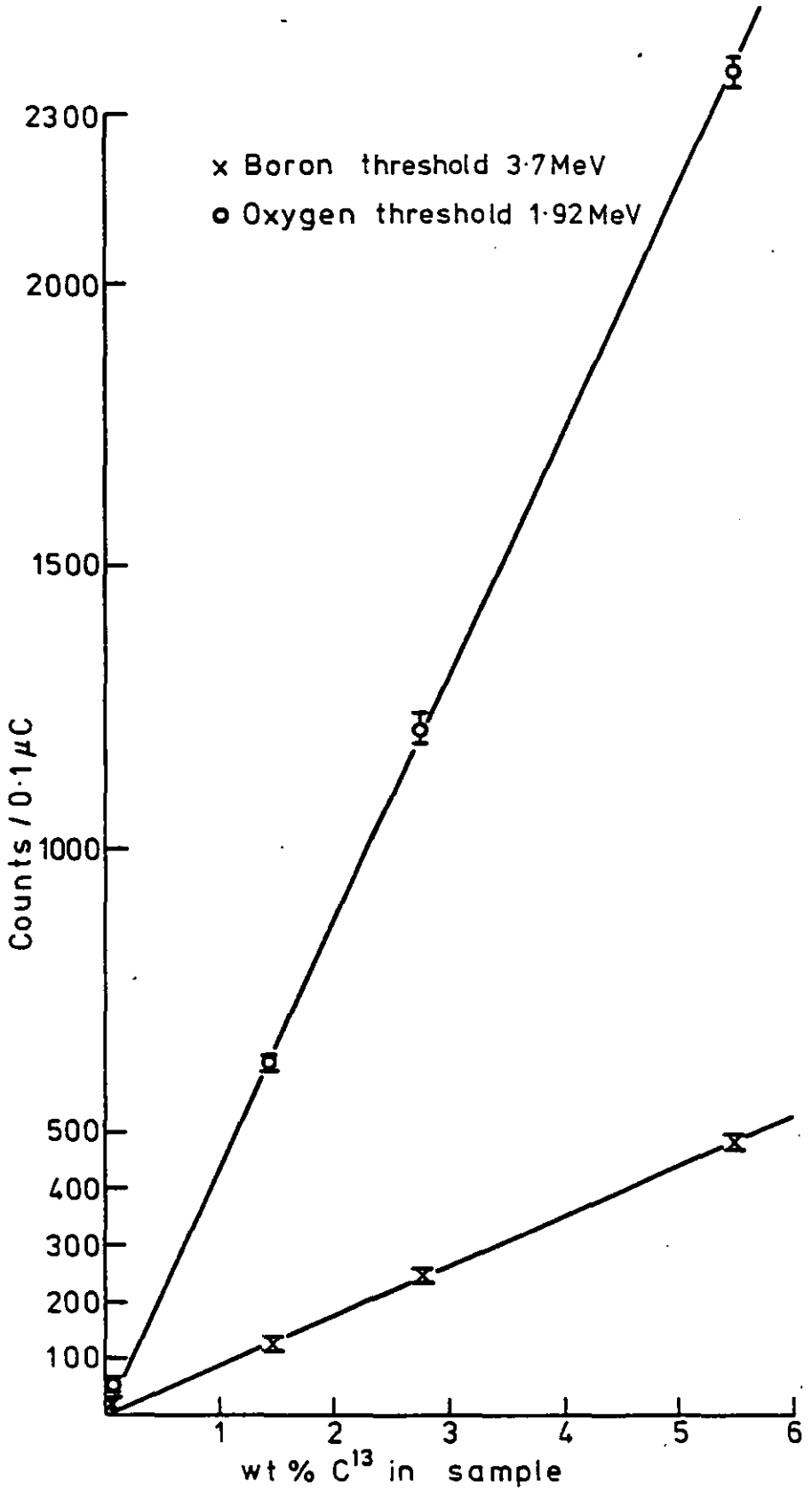

FIG.5·2. (α,n) CALIBRATION CURVE OF ^{13}C IN $BaCO_3$

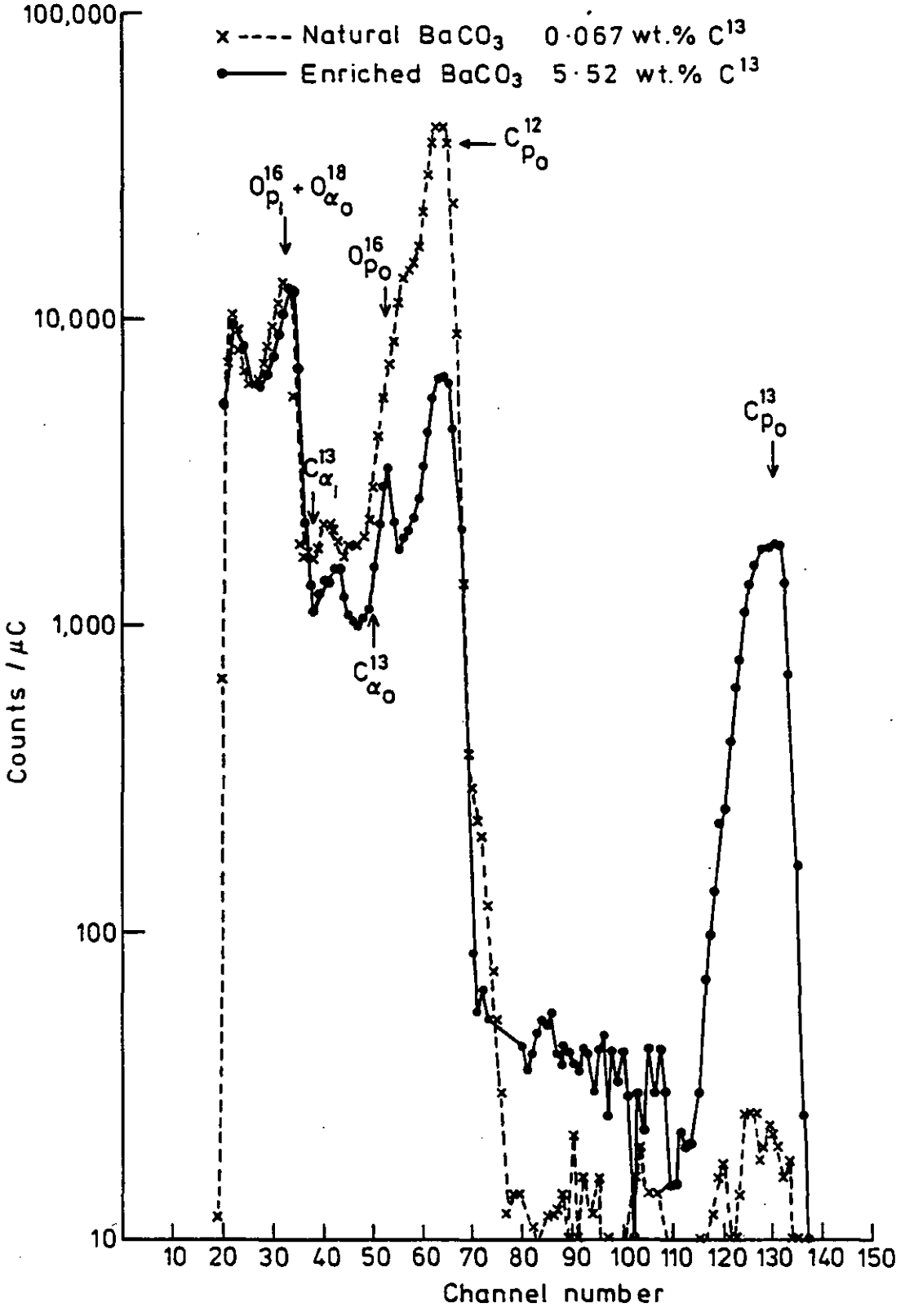

FIG. 5·3. (d, p) SPECTRA OF NATURAL AND ENRICHED ^{13}C SAMPLES OF $BaCO_3$. E_{OD} = 1·3 MeV, θ = 135°

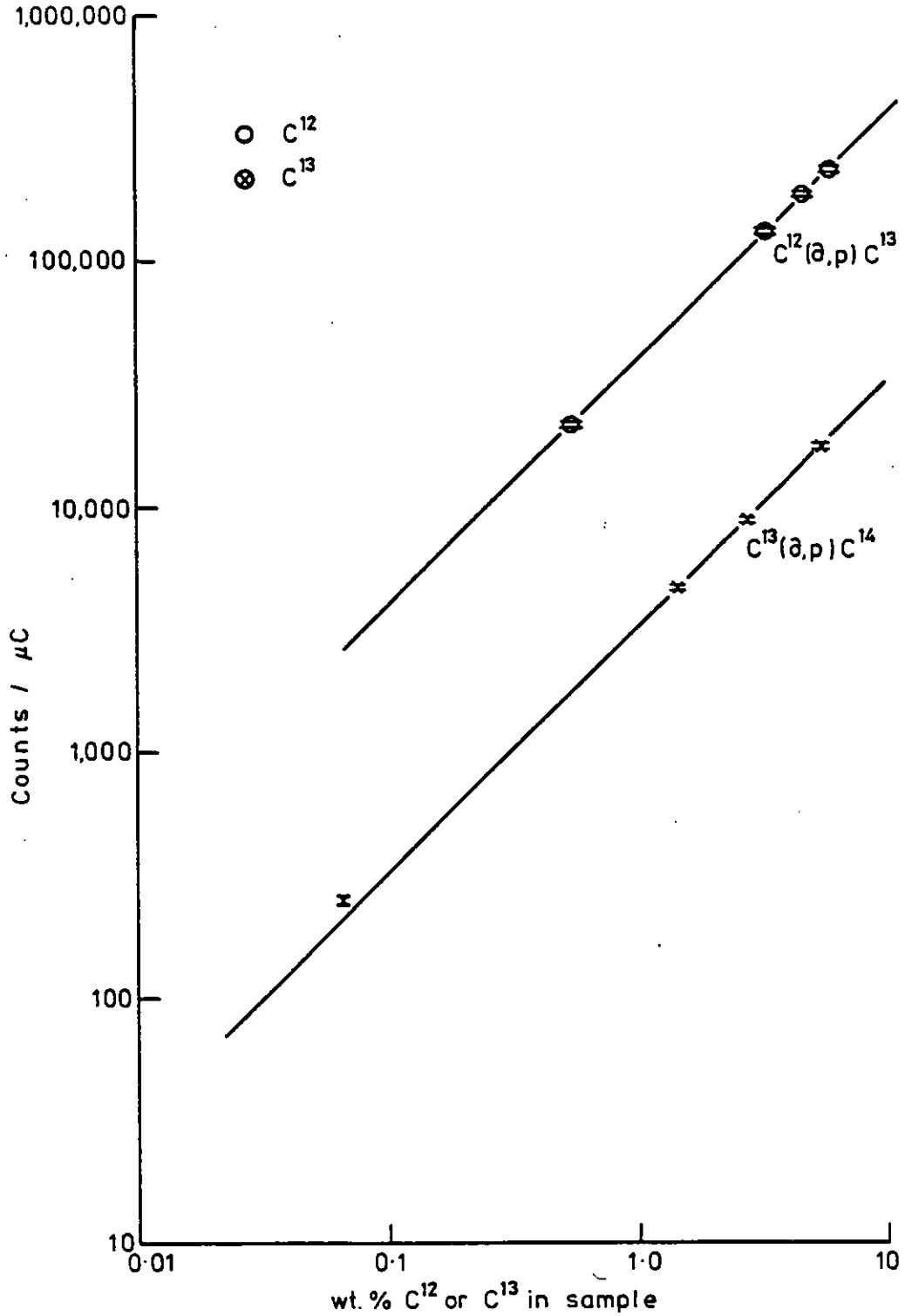

FIG. 54.(∂, p) CALIBRATION CURVES OF C^{13} AND C^{12} IN $BaCO_3$ E_{od}=1·3 MeV
$\theta = 135°$.

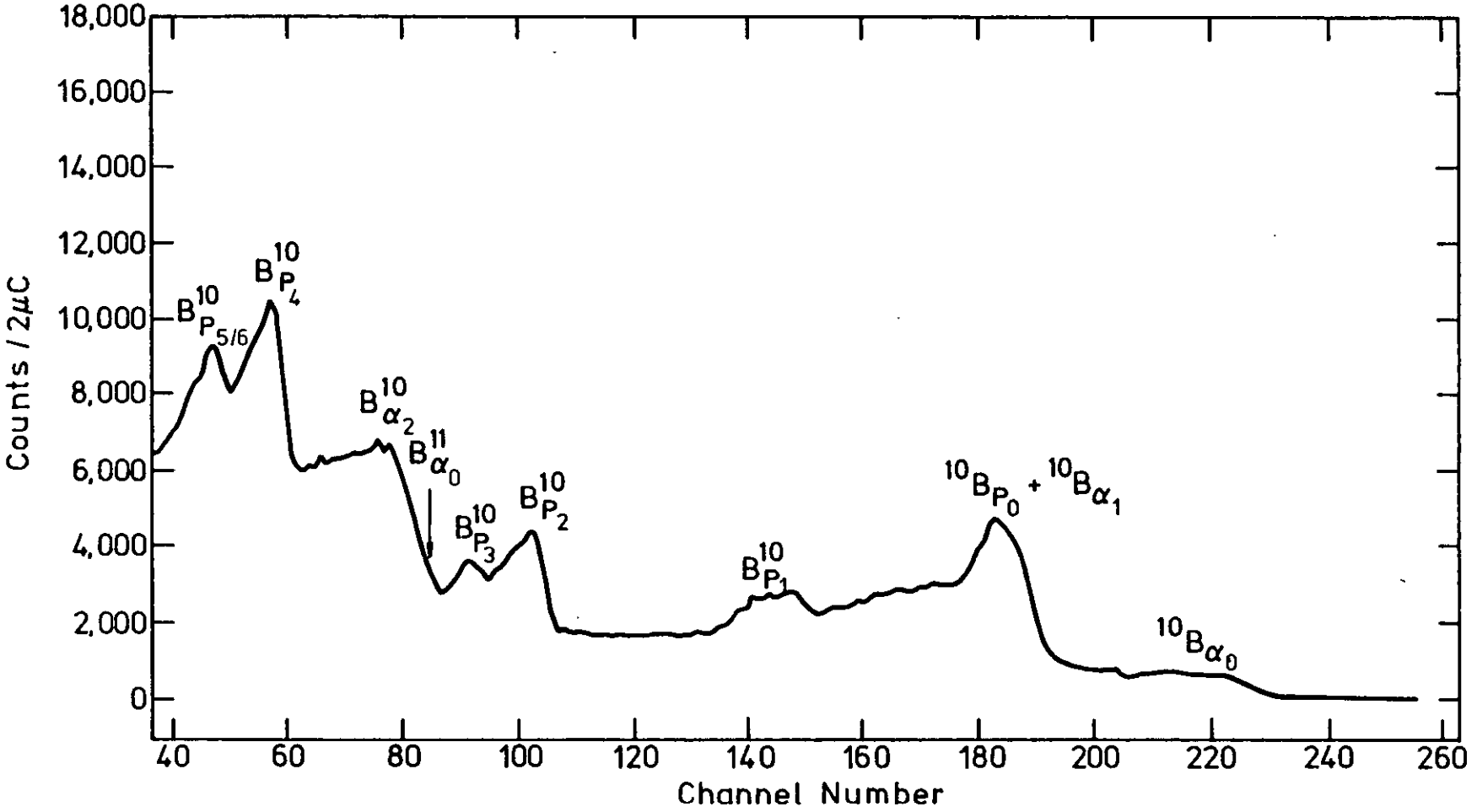

FIG.5·5.(d,p) SPECTRUM OF SPECPURE BORON, $E_{OD} = 1{\cdot}3$ MeV, $\theta = 135°$

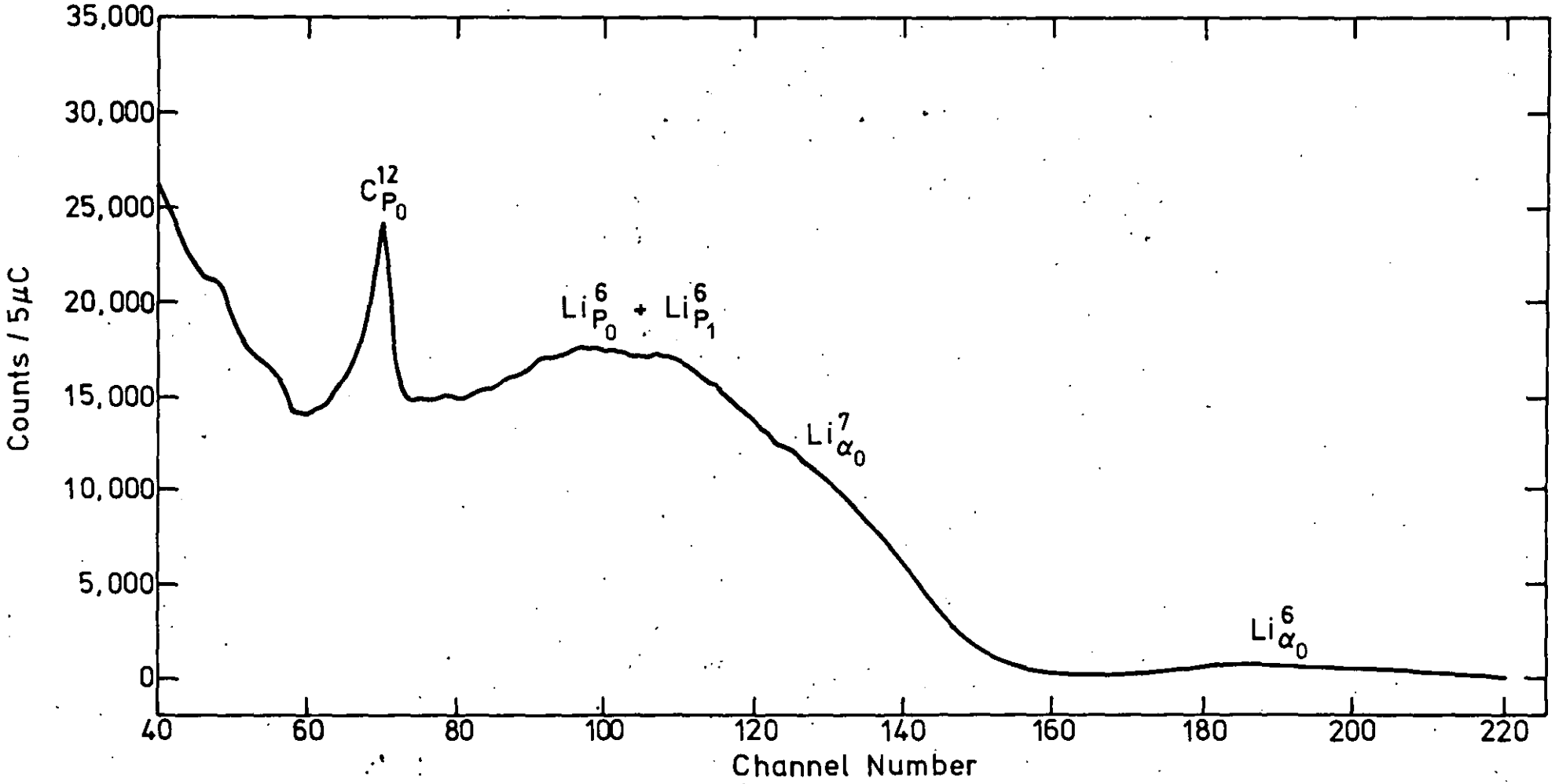

FIG.5·6. (d,p) SPECTRUM OF $LiNbO_3$, $E_{OD} = 1{\cdot}3$ MeV, $\theta = 135°$

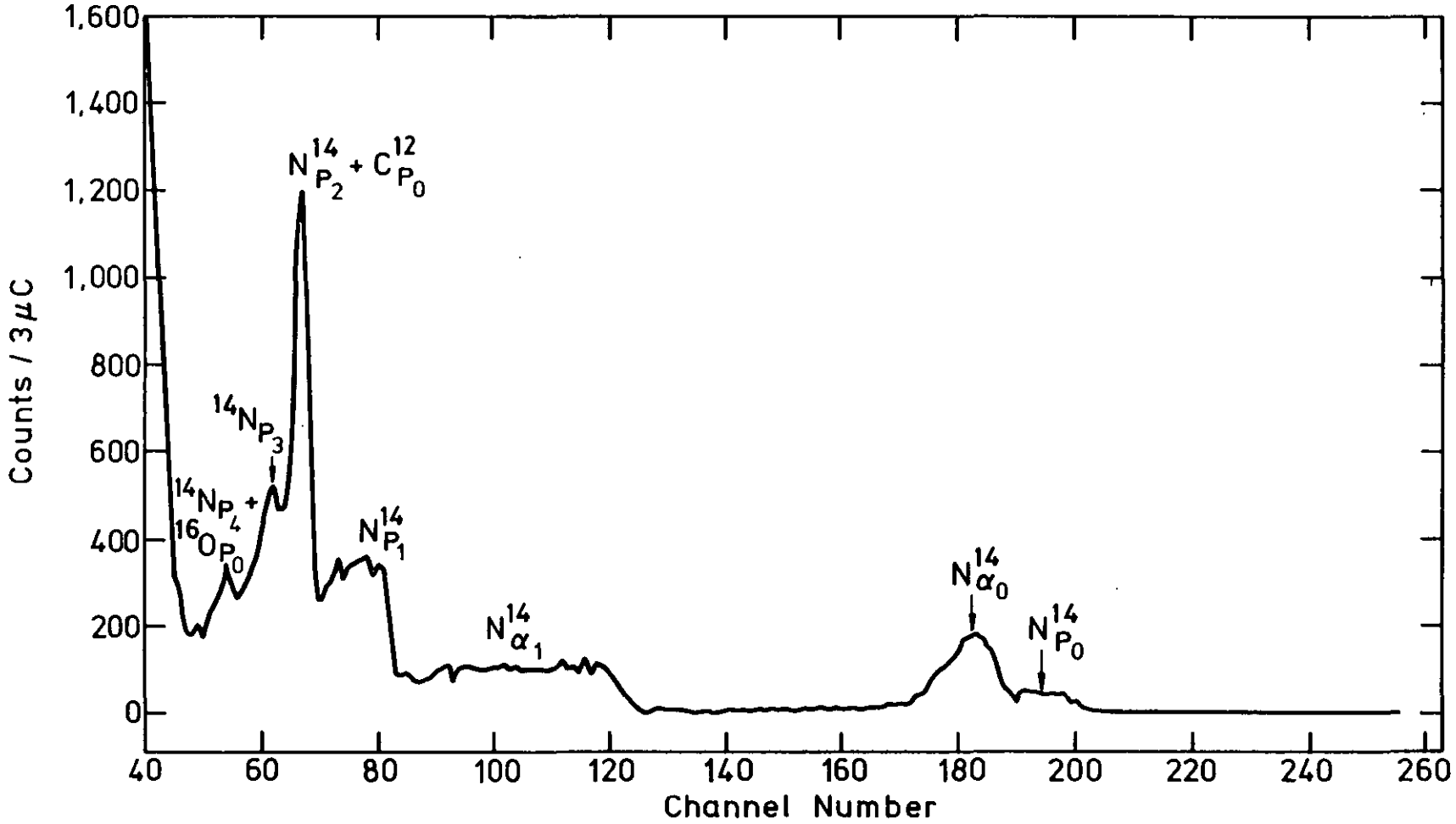

FIG.5·7.(d,p) SPECTRUM OF NITROGEN, E_{OD}= 1·3 MeV, θ = 135°

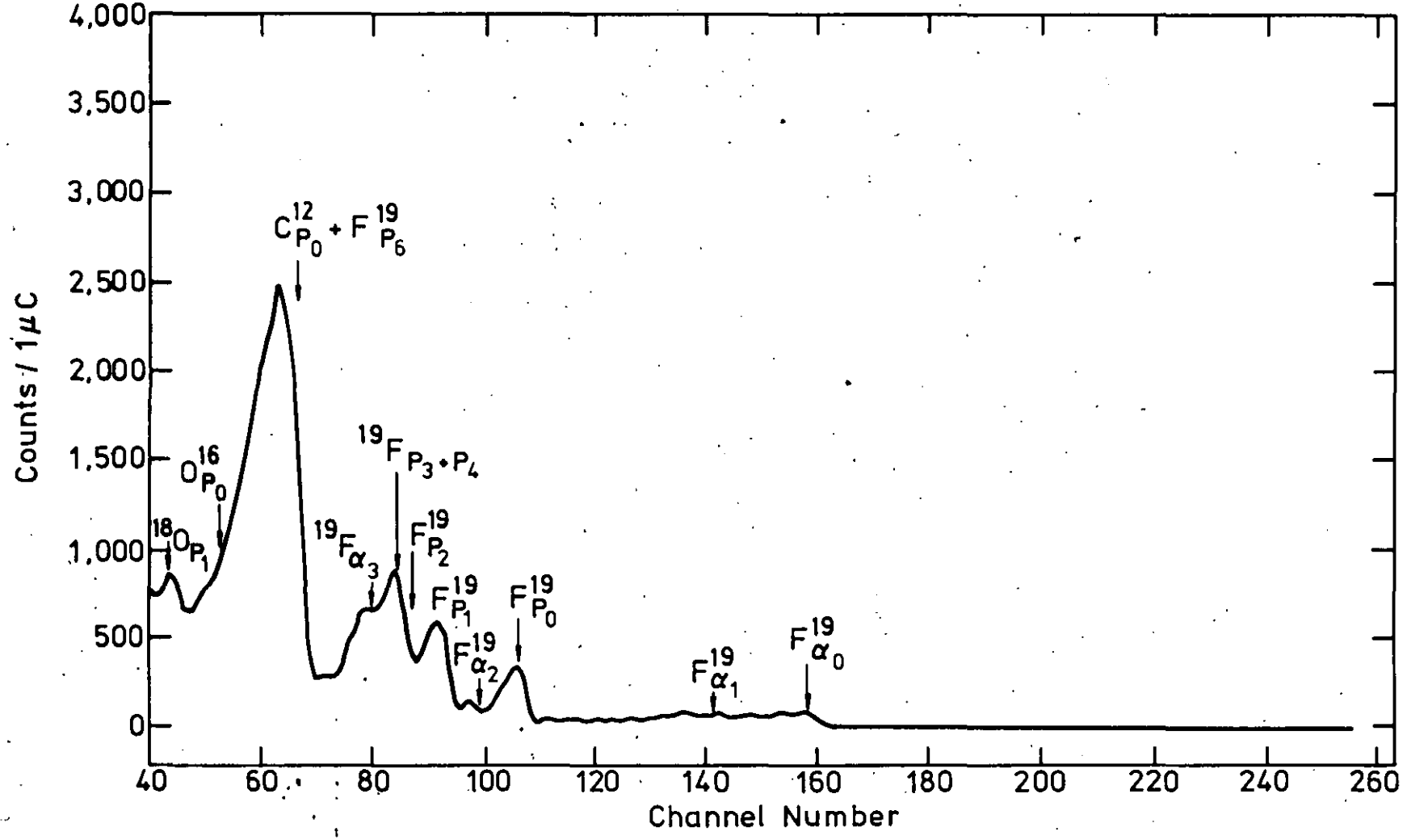

FIG.5·8.(d,p) SPECTRUM OF SrF_2, E_{OD}= 1·3 MeV, θ = 135°

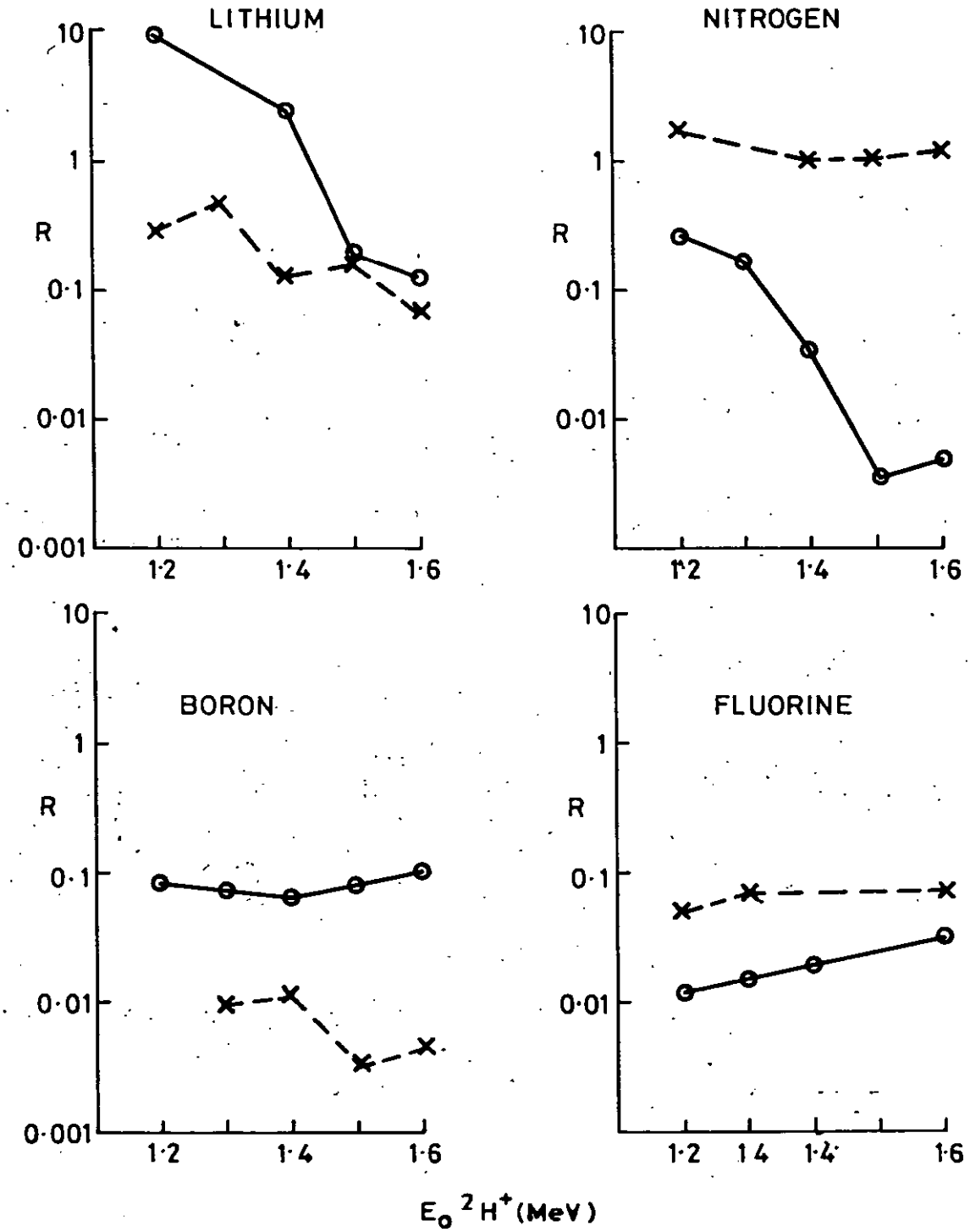

R = (YIELD OF 1 Wt % INTERFERENCE/μC)/(YIELD 1 Wt % ^{13}C OR ^{12}C/μC) CORRECTED FOR STOPPING POWER DIFFERENCES.

o——— ^{13}C x— — — — ^{12}C

ALL SUBSEQUENT SIMILAR FIGURES FOLLOW THIS SAME NOTATION

FIG 5·9 (d,p) THE INFLUENCE OF INCIDENT BEAM ENERGY ON THE INTERFERENCE YIELD.

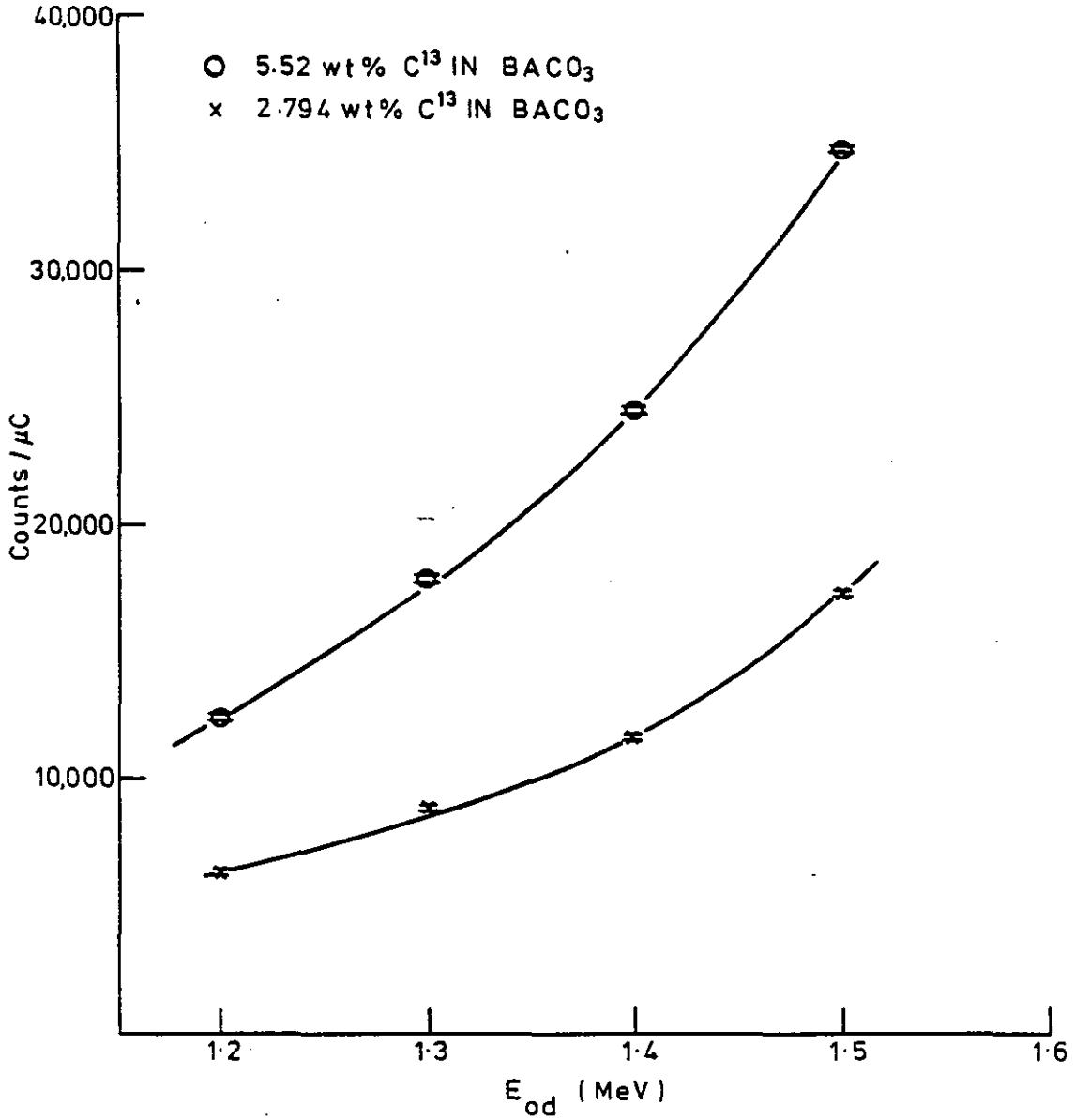

FIG.5·10(∂, p) VARIATION OF C^{13} YIELD WITH DIFFERENT INCIDENT BEAM ENERGIES.

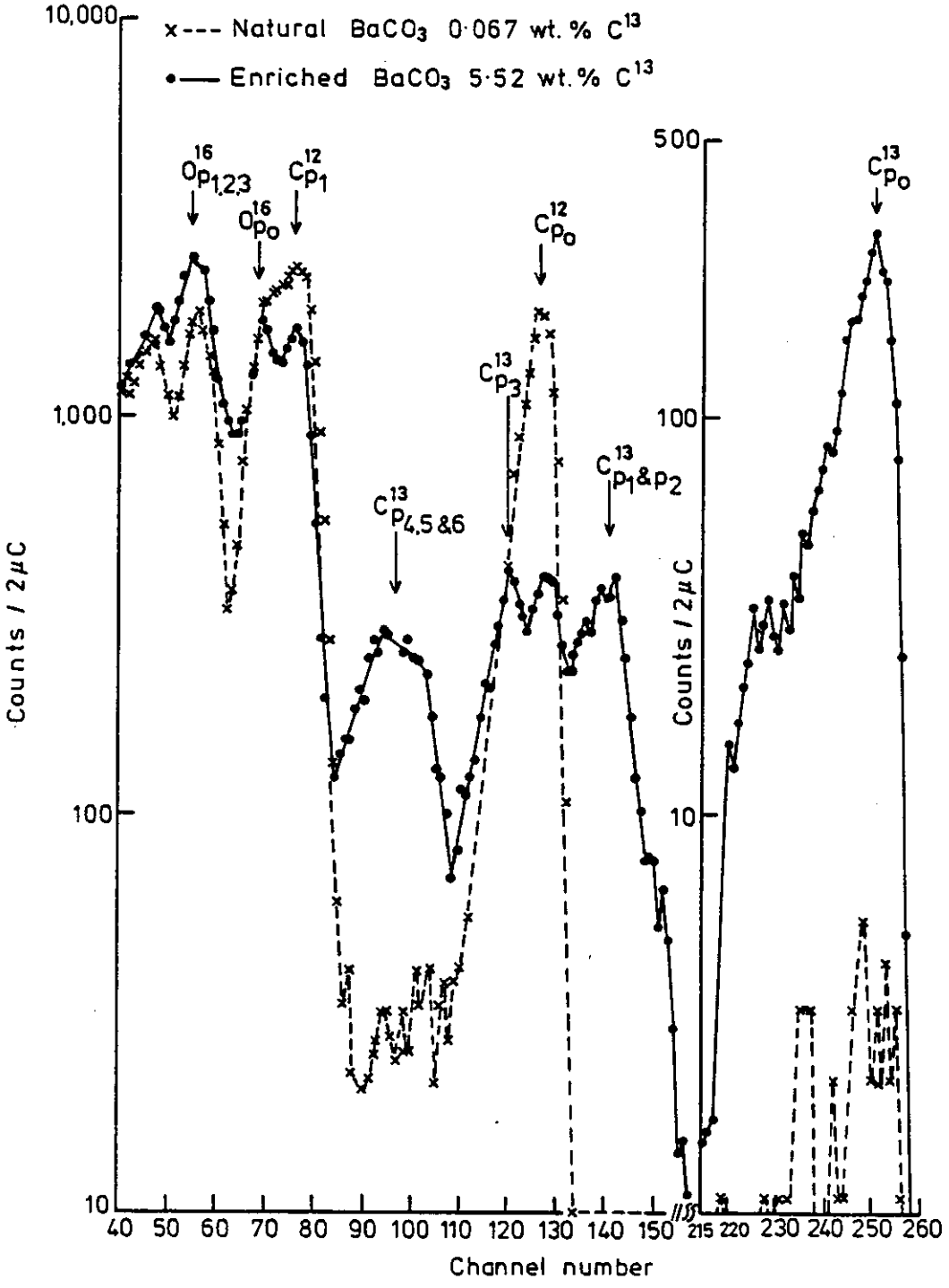

FIG. 5.11. (^{3}He, p) SPECTRA OF NATURAL AND ENRICHED ^{13}C SAMPLES OF $BaCO_3$. $E_{0\,^3He}$ = 2·8 MeV, θ = 135°

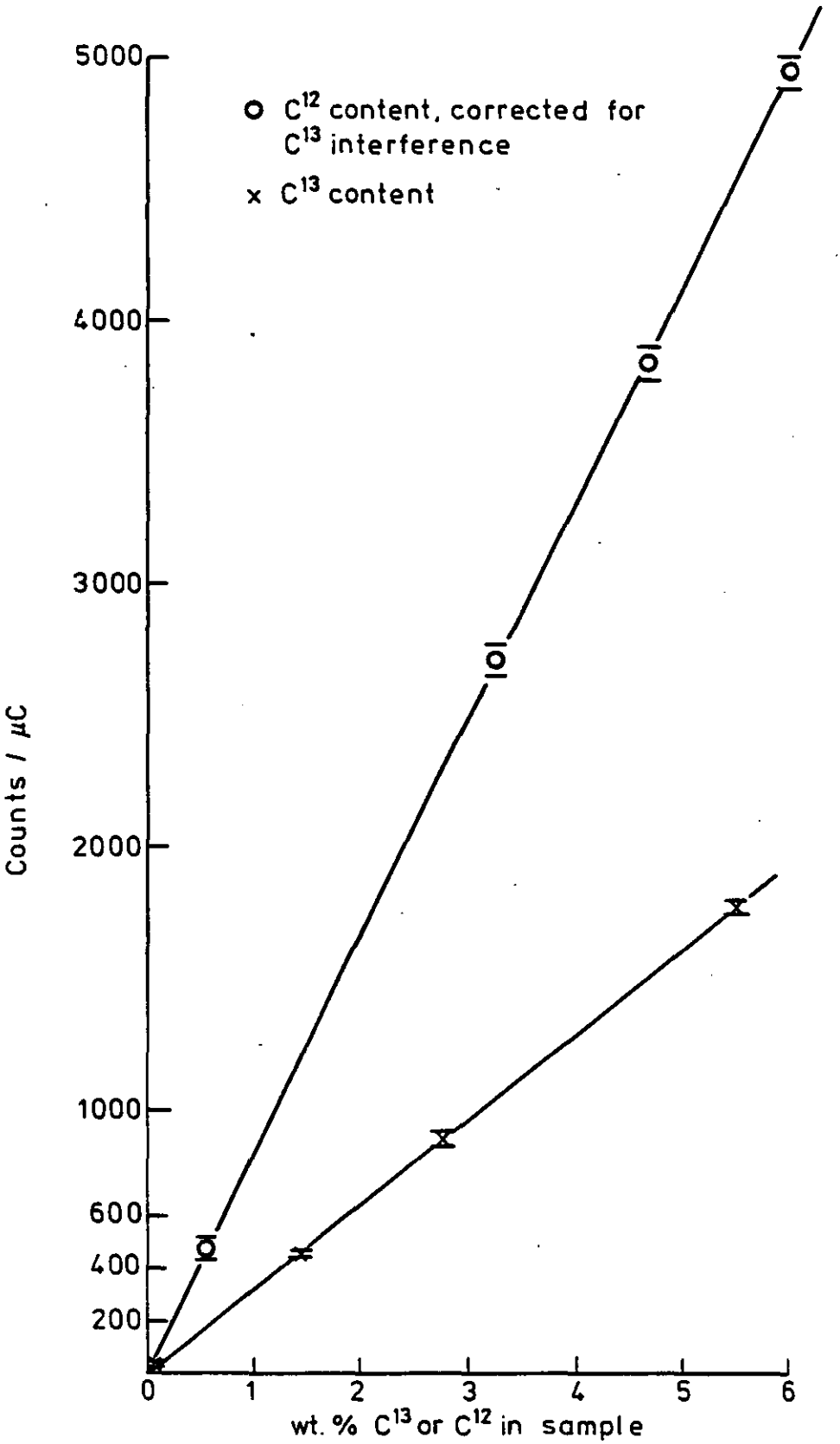

FIG.5·12(He^3,p) CALIBRATION CURVES OF C^{13} AND C^{12} IN $BaCO_3$. E_o He^3 = 2·8 MeV. θ = 135°

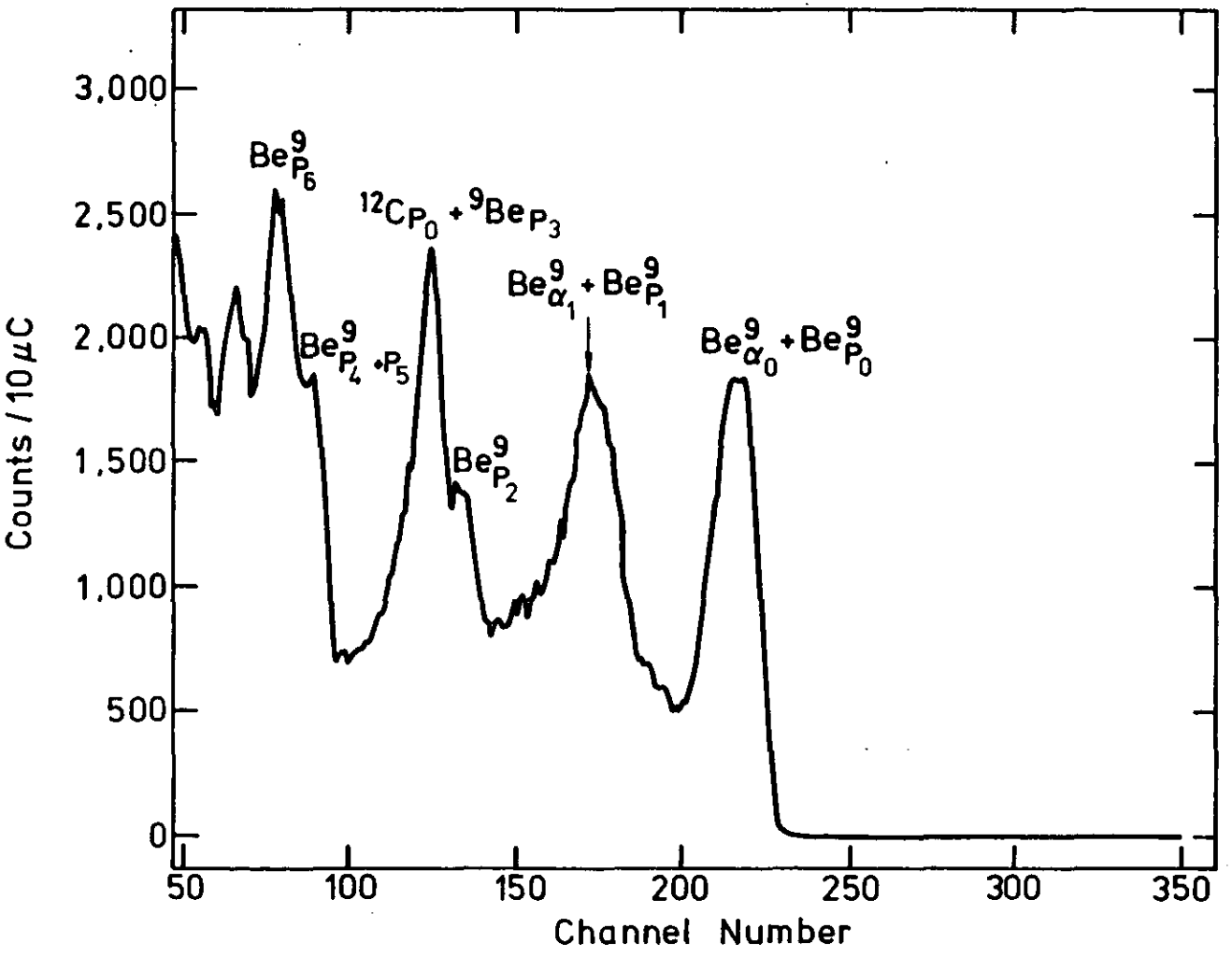

FIG.5·13. (^{3}He,p) SPECTRUM OF BERYLLIUM, $E_0{}^3He^+ = 2{\cdot}8$ MeV, $\theta = 135°$

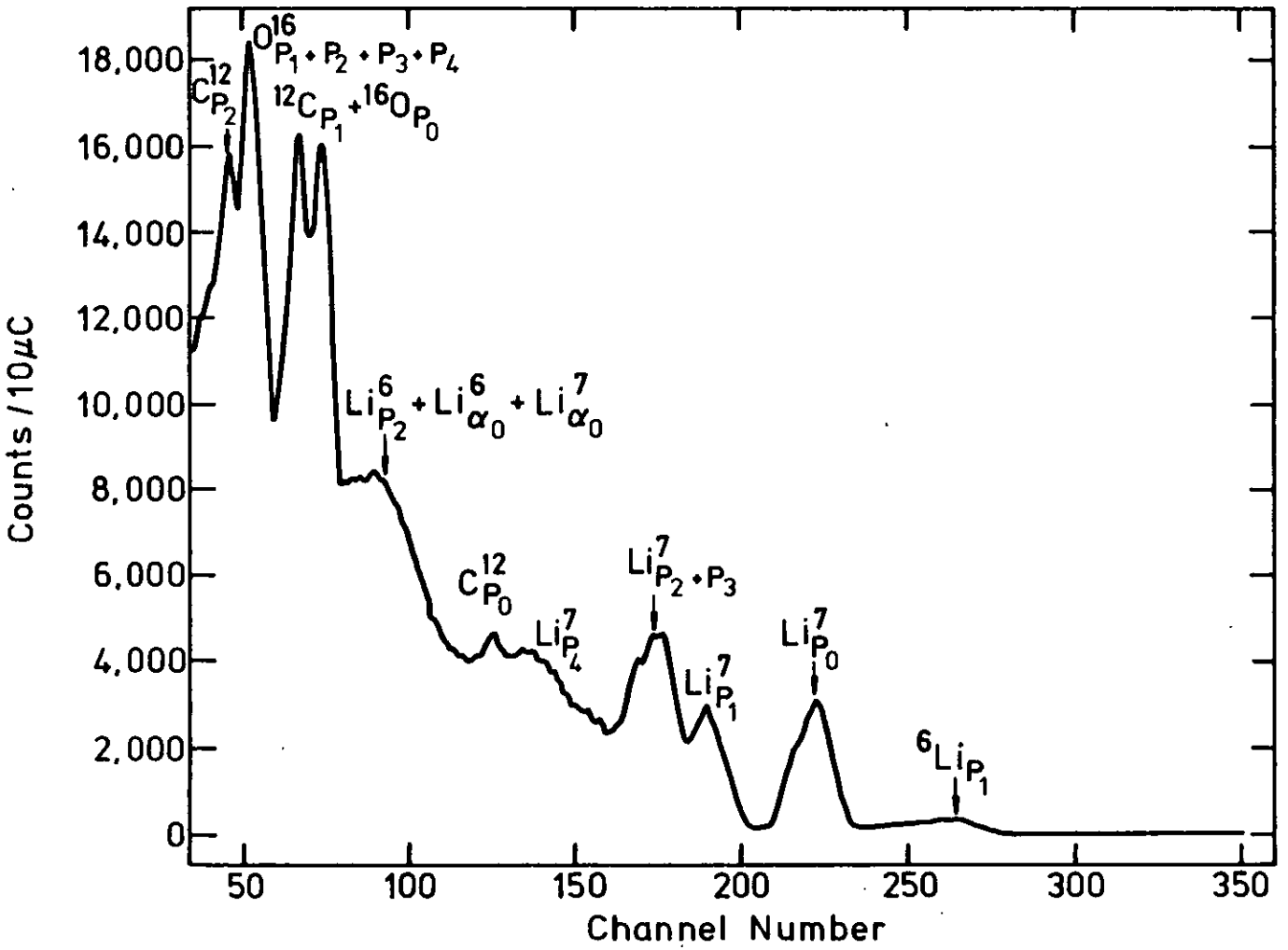

FIG. 5·14. (^{3}He, p) SPECTRUM OF $LiNbO_3$, E_0 $^3He^+ = 2{\cdot}8$ MeV, $\theta = 135°$

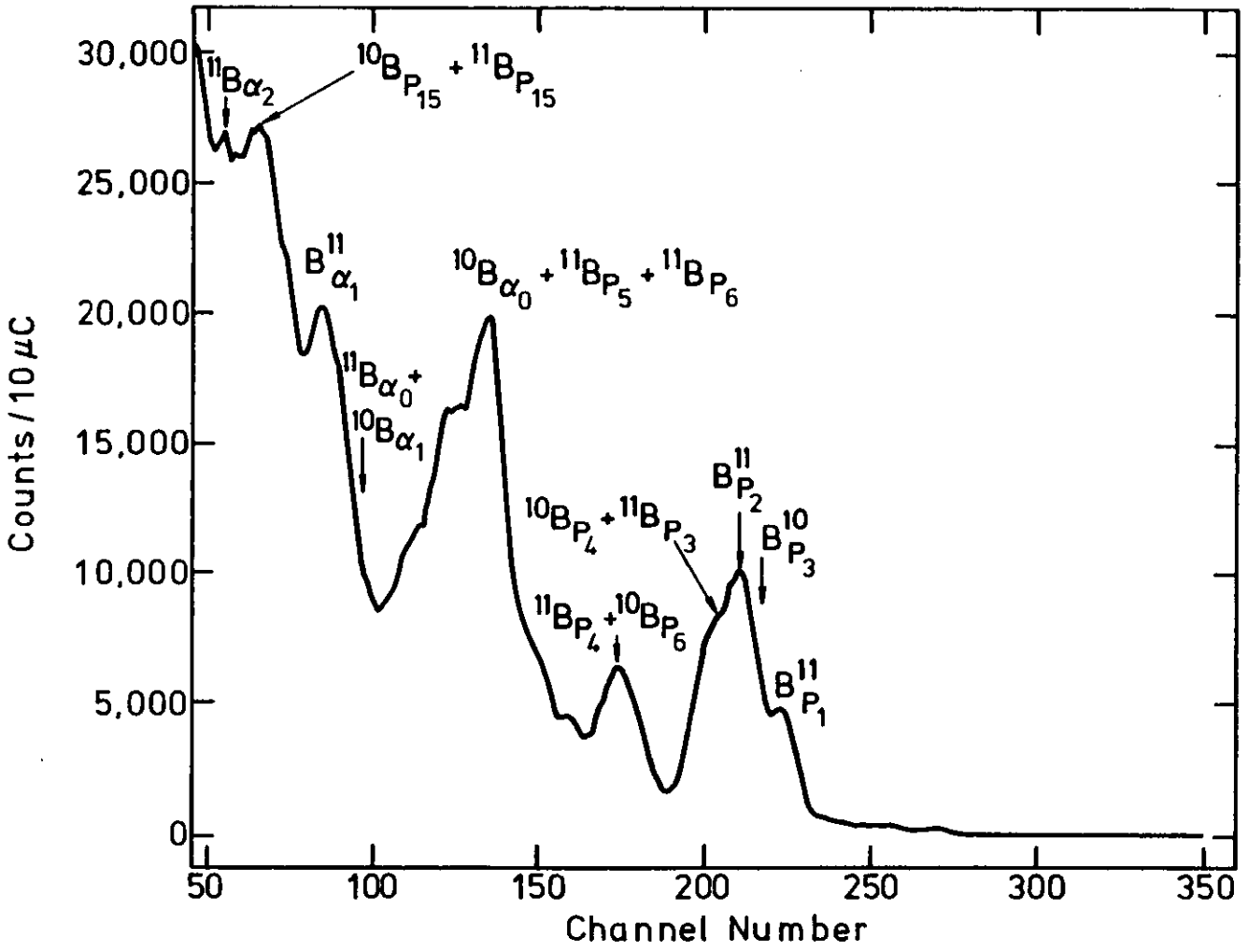

FIG. 5·15. (^{3}He,p) SPECTRUM OF SPECPURE BORON.
E_0 $^3He^+ = 2{\cdot}8$ MeV, $\theta = 135°$

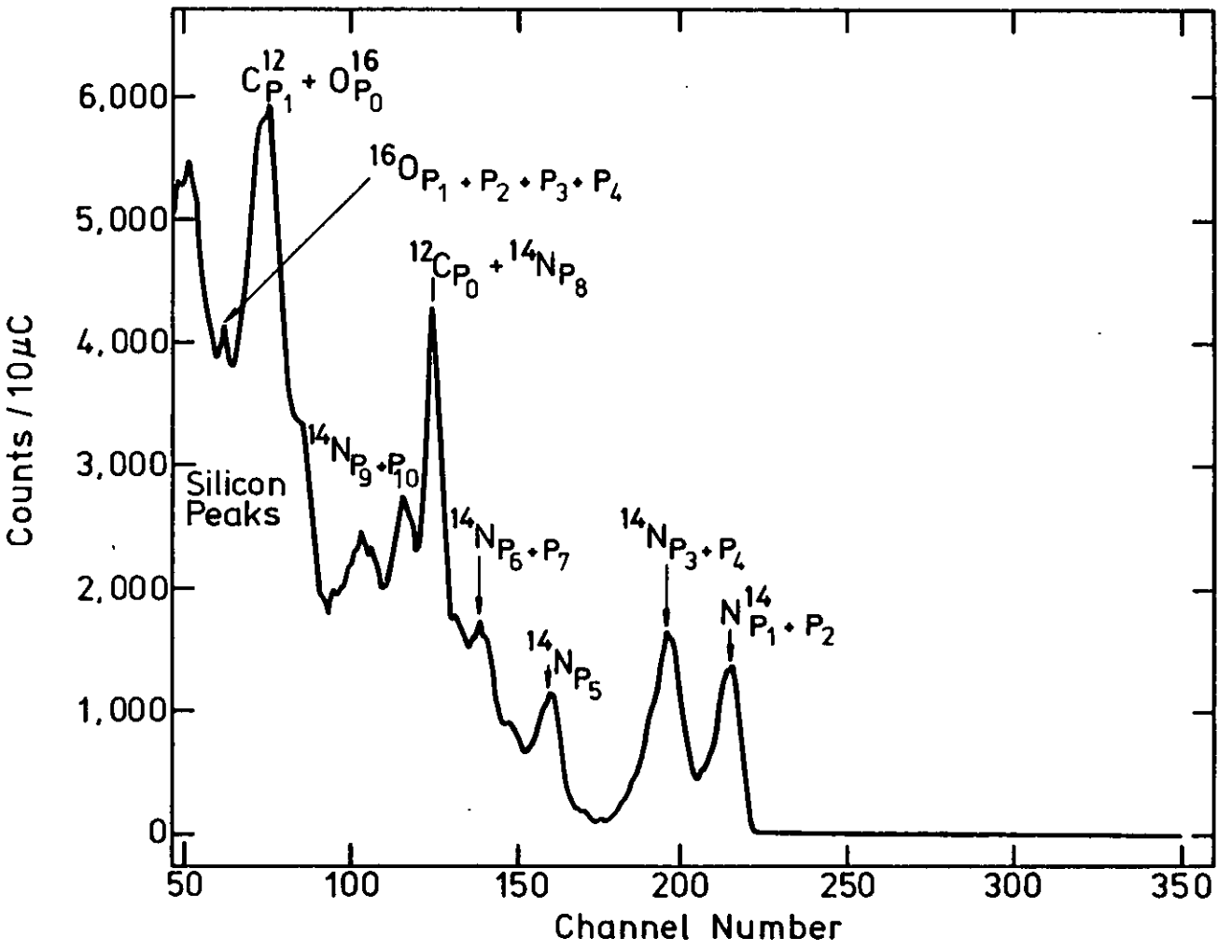

FIG. 5·16. (^{3}He, p) SPECTRUM OF SILICON NITRIDE.
$E_0\ ^3He^+ = 2{\cdot}8$ MeV, $\theta = 135°$

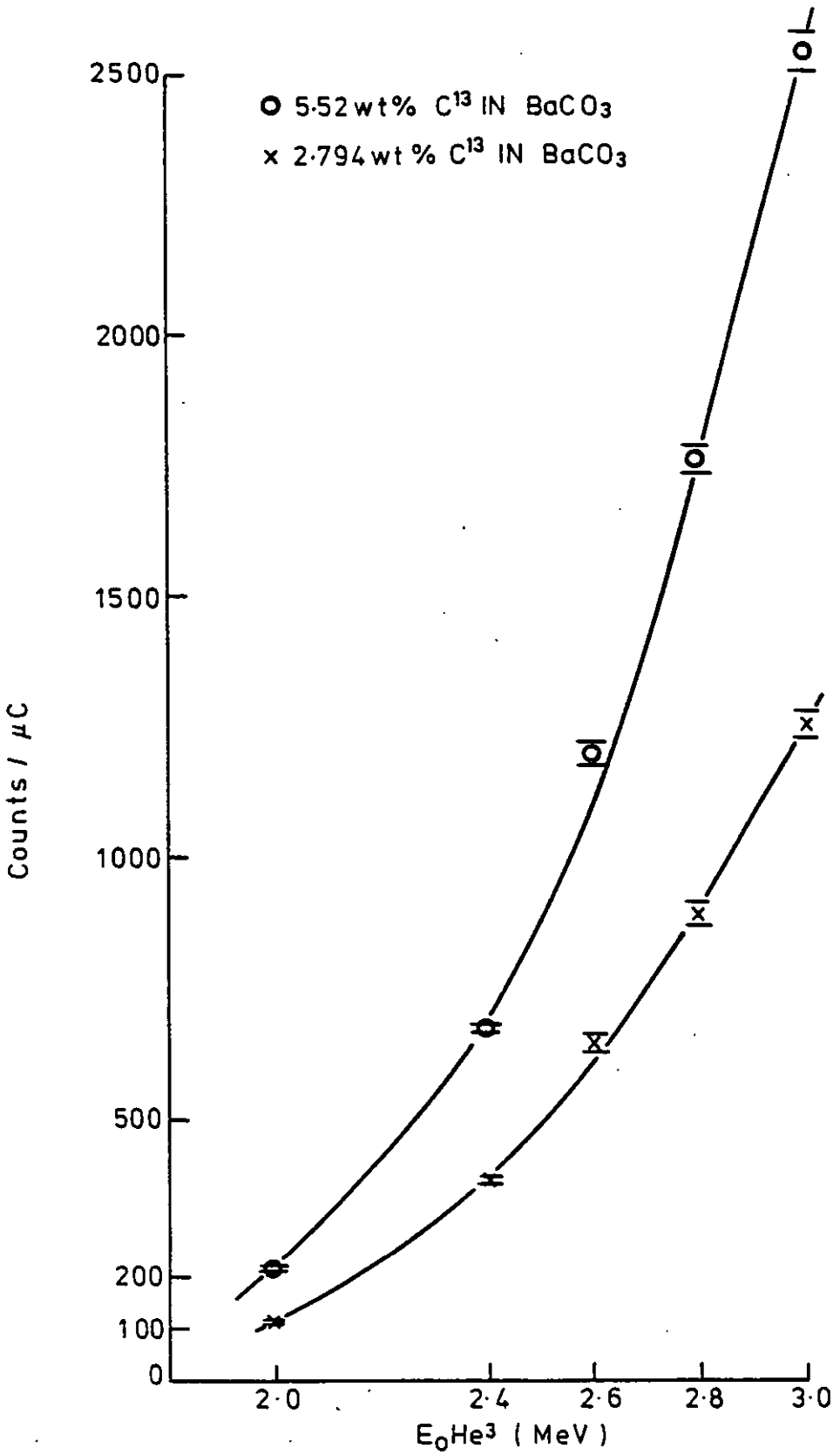

FIG.5·17.(He^3,p) VARIATION OF C^{13} YIELD WITH DIFFERENT INCIDENT BEAM ENERGIES.

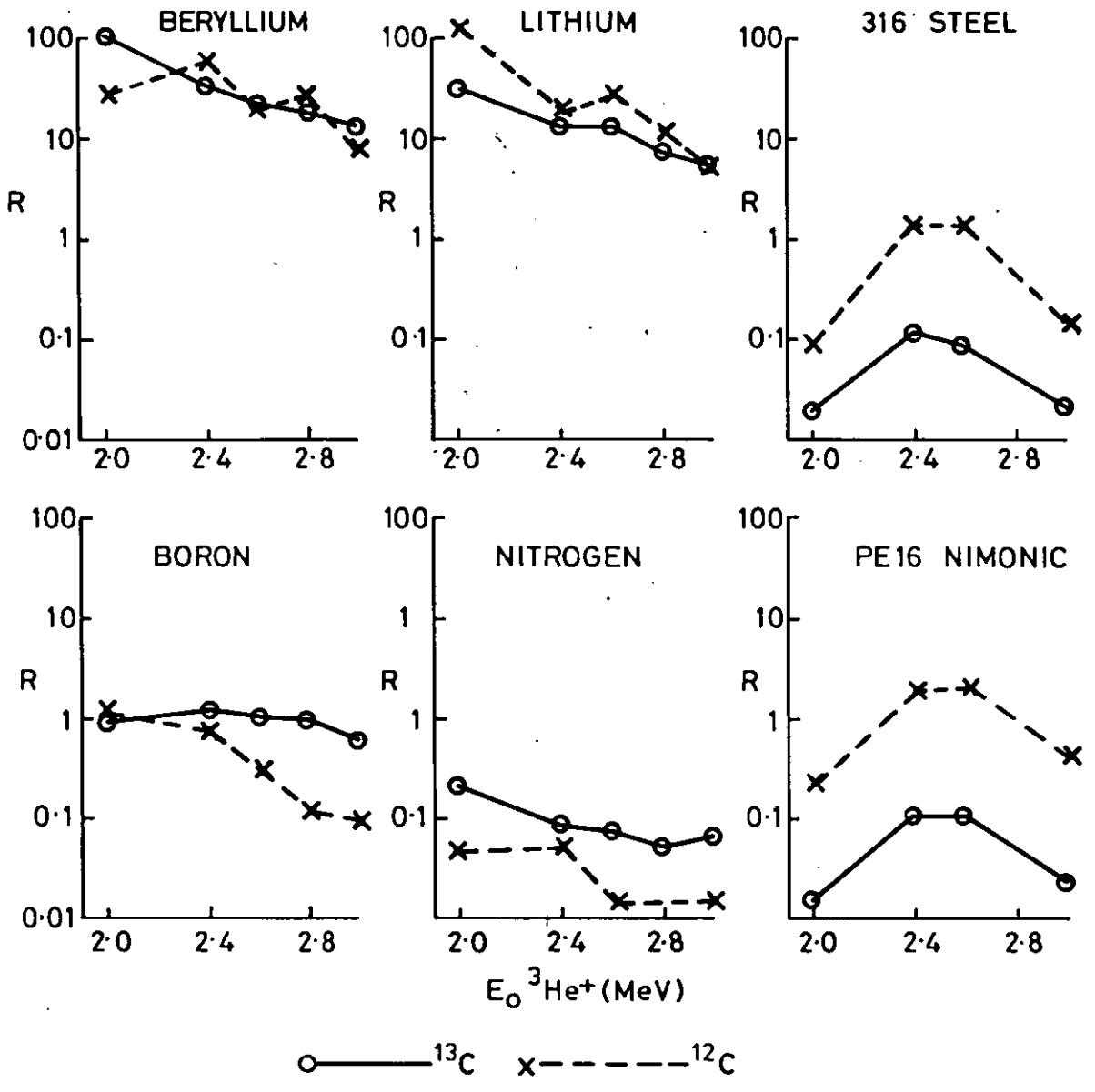

FIG 5·18 (^{3}He,p) THE INFLUENCE OF INCIDENT BEAM ENERGY ON THE INTERFERENCE YIELD.

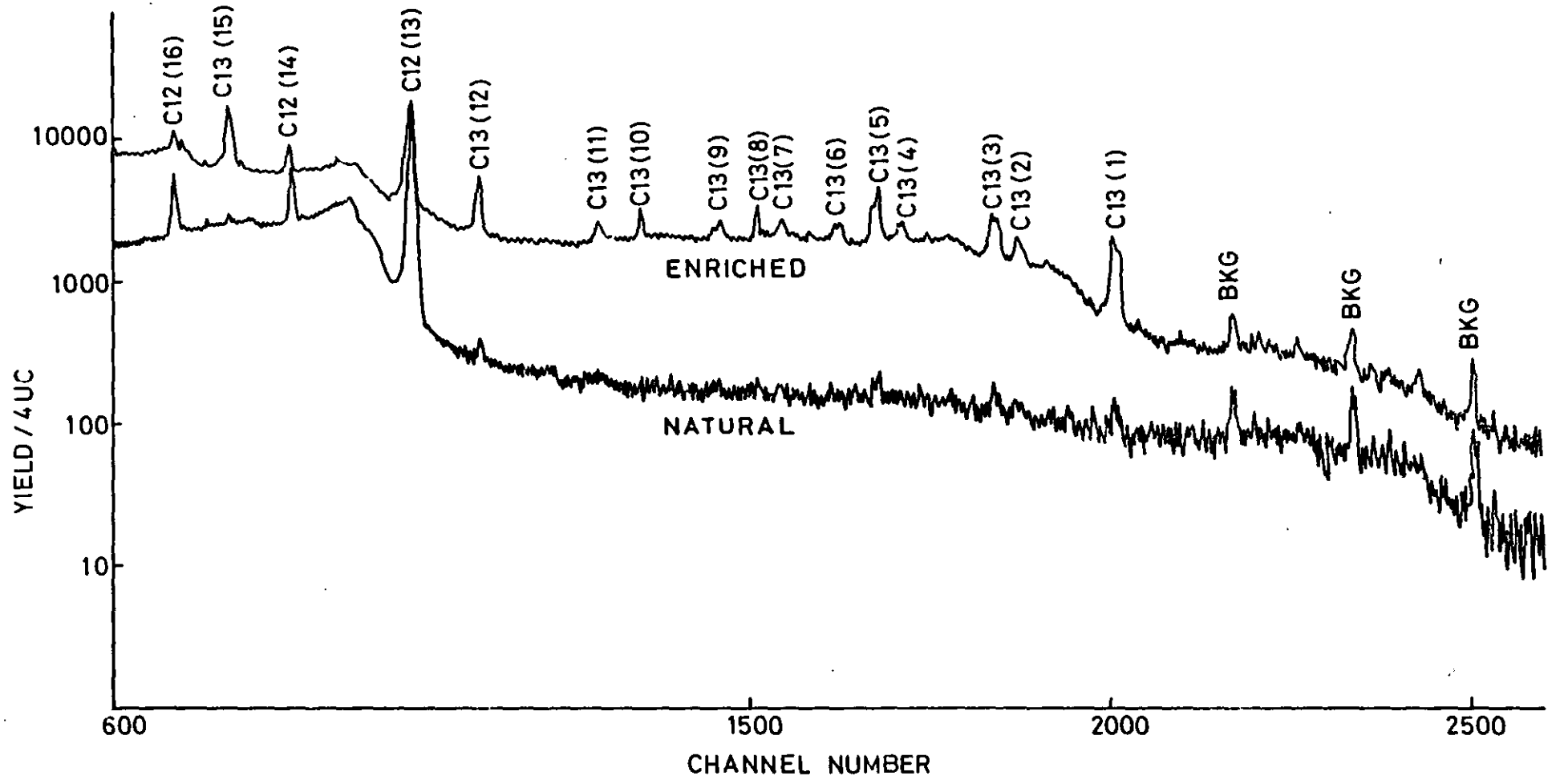

FIG. 5·19. GAMMA SPECTRA OF NATURAL AND ^{13}C ENRICHED TARGETS OF $BaCO_3$, $E_{OD} = 1{\cdot}5$ MeV, $\theta = 0°$

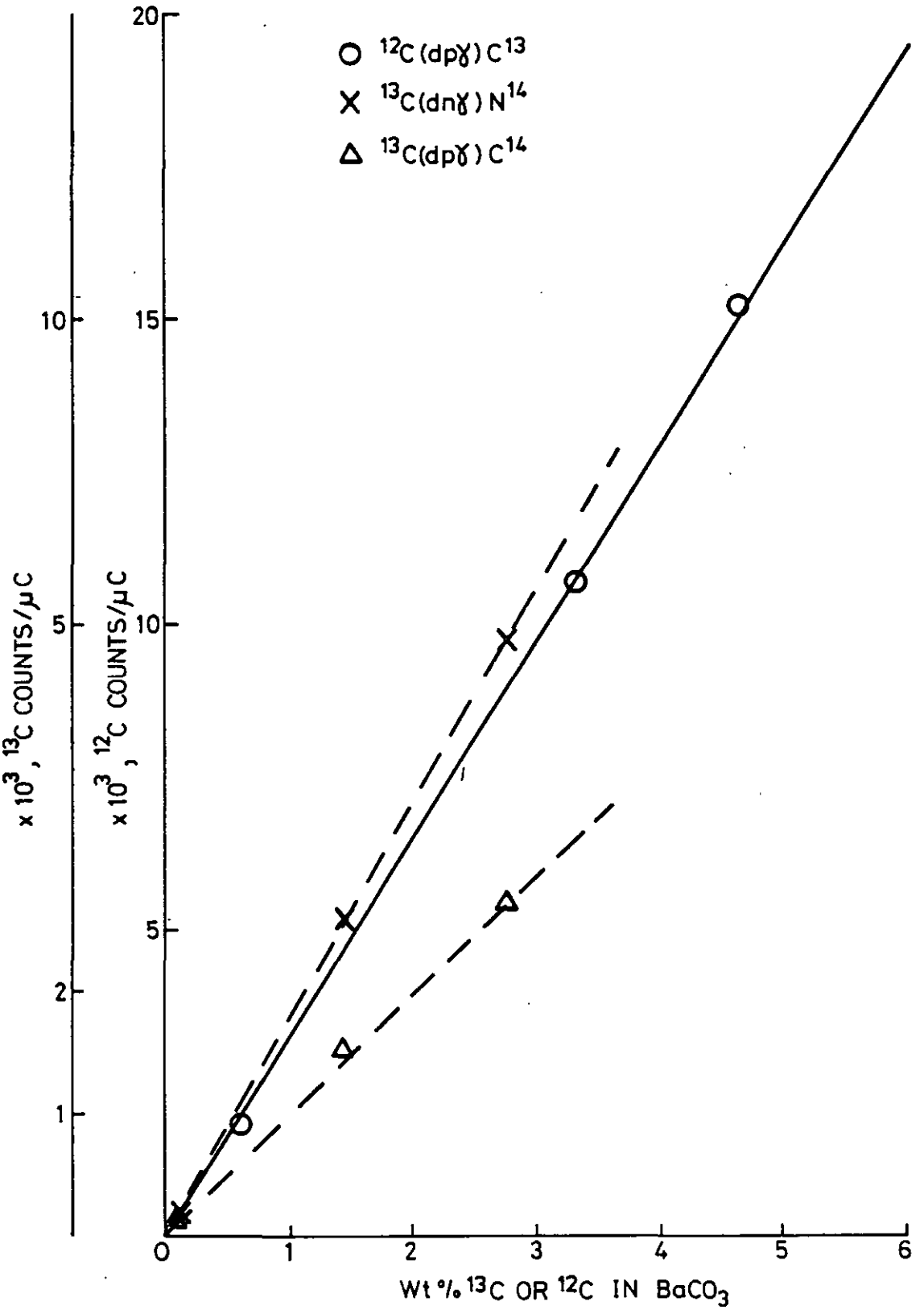

FIG. 5·20. CALIBRATION CURVES OF THE ABOVE THREE DEUTERON INDUCED γ PEAKS. $E_{OD} = 1{\cdot}5$ MeV, $\theta = 0°$

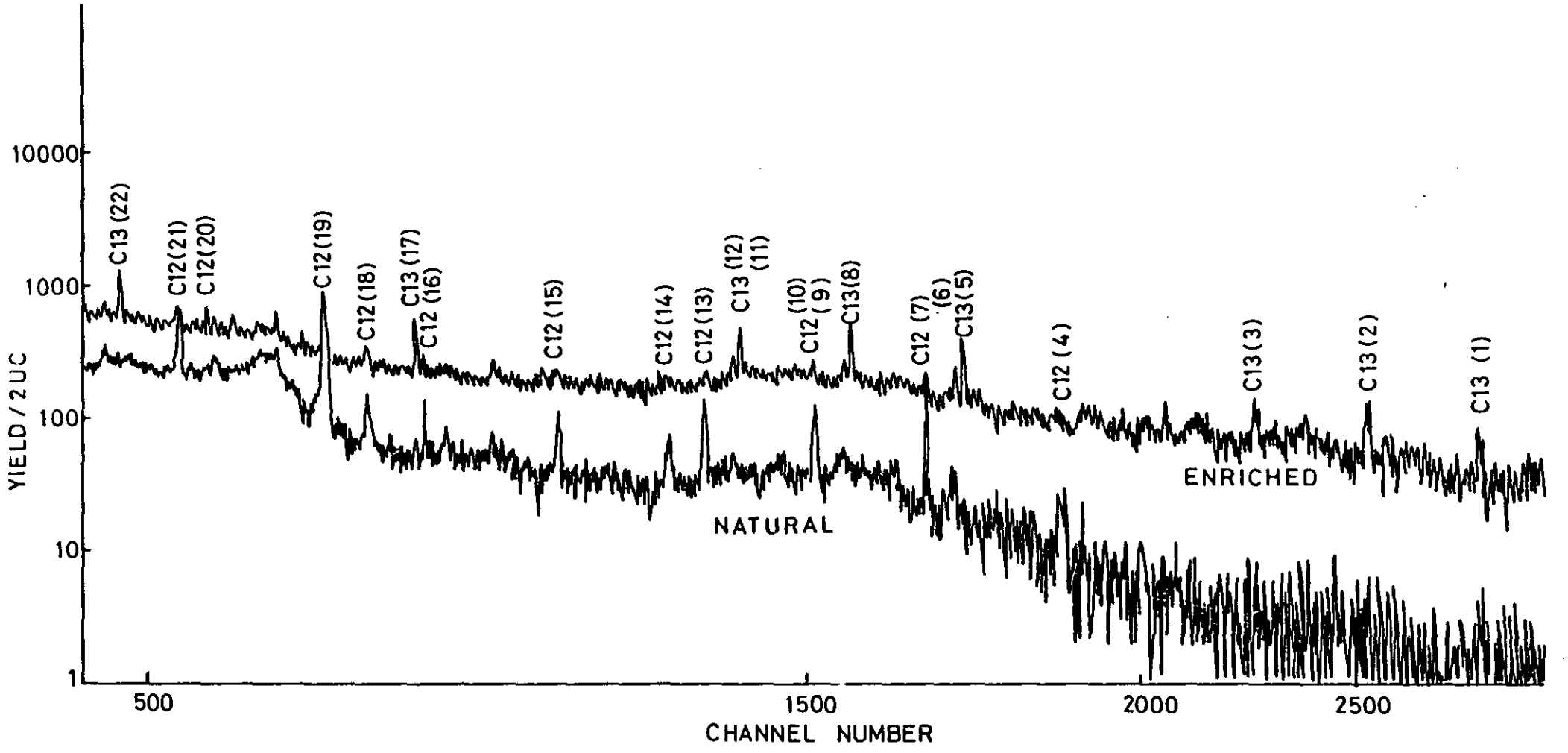

FIG. 5·21. GAMMA SPECTRA OF NATURAL AND ^{13}C ENRICHED TARGETS OF $BaCO_3$, $E_{^3He^+} = 2{\cdot}8$ MeV, $\theta = 0°$

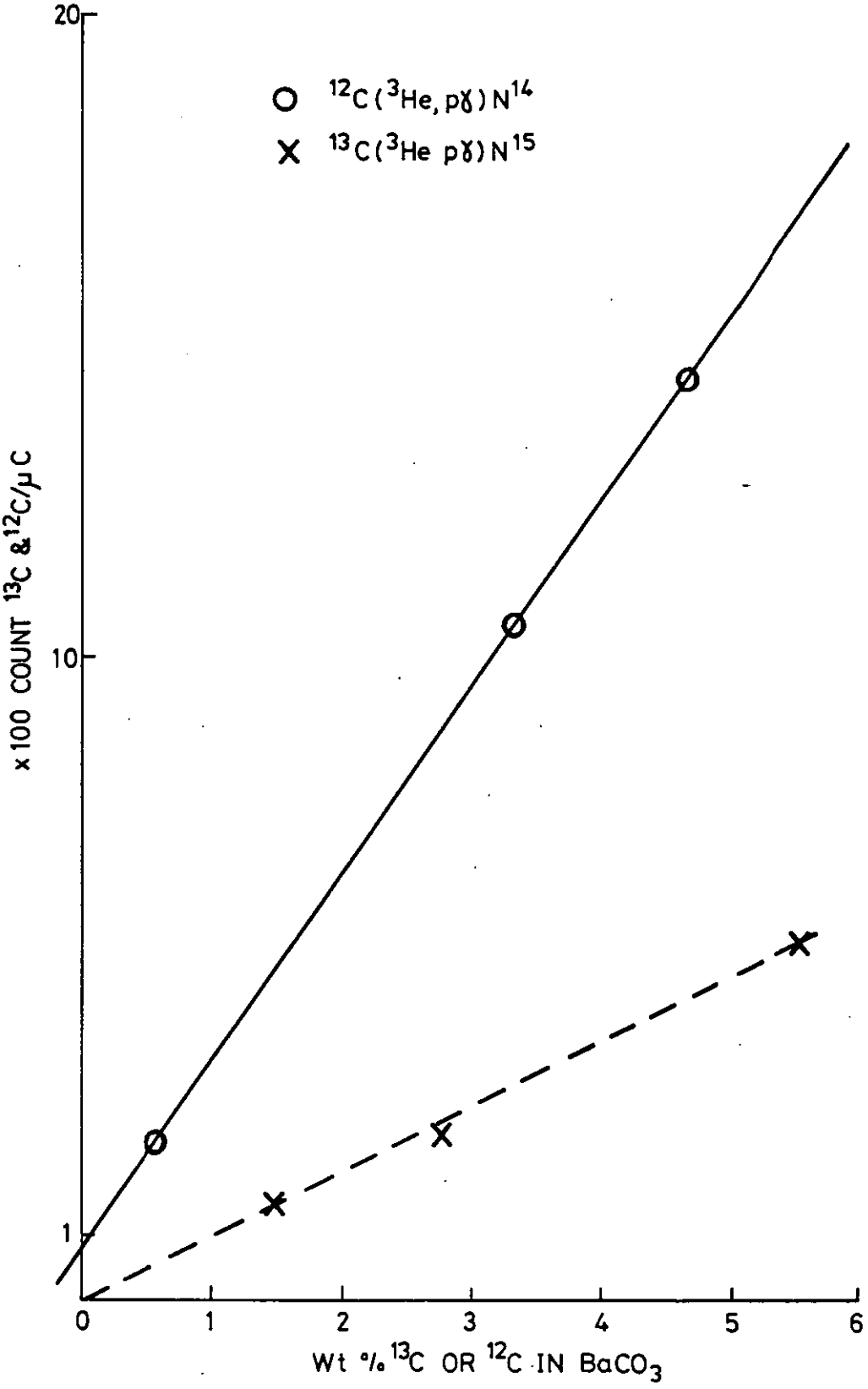

FIG. 5·22. CALIBRATION CURVES OF THE ABOVE TWO ^{3}He INDUCED γ PEAKS, $E_{O\,^{3}He^{+}} = 2{\cdot}8$ MeV, $\theta = 0°$

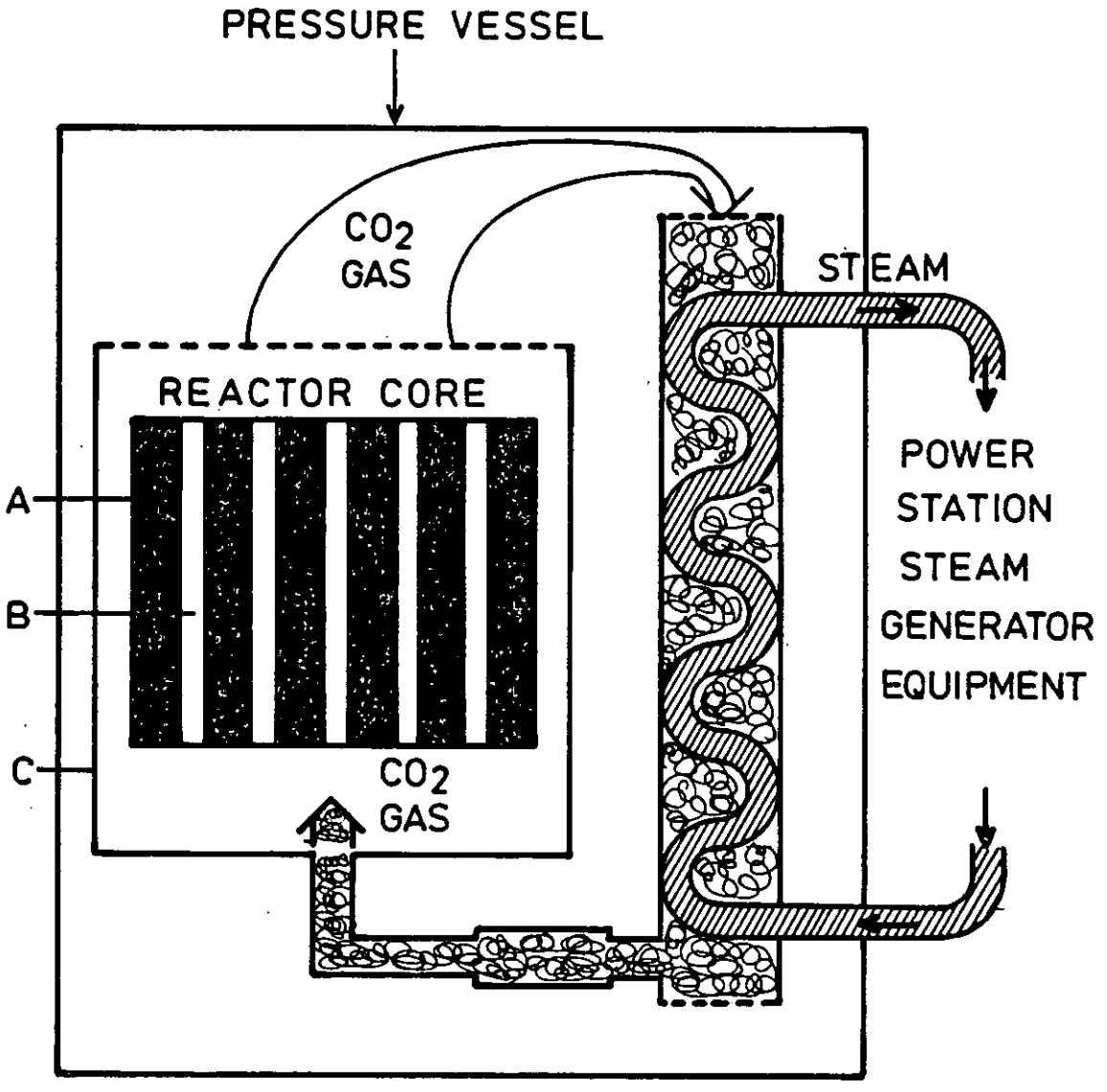

A - GRAPHITE MODERATOR
B - FUEL ELEMENTS
C - REACTOR

FIG. 6.1 SCHEMATIC DIAGRAM OF AN ADVANCED GAS COOLED REACTOR.

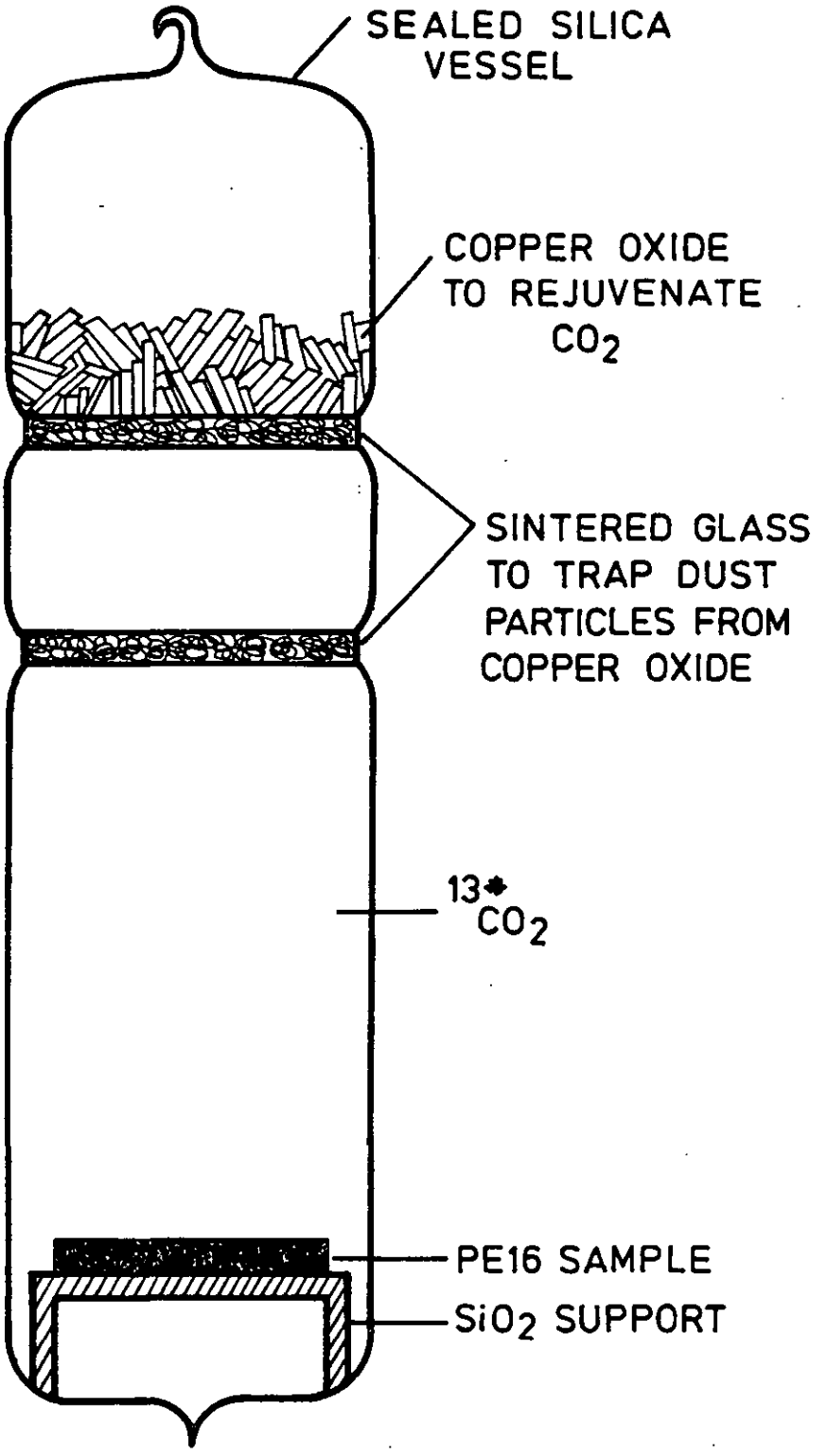

FIG. 6.2 SILICA VESSEL USED DURING ^{13}C LABELLING EXPERIMENTS ON PE16

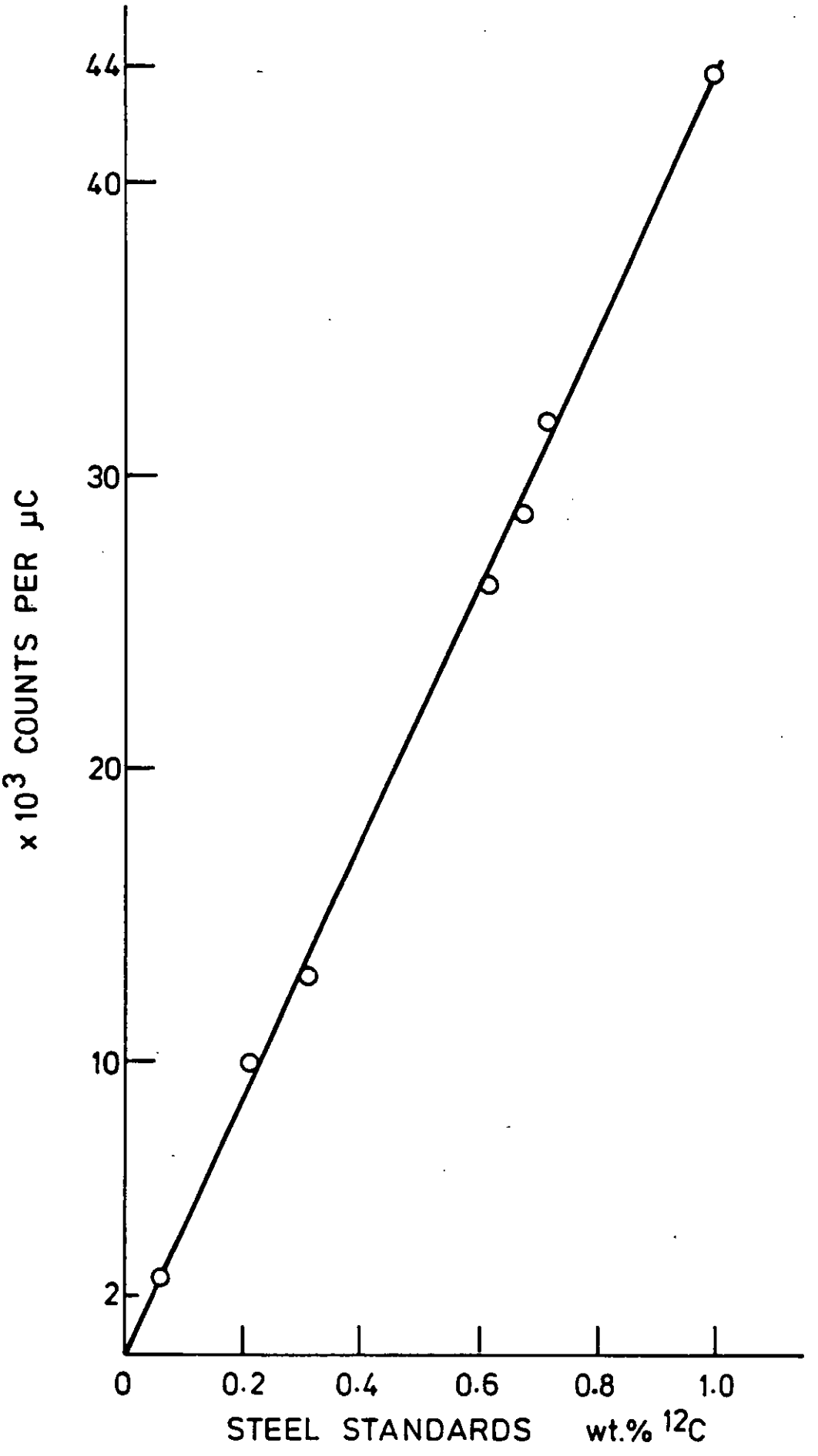

FIG. 6.3 TYPICAL CALIBRATION CURVE FOR ^{12}C STANDARDS IN STEEL, $E_o d = 1.3$ MeV, $\theta = 135°$

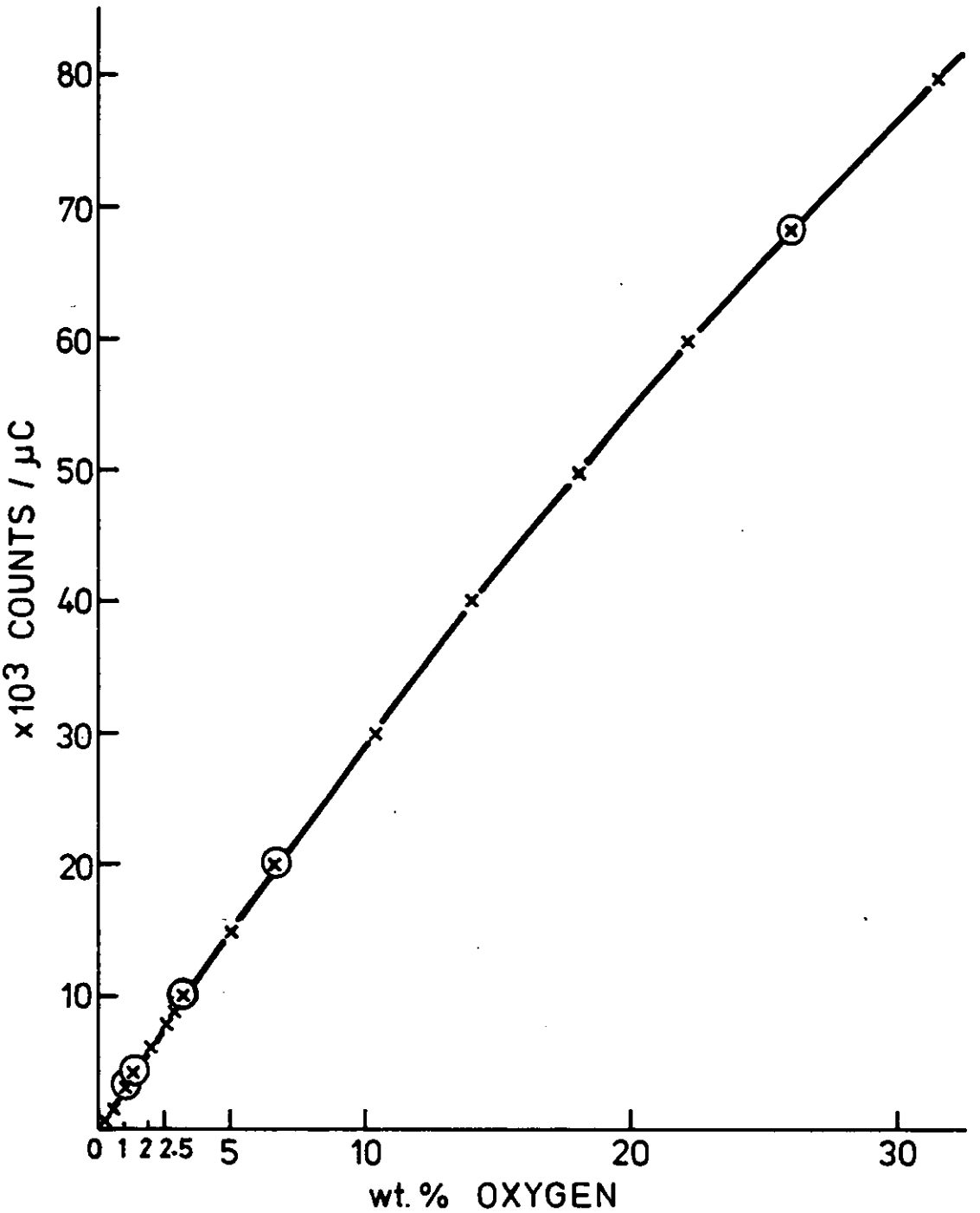

FIG. 6.4 CALIBRATION CURVE FOR OXYGEN STANDARDS IN ZIRCONIUM, $E_o d = 1.1$ MeV, $\theta = 135°$

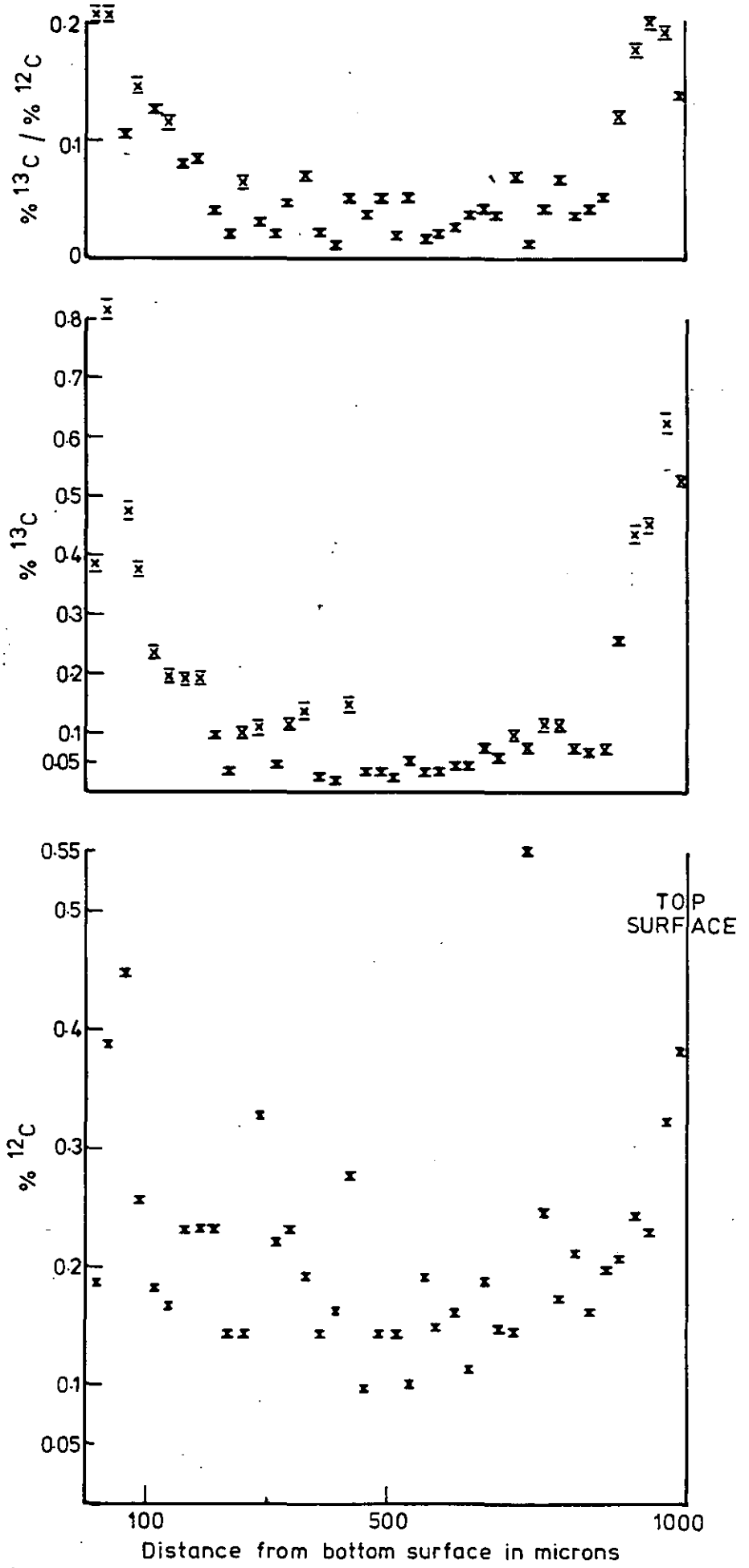

FIG. 6·5 AVERAGE PROFILES OF CARBON DATA IN PE16/21 TREATED FOR 1096 HOURS AT 800°C. IN $^{13}CO_2$ SPATIAL RESOLUTION 25 µm

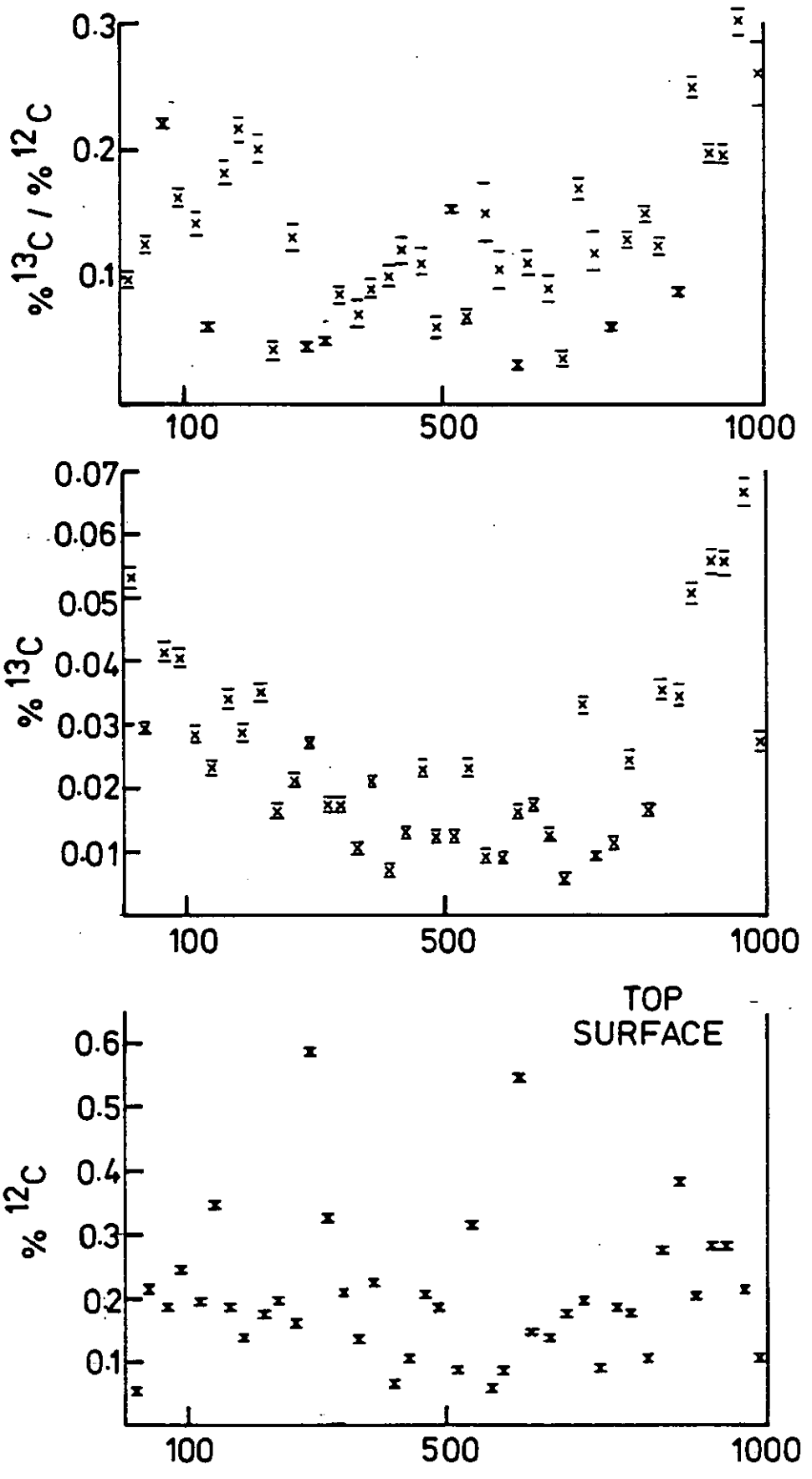

FIG. 6.6 AVERAGE PROFILES OF CARBON DATA IN PE16/23 TREATED FOR 4029 HOURS AT 800°C IN $^{13}CO_2$. SPATIAL RESOLUTION 25 µm.

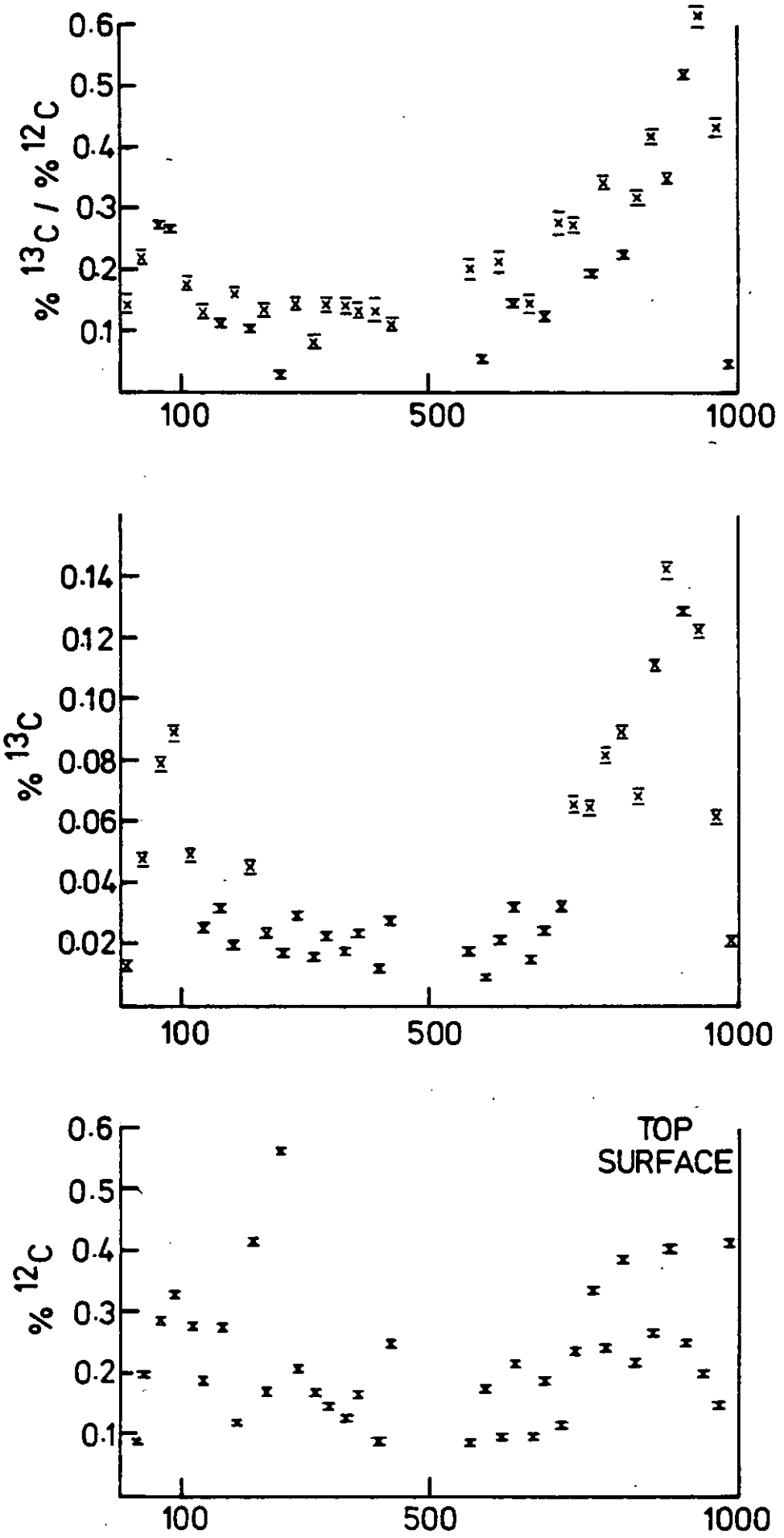

FIG. 6.7 AVERAGE PROFILES OF CARBON DATA IN PE16/24 TREATED FOR 4601 HOURS AT 800°C IN $^{13}CO_2$. SPATIAL RESOLUTION 25μm.

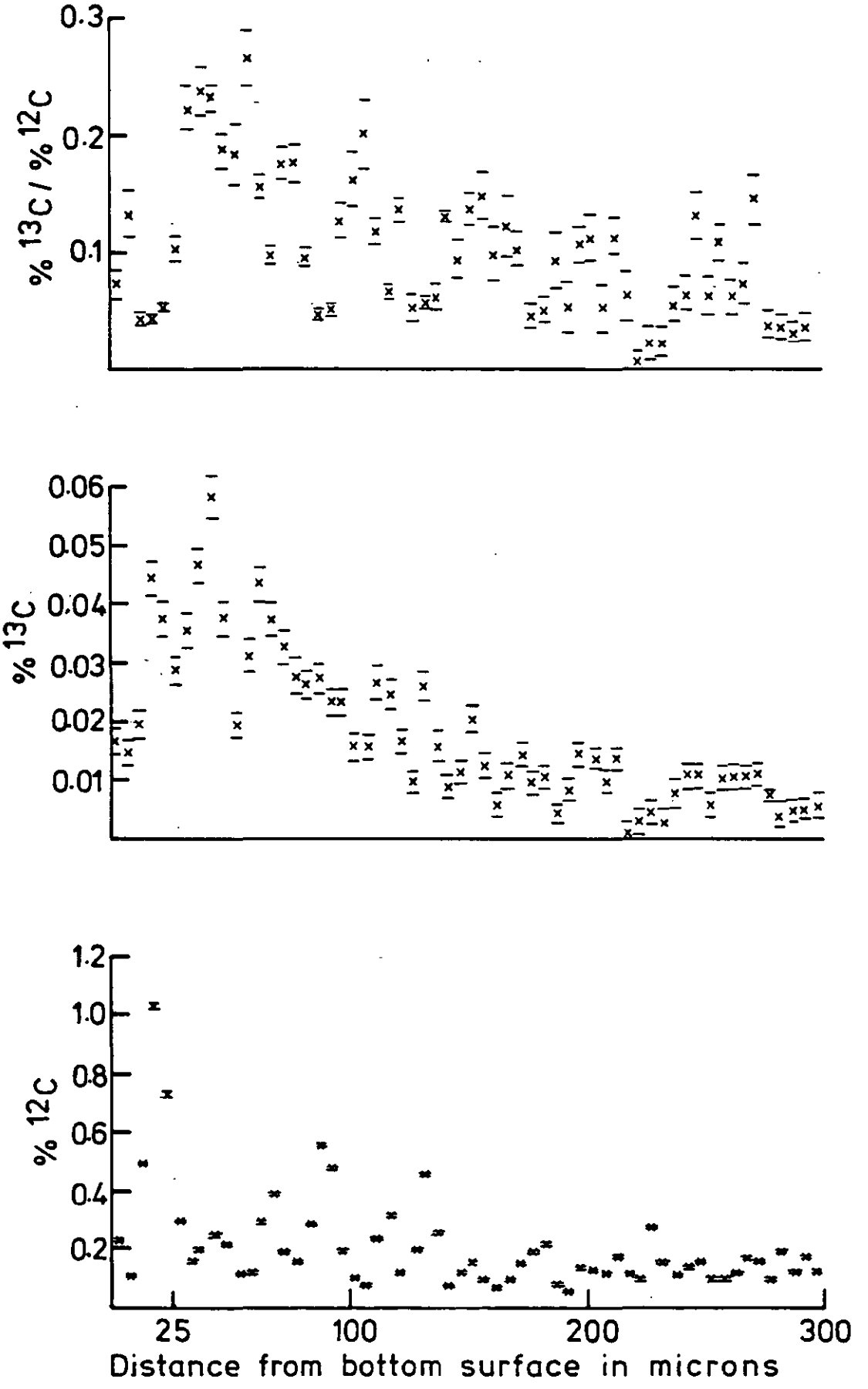

FIG. 6.8 AVERAGE PROFILES OF CARBON DATA IN PE16/21 TREATED FOR 1096 HOURS AT 800°C IN $^{13}CO_2$. SPATIAL RESOLUTION 5 μm.

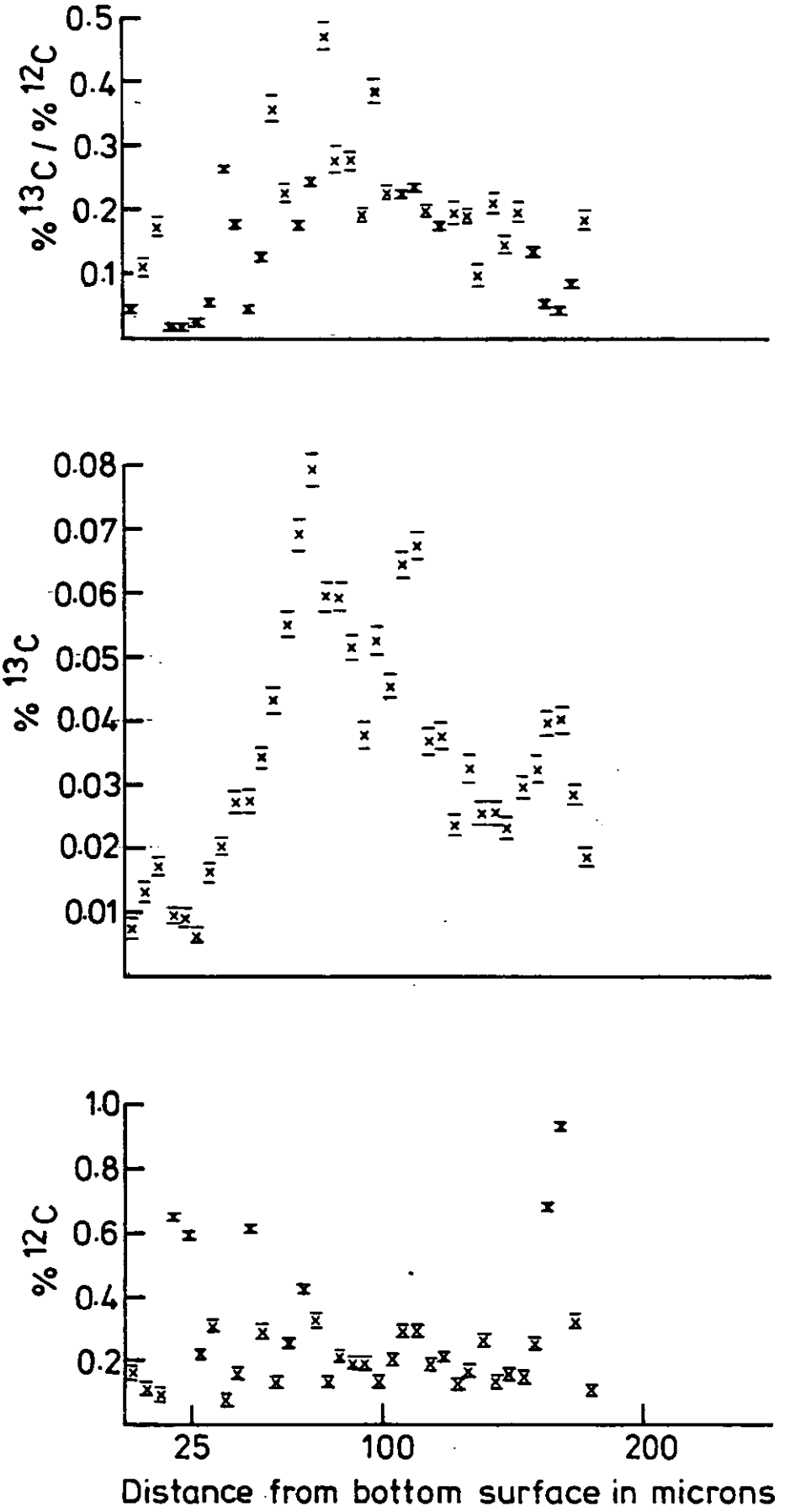

FIG. 6.9 AVERAGE PROFILES OF CARBON DATA IN PE16/23 TREATED FOR 4029 HOURS AT 800°C IN $^{13}CO_2$. SPATIAL RESOLUTION 5 µm.

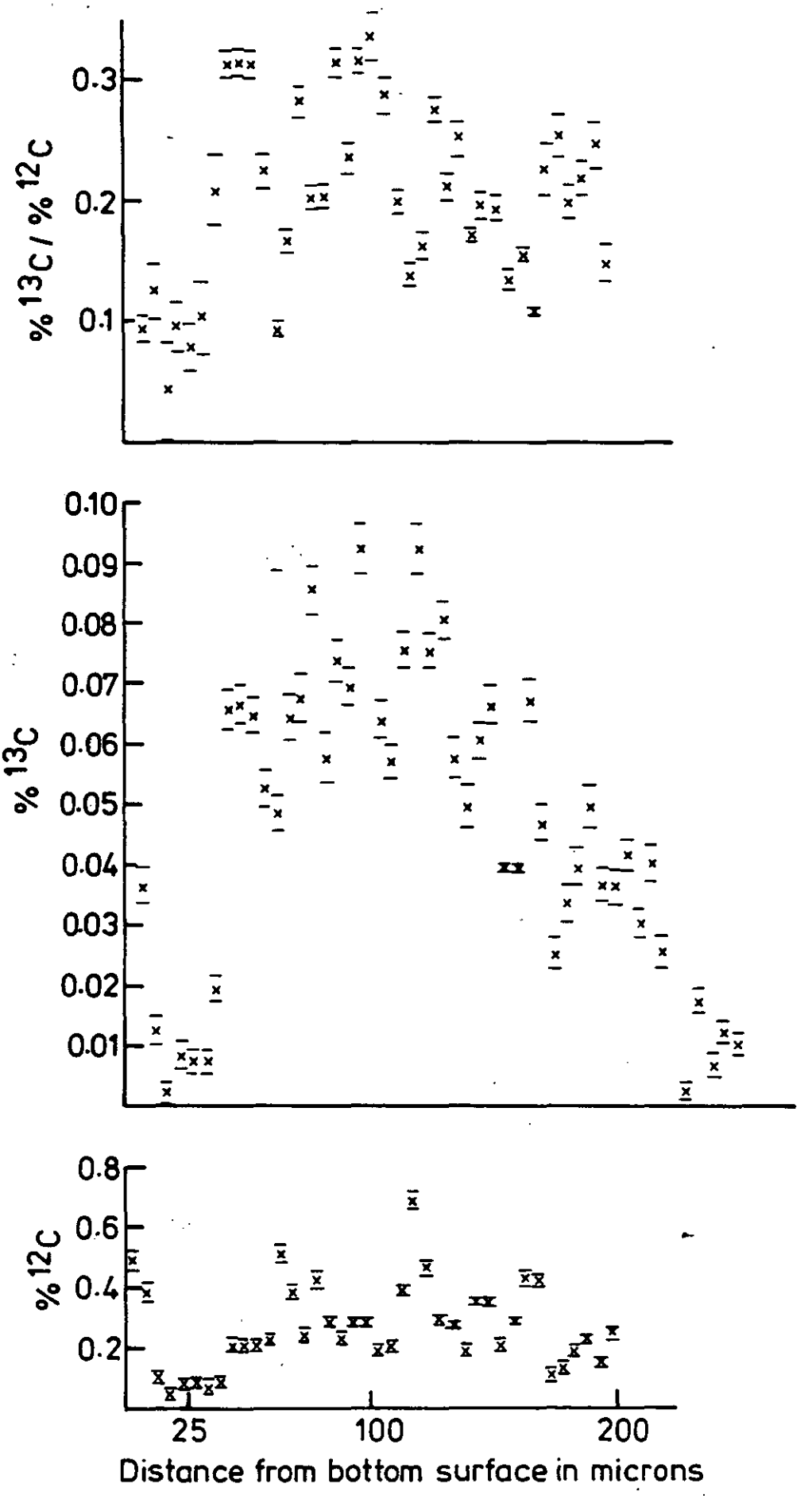

FIG. 6.10 AVERAGE PROFILES OF CARBON DATA IN PE16/24 TREATED FOR 4601 HOURS AT 800°C IN $^{13}CO_2$ SPATIAL RESOLUTION 5μm.

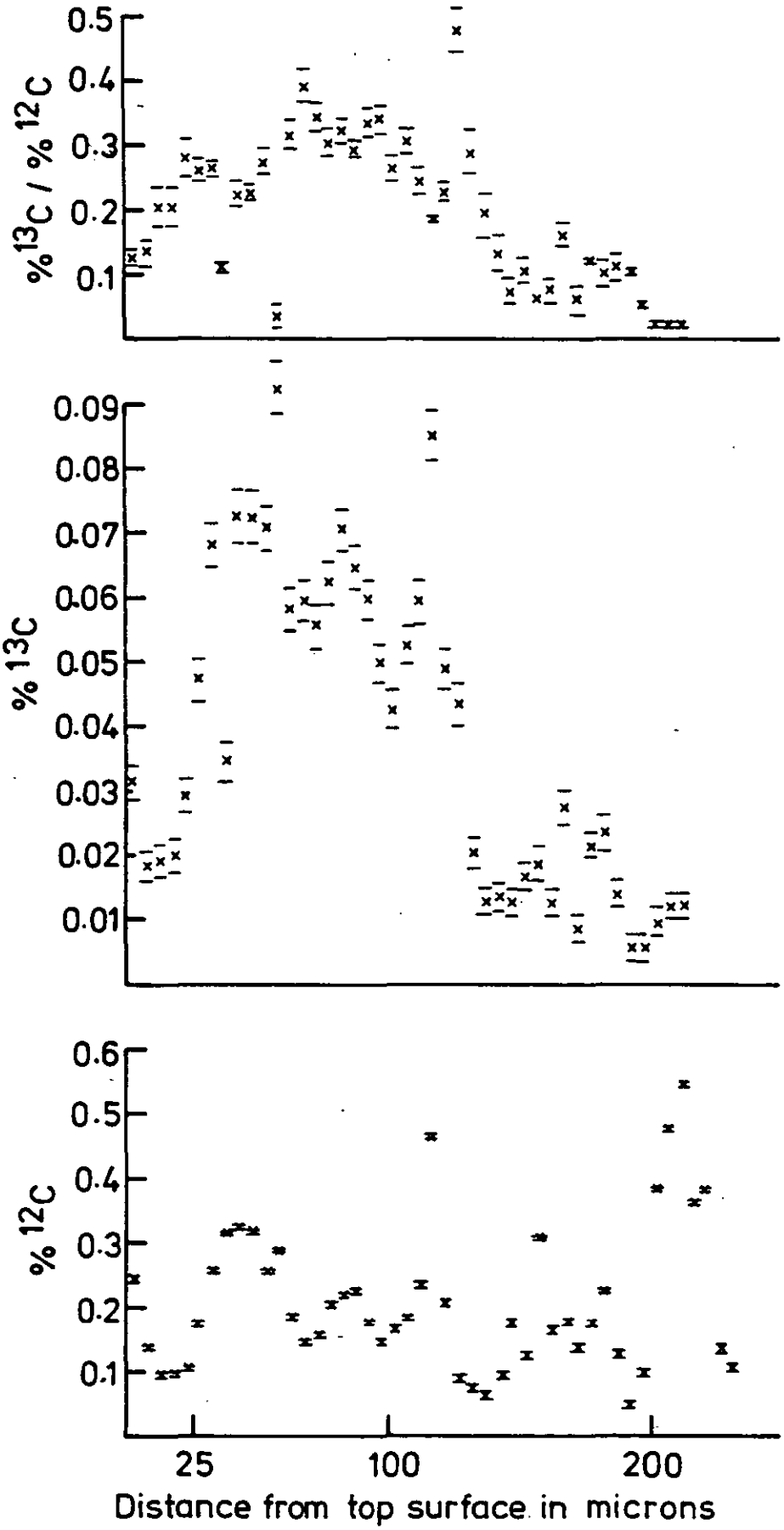

FIG. 6.11 AVERAGE PROFILES OF CARBON DATA IN PE16/21 TREATED FOR 1096 HOURS AT 800°C IN $^{13}CO_3$. SPATIAL RESOLUTION 5μm.

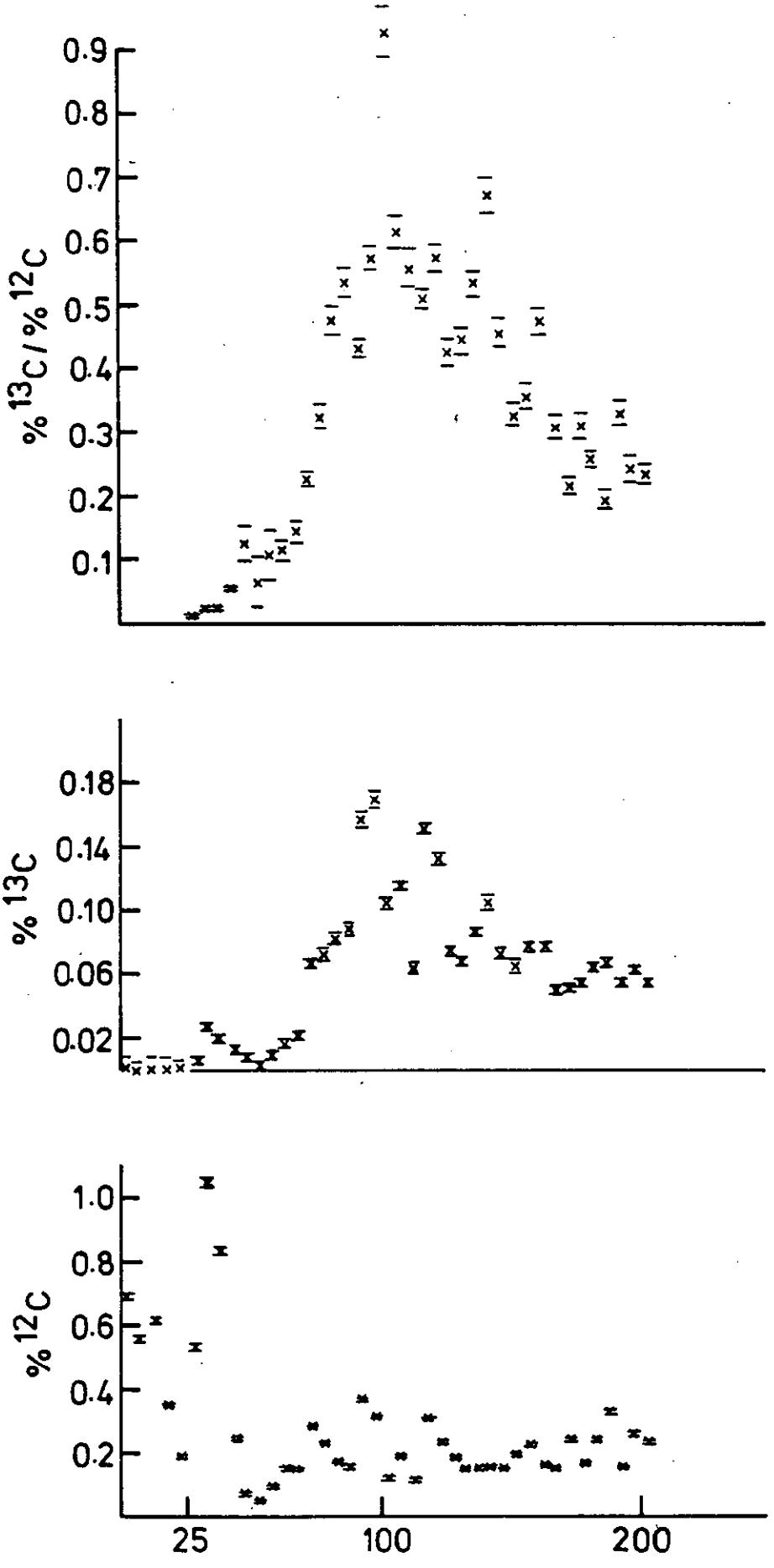

FIG. 6.12 AVERAGE PROFILES OF CARBON DATA IN PE16/24 TREATED FOR 4601 HOURS AT 800°C IN $^{13}CO_2$. SPATIAL RESOLUTION 5 µm.

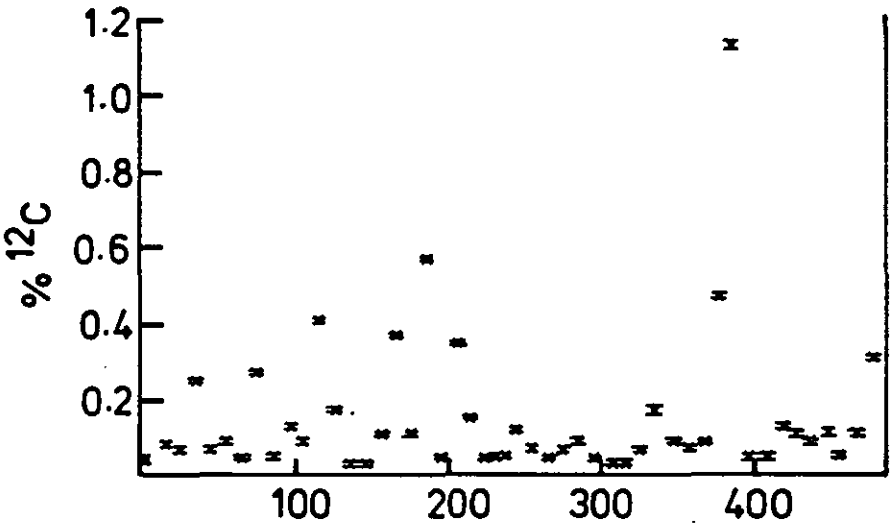

FIG. 6.13 AVERAGE PROFILE OF ^{12}C IN PE16 ARCHIVE MATERIAL. SPATIAL RESOLUTION 10μm.

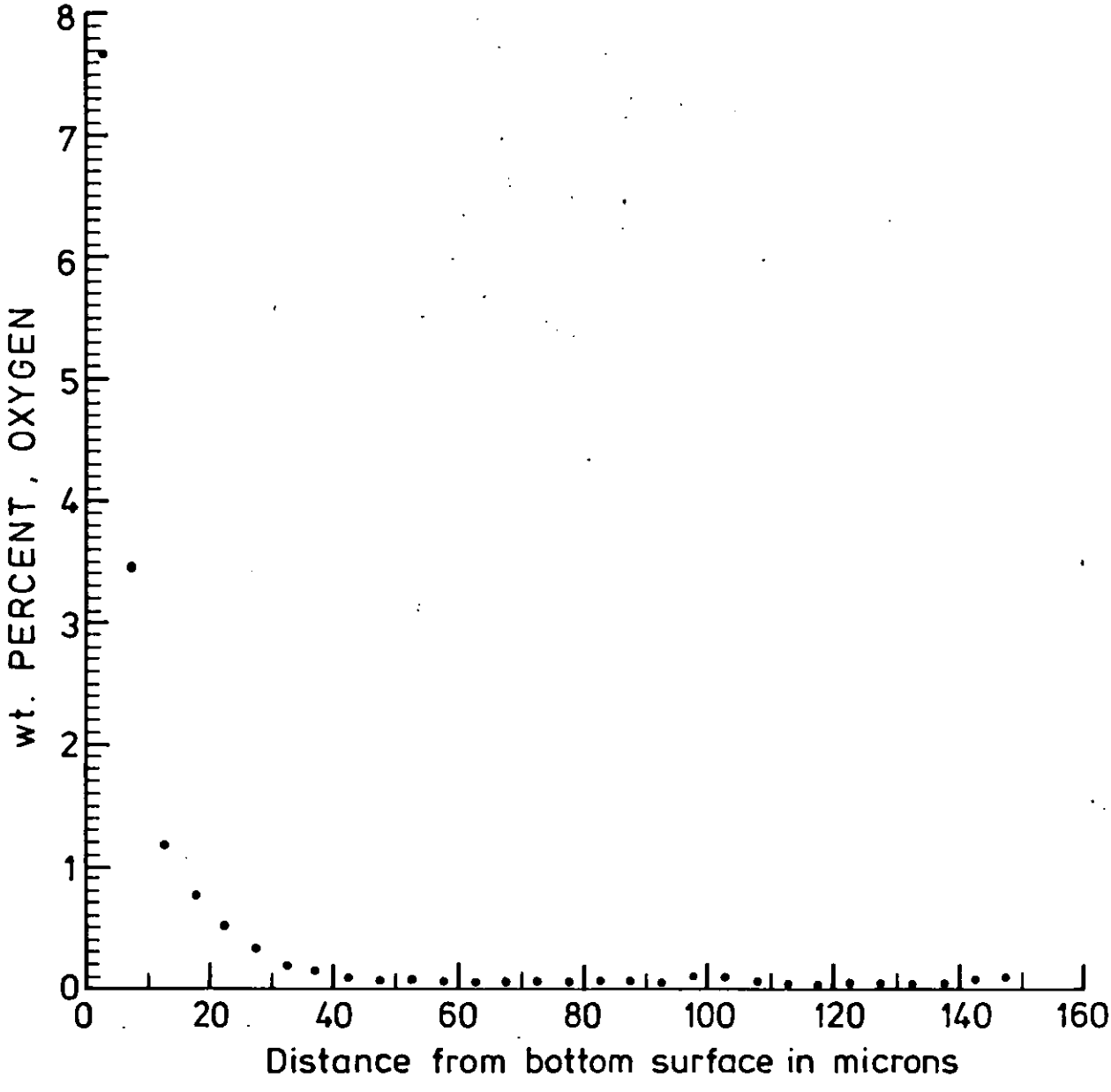

FIG. 6.14 OXYGEN PROFILE IN PE16/24 TREATED AT 800°C IN $^{13}CO_2$. SPATIAL RESOLUTION 5μm.

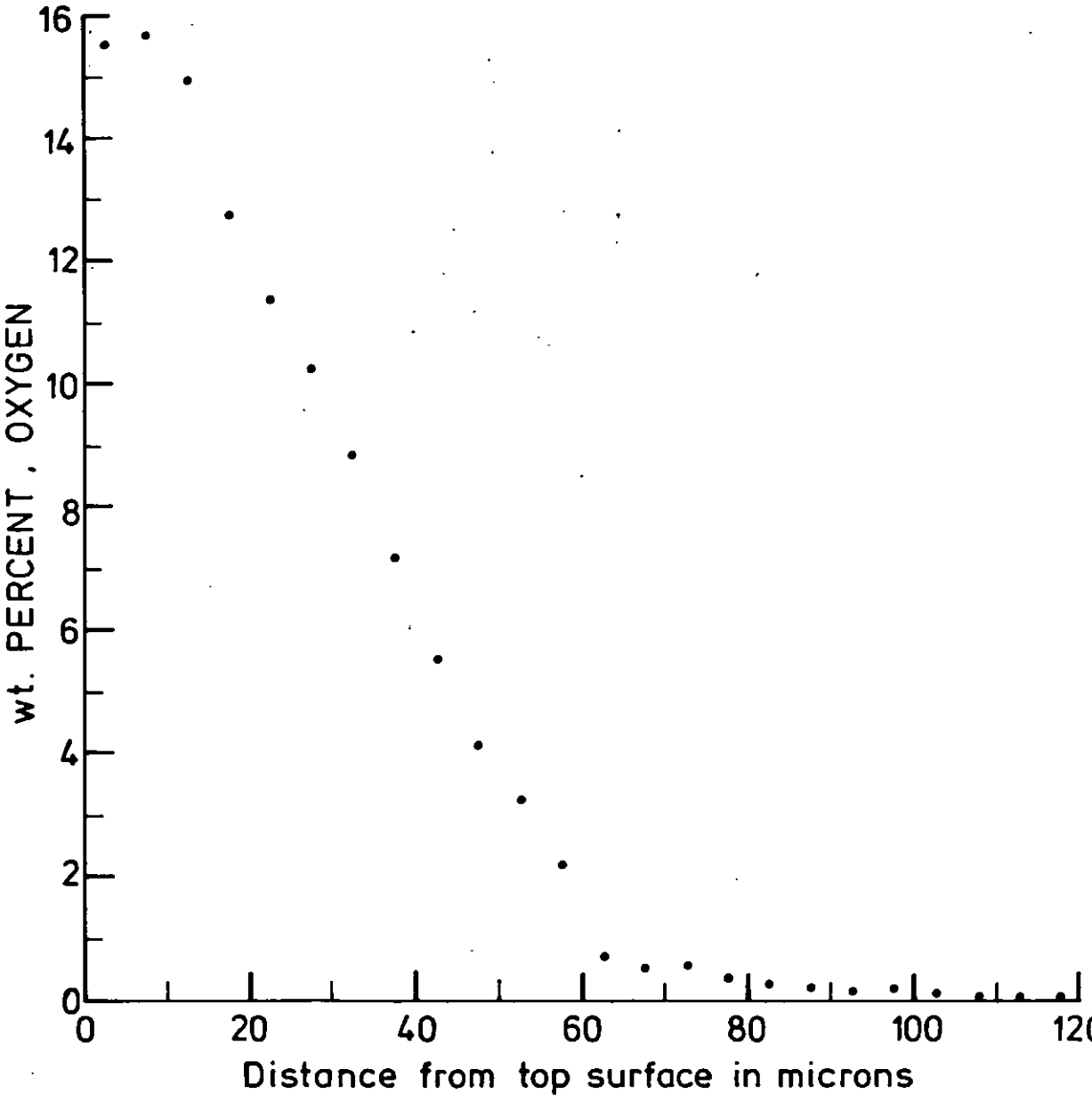

FIG. 6.15 OXYGEN PROFILE IN PE16/24 TREATED AT 800°C IN $^{13}CO_2$. SPATIAL RESOLUTION 5 μm.

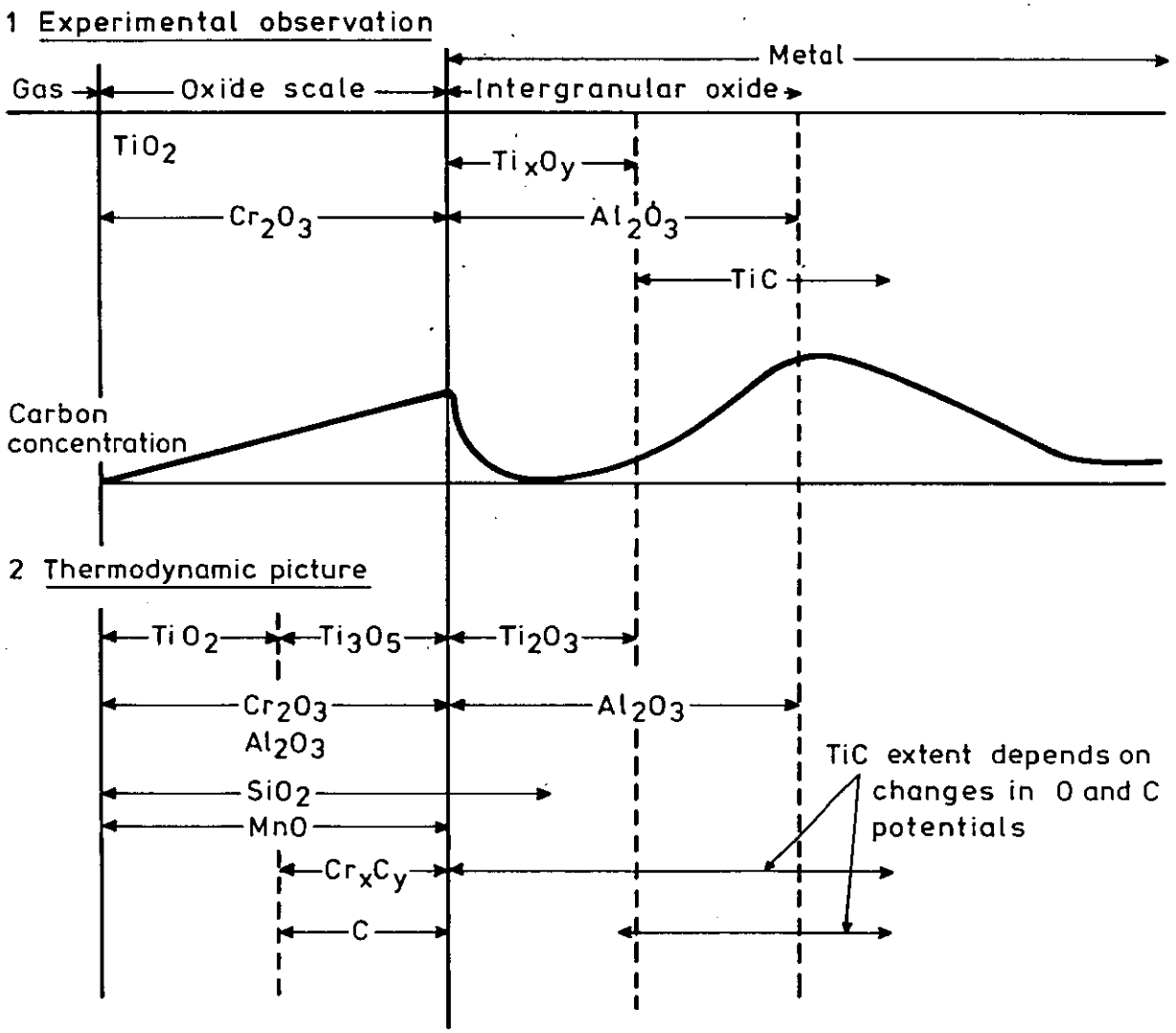

FIG. 6.16 DIAGRAMMATIC REPRESENTATION OF THE PRINCIPAL STABLE PHASES OBSERVED EXPERIMENTALLY AND PREDICTED THERMODYNAMICALLY (107, 110)

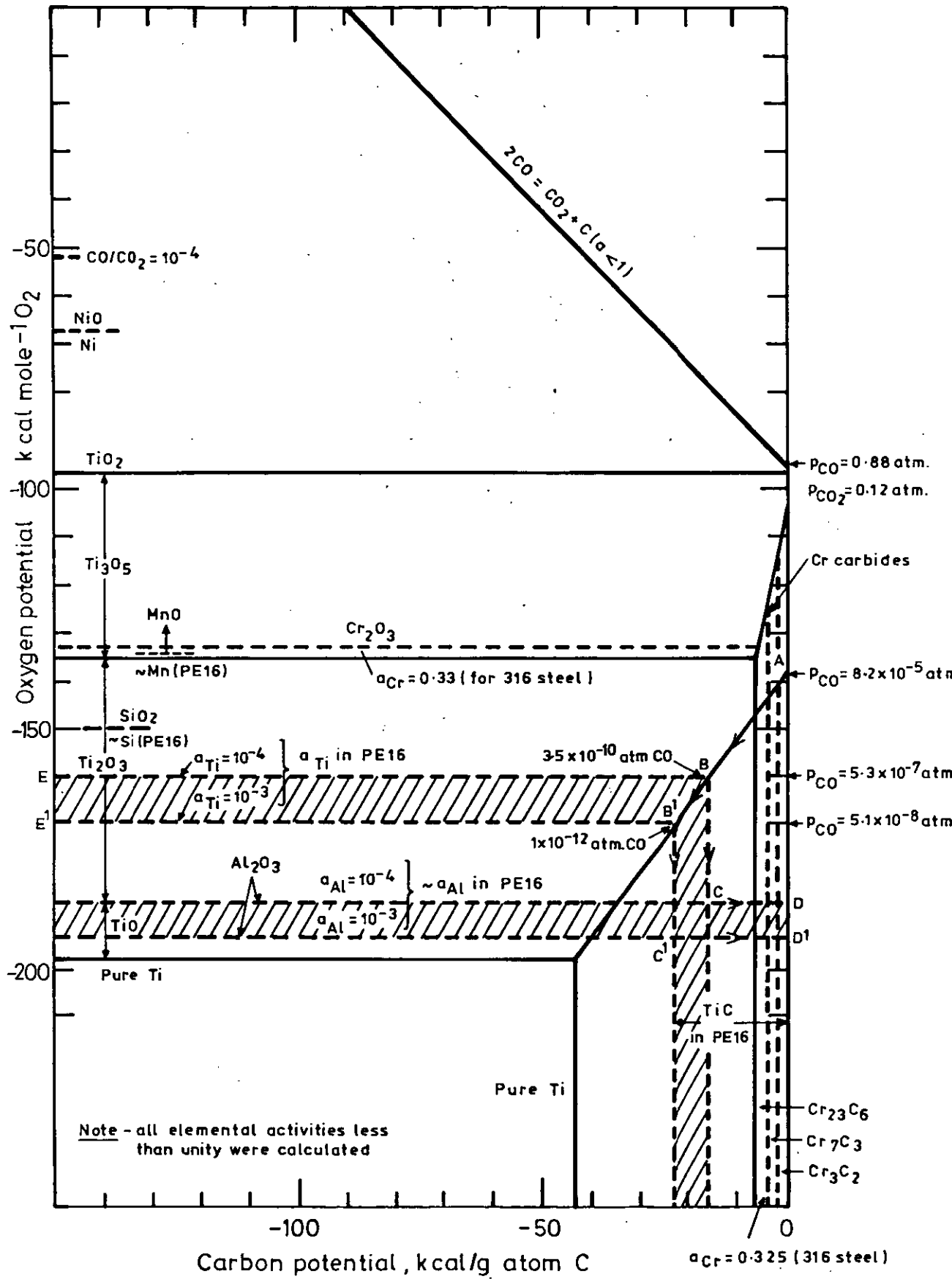

FIG. 6.17 OXYGEN AND CARBON RELATIVE POTENTIALS FOR THE OXIDATION OF THE PE16 ALLOY IN CARBON DIOXIDE AT 800°C.(107,110)

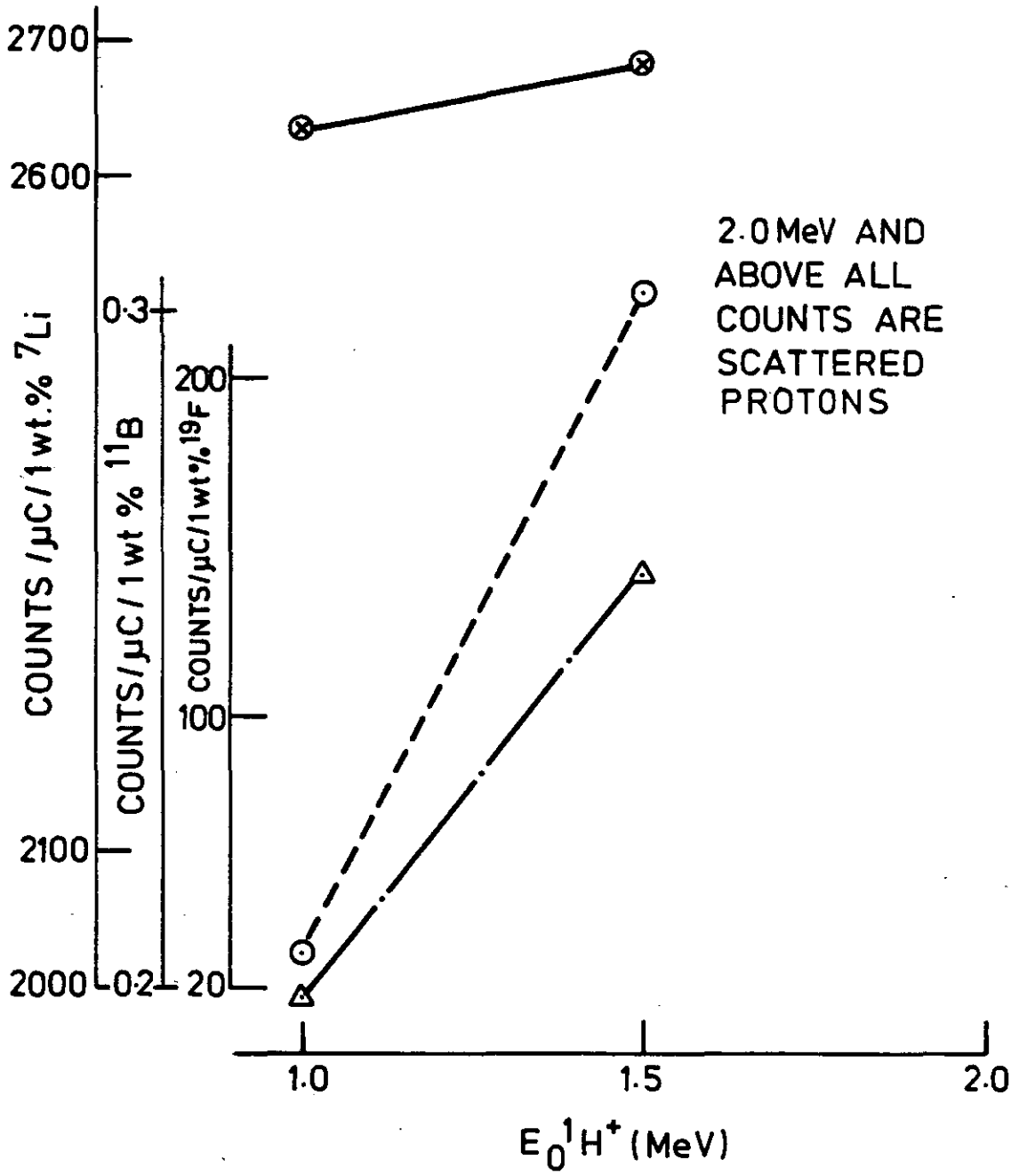

FIG. 7.1 VARIATION OF YIELD WITH BEAM ENERGY FOR ^{7}Li AND THE MOST LIKELY INTERFERENCES USING THE (p,α) REACTION. θ=135°.

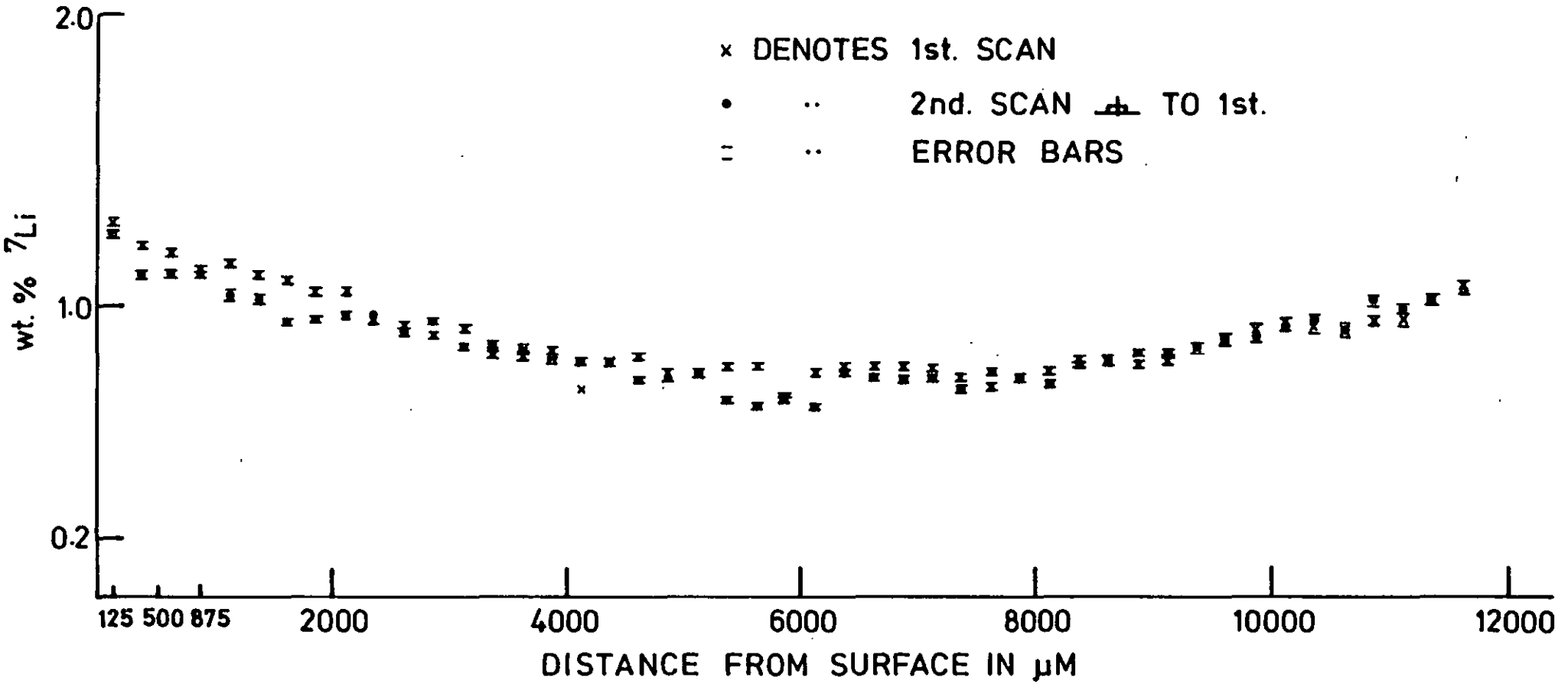

FIG. 7.2 ^{7}Li DISTRIBUTIONS ACROSS B_4C, SAMPLE 197, MEASURED USING ^{7}Li (p,α) α REACTION
E_{op} = 1.5 MeV, θ = 135° (SPATIAL RESOLUTION, 250 μm.)

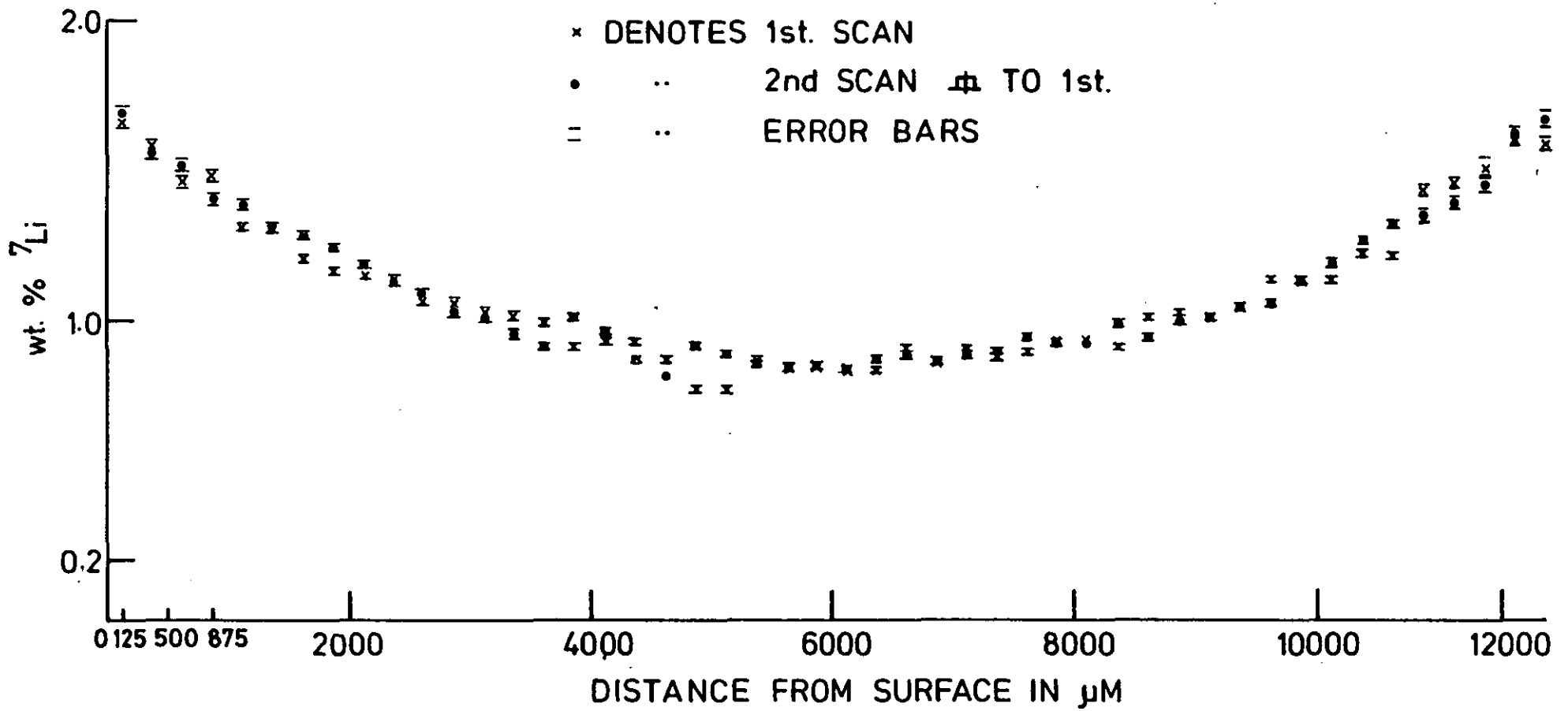

FIG. 7.3 ^{7}Li DISTRIBUTIONS ACROSS B_4C, SAMPLE 185, MEASURED USING $^{7}Li(p,\alpha)\alpha$ REACTION
$E_{op} = 1.5$ MeV, $\theta = 135°$ (SPATIAL RESOLUTION, 250 μM)

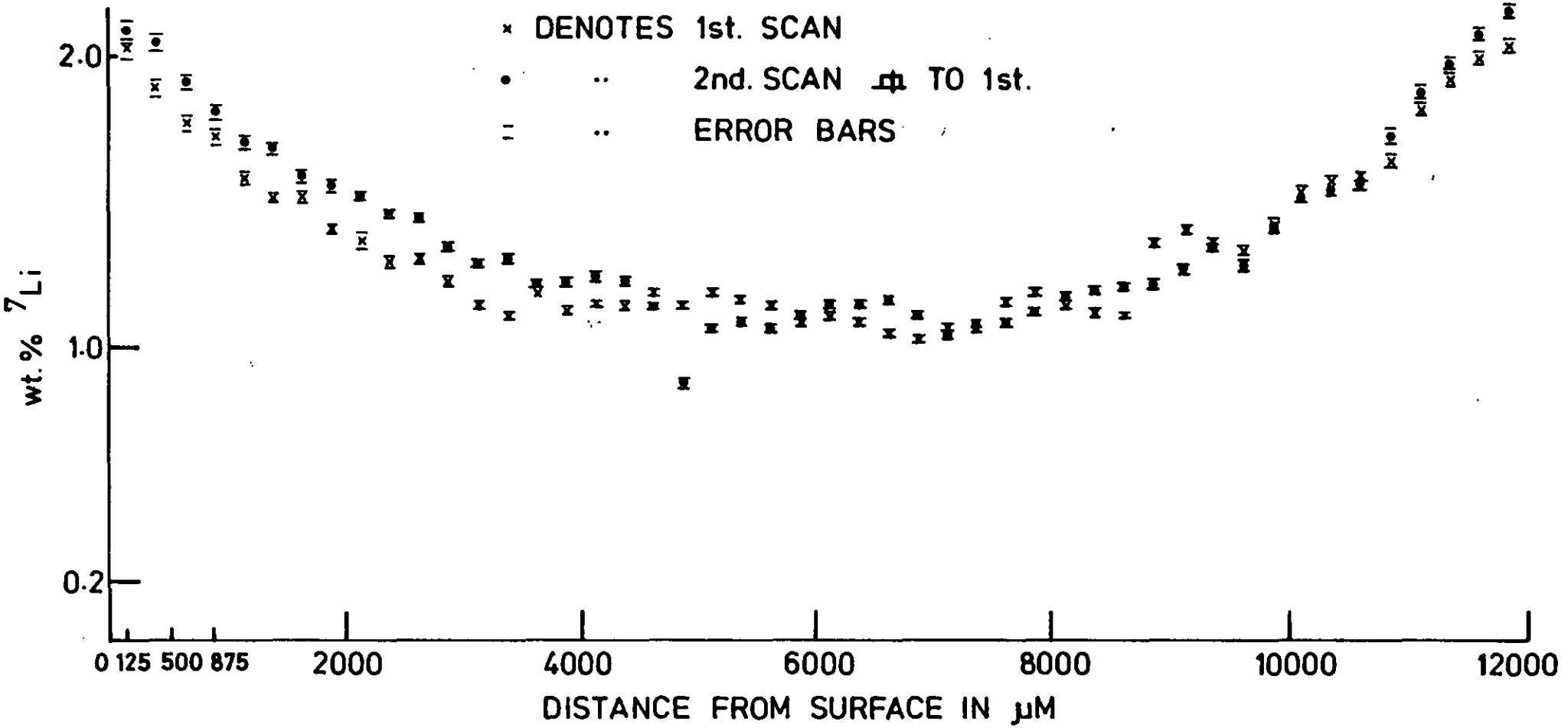

FIG. 7.4 ^{7}Li DISTRIBUTIONS ACROSS B_4C, SAMPLE 172, MEASURED USING ^{7}Li(p,α)α REACTION
E_{op} = 1·5 MeV, θ = 135°, (SPATIAL RESOLUTION, 250 μM)

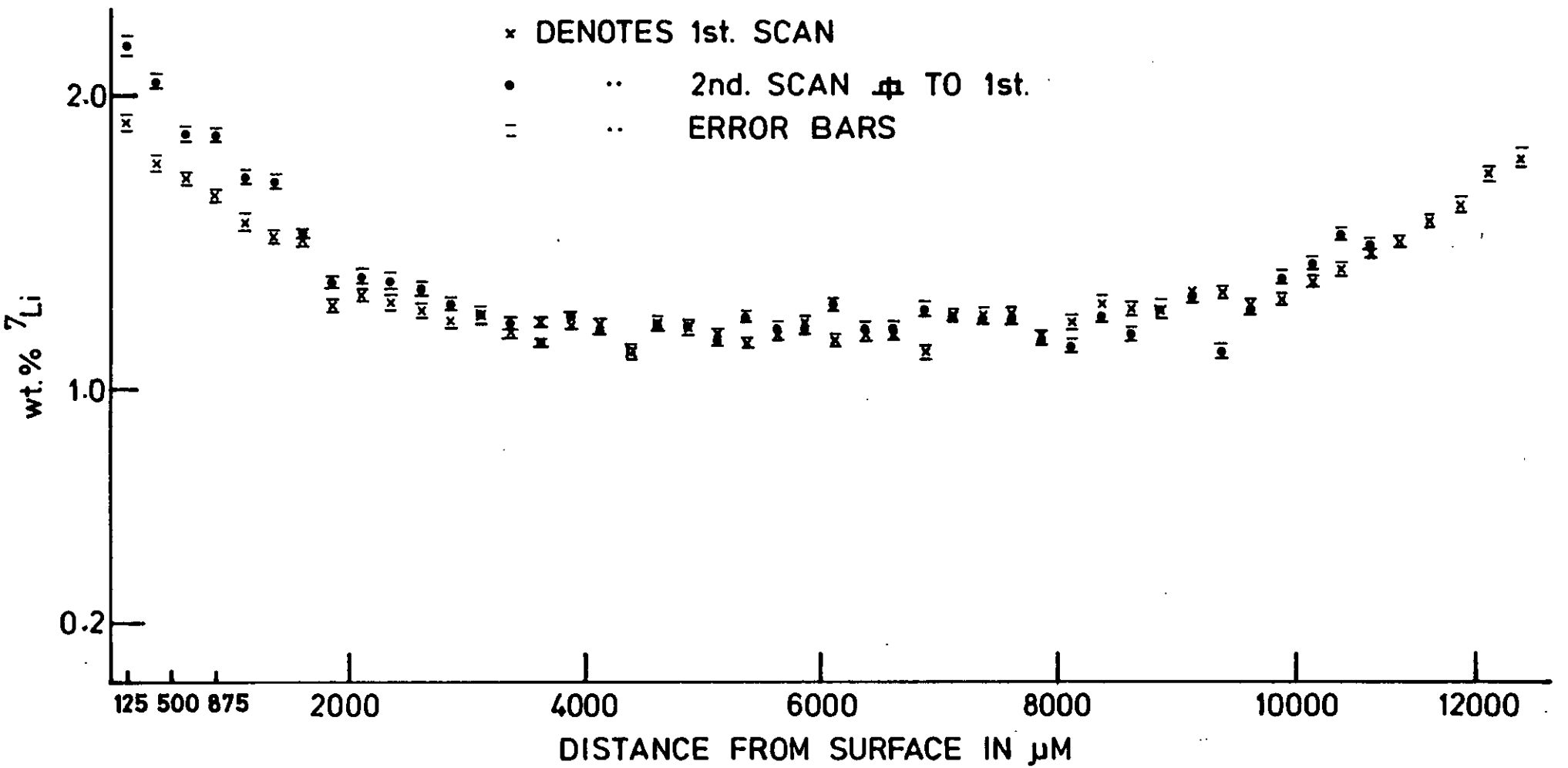

FIG. 7.5 ^{7}Li DISTRIBUTIONS ACROSS B_4C, SAMPLE 160, MEASURED USING $^{7}Li(p,\alpha)\alpha$ REACTION
E_{op} = 1.5 MeV, θ = 135°, (SPATIAL RESOLUTION, 250 μM)

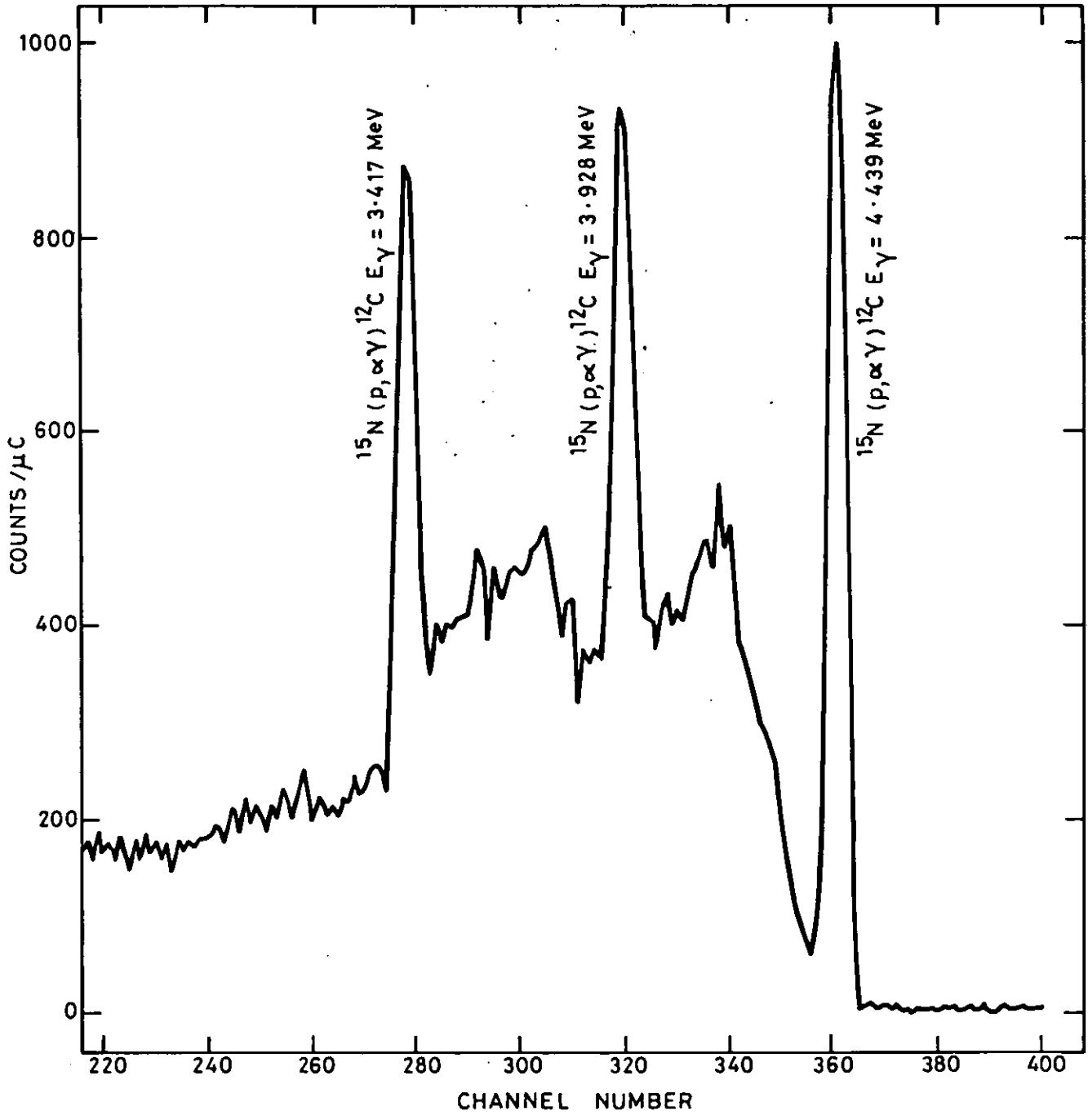

FIG. 8·1. GAMMA SPECTRUM OF ENRICHED UREA (44·5 wt % ^{15}N). (Ge(Li) DETECTOR).

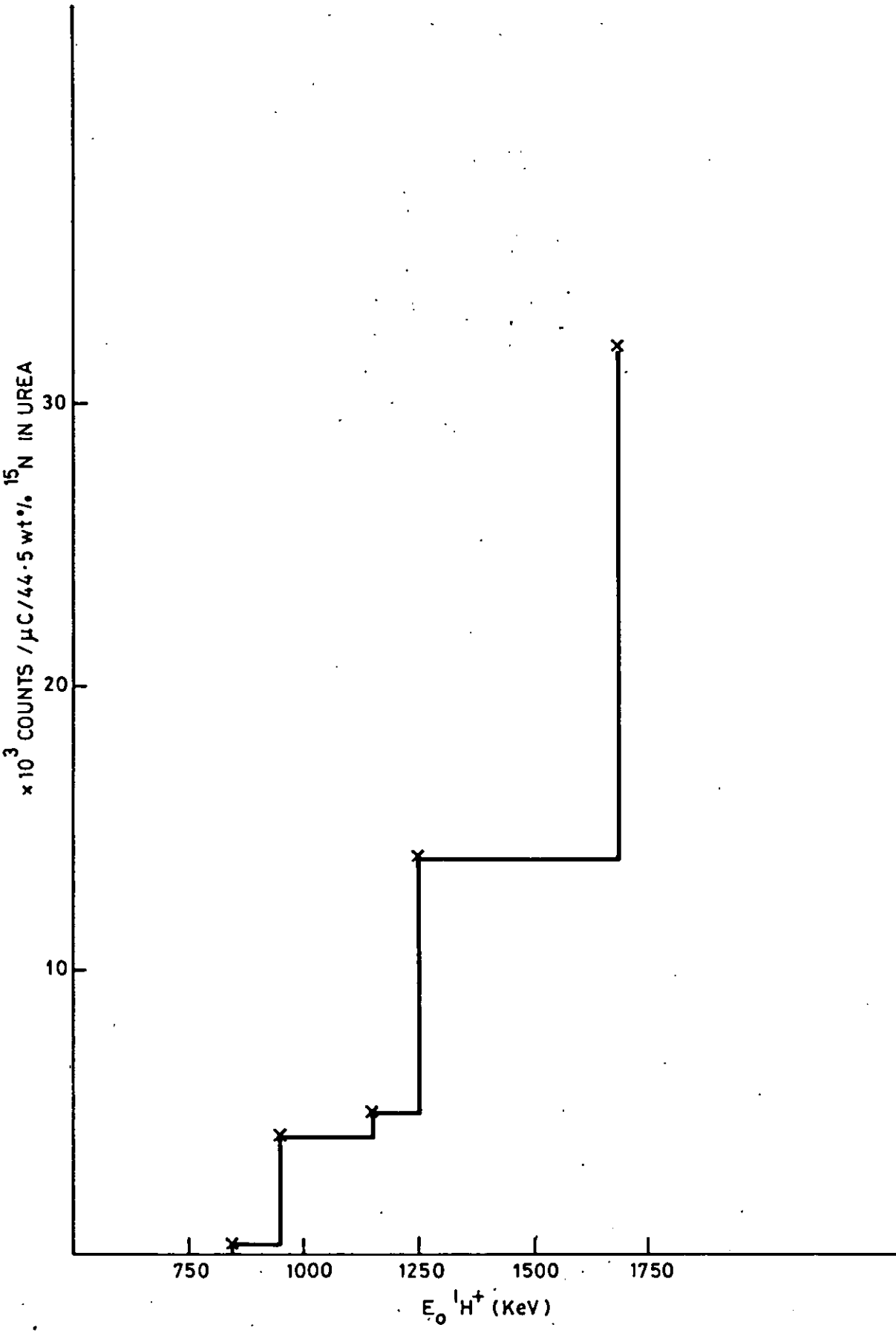

FIG. 8·2. VARIATION OF γ YIELD FROM ^{15}N (p, $\alpha\gamma$) ^{12}C REACTION AT DIFFERENT BEAM ENERGIES. (Ge(Li) DETECTOR.

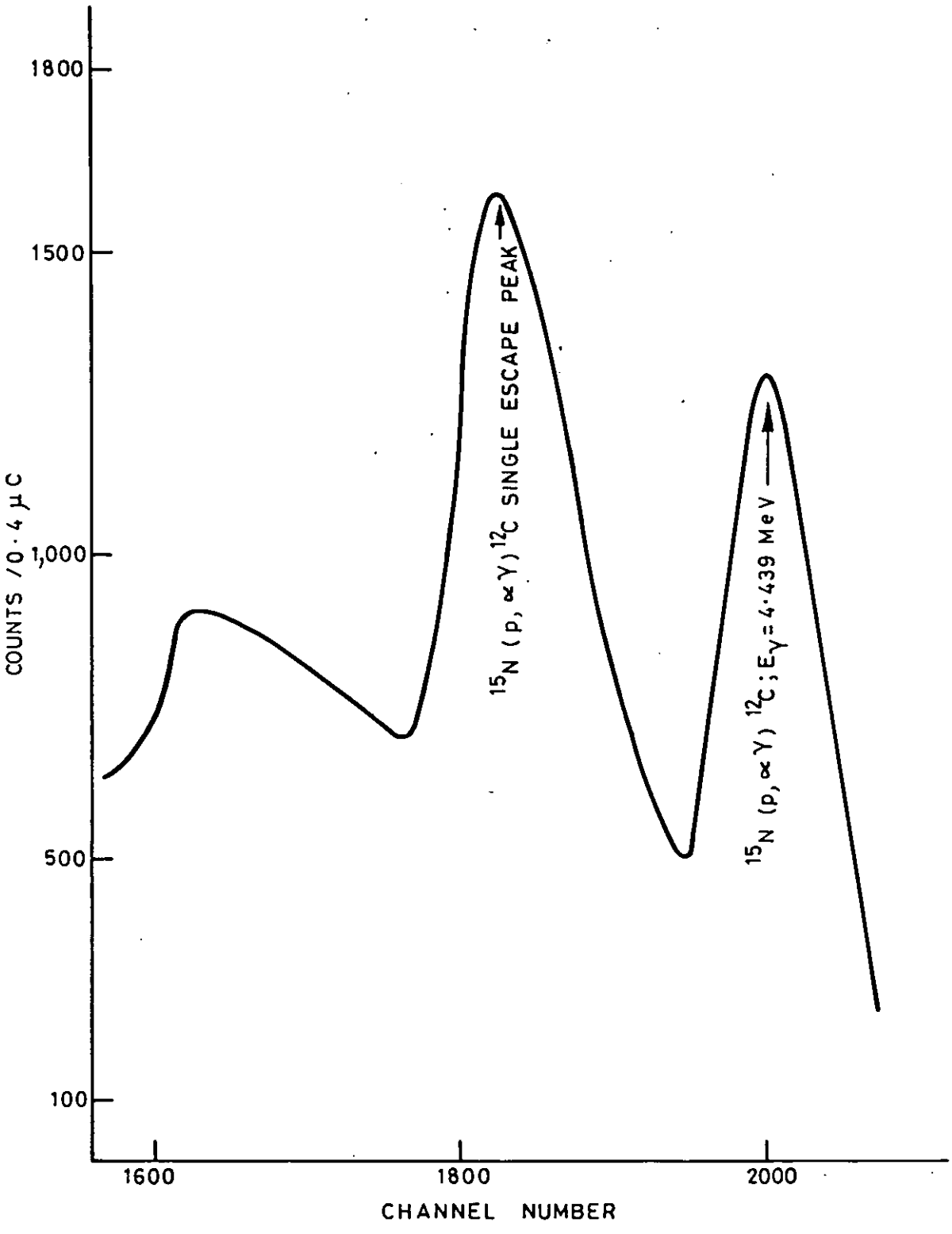

FIG. 8·3. γ SPECTRUM OF UREA ENRICHED IN ^{15}N (44·5 wt % ^{15}N) (Na I (Tℓ) DETECTOR) $\theta = 0°$, $E_{op} = 1·69$ MeV.

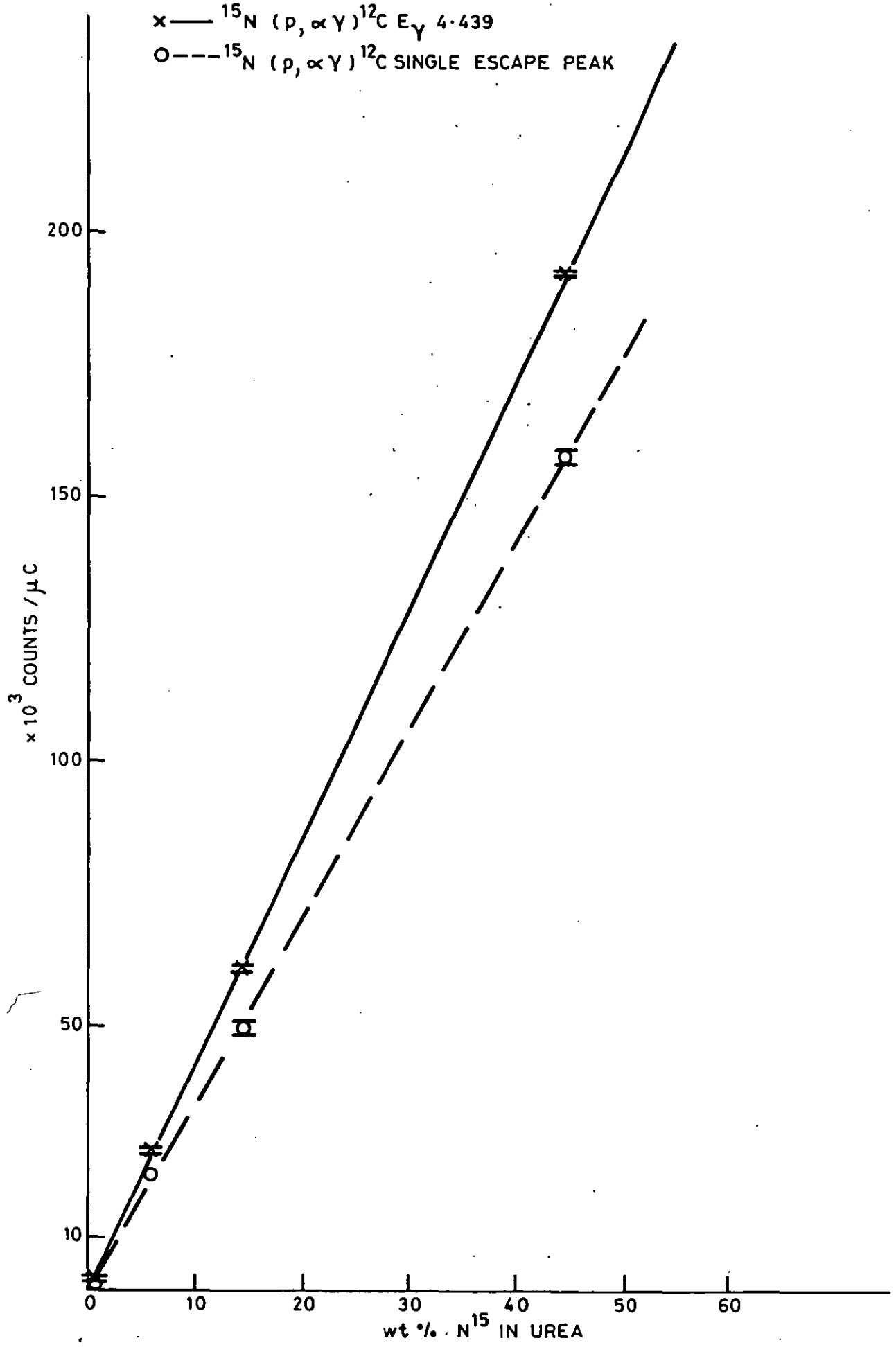

FIG. 8·4. CALIBRATION CURVE FOR ^{15}N CONTENT IN UREA
Na I (Tℓ) DETECTOR, E_{op} = 1·69 MeV.

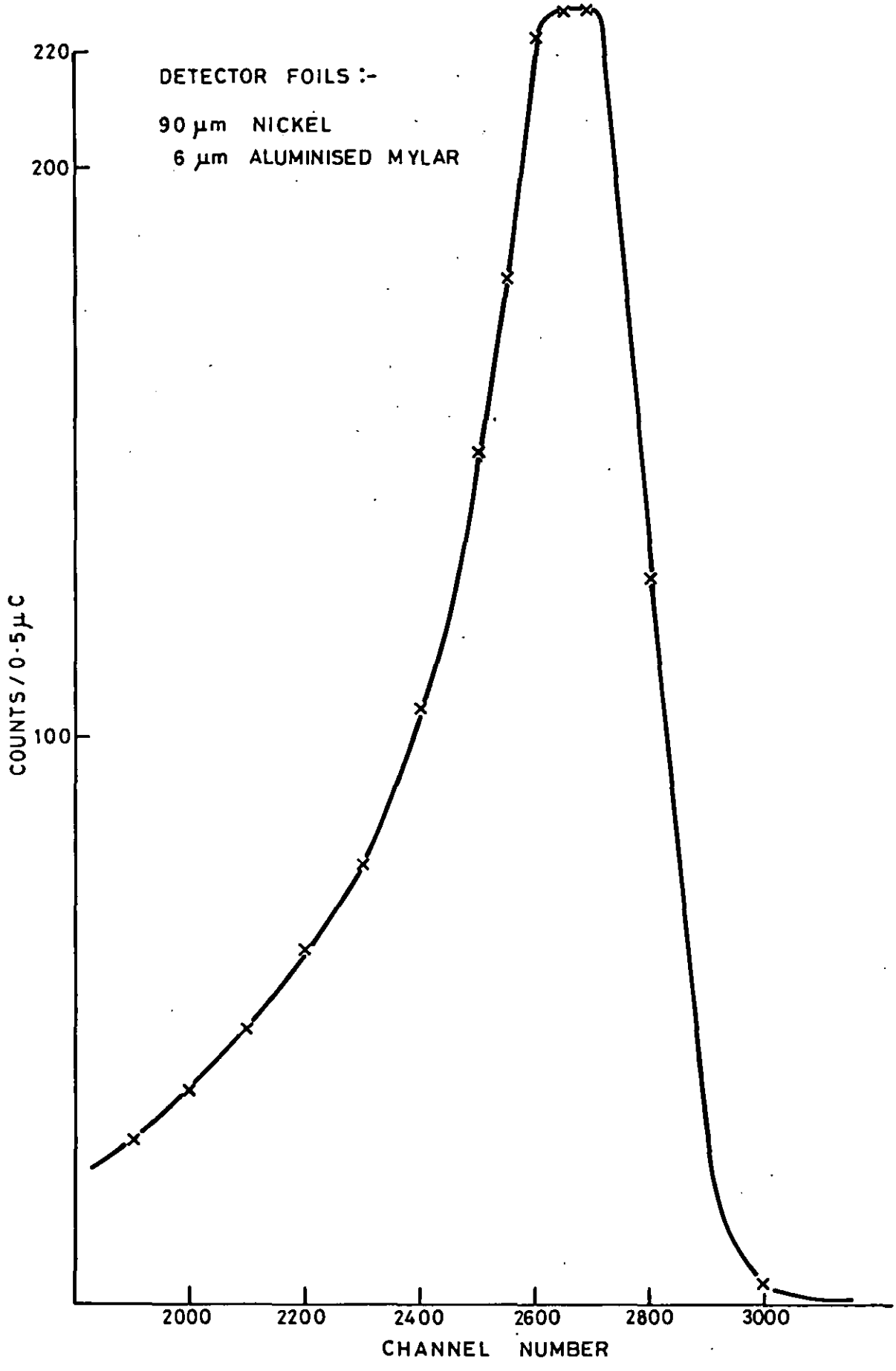

FIG. 8·5. PROTON SPECTRUM FROM $^{14}N(d,p)^{15}N$ REACTION. 150 mm^2 ANNULAR SURFACE BARRIER DETECTOR E_{od} = 1·9 MeV.

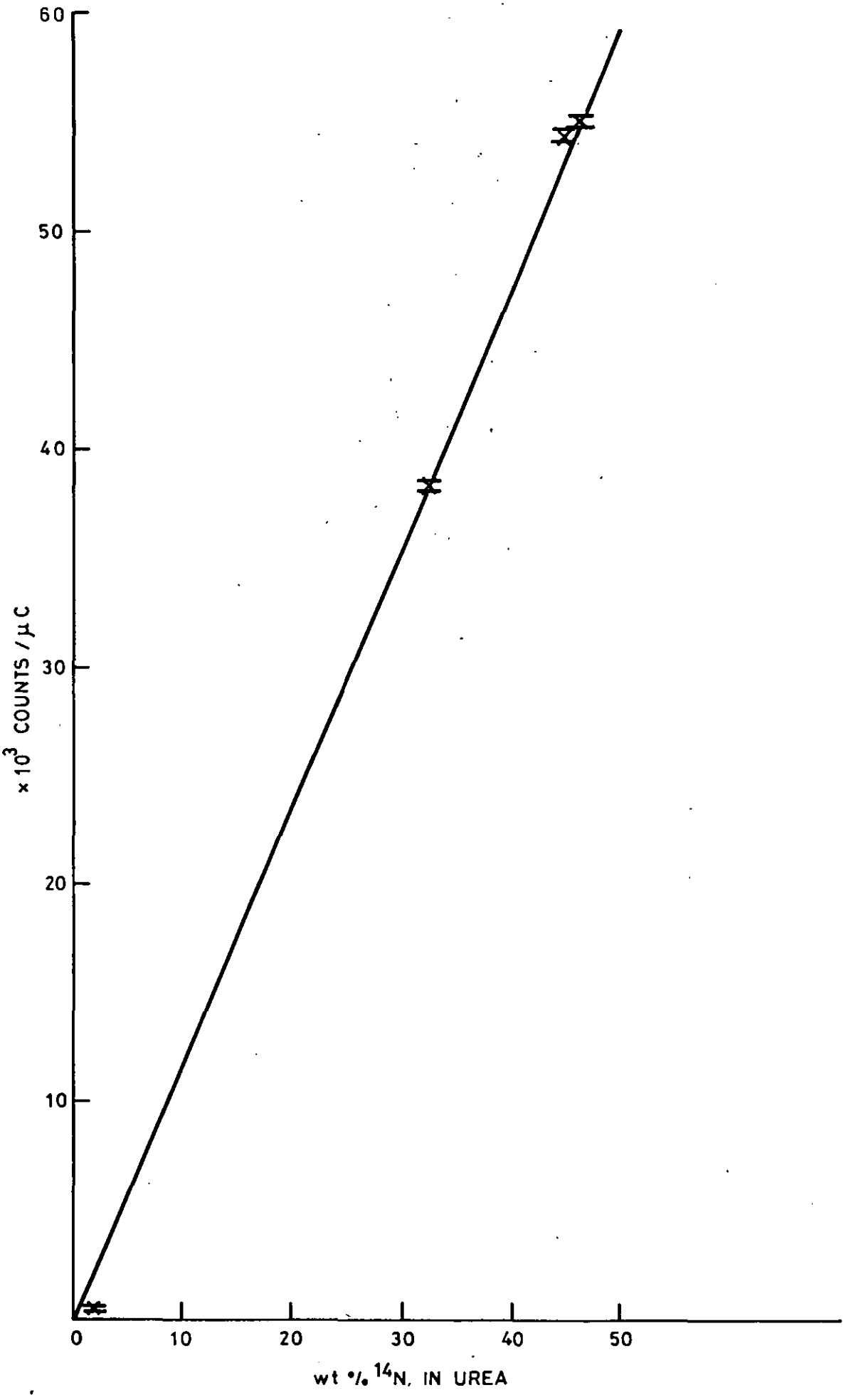

FIG. 8·6. CALIBRATION CURVE FOR ^{14}N CONTENT IN UREA
150 mm² ANNULAR SURFACE BARRIER DETECTOR
E_{od} = 1·9 MeV, $^{14}N(d,p)^{15}N$.

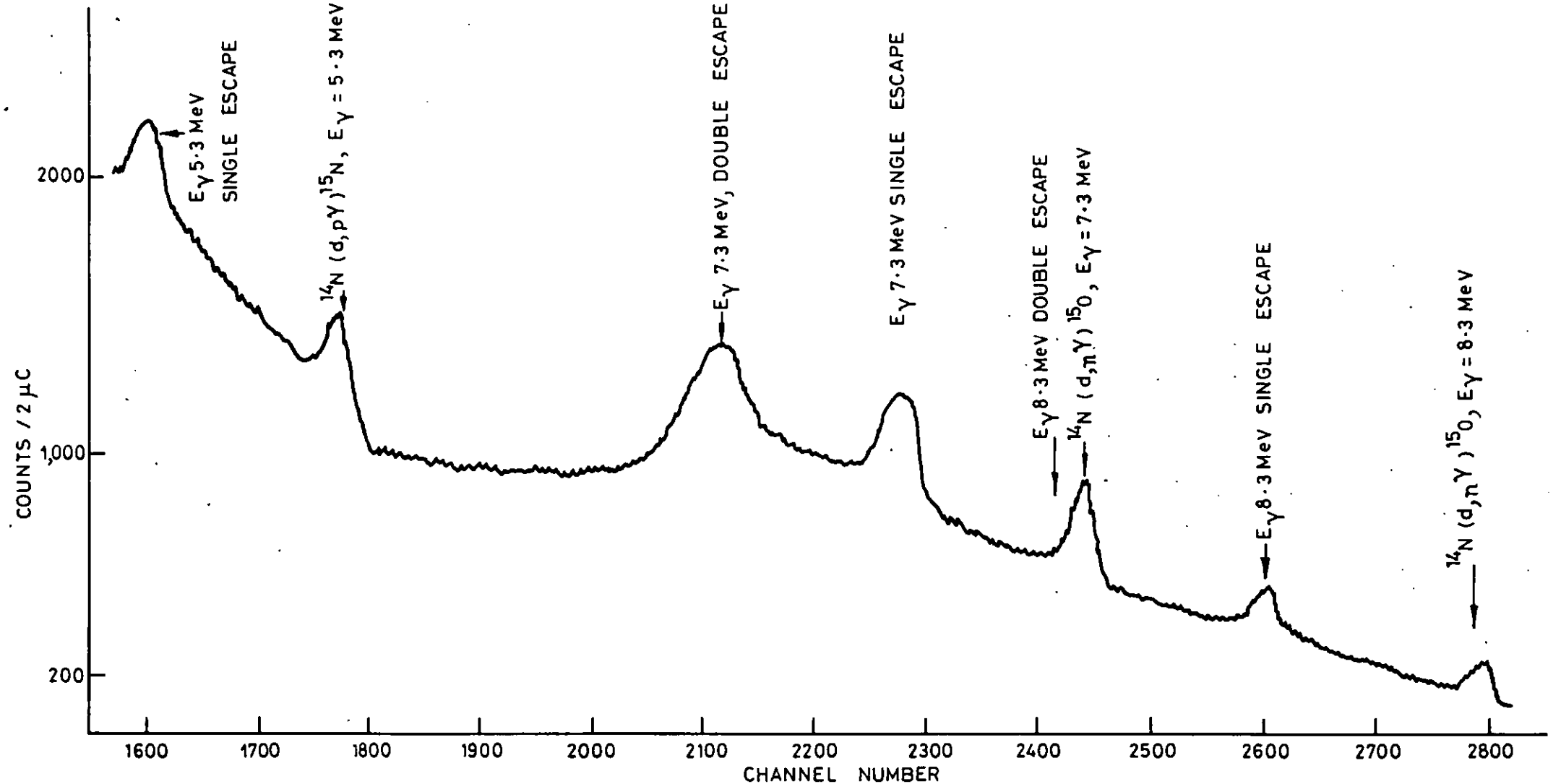

FIG. 8·7. γ SPECTRUM OF NATURAL UREA USING 1·9 MeV $^{2}H^{+}$ BEAM. θ = 0°, GeLi DETECTOR.

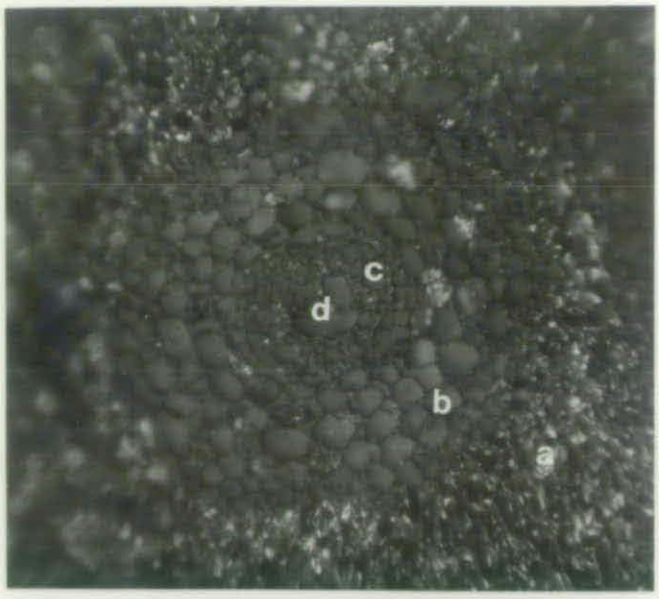

(i) Before bombardment (a) cellulose mounting matrix;
(b) the cortical "storage larder" cells;
(c) the stele ≙ 60 μm bounded by the endodermis;
(d) the central xylen vessel ≙ 80μm.
Average b + c ≙ 250μm

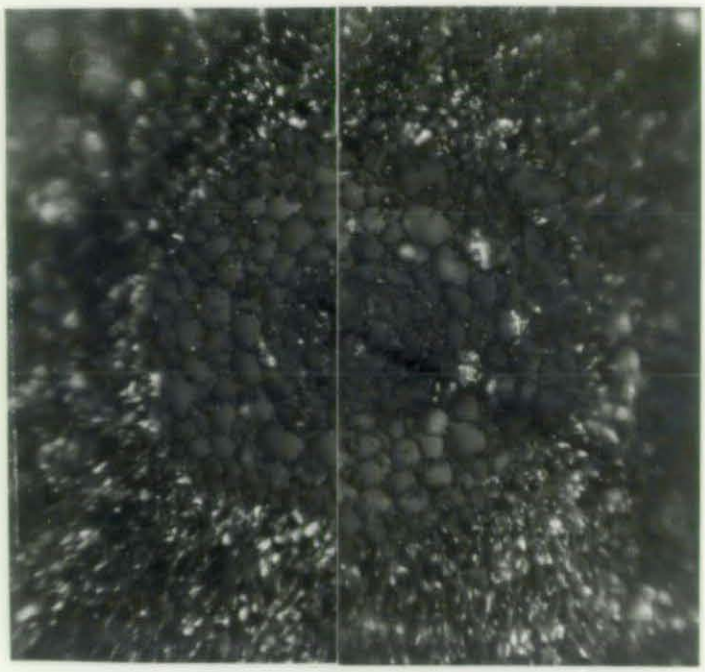

(ii) After bombardment
2μC dose of 1.9 MeV $^{2}H^{+}$.
← denotes scanned beam path.

Figure 8.8
Photographs of 100µm barley root sections mounted on nickel blocks, flashed with 2µm carbon.
(i) before and (ii) after microbeam bombardment.

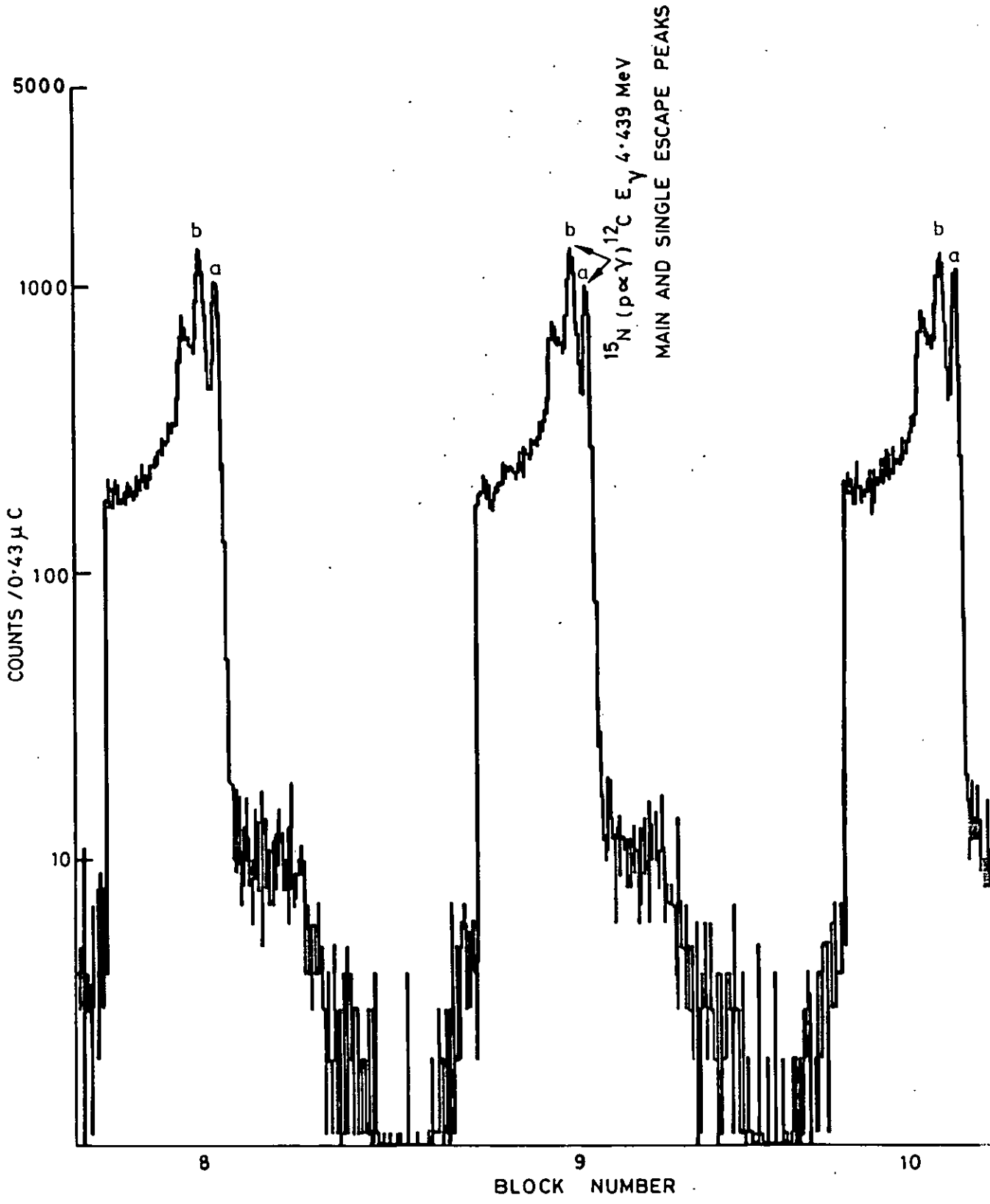

FIG. 8·9.
3 OF THE 16 SPECTRA OF A 2 PARAMETER γ SPECTRUM OF AN ENRICHED UREA STANDARD (44·5wt% ^{15}N) OBTAINED USING ^{15}N (p∝γ) ^{12}C REACTION AND A Na I (Tℓ) DETECTOR.

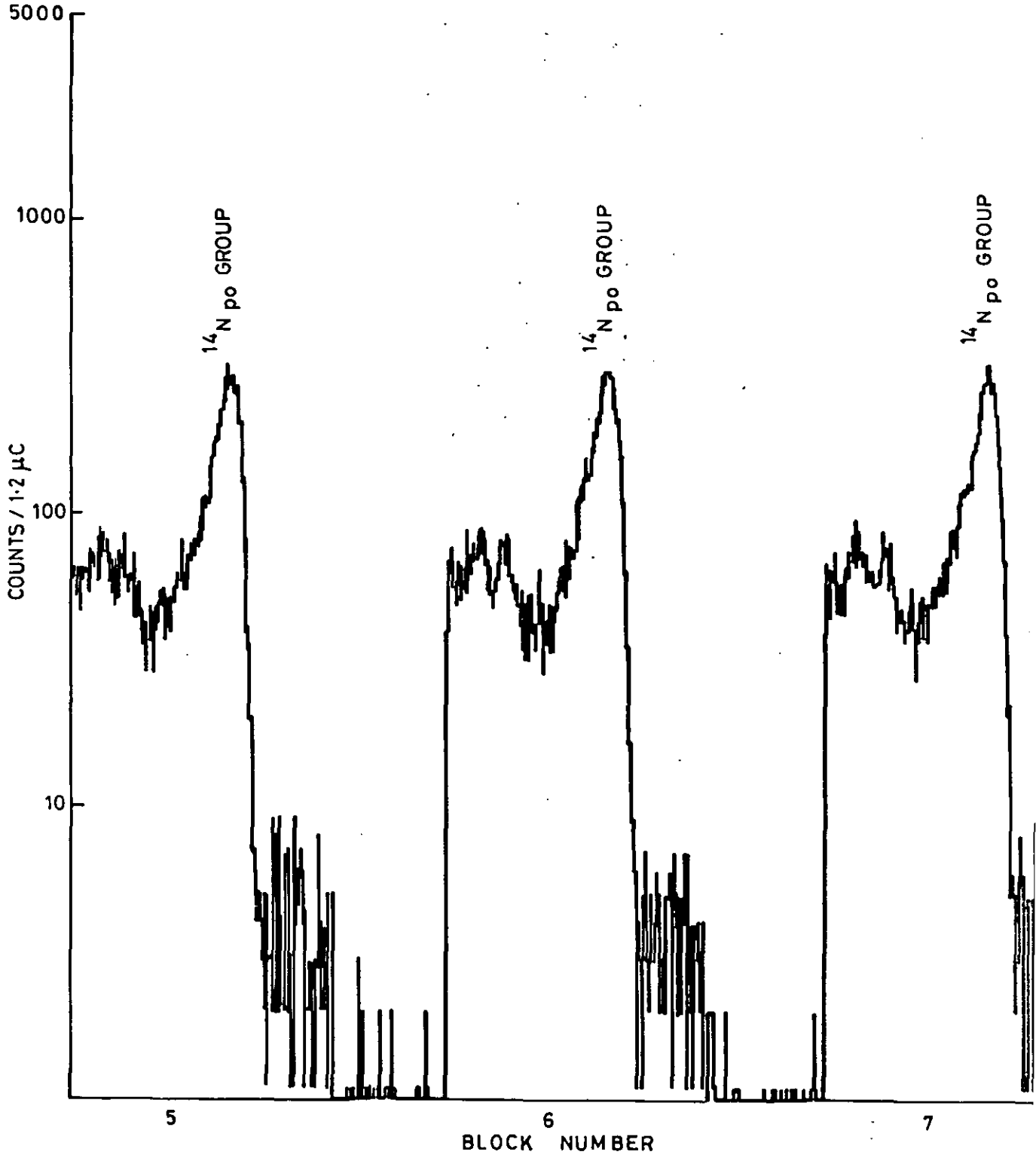

FIG. 8·10.
3 OF THE 16 SPECTRA OF A 2 PARAMETER PROTON SPECTRUM OF A NATURAL UREA STANDARD OBTAINED USING THE ^{14}N (d,p) ^{15}N REACTION AND A 150 mm^2 ANNULAR SURFACE BARRIER DETECTOR. E_{od} = 1·9 MeV.

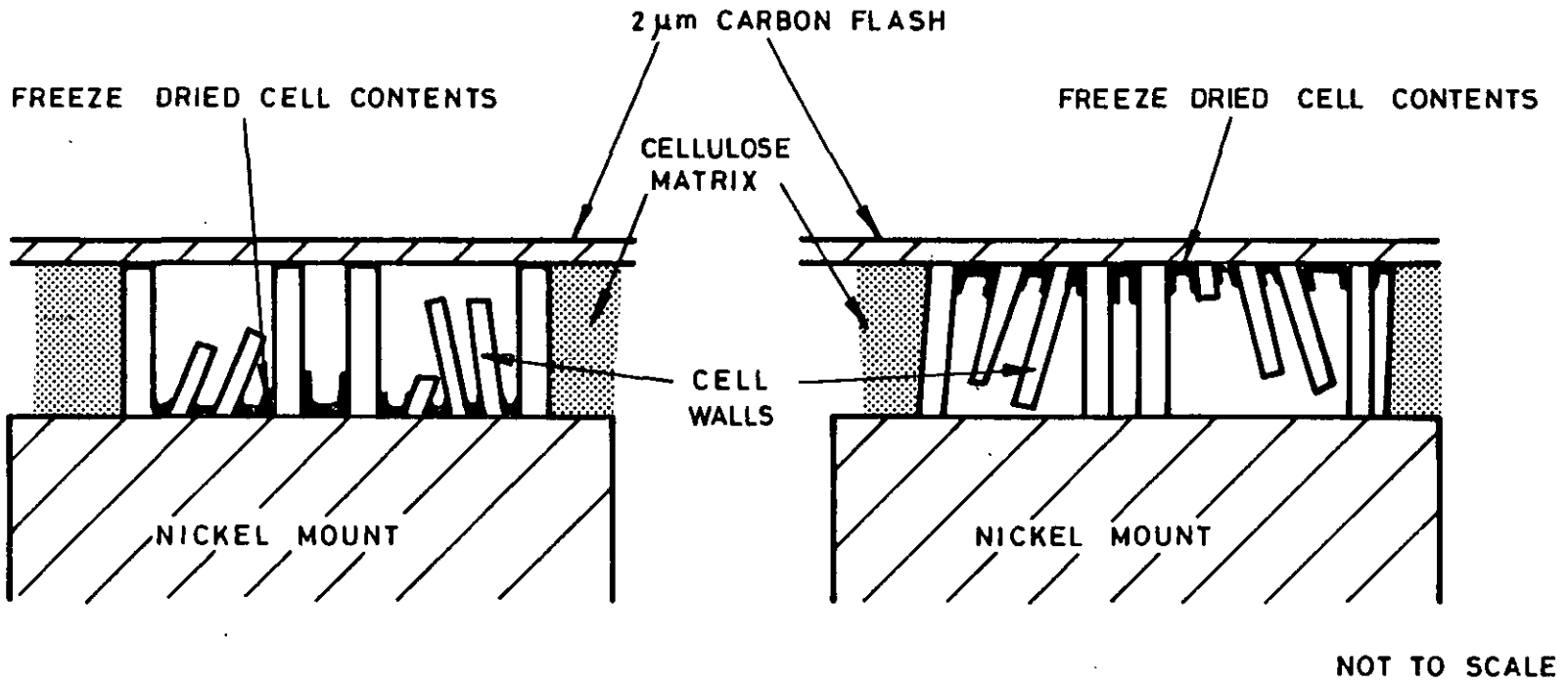

FIG. 8·11. SCHEMATIC DIAGRAM SHOWING THE MOUNTING OF BARLEY ROOT SECTIONS READY FOR MICROBEAM ANALYSIS.

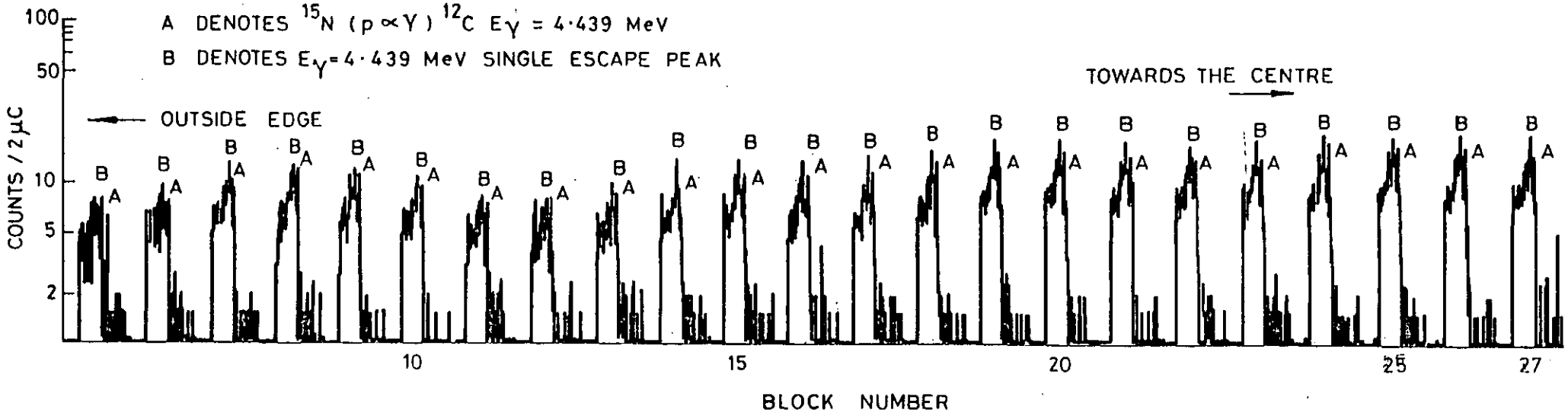

FIG. 8·12. DUAL PARAMETER Y - SPECTRUM OF A BARLEY ROOT LABELLED FOR 48 HOURS IN THE ^{15}N LABELLED CULTURE B (GIVEN IN TABLE 8.4). OBTAINED USING THE ^{15}N (p, ∝Y) ^{12}C REACTION (E_{op} = 1·69 MeV). AND A Ge(Li) DETECTOR.

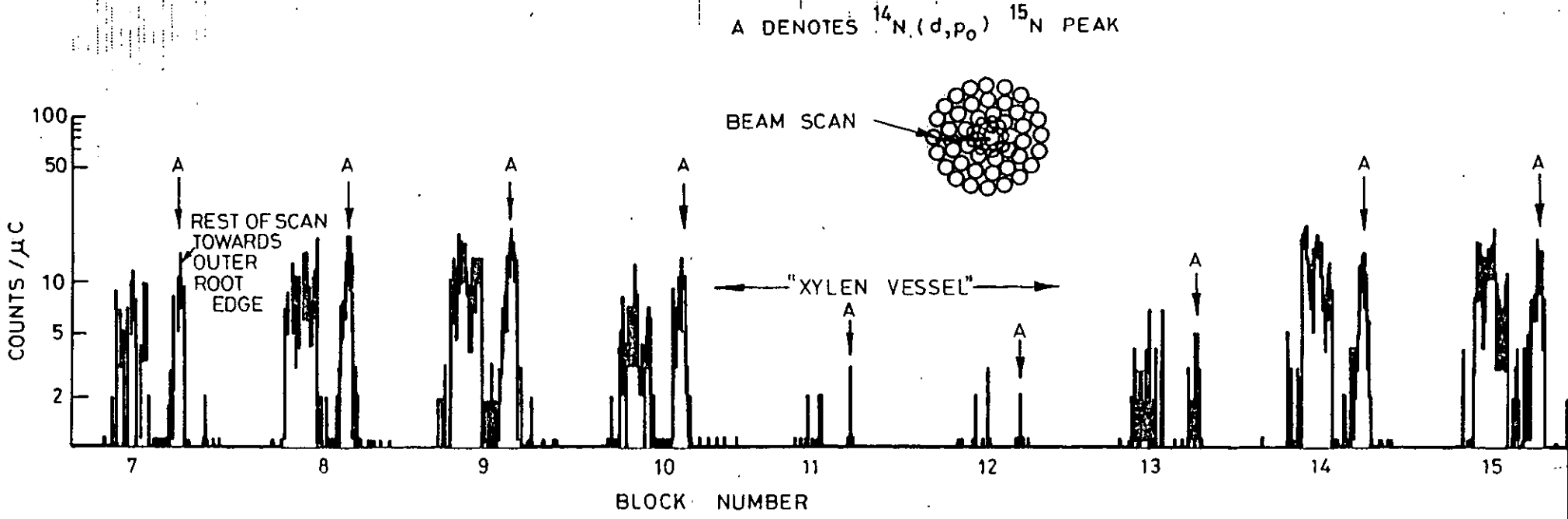

FIG. 8·13. DUAL PARAMETER PROTON SPECTRUM OF A 100 μM THICK BARLEY ROOT SECTION TREATED FOR 24 HOURS IN ^{15}N LABELLING CULTURE B. BEAM SCANNED ACROSS THE SECTION'S CENTRAL VOID REGION E_{od} = 1·9 MeV, θ = 135°.

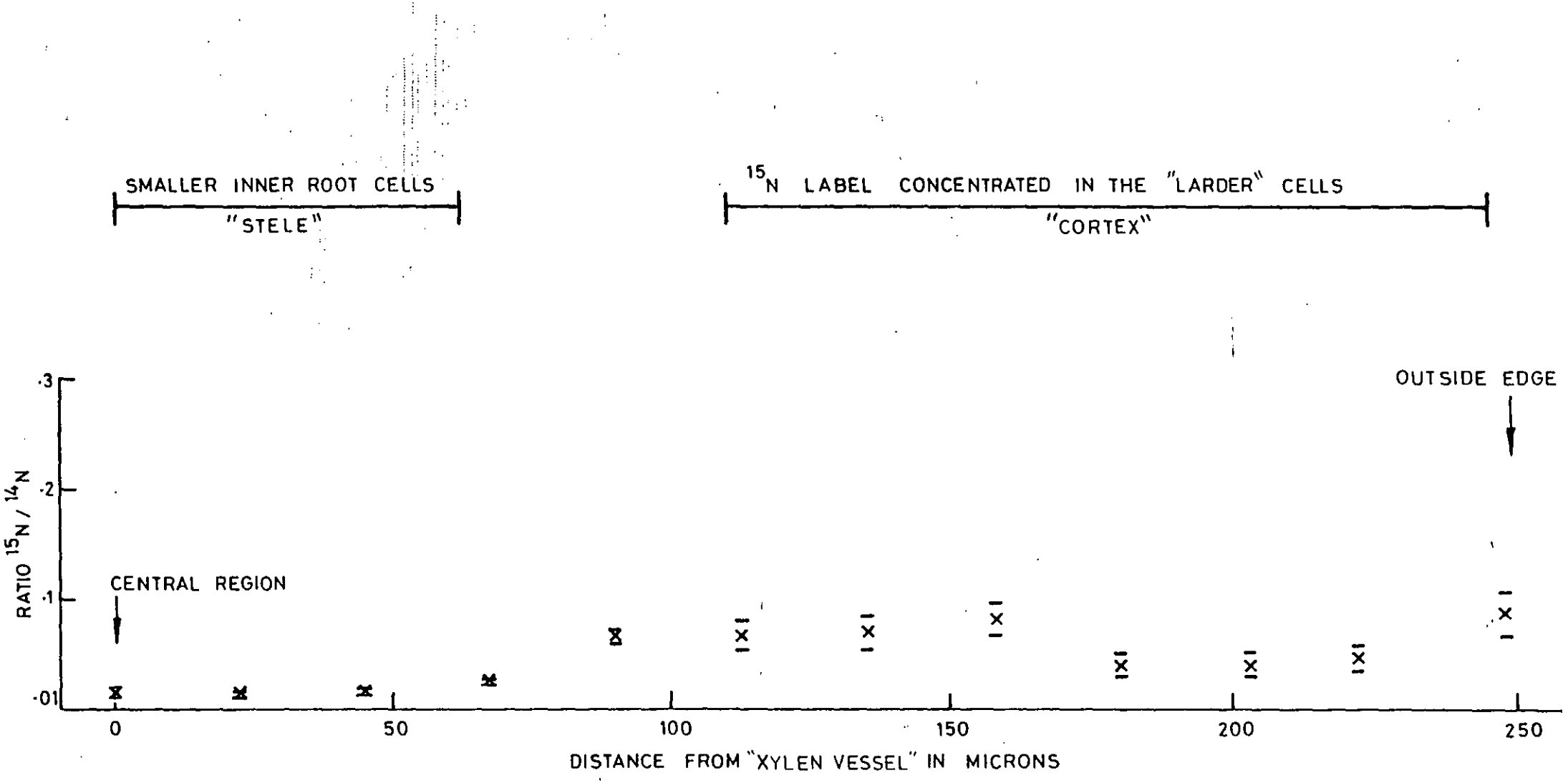

FIG. 8·14. PROFILE OF THE AVERAGE RATIO wt % ^{15}N : wt % ^{14}N ACROSS BARLEY ROOT SECTIONS LABELLED FOR 2 HOURS IN ^{15}N CULTURE B (SPATIAL RESOLUTION 19 μm).

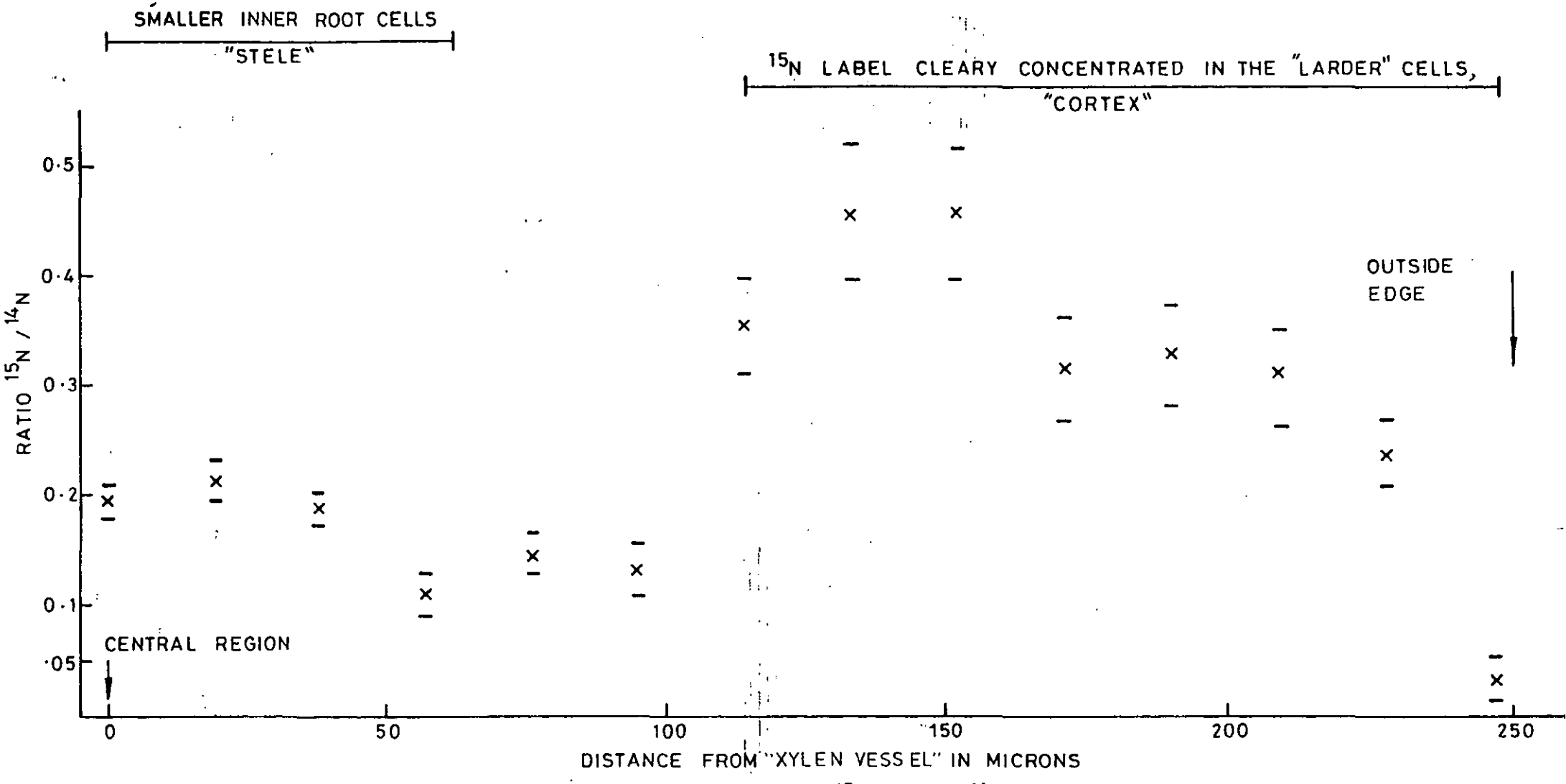

FIG. 8·15. PROFILE OF THE AVERAGE RATIO wt% ^{15}N : wt% ^{14}N ACROSS BARLEY ROOT SECTIONS LABELLED FOR 24 HOURS IN ^{15}N CULTURE B (SPATIAL RESOLUTION 19 µm).

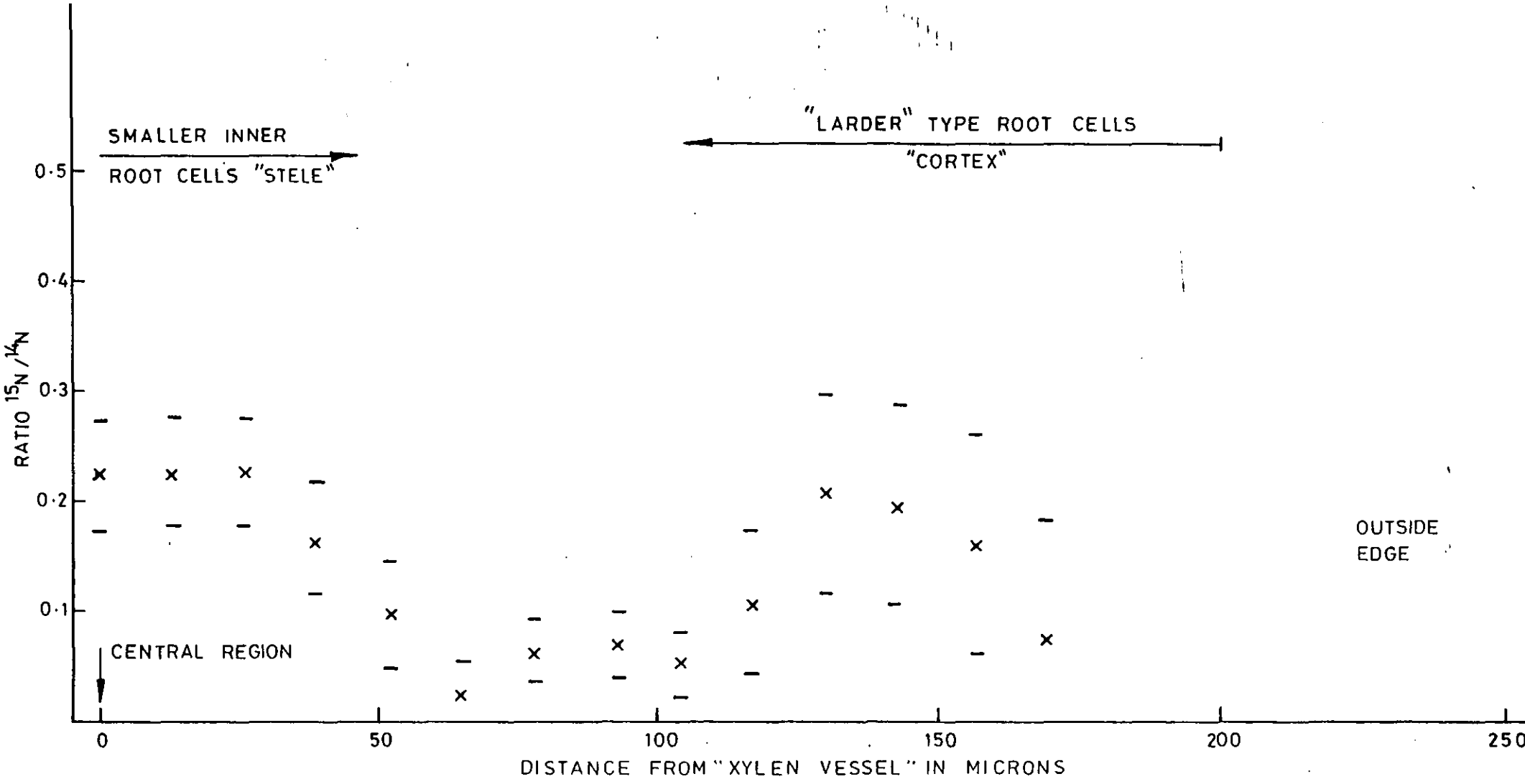

FIG. 8·16. PROFILE OF THE AVERAGE wt% ^{15}N/wt% ^{14}N RATIO ACROSS BARLEY ROOT SECTIONS TREATED INITIALLY FOR 24 HOURS IN ^{15}N CULTURE B AND SUBSEQUENTLY IN ^{14}N CULTURE A FOR A FURTHER 24 HOURS (SPATIAL RESOLUTION 13 μm).